Classification of Breast Malignancy using Optimised Advanced Diffusion-Weighted Imaging; and Surgical Planning for Breast Tumour Resection using MR-guided Focused Ultrasound

Nina Louise Purvis, MPhys (Hons.)

PhD by Thesis

Doctor of Philosophy (Medical Sciences)

The University of Hull and The University of York

Hull York Medical School

August 2016

Author's Declaration

I confirm that this work is original and that if any passage(s) or diagram(s) have been copied from academic papers, books, the internet or any other sources these are clearly identified by the use of quotation marks and the reference(s) is fully cited. I certify that, other than where indicated, this is my own work and does not breach the regulations of HYMS, the University of Hull or the University of York regarding plagiarism or academic conduct in examinations. I have read the HYMS Code of Practice on Academic Misconduct, and state that this piece of work is my own and does not contain any unacknowledged work from any other sources. I confirm that any patient information obtained to produce this piece of work has been appropriately anonymised.

Abstract

Intravoxel Incoherent Motion Imaging (IVIM) is a non-invasive MR-imaging technique that enables the measurement of cellularity and vascularity using diffusion-weighted (DW)-imaging. IVIM has been applied to various cancer types including breast cancer, and is becoming more popular but lacks standardisation. The quantitative parameters; diffusion, *D*, perfusion fraction, *f*, and pseudo micro capillary diffusion, *D** are thought to be correlated with tumour physiognomies such as proliferation, angiogenesis and heterogeneity.

In Part 1 of this thesis, an optimised clinical b-value protocol is produced using a robust statistical method. This optimised protocol and various fitting methodologies are investigated in healthy volunteers, and then the most precise approach is applied in a clinical trial in patients following diagnosis of breast cancer, before treatment, to correlate IVIM parameters with breast cancer grade, histological type and molecular subtype with statistically significant results supporting IVIM's potential as a non-invasive biomarker for malignancy. Monte Carlo simulations support this clinical application, where real data mean squared errors due to SNR limitations lie within simulated errors. A computed DW-imaging program is also presented to produce better quality images than acquired high b-value images as an adjunct to the optimised IVIM protocol.

In Part 2 of this thesis, MR-guided Focused Ultrasound (MRgFUS) is explored as a means to create a pre-surgical template of thermally induced palpable markers to enable a surgeon to resect occult lesions and potentially reduce positive tumour margin status and local recurrence after breast conserving surgery. A surrogate animal model with pseudo lesion is presented, as well as a clinical tool to plan spot markers around a lesion as seen on MRI.

Publications and Conferences

Purvis NL, Gibbs P, Pickles MD, Turnbull LW. MRI & Ultrasound: A Synergistic to the Localisation and Treatment of Malignancy, HYMS Postgraduate Research Conference, York, 2014.

Purvis NL, Gibbs P, Pickles MD, Turnbull LW. MRI & Ultrasound: A Synergistic to the Localisation and Treatment of Malignancy, Yorkshire Cancer Research Annual Scientific Meeting, Harrogate, 2014

Purvis NL, Gibbs P, Pickles MD, Turnbull LW. MRI & Ultrasound: A Synergistic to the Localisation and Treatment of Malignancy, ISMRM British Chapter, Cardiff, 2014.

Purvis NL, Gibbs P, Pickles MD, Turnbull LW. Optimisation of b-value Distribution for Intravoxel Incoherent Motion (IVIM) Imaging of Breast Cancer with Clinical Results, ISMRM Annual Postgraduate Meeting, GSK Stevenage, 2015.

Purvis NL, Gibbs P, Pickles MD, Turnbull LW. Optimisation of b-value Distribution for Intravoxel Incoherent Motion (IVIM) Imaging of Breast Cancer with Clinical Results, ISMRM 23rd Annual Meeting and Exhibition, Toronto, 2015.

Purvis NL, Gibbs P, Pickles MD, Turnbull LW. Investigation of the Presence and Repeatability of Intravoxel Incoherent Motion (IVIM) in Breast Parenchyma of Healthy Volunteers using an Optimised b-value Scheme, ISMRM 23rd Annual Meeting and Exhibition, Toronto, 2015.

Purvis NL, Gibbs P, Pickles MD, Turnbull LW. Optimisation of b-value Distribution for Intravoxel Incoherent Motion (IVIM) Imaging of Breast Cancer with Clinical Results, HYMS Postgraduate Research Conference, Hull, 2015.

Purvis NL, Gibbs P, Pickles MD, Turnbull LW. Optimisation of b-value Distribution for Intravoxel Incoherent Motion (IVIM) Imaging of Breast Cancer with Clinical Results, Yorkshire Cancer Research Annual Scientific Meeting, Harrogate, 2015.

Purvis NL, Gibbs P, Pickles MD, Turnbull LW. Optimisation of b-value Distribution for Intravoxel Incoherent Motion (IVIM) Imaging of Breast Cancer with Clinical Results, ESMRMB, Edinburgh, 2015.

Acknowledgements

Firstly, I would like to thank Yorkshire Cancer Research for my PhD scholarship, and for their funding towards this research through the CMRI YCR endowment. Thank you to the universities of Hull and York, and to Hull York Medical School for their support during my research.

Thank you to all CMRI staff, especially the university's former radiographers Dan and Julie for teaching me how to scan and for their company when in the scan room. Thanks to my fellow students Michael and Lawrence (now postdoctoral researcher), especially for helping me with MATLAB and for being good lab mates. Thank you to the former Scientific Director of the CMRI, Professor Lindsay Turnbull, for being an inspiring medic and scientist.

A huge thank you to the dozens of healthy volunteers who allowed me to scan their breasts to develop the IVIM protocol – it is a very personal and claustrophobic experience. Your time and kindness have hopefully helped further breast cancer research. A special mention for repeat and long distance volunteers – Kate, Mel and Debbie!

Thank you to my second supervisor, Dr Martin Pickles, for teaching me about MRI and its clinical application, and for always having a sense of humour even when drawing ROIs on hundreds of breast MRIs. You have made an impression on me to always work harder and put the hours in – a lesson that I should have perhaps learned earlier but I got there eventually.

I cannot put into words how thankful I am to my supervisor, Dr Peter Gibbs, for his patience and support throughout the highs and lows of the four years of my PhD. It has been an honour to study under such an intelligent and kind supervisor. I started off with you as a boss, and I finish this PhD with you as my friend. Hopefully I can repay your kindness one day. Now you have Theo, who is definitely worth all of the hard work and stress – I think!

I would obviously like to say thank you to my family. I am sure they think I will never graduate and get a real job; but I promise I will after medical school! To my grandparents, who always tell me how proud they are - I'll buy you that expensive car one day, granddad. To my parents, who support me no matter what direction I take with my life and career. I love you both very, very much and you are both wonderful people and parents.

Thank you to my life-long friends – from school (Jodie, Joanna, Tracy, and the rest of the gang), my undergraduate studies (Janine) and Hull life in general (Chelsey). Thank you for the good times and support over these 4 years, and the rest. Especially Amy and Becky, my non-biological sisters. I love you both.

Thank you to my partner, Adam, who came into my life at just the right time and I have no doubt that without you, this thesis would not have been finished.

Finally, I am humbled everyday by patients, their support networks, my mentors and colleagues. It is this network in medicine that has kept my interest and purpose.

In loving memory of Verona Dixon.

I wish you could have read this.

List of Tables

List of Figures

Table of Contents

1. Magnetic Resonance Imaging

1.1. Introduction and History

Magnetic Resonance Imaging (MRI) is an imaging technique predominantly used in medicine to produce detailed images of anatomy inside the human body. MRI has evolved from its recognised medical beginnings in the 1970s (1) to become the imaging method of choice for a large proportion of radiological examinations, especially in cancer imaging. MRI uses the concept of Nuclear Magnetic Resonance (NMR), which deals with isotopes in a magnetic field with respect to the distribution and behaviour of their magnetic moments. The NMR sensitivity of hydrogen nuclei (protons) is greater than that of any other nuclei, due to their non-zero spin and lack of electron shielding. Hydrogen as an element is abundant in the human body. The structural composition of a tissue is influenced by the distribution of hydrogen nuclei within it, allowing excellent tissue contrast. This is why MRI is particularly suited to medical applications. Other nuclei, such as sodium and carbon, may also be imaged. There are a wide variety of MR techniques available, with this thesis concentrating predominantly on diffusion-weighted imaging (DWI). MRI is used routinely in cancer localisation, diagnosis, and follow-up without exposing the patient to ionising radiation. An overview of the key physical principles is detailed in this chapter, as MRI serves as the main tool of enquiry in much of this thesis.

1.2. Spin and the Nuclear Magnetic Resonance Phenomenon

1.2.1. Nuclei and Magnetic Moments

MRI is achieved by exploiting the signal from the nuclei of hydrogen atoms (^{1}H). A hydrogen atom consists of a single proton and a single electron orbiting the nucleus. The proton has a positive charge and the electron has a negative charge, meaning the atom, as a whole, is electrically neutral. The proton of the hydrogen atom is of great significance in MRI, shown in Figure 1.1 below.

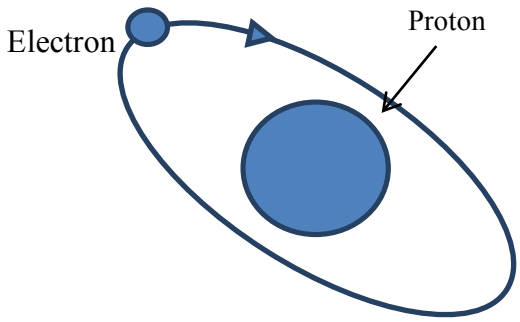

Figure 1.1: A hydrogen atom with a nucleus consisting of a single proton and a single electron orbiting the nucleus.

In addition to its positive charge, the proton possesses spin. This is an intrinsic property of most elementary particles. An analogy to visualise this property is to imagine the proton is rotating about its axis like a spinning top. As a rotating mass (m), the proton has angular momentum (**J**) and strives to retain the orientation of its rotation axis. As a rotating mass with an electrical charge, an electric field is generated and the proton additionally has a magnetic moment (**μ**) shown in Figure 1.2 below.

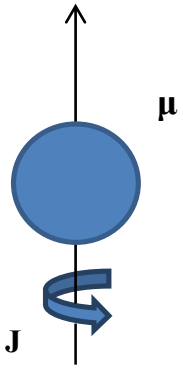

Figure 1.2: A charged particle with angular momentum, J, spinning on its axis, which produces a magnetic moment, μ.

The magnetic moment is directly proportional to the angular momentum (Note that vectors are written in an upright bold font while their corresponding magnitudes are in italics) shown by;

$$\boldsymbol{\mu} = \gamma \mathbf{J}$$

Equation 1.1

where γ is the gyromagnetic ratio. For the hydrogen nucleus (proton) $\gamma = 42.58\ MHz\ T^{-1}$.

1.2.2. Derivation of the Larmor Equation: Classical Mechanics

The motion of a magnetic moment in an external magnetic field ($\mathbf{B_0}$) can be considered classically. When this moment is exposed to $\mathbf{B_0}$ a torque is exerted on the moment given by;

$$\mathbf{T} = \boldsymbol{\mu} \wedge \mathbf{B_0}$$

Equation 1.2

where **T** is the torque. The torque acts in a direction perpendicular to both **μ** and **B** and can be equated to the rate of change of angular momentum, described by;

$$\frac{d\mathbf{J}}{dt} = \boldsymbol{\mu} \wedge \mathbf{B_0}$$

Equation 1.3

Using Equation 1.1, this leads to the equation of motion within a main magnetic field;

$$\frac{d\boldsymbol{\mu}}{dt} = \boldsymbol{\mu} \wedge \gamma \mathbf{B_0}$$

Equation 1.4

This shows that changes in **μ** are perpendicular to both $\mathbf{B_0}$ and **μ** thus not allowing the proton to perfectly align with $\mathbf{B_0}$, instead forcing it to precess about $\mathbf{B_0}$. The precessional frequency ($\boldsymbol{\omega_0}$), the rate at which the proton precesses around $\mathbf{B_0}$, is proportional to the external magnetic field, as shown by the Larmor equation below. Figure 1.3 depicts this diagrammatically.

$$\boldsymbol{\omega_0} = -\gamma \mathbf{B_0}$$

Equation 1.5

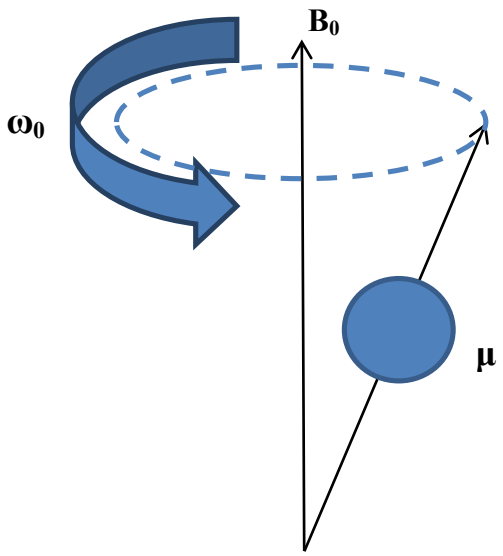

Figure 1.3: A magnetic moment μ precessing around B_0 at the precessional frequency ω_0.

1.2.3. Derivation of the Larmor Equation: Quantum Mechanics

A magnetic moment in an applied external magnetic field has been considered classically thus far. This phenomenon may also be described using quantum mechanics, as follows.

The total angular momentum (**J**) of an isolated particle can only take certain discrete values and its magnitude is given by;

$$|\mathbf{J}| = \hbar\sqrt{I(I-1)}$$

Equation 1.6

where $\hbar$ is Planck's constant divided by 2π and I is the spin quantum number. The only measurable components of **J** are the eigenvalues $J_z = m_z\hbar$. Therefore;

$$\mu_z = \gamma m_z \hbar$$

Equation 1.7

where μ_z is the measurable component of **μ**. The magnetic quantum number m_z can take any of the (2I+1) values in the series –I, -I+1, -I+2… I-2, I-1, I.

The value of the spin quantum number I obeys the following rules due to the pairing nature of nucleons. Nuclei with an odd mass number have half-integral spin (for example ^{1}H,

used in MRI). Nuclei with an even mass number and an even atomic number have zero spin (for example ^{16}O and ^{12}C). Nuclei with an even mass number and an odd atomic number have integral spin (for example ^{14}N). Isotopes with I = 0 are also NMR insensitive. This is summarised for some of the most recognisable elements in Table 1.1.

Nucleus	Spin quantum number (I)	Number of energy states (N)
^{19}F	$1/2$	2
^{1}H	$1/2$	2
^{13}C	$1/2$	2
^{23}Na	$3/2$	4
^{17}O	$5/2$	6

Table 1.1: Spin quantum number and energy states for various nuclei.

In the absence of an externally applied magnetic field, if two or more spin states of a nucleus are all at the same energy level, they are said to be degenerate. Once this degeneracy has been pertubated, in this case after the application of an external magnetic field, an extra term is introduced into the nuclear Hamiltonian as the energy levels split. The energy of a magnetic moment (U) is given by;

$$\mathbf{U} = -\mu_z \mathbf{B_0}$$

Equation 1.8

From Equation 1.7 this gives;

$$\mathrm{U} = -\gamma m_z \hbar \mathbf{B_0}$$

Equation 1.9

Equation 1.9 shows that the energy of a magnetic moment is directly proportional to the strength of the externally applied magnetic field. Transitions can be induced between the split energy levels of the system according to the selection rule as in Equation 1.10;

$$\Delta m_z = \pm 1$$

Equation 1.10

Provided the Bohr frequency condition is met via;

$$\Delta U = \hbar\boldsymbol{\omega_0} = |-\gamma \Delta m_z \mathbf{B_0}|$$

Equation 1.11

Equation 1.11 reduces to the Larmor equation;

$$\boldsymbol{\omega_0} = \gamma \mathbf{B_0}$$

Equation 1.12

Therefore energy at the Larmor frequency must be delivered for transitions between energy states to occur. This required frequency of radiation is proportional to the magnetic field strength. Protons have a gyromagnetic ratio of 42.58 $MHz\ T^{-1}$, resulting in a Larmor frequency of 127.74 *MHz* at 3.0 *T*.

A combined picture of magnetic moments in an externally applied magnetic field has been presented. Individual protons will obey quantum mechanics, while classical mechanics can describe their average behaviour.

1.2.4. Macroscopic Magnetisation

In the absence of an external magnetic field, the sum of all magnetic moments is zero, shown in Figure 1.4.

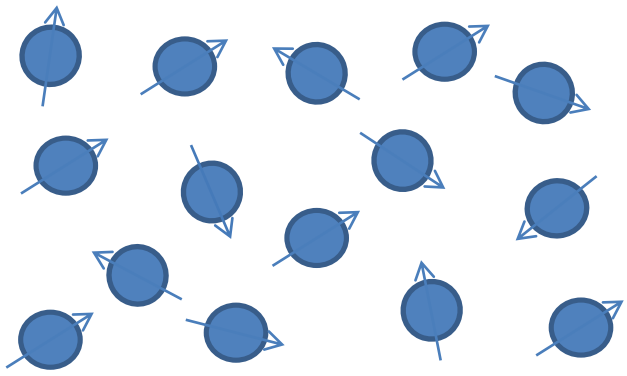

Figure 1.4: The magnetic moments of protons in the absence of an external magnetic field. The sum of all magnetic moments is zero because they are oriented in a random fashion.

In the case of a hydrogen proton, there are two energy states. It has a spin up or parallel state of +½ and a spin down or antiparallel state of -½. Figure 1.5 shows the energy states of a hydrogen nucleus.

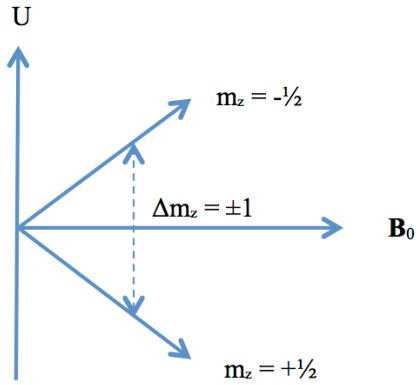

Figure 1.5: The energy states of a hydrogen nucleus.

Spins are divided between the Zeeman energy levels according to the Boltzmann distribution;

$$\frac{N\downarrow}{N\uparrow} = e^{-\frac{\Delta U}{k_B T}} = e^{-\frac{\gamma \hbar B_0}{k_B T}}$$

Equation 1.13

where k_B is the Boltzmann constant, T is the absolute temperature, N ↓ is the number of spins in the high energy state (anti-parallel) and N ↑ is the number of spins in the low energy state (parallel).

In the human body there are many millions of protons available from the abundance of water (and hence hydrogen). The spins with lower energy states (spin up or parallel) are naturally more abundant due to this state having higher stability than that of the higher energy state (spin down or anti-parallel). This can be approximated to;

$$N\uparrow - N\downarrow \approx \frac{\gamma \hbar N B_0}{2k_B T}$$

Equation 1.14

where N is the total number of spins. As a result of this small difference there exists a macroscopic net magnetisation, M_0, of the system. The net magnetisation can be described by;

$$\mathbf{M_0} = \sum_j \boldsymbol{\mu_j}$$

Equation 1.15

The equation of motion (Equation 1.4) can then be modified to account for the sum of all the magnetic moments;

$$\frac{d\mathbf{M_0}}{dt} = \mathbf{M_0} \hat{} \gamma \mathbf{B_0} = \gamma \mathbf{M_0} \hat{} \mathbf{B_0}$$

Equation 1.16

where $\mathbf{B_0}$ is the applied magnetic field. This corresponds to a precession of the net magnetisation around the applied field. The nuclei are randomly distributed around the cone of precession. Using Equation 1.14, the magnitude of the net magnetisation (M_0) is;

$$\mathrm{M_0} = (\mathrm{N}\uparrow - \mathrm{N}\downarrow)\mu_z = \frac{\gamma \hbar \mu_z N \mathrm{B_0}}{2k_B T}$$

Equation 1.17

Recalling $\mu_z = \gamma \hbar m_z$ and $m_z = ½$;

$$\mathrm{M_0} = \frac{\gamma^2 \hbar^2 B_0 N}{4k_B T}$$

Equation 1.18

Figure 1.6 demonstrates these spin states precessing around an external magnetic field with a net magnetisation.

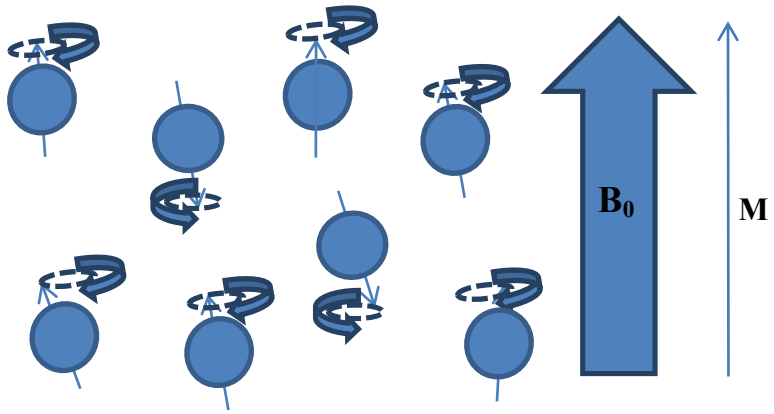

Figure 1.6: Parallel and antiparallel spin states precessing around the external main magnetic field, B0. M is the net magnetisation vector. The transverse components are cancelled since the spins are equally distributed about the cone of precession.

From Equation 1.18 it can be seen that the net magnetisation is affected by the number of spins, the gyromagnetic ratio, the magnetic field strength and the temperature. In practise, the only thing that can be changed is the magnetic field strength, which is why scientists endeavour to increase the field strength of commercial MRI scanners.

1.3. The Rotating Frame of Reference

Energy transitions are induced by the use of a time-dependent magnetic field. The macroscopic magnetisation precesses around the total applied field. This motion is difficult to visualise in the laboratory frame of reference so it is useful to introduce the concept of a rotating frame of reference, rotating at the Larmor frequency. Application of the time dependent field thus corresponds to rotation around this field in the rotating frame.

1.4. Radiofrequency Pulses

Energy can be introduced into a stable spin system by applying an electromagnetic (EM) wave of the same frequency as the Larmor frequency. The required EM wave is generated by a radio transmitter and applied to the object to be imaged by means of an antenna coil. The process of this energy absorption is known as excitation of the spin system. An excitation radiofrequency (RF) pulse applied on-resonance for a finite amount of time is termed the $\mathbf{B_1}$ field. This RF pulse results in the longitudinal (M_z) magnetisation being tipped away from the z-axis towards the transverse (xy-) plane perpendicular to the direction of the main magnetic field. The precessional frequency around $\mathbf{B_1}$ is given by;

$$\boldsymbol{\omega_1} = \gamma \mathbf{B_1}(t)$$

Equation 1.19

The magnetisation can be rotated through any desired angle by applying the $\mathbf{B_1}$ field for a certain length of time. The flip angle can be easily manipulated by adjusting either the duration or strength of the applied field. By applying a 180° RF pulse, excess spins will exist in the higher energy state caused by an inversion of the equilibrium population difference; whilst a 90° RF pulse will equalise the spin populations and individual spins will cluster together in the cone of precession. The angle of rotation, known as the flip angle, can be shown in the rotating frame of reference by;

$$\theta = \gamma B_1 \tau$$

Equation 1.20

where τ is the duration of the RF pulse and B_1 is the amplitude of the applied field for the duration of the pulse.

1.5. Relaxation

After the excitation of an RF pulse, the system loses energy and returns to equilibrium. The spins that are in the transverse plane dissipate energy and realign with the B_0 field in the longitudinal plane. This process is known as relaxation.

Immediately after excitation, the net magnetisation vector rotates in the transverse plane (M_{xy}). When transverse magnetisation is present, it precesses about the longitudinal axis which has the effect of an electrical generator and induces an alternating voltage of the same frequency as the Larmor frequency in a receiver coil. This is the NMR signal. The NMR signal fades rapidly due to two independent processes that reduce transverse magnetisation and thus cause a return to the stable state present before excitation. The two processes are spin-lattice interaction (T_1 relaxation) and spin-spin interaction (T_2 relaxation).

1.5.1. T1 (Spin- lattice) Relaxation

Immediately after the RF pulse is terminated, transverse magnetisation decays and spins gradually re-align with the longitudinal axis of $\mathbf{B_0}$. As transverse magnetisation (M_{xy}) decays, the longitudinal magnetisation (M_z) is slowly restored. This process is known as longitudinal recovery or T_1 recovery.

The nuclei can only return to their original state by dissipating their energy into their surroundings or lattice, hence the name spin-lattice relaxation. The time constant for this recovery is T_1, known as the longitudinal relaxation time. At $t = T_1$, 63% of the signal has been recovered. It is dependent on the magnetic field strength of B_0 and the internal motion of molecules (Brownian motion). This is shown in Figure 1.7.

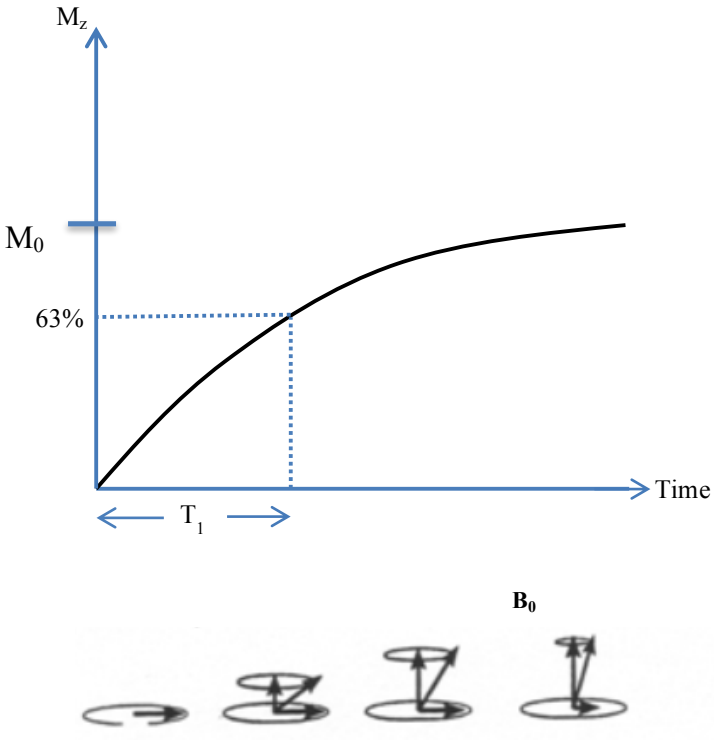

Figure 1.7: A graphical representation of the recovery of the longitudinal magnetisation, which follows an exponential curve. Longitudinal magnetisation has returned to 63% of its final value after time T1. The spiralling arrow depicts the net magnetisation vector realigning with B_0.

1.5.2. T2 (Spin-Spin) Relaxation

Immediately after excitation, all spins precess synchronously. They are in phase with one another. Phase coherence is lost after the RF pulse is removed. The individual magnetisation vectors begin to cancel each other out instead of adding together. The resulting vector sum, the transverse magnetisation, becomes smaller and then disappears, and with it the MR signal. Transverse relaxation is the decay of transverse magnetisation because spins lose their phase coherence and dephase. Coherence is lost in two ways.

The first process is an energy transfer, which occurs between spins as a result of local changes in the magnetic field. Such fluctuations are due to the fact that spins are associated with small magnetic fields that interact with each other. Spins precess faster or slower depending on the magnetic field variations they experience. The overall result is a cumulative loss of phase coherence. This dephasing occurs with time constant T_2, known as the transverse relaxation time. At $t = T_2$, 63% of the signal has been lost. This is shown in Figure 1.8 below.

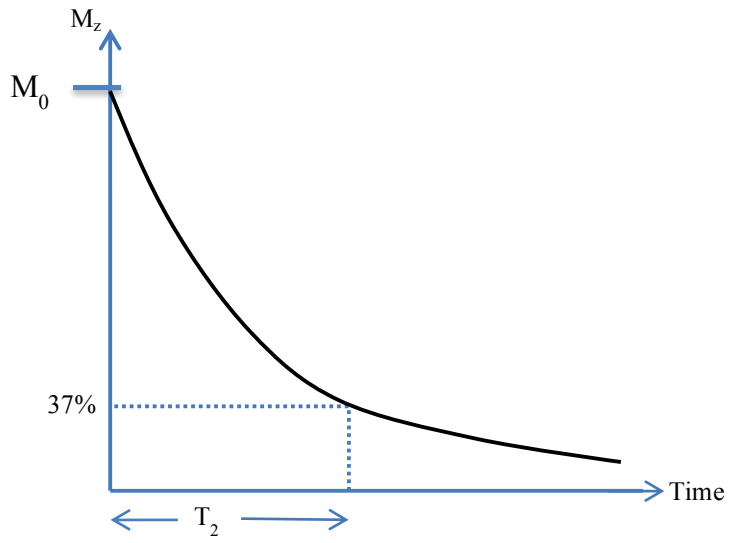

Figure 1.8: A graphical representation of the loss of the transverse magnetisation, which follows an exponential curve. Transverse magnetisation has lost 63% of its final value after time T2.

The second process is due to time-independent inhomogeneities of the external magnetic field B_0. These are intrinsic homogeneities that are caused by the magnetic field generator itself and by the object or person being imaged. This contribution to dephasing results in a signal decay faster than the T_2 time constant, and the summation of T_2 effects with these inhomogeneities is called T_2^*. T_1 and T_2 relaxation processes are completely independent of each other, but occur simultaneously at different rates.

1.5.3. Free Induction Decay

The signal detected in the transverse plane is determined by the relaxation processes described in 1.5.2. If nothing is affecting the homogeneity of the magnetic field all of the spins will be spinning at the same resonance frequency, the Larmor frequency. The signal in the absence of

any magnetic gradients is known as Free Induction Decay (FID). An FID has no positional information and decays exponentially. The initial amplitude of the signal is determined by the portion of the net magnetisation vector that has been tipped onto the transverse plane. The maximum signal is obtained when the flip angle is 90°. The decay curve is the signal envelope. In clinical conditions, the NMR signal decays faster than T_2 would predict since the main external field is not absolutely homogeneous. As previously described, pure T_2 decay is a function of completely random interactions between spins. In reality, the signal envelope height is determined by T_2*, the sum of effects due to T_2, and intrinsic inhomogeneities that are caused by the magnetic field generator itself and by the object or person being imaged.

$$\frac{1}{T_2^*} = \frac{1}{T_2} + \frac{1}{T_2'}$$

Equation 1.21

where T_2' is the time constant of the decay due to magnetic field inhomogeneities described in Section 1.5.2. Figure 1.9 shows the signal envelope of free induction decay.

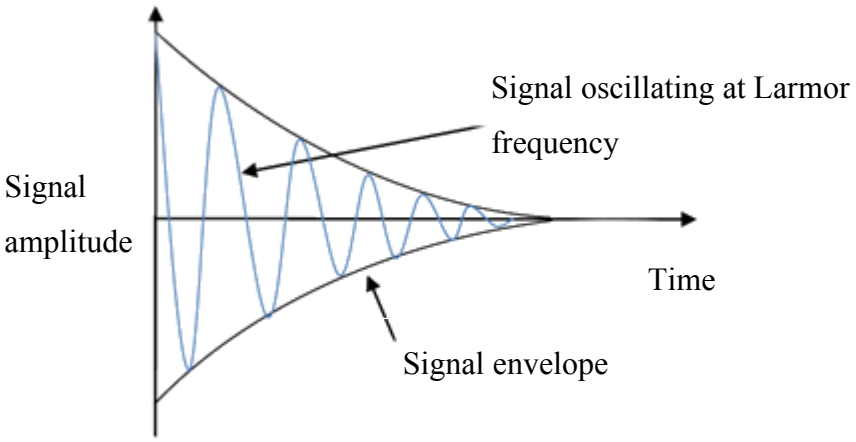

Figure 1.9: Free induction decay. The signal envelope decays with a time constant T2*.

1.6. Bloch Equations

After perturbation the spin system returns to equilibrium via the dissipation of energy to the surrounding lattice and neighbouring spins. These relaxation processes were incorporated into the equation of motion phenomenologically by Felix Bloch in 1946. These are;

$$\frac{dM_x}{dt} = \gamma[\mathbf{M}\hat{}\mathbf{B}]_x - \frac{M_x}{T_2}$$

Equation 1.22

$$\frac{dM_y}{dt} = \gamma[\mathbf{M}\hat{}\mathbf{B}]_y - \frac{M_y}{T_2}$$

Equation 1.23

$$\frac{dM_z}{dt} = \gamma[\mathbf{M}\hat{}\mathbf{B}]_z - \frac{M_z - M_0}{T_1}$$

Equation 1.24

where $B_x = B_1 \cos \omega t$, $B_y = B_1 \sin \omega t$ and $B_z = B_0$. $M_{x,y,z}$ is the magnitude of magnetisation in the x-, y-, and z-axis respectively. **M^B** is the vector cross product of **M** and **B**.

The evolution of the transverse (M_x, M_y) and longitudinal (M_z) magnetisation components are independent relaxation processes as explained in section 1.5.

In most circumstances it is assumed that $T_2 << T_1$ so that transverse relaxation is completed before longitudinal relaxation commences. T_1 controls return to equilibrium and at equilibrium there is no transverse magnetisation. Therefore, T_2 relaxation must be completed before T_1 relaxation is completed.

The recovery of the longitudinal magnetisation after excitation is given in Equation 1.24. After a 90º RF excitation pulse $M_z(0)=0$ giving;

$$M_z = M_0 \left[1 - e^{-\frac{t}{T_1}}\right]$$

Equation 1.25

After a 180º RF inversion pulse $M_z(0)=-M_0$, giving;

$$M_z = M_0 \left[1 - 2e^{-\frac{t}{T_1}}\right]$$

Equation 1.26

After application of an RF excitation pulse, the transverse magnetisation decays in the rotating frame of reference as;

$$\frac{\partial M_{x,y}}{\partial t} = -\frac{M_{x,y}}{T_2}$$

Equation 1.27

After a 90º RF excitation pulse, the solution for the recovery of transverse magnetisation is;

$$M_{x,y} = M_{x,y}(0)e^{-\frac{t}{T_2}}$$

Equation 1.28

1.7. Signal Detection

In signal detection a coil is used for transmission and detection. This may be one coil that does both, or separate coils. At the end of the pulse the receiver is gated open, and the EMF induced in the receiver coil detects the component of magnetisation in the transverse plane. This is shown in Figure 1.10.

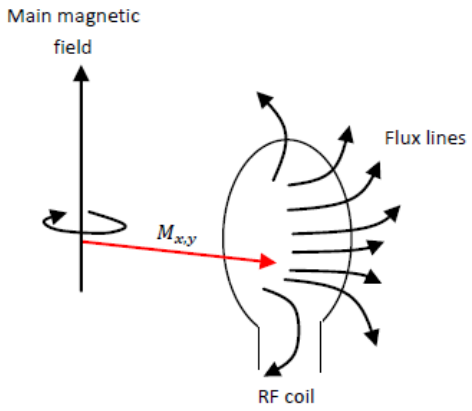

Figure 1.10: A signal is induced and detected by the same coil.

1.8. Electronic shielding

The sample or patient present within the MRI scanner has an effect on the externally applied field. The orbital electrons around the nucleus produce small magnetic fields, which in turn shield the nucleus from the full influence of B_0 causing the effective field at the nucleus to become;

$$B_{eff} = (1 - \sigma)B_0$$

Equation 1.29

where σ is the shielding constant. Since the local electronic environment causes the shielding effect, σ therefore varies with nuclear position within the molecule. The resonance condition thus can be described by;

$$\omega_0 = \gamma(1-\sigma)B_0$$

Equation 1.30

Variations in resonant frequency will be caused by variations in σ.

1.9. Chemical Shifts

The Larmor frequencies for two different nuclei in different chemical environments are given by;

$$\omega_1 = \gamma(1-\sigma_1)B_0$$

Equation 1.31

$$\omega_2 = \gamma(1-\sigma_2)B_0$$

Equation 1.32

The chemical shift, given by the difference of these two equations, is;

$$\Delta\omega = \omega_1 - \omega_2 = \gamma(\sigma_2 - \sigma_1)B_0$$

Equation 1.33

The chemical shift is seen to be field dependent. These chemical shifts allow molecular structure to be seen in NMR spectroscopy. It is useful to eliminate the chemical shift field dependence by using a relative chemical shift;

$$\delta = \frac{\omega_1 - \omega_2}{\omega_2}.10^6 = \frac{\sigma_2 - \sigma_1}{1-\sigma_2}.10^6\ ppm$$

Equation 1.34

For proton NMR spectroscopy, shifts are made relative to tetramethylsilane (TMS). The frequency difference between peaks becomes larger with increasing field strength but δ remains constant enabling easier comparison. An example NMR spectra is shown in Figure

1.11. Spectroscopy is particularly useful in assessing the tumour microenvironment and assessing tumour metabolism.

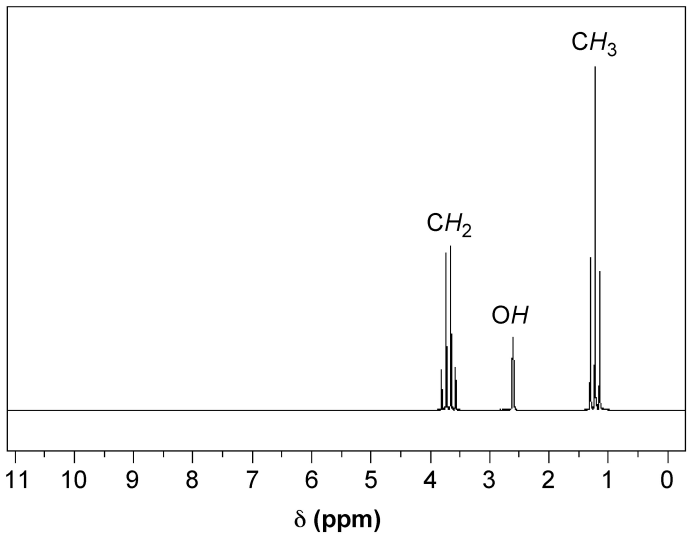

Figure 1.11: A H_1 NMR spectra of ethanol (CH_3CH_2OH). (2)

1.10. Spatial Encoding

MR imaging generates cross-sectional images of the human body. The encoding of MR signal with spatial information is essential for the isolation of finite volumes (voxels) from the patient, and is routinely known as spatial encoding. Gradient coils that are used to apply gradients in the x-, y- and z-axis achieve spatial encoding. The three gradients are known as slice selection, frequency encoding and phase encoding.

1.10.1. Slice selection

To image a pre-defined slice of tissue, the magnetic field is made inhomogeneous in a linear fashion along the z-axis. This is achieved with the application of a linear field gradient, known as the slice selection gradient. The Larmor frequencies thus change gradually along the axis and each slice perpendicular to direction of gradient now has its own unique frequency. Hence, the application of a tailored RF pulse that matches the Larmor frequency of the desired slice will only excite spins within the chosen slice while other spins remain unaffected. Changing the axis in which the gradient is applied can vary the orientation. Sagittal, coronal and axial images can be obtained, as well as oblique and double oblique images.

The slice thickness depends upon the RF pulse bandwidth and the applied gradient field strength.

1.10.2. Phase Encoding

Phase encoding is when a gradient is applied after excitation in order to spatially discriminate signal along the y-axis. This phase encoding gradient alters the Larmor frequencies of the spins according to their location along the applied gradient. The excited spins experiencing higher strengths in the gradient gain phase relative to the slower precessing spins in the lower strength parts of the gradient. There is a resulting phase shift of the spins relative to each other. The degree of phase shift is determined by the duration and amplitude of the applied phase encoding gradient and by the location of precessing spins along it. When the gradient is removed, spins return to their initial rate of precession yet are now ahead or behind in phase relative to their previous state. Phase now varies along the y-axis in a linear fashion.

The difference in phase between spins is limited to ±180°, therefore there is an inability to localise position along a gradient with only one phase encoding step since two spins may be at different phases but express the same phase shift. The phase encoding gradient is repeated N times (N equals the phase matrix) with different gradient strengths including a reference with no gradient strength to account for this. A Fourier transform is then applied to determine each spins position within the main magnetic field.

1.10.3. Frequency Encoding

The MR signal is encoded by changes in frequency along the x-axis. The frequency encoding gradient is a static gradient field that causes a range of Larmor frequencies to exist linearly in the direction in which it is applied. Spins that experience a higher magnetic field precess at higher frequencies than spins experiencing a lower magnetic field. A frequency spectrum is collected from the MR signal. A Fourier transform (FT) can then be used to separate the signal into different frequency components, with the amplitude of each frequency component reflecting the number of spins precessing at that frequency. The frequency encoding gradient is usually applied after the phase encoding gradient.

In summary, the frequency locates the MR signal along the x-axis and the phase distribution within each frequency provides the origin of the MR signal on the y-axis. When all gradients have been applied, the encoded signal is produced and fills one line of K-space.

1.11. K space

Data collected from the MR signal is stored in a mathematical area known as K-space. It is a matrix of digitised MR data that represents the MR image before Fourier transformation is performed. K-space has two axes, with the horizontal axis representing frequency information and the vertical axis representing the phase information. Each line in K-space corresponds to one measurement and one line is acquired for each phase encoding step. The centre line (gradient isocentre) is filled with data that is unaffected by the phase encoding gradient. The lines in K-space do not correspond to each line in the resulting MR image. Rather, data in the centre of K-space primarily determines contrast in the image while the periphery data primarily contains high spatial resolution information such as that found in edges. It is important to acquire full K-space data to produce the image. Partially filled K-space can be used to reconstruct a reasonable image quicker, provided more than half of the K-space is filled. The remaining K-space lines of data can be either filled with zeroes or extrapolated based on the already acquired data.

Prior to the filling of K-space, the signal needs to be demodulated. This results in real and imaginary parts of the signal and consequently each point in K-space has two components, one real and one imaginary. After K-space is filled, an MR image is created by the application of a 2D-FT. A magnitude image is produced from the real and imaginary components of the K-space data.

1.12. Echo Formation

1.12.1. Spin Echo

A spin echo is a simple sequence employed by all MRI scanners. Spin echoes are usually formed by using a 90º RF excitation pulse and a 180º RF refocusing pulse. The 180º refocusing pulse gives a true T_2 signal as opposed to a T_2^* signal. Spin echo sequences can be used to quantify T_2 in NMR by varying the echo time (T_E).

As previously explained, after a 90º RF excitation pulse, the spins precess in phase in the transverse (xy-) plane at the Larmor frequency. Due to transverse relaxation effects (spin-spin, or T_2 and T_2') spins experience a change in precessional frequency and thus a loss of phase coherence. The loss of phase coherence due to T_2 effects is random and incoherent. The loss of phase coherence due to T_2' effects (intrinsic magnetic field homogeneities that are

caused by the magnetic field generator itself and by the object or person being imaged) is constant and coherent. It is this particular property of $T_2^{'}$ effects that is exploited during this sequence. After a time $T_E/2$, the application of a 180º RF refocusing pulse rotates the system about the x-axis. This allows the spins at higher precessional frequencies to converge with those at lower precessional frequencies. After a further time of $T_E/2$, an echo is produced. The signal observed from the spin echo has a pure T_2 component only since any dephasing of spins due to magnetic field homogeneities has been compensated for by the 180º RF refocusing pulse. Pure T_2 effects are not recovered since spins are exchanging energy with their neighbours in a random incoherent fashion. The magnitude of the echo is given by;

$$S_{SE} = S_0 e^{-\frac{T_E}{T_2}}$$

Equation 1.35

where S_0 is the initial amplitude of the FID.

Figure 1.12 shows the stages of a spin echo diagrammatically.

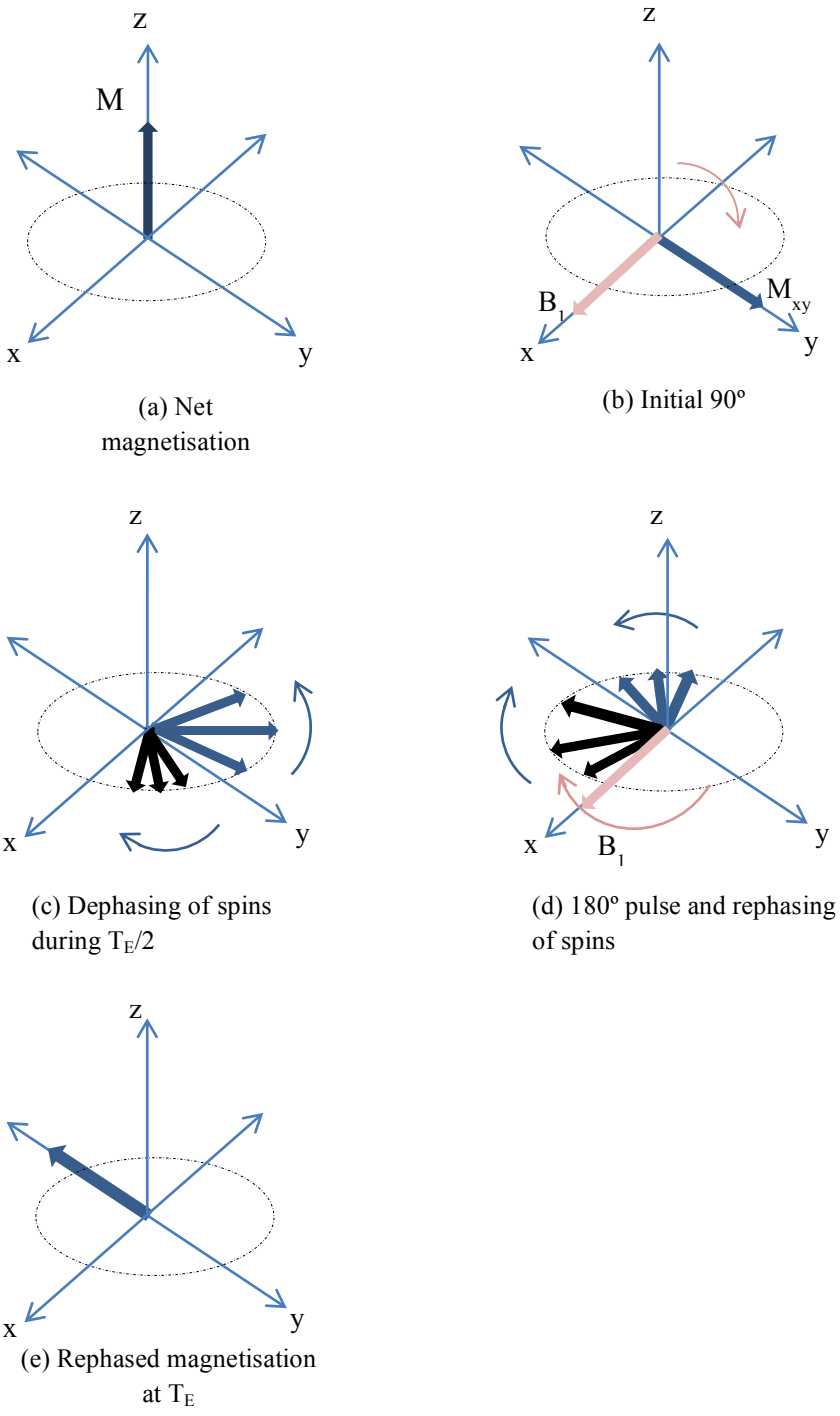

Figure 1.12: The stages of a spin echo sequence; (a) the net magnetisation vector aligned with B0; (b) the application of an RF excitation 90º pulse and the consequential alignment of the net magnetisation vector in the transverse plane; (c) the coherent dephasing of spins; (d) the application of an RF refocusing 180º pulse at TE/2 and the consequential rephasing of spins; (e) the recovered net magnetisation vector in the transverse plane and spin echo formation after TE.

To calculate the T_2 value of a sample the spin-echo experiment must be repeated a number of times with varying values of T_E. It is necessary to wait a time of $5T_1$ between each spin-echo experiment. Figure 1.13 shows a spin echo graphically.

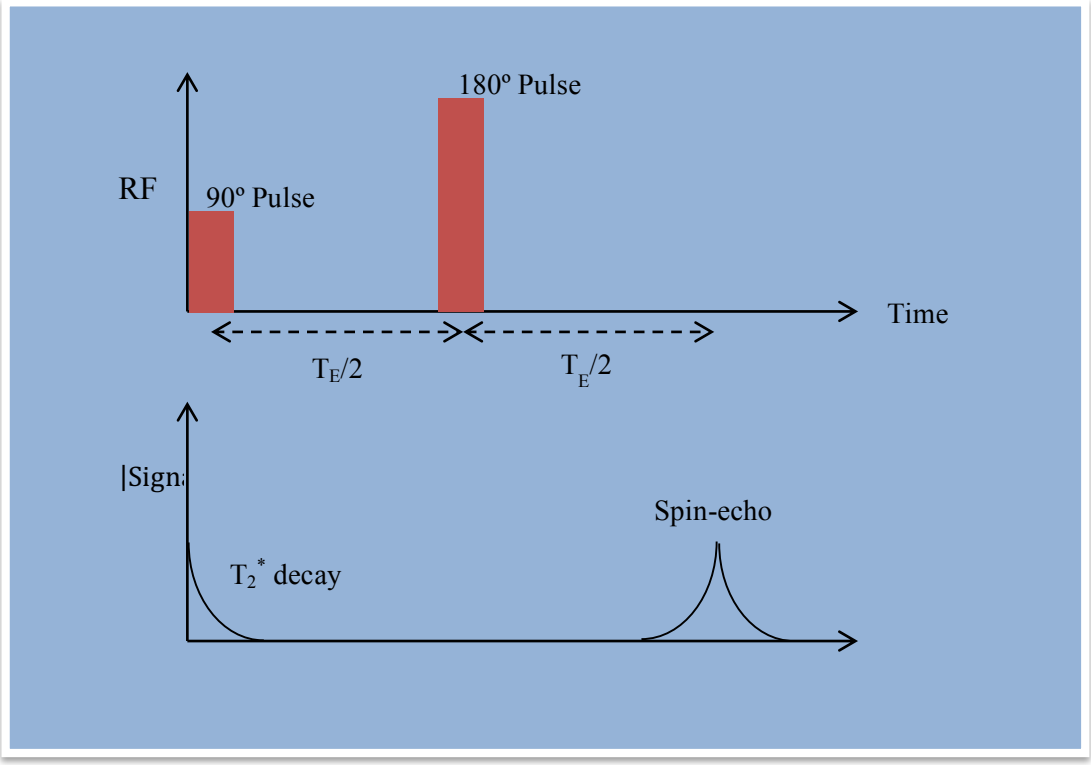

Figure 1.13: A graphical representation of a spin echo sequence.

1.12.2. Gradient Echo

A gradient echo sequence involves a technique that also generates an echo. However, this sequence differs from a spin echo in that the echo is produced by the application of magnetic field gradients instead of an RF refocusing pulse. Firstly, an RF excitation pulse is applied. The flip angle is often lower than 90º and is variable; this causes the magnetisation in the transverse plane to be decreased. The fraction of magnetisation tipped into the transverse plane and the quantity of magnetisation left on the longitudinal axis is determined by the flip angle. Next, a negative lobe gradient is applied which accelerates the dephasing of spins in the transverse plane. A gradient is an additional magnetic field, which alters the magnitude of B_0 in a linear fashion in the direction it is applied. Spins that experience an increased magnetic field due to the gradient precess at a higher frequency while those spins that experience a lower magnetic field precess at a lower frequency, resulting in a loss of phase coherence.

Dephasing due to a gradient is achieved much faster than in pure T_2 free induction decay. The gradient is then reversed to produce a positive lobe. Spins that were experiencing an increased magnetic field now experience a lower magnetic field and vice versa. The spins rephase and produce an echo. The positive gradient can only rephase the actions of the negative gradient, unlike the spin echo technique which corrects dephasing due to magnetic field homogeneities (T_2'). The gradient echo technique produces T_2^* weighted images. The magnitude of the echo is given by;

$$S_{GE} = S_0 e^{-\frac{T_E}{T_2^*}}$$

Equation 1.36

Figure 1.14 shows the stages of a gradient echo diagrammatically.

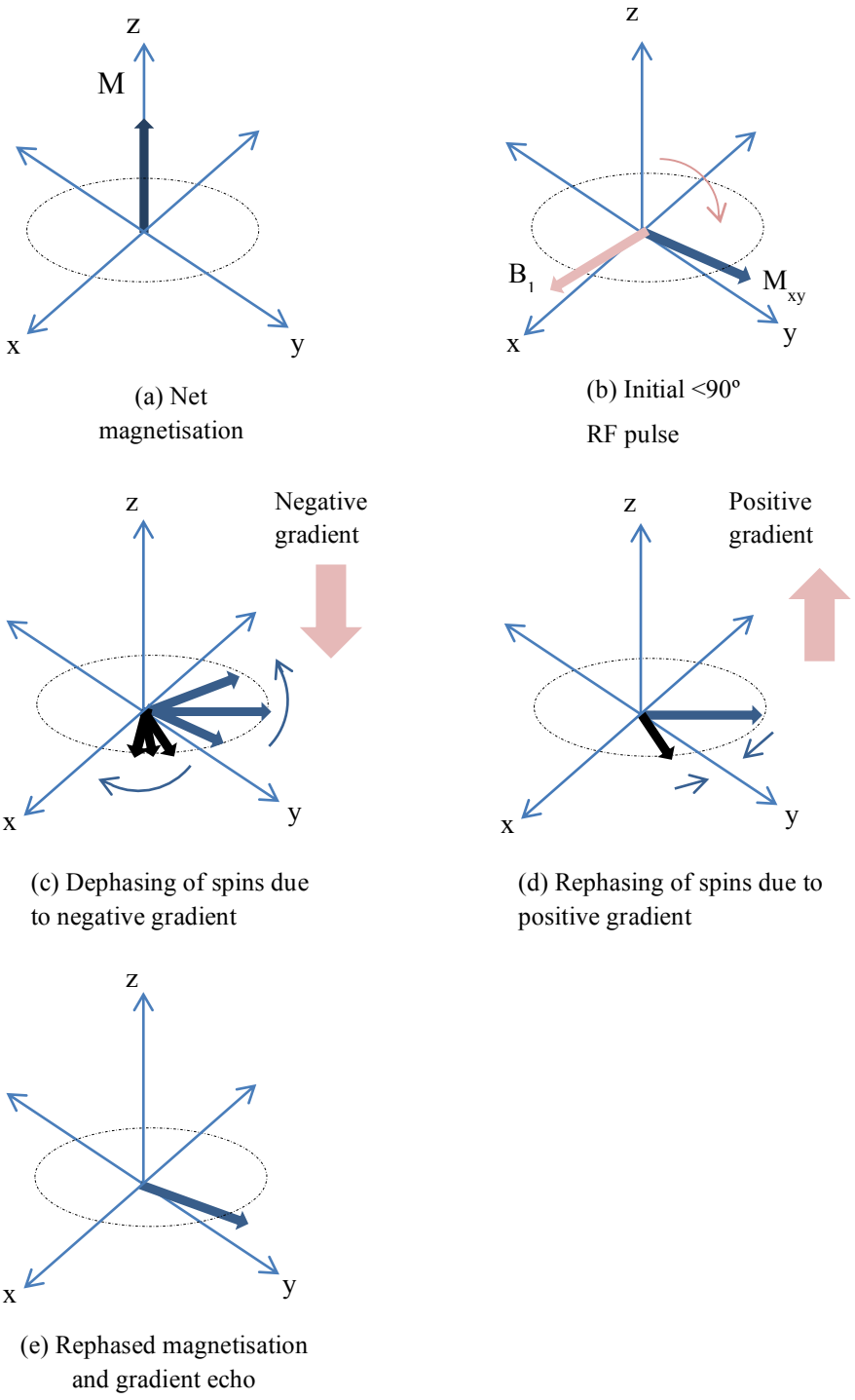

Figure 1.14: The stages of a gradient echo sequence; (a) the net magnetisation vector aligned with B0; (b) the application of an RF excitation pulse (less than 90º) and the consequential alignment of the net magnetisation vector; (c) the rapid dephasing of spins due to a negative lobe gradient; (d) the rapid rephasing of spins due to a positive lobe gradient; (e) the recovered net magnetisation vector and gradient echo formation.

Figure 1.15 shows a gradient echo graphically.

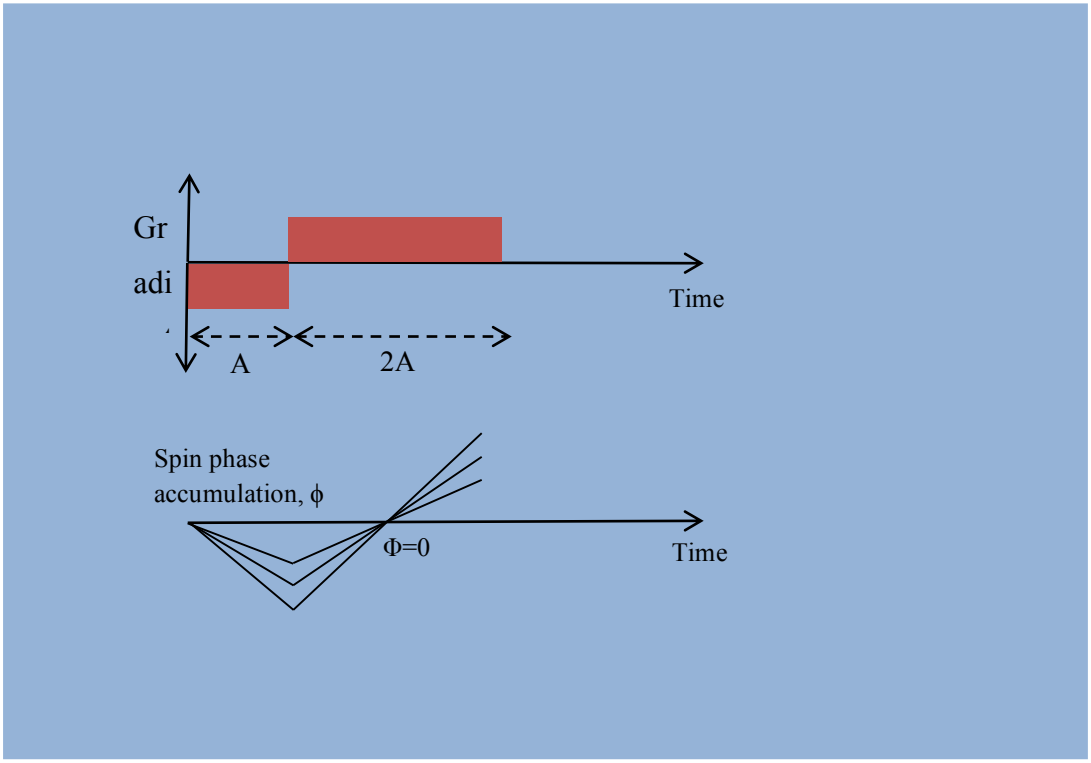

Figure 1.15: Gradient application diagram of a gradient echo sequence. Initial negative gradient is applied to dephase the spins, and then a positive gradient is applied to rephase the spins. Spins are rephased when negative and positive gradient are equal, and spins continue to dephase if the positive gradient is left on.

1.13. Basic Imaging Sequences

Now that the basic physical components of an MRI sequence have been described, these components can all be illustrated in one diagram. Such a diagram is known as a pulse sequence diagram.

1.13.1. Spin-Echo Imaging

Figure 1.16 shows a pulse sequence diagram for a spin echo sequence.

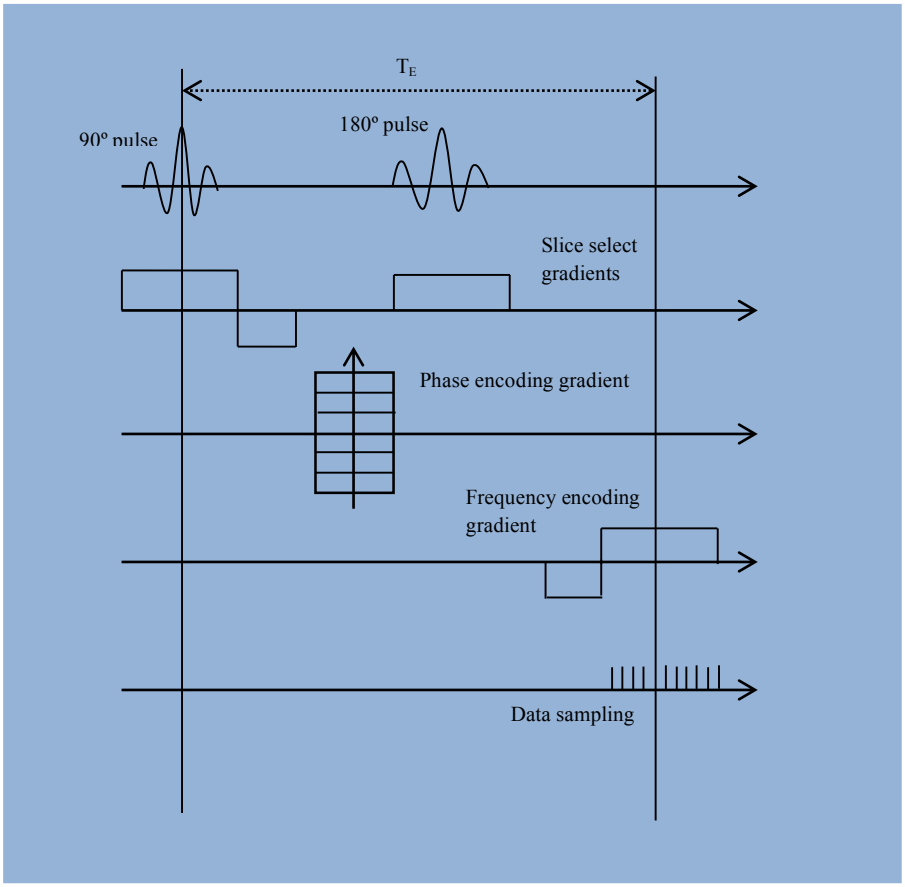

Figure 1.16: A pulse sequence diagram for a spin echo sequence.

An initial 90º pulse is applied in conjunction with a slice select gradient. The phase encoding gradient creates phase differences along the phase encoding axis. A refocusing 180º pulse is applied after $T_E/2$. A spin echo is formed at T_E. A frequency encoding gradient is applied during echo formation. During the read out gradient an analogue to digital converter samples the signal. After a time T_R (Repetition time) the process is repeated with a different phase encoding gradient amplitude. A 2D-FT is performed on the sample to produce an image.

Multi slice imaging is a method of reducing the acquisition time per slice in spin echo imaging. Several slices of tissue are selectively excited in turn during the repetition time interval. This utilises time normally spent waiting for longitudinal recovery prior to re-excitation.

1.13.2. Gradient Echo Imaging

Figure 1.17 shows a pulse sequence diagram for a gradient echo sequence.

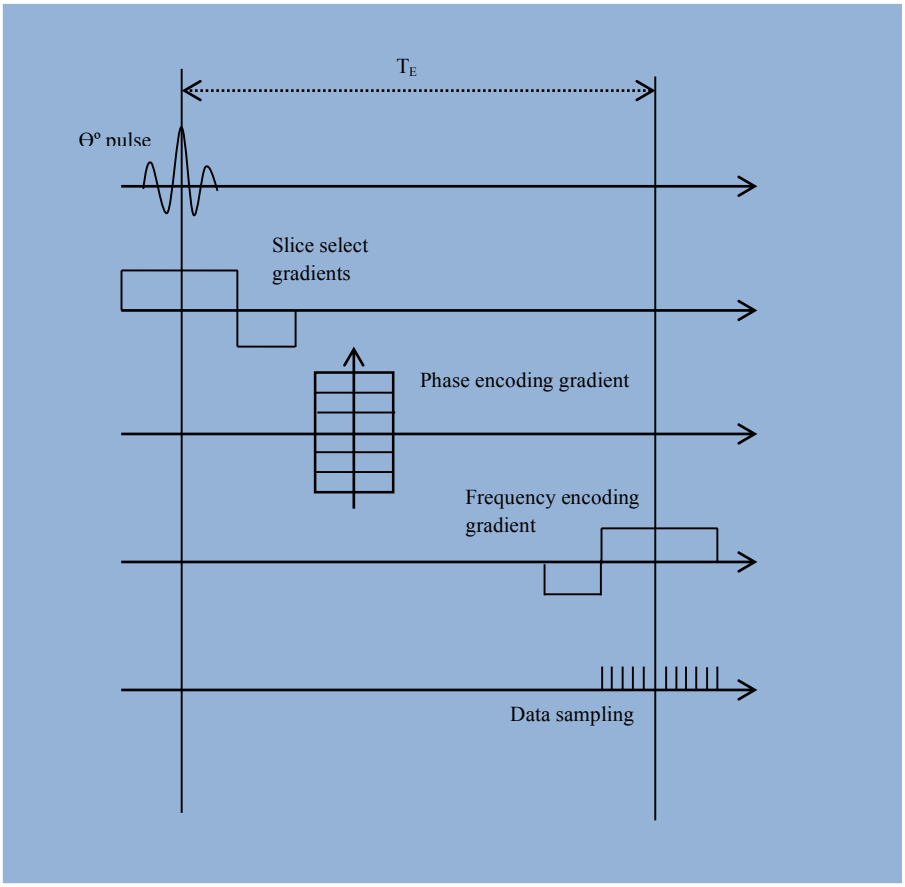

Figure 1.17: Pulse sequence diagram for a gradient echo sequence.

An initial flip angle, usually less than 90º, is chosen and the pulse is applied in conjunction with a slice select gradient. The phase encoding gradient creates phase differences along the phase encoding axis. A negative frequency encoding gradient is applied to dephase the spins. A positive frequency encoding gradient is applied during echo formation. During the readout gradient an analogue to digital converter samples the signal. After a time T_R (usually short) the process is repeated with a different phase encoding gradient amplitude. A 2D-FT is performed on the sample to produce an image.

1.13.3. Fast Spin Echo Imaging

After the initial 90º pulse in a spin echo sequence, multiple 180º pulses are applied to generate a train of echoes. The phase encoding gradient is changed for each echo. This allows several frequency encoding lines to be collected after each excitation pulse.

Single shot fast spin echo (SSFSE) is possible which allows all of the phase encoding lines to be collected after a single RF excitation. The advantages of this technique are that the acquisition time is reduced considerably and heavily T_2 –weighted images are easily produced. This technique can, however, lead to spatial blurring and the RF pulses lead to a high deposition of energy.

1.13.4. Echo Planar Imaging

Echo planar imaging (EPI) can be described as an addition to a spin echo or gradient echo sequence (the acquisition module) that provides a means of filling K-space in one T_R interval. K-space is sampled via rapid gradient reversals and echo collection. The image contrast is determined by the acquisition module used. Following the application of the acquisition module, the frequency encoding gradient is switched between positive and negative lobes, sampling the FID. With each application of a frequency encoding gradient, one line of K-space is filled. A blipped gradient in the phase encoding direction is applied while the readout gradient is switched, and steps through lines of K-space to be filled. Implementation of EPI requires excellent gradient performance. EPI is the basis of Diffusion MRI, an imaging technique implemented in the research carried out in this thesis and described in detail in Chapter 3.

1.14. SNR

The MR signal can be degraded by noise. Image noise results from a number of different factors. These include imperfections of the MR system e.g. magnetic field inhomogeneities and thermal noise from the RF coils, and patient related factors e.g. movement due to respiration. The relationship between the MR signal and the amount of image noise present is expressed as the signal-to-noise ratio (SNR).

A high (increased) SNR is desirable in MRI. The SNR is dependent on the following parameters:

- Slice thickness
- Receiver Bandwidth
- Field of View, FOV
- Size of the (image) matrix

- Number of averages, NAV
- Repetition time, T_R
- Echo time, T_E
- Flip angle
- Magnetic field strength
- The selection of the transmit and receive (RF) coil

To improve the SNR and thus get better anatomical images, changes can be made to certain parameters but often these come with compromises. For example, the slice thickness can be increased to increase voxel size thus encompassing more protons to get more signal (increasing the SNR), however this decreases the spatial resolution. Dedicated anatomical coils are used routinely, which are designed to encompass the whole region of interest and limit the space between the coil and anatomy.

1.15. The MRI Scanner

A typical clinical imaging MRI scanner has several key components to enable the physics described thus far to be executed and produce anatomical images. The magnet is the main component, with clinical MRI scanners usually housing large superconducting magnets, which are cooled using cryogens such as liquid helium. This allows a strong magnetic field to be achieved, typically up to 3.0 *T* and even up to 11.0 *T* in state-of-the-art establishments for clinical research. This static magnetic field is inherently non-uniform and so its homogeneity is optimised using metal sheets and electrical coils. This is called shimming. There is a large degree of magnetic shielding by incorporating thick iron walls into the scan room as well as a faraday cage around the scanner area for exclusion of external interference and thus improvement of SNR. Gradient systems apply and alter the magnetic field, RF generator and receiver coils generate pulses and receive signal, and a computer system coordinates these processes and processes data. Figure 1.8 shows these layers of basic components in an MRI scanner.

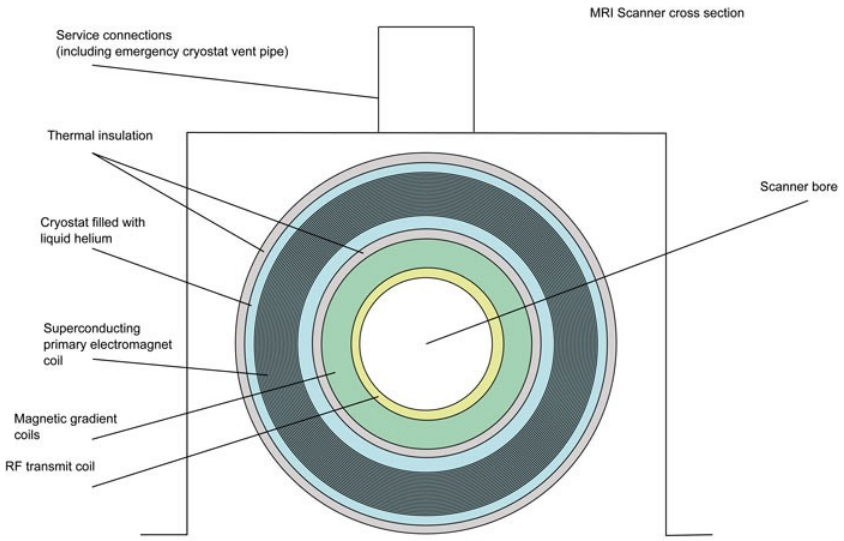

Figure 1.18: Basic components of an MRI scanner (3).

2. Breast Cancer and the Role of MRI in Cancer Imaging

2.1. An Overview of Breast Cancer

Breast cancer is one of the most common human neoplasms worldwide, and is the most common cancer in the UK. Over 60,000 women are diagnosed with breast cancer each year in the UK alone. Breast cancer also affects men, with several hundred cases diagnosed each year in the UK. Three hundred and forty men were diagnosed in 2015. On average, 1 in 8 women and 1 in 870 men will develop breast cancer in their lifetime (4).

More people than ever are surviving breast cancer thanks to better awareness, screening and treatments - 65% of women have a 20-year survival, and 90% have a 5-year survival (5). However, around 1000 women still die each month in the UK from breast cancer so there is still much to be done in terms of cancer research to prevent, diagnose and tailor the most effective treatment. In the UK, the breast screening program was introduced in the late 80s and was the first of its kind. It provides free breast cancer screening mammography every three years for all women in the UK aged between 50 and 70, with an initiative to widen this age range in the future. This means cancers of the breast are detected earlier. This improves survival with earlier intervention, but can also lead to over treatment.

Breast cancer is a class of diseases that is indiscriminating of person and tissue type. It can occur by chance, due to random mutations in DNA, but there are also factors that may increase the likelihood of developing breast cancer. Breast cancer is associated with the Western lifestyle, and incidence rates are therefore highest in countries with advanced economies. Obesity, smoking, alcohol consumption, air pollution, ionizing radiation, and oral contraceptives are some lifestyle factors that increase the risk of breast cancer (6). Breast cancer is, however, multifactorial thus biological and physiological factors such as age, gender, estrogen levels and genetic susceptibility are also influencers (6). Genetic predisposition causes around 5% of identified breast cancers. Notably, the BRCA1 and 2 mutations, which are mutations in tumour suppressor genes, increase the risk of an individual getting breast cancer by 60% (7, 8). The most common age of diagnosis is around 60 years old for women, due to screening, and younger women generally present with more unfavourable cancers (9, 10). Women who have had children and have breast-fed are likely to have lower risk of obtaining the disease than women who have not (11). Still, even for women absent

known risk factors, they are still at risk of breast cancer from random mutations as well as aging and gender.

The pathway of diagnosis of breast cancer is usually through physical examination of the breasts by a healthcare provider and screening or querying using an imaging method called mammography (12). Screening may also be done with MRI in high-risk patients. Mammography is a breast specific x-ray machine to detect cancer. If a lesion is suspected to be malignant, an ultrasound-guided or MRI-guided biopsy of the lesion may be taken to send for pathological analysis. MRI biopsies are only performed if no lesion is seen on mammography, tomosynthesis or second look ultrasound.

Breast cancer is not just one disease; it is many diseases with varying molecular structures and symptoms. Breast cancer is invasive when there is invasion of cells through basement membrane in the ducts or lobules. Cancer cells may travel to other parts of the body where they can grow and form new tumours. This happens when the cancer cells get into the body's bloodstream or lymph vessels. The process of cancer spreading is called metastasis. Non-invasive (in situ) breast cancer occurs when the cancerous cells remain within the breast tissue lobules or ducts. The sample is biopsied to determine the type of cancer (e.g. ductal or lobular), whether it is invasive, and which molecular prognostic markers are expressed. Immunohistochemical tests as a surrogate for genetic testing to categorise molecular subtype is common in clinic – they are also known as molecular prognostic markers. These include the hormonal receptor status of oestrogen (ER) and progesterone (PR), scored out of 8 with 0-2 being negative and 3-8 being positive. The presence of these receptors in significant quantity is associated with better prognosis and suggests a greater likelihood of response to hormone manipulation, for example, the use of the drug Tamoxifen. The oncogene, HER2, is also usually tested for. Treatment using Herceptin is only effective when HER2 is expressed. Thus, a ‘triple negative’ of ER, PR and HER2 is associated with worse treatment response in patients (13, 14). Prognostic markers are indicators of growth, invasion, and metastatic potential. The molecular subtypes are outlined below in Table 2.1 using the results from the three common immunohistochemical tests to categorise.

Subtype	Results of molecular prognostic marker tests*	Occurrence
Luminal A	ER-positive and/or PR-positive HER2-negative	30-70%
Luminal B	ER-positive and/or PR-positive HER2-positive	10-20%
Triple negative/ basal-like	ER-negative PR-negative HER2-negative	15-20%
HER2 type	ER-negative PR-negative HER2-positive	5-15%
*These are the most common reports for each subtype. However, not all tumors within each subtype have these features. ER positive = estrogen receptor-positive ER negative = estrogen receptor-negative PR positive = progesterone receptor-positive PR negative = progesterone receptor-negative HER2 positive = HER2 receptor-positive HER2 negative = HER2 receptor-negative		

Table 2.1: Molecular subtypes of breast cancer (15).

MRI is often used to screen women with high risk for breast cancer including family history, as well as mammography. If a biopsy confirms suspicions, MRI may be used to demarcate the extent of cancer including lymph nodes, problem solve if there are further queries, to plan surgery or other treatments, and to monitor treatment response over the months and years. MRI allows not only the qualitative assessment of morphology; but also, the quantification of many biomarkers and parameters such as pharmacokinetic analysis of contrast agents, relaxation times, and the apparent diffusion coefficient. The application of

MRI to diagnose using biomarkers to categorise the molecular subtypes and more is explored through Chapters 5-9. Chapters 10-11 look at MRI as an adjunct or tool for treatment planning and monitoring.

Treatment methods include surgery to remove cancer and in some cases specialised plastic surgery to reconstruct the breast – this may be breast-conserving surgery known as a wide local excision or full removal of the breast known as a mastectomy (16-18). A sentinel lymph node biopsy may also be carried out. Occult lesions can cause problems when a surgeon cannot feel the tumour to cut around, leading to positive margin status that can lead to reoperation or reoccurrence of the cancer. Current methods of localisation of impalpable tumours include stereotactic biopsy which uses mammography as image guidance, or ultrasound-guided placement of guide wires through the lesion for surgical excision. A solution to the problems faced in locating impalpable lesions using MRI and ultrasound is explored further in Chapter 10. Radiation therapy is also combined with surgery to cause necrosis of any other tumour cells to decrease chance of recurrence. These treatments are usually further combined with chemotherapy and hormonal therapies; there are many drugs available to treat breast cancers and the triple approach of surgery, chemotherapy and radiotherapy is currently standard in hospitals. Still, patients may not conquer the disease using only these tools. There are a multitude of other non-standard and experimental treatments such as targeted hyperthermia and targeted drug delivery. One such method, high-intensity focused ultrasound (HIFU) is explored in Chapter 11 with regard to MRI as guidance for therapy. The diagnosis and treatment of breast cancer is a multifarious operation, with imaging being one of the core components, still with much unsubstantiated potential.

2.2. Role of MRI in Breast Cancer

The role of imaging in detecting, treating, and monitoring cancer is essential not only in clinically detecting and managing cancer as we currently know it, but is key in research in order to one day win the fight against the disease. Imaging modalities allow us to diagnose cancers to a degree with reporting before pathology, to plan and tailor treatments such as surgery and radiotherapy, and to monitor high-risk patients and a patient's treatment regime for effectiveness. In research, imaging tools have helped apprehend cancers in more detail to aid diagnosis and to evaluate the efficacy of innumerable new drugs and treatments. The gold

standard would be to one day image a cancer and know exactly what it is and how to treat it, which is quicker than taking biopsies and sending for analysis in a lab.

MRI is regarded as a powerful and versatile imaging tool in cancer. This is due to its ability to image all soft tissues in great detail. Cancer can affect all types of tissues and thus an imaging modality that can visualise all tissues is essential. MRI is not a totally dominant method in cancer imaging and its allied modalities are x-ray, CT, PET and US. PET is particularly important for staging, and as previously described x-ray is important for screening and US for biopsy. Cancer has several physiognomies that can tell us how it may respond to treatment and what the prognosis for the patient may have. These physiognomies are being scrutinised in imaging research to look for biomarkers and parameters that can quantitatively describe the tumour microenvironment on a molecular level like pathology.

Tumour heterogeneity is one so-called physiognomy of cancer (19). Heterogeneity describes differences between tumours of the same type in different patients, and between cancer cells within a tumour in the same patient. This comprises cellular morphology, gene expression, metabolism, motility, proliferation, and metastatic potential. It is not surprising that heterogeneity causes many problems when planning effective treatments with no two cancers being the same. A tumour may have necrosis that inhibits the effective delivery of drugs or become resistant to treatment as it mutates and changes. Being able to map this characteristic through imaging would be a feat that would change the direction of treatments towards personalised medicine – treatment personalised to that particular cancer in that particular person.

Another main cancer physiognomy is angiogenesis (20). This is the physiological process by which new blood vessels form. As tumours grow they need a blood supply and this vasculature is built in a dysfunctional and abnormal manner – unlike normal tissues. Understanding and quantifying the vasculature within a tumour can tell us much information. The blood vessel network is what allows many drugs to reach the tumour and be effective. There are many drugs to inhibit angiogenesis to hinder the delivery of nutrients for growth of the tumour. Angiogenesis is often a signature of particular molecular subtypes of breast cancer. Some may be well perfused, and others not. MRI having the ability to not only map this, but quantify on a molecular level, would enable very effective monitoring of response and diagnosis.

Additionally, proliferation of cancer cells is an important feature of malignancy (21). Cancers can grow very quickly, and in very particular ways depending on the molecular subtype. The density, shape, fluid pressure, location, and distribution of these cells are all characteristics of proliferation that would be beneficial to image and quantify. The cells, which are the building blocks of the cancer, obviously contain the DNA and many pathways and mechanisms that can be inhibited with drugs. The ways in which these building blocks are distributed is something that could be a prognostic factor for therapy response. Diffusion imaging can image the molecular motion of water, which makes up much of the cytoplasm in cells.

Advanced diffusion MR imaging has the potential for acquiring anatomical images and further quantifying these physiognomies of breast cancer via diffusion and perfusion parameters (outlined in Chapter 3). Diffusion parameters have been shown to correlate with prognostic factors and cancer physiognomies (22). The level of complexity of breast cancers means that there needs to be a shift in line with the improvements in technology to further understand the tumour microenvironment using imaging. This will allow personalised medicine to become a common reality in hospitals with the tailoring of personal, effective treatment regimes using imaging to immediately diagnose without biopsies and allow concurrent monitoring of treatment without ionising radiation. Thus, developing an accurate non-invasive MRI method may greatly improve the efficacy of drug timing and delivery as well as quantifying tumour physiognomies. Many MR imaging protocols exist with great potential, and the accuracy and precision of these needs to be improved so they may be used routinely with confidence.

The main focus of this thesis, Part 1, is the use of advanced diffusion imaging to understand and better characterise the tumour microenvironment of breast cancer, especially in malignancy types and molecular subtypes. To achieve this, optimisation of Intravoxel Incoherent Motion (IVIM) imaging protocols and the investigation of post-processing methods were carried out in healthy volunteers, and then protocols were applied clinically to look at IVIM parameters and their correlation with tumour physiognomies characterised by subtyping. Quantitative MRI may improve upon morphological imaging. The ultimate goal is to present a scan that can diagnose and have the potential to predict prognostic outcomes based on quantitative imaging to be part of a personalised medicine regime.

Additionally, in Part 2, this thesis furthers research of MRI and high intensity focused ultrasound as tools for surgical planning. A clinical surgical planning tool is presented, with the optimisation of an animal pseudo tumour model and a full feasibility test. Utilising MRgFUS to mitigate reoperation and positive tumour margin status would be beneficial for breast cancer patients undergoing breast conserving surgery.

Part 1: Advanced Diffusion-weighted Imaging in Breast Cancer

3. Diffusion-weighted Imaging and Intravoxel Incoherent Motion Imaging

3.1. Diffusion-weighted Imaging

Diffusion-weighted imaging (DWI) is an MRI technique that exploits Brownian motion of water molecules to generate contrast in images (23). Since biological tissues are water based, and different tissues have different concentrations of water, this is ideal for visualising anatomy and diseases, such as cancer. Molecular diffusion can be mapped, reflecting restricted interactions of water molecules with macromolecules, fluids, fibers and membranes. This allows tissue architecture to be probed using MRI through non-invasive means. The heterogeneity, angiogenesis and proliferation of tumours could be probed and quantified quickly using DWI – and this has been explored using various advanced methods. In DWI, the intensity of each voxel reflects the apparent rate of water diffusion at that location. The mobility of water is driven by thermal effects, and is highly dependent on the cellular environment. Diffusion parameters have the potential to be excellent biomarkers of malignancy and response to therapy in cancer, of which much research has suggested (24-33).

The sensitivity of MR signals to diffusion originated from the pioneering work of Hahn (34), describing that dephasing was occurring because of diffusion properties, as a result introducing the concept of a diffusion coefficient to quantify this decades later in vivo (35, 36). Carr and Purcell introduced a method to measure the molecular self-diffusion in fluids (37). A modification of this technique, the Carr-Purcell-Meiboom-Gill sequence (CPMG), consisting of a 90° RF pulse followed by an echo train induced by successive 180° pulses, is useful for acquiring T2 weighted images.

Stejskal and Tanner introduced the present prevalent method for acquiring diffusion weighted MR images (38). The sequence consists of a 90° and 180° spin echo pair of RF pulses with large and equal gradients placed on either side of the 180° pulse. Named the pulsed gradient spin echo (PGSE) sequence, the gradient pulse duration is shortened in comparison to previous methods. Diffusion driven displacements of water molecules are encoded in the MR signal through variations of the magnetic field in space caused by magnetic field gradient pulses.

LeBihan pioneered clinical diffusion imaging in the 1980s (36, 39-43). The sequences implemented at the time produced images heavy in artifacts. Echo Planar Imaging (EPI) (see

Chapter 1) is now the underlying sequence implemented in modern diffusion imaging with the PGSE method applied. The degree of sensitivity to diffusion is described by the b-value, which was introduced to take into account the intensity and time profile of the gradient pulses used both for diffusion encoding and MR spatial encoding. The overall effect of diffusion in the presence of those gradient pulses is signal attenuation, and so the MR imaging signal becomes diffusion weighted.

The b-value can be controlled by manipulating the strength of the gradient, G, the gradient duration, δ, and the timing between gradients, Δ, as shown below;

$$b = \gamma^2 \delta^2 G^2 (\Delta - \frac{\delta}{3})$$

Equation 3.1

where γ = the gyromagnetic ratio. This b-value is measured in *s/mm*^{2}.

DWI works because all the spins accumulate random and unique phase changes as they move about within the gradient. This leads to a net loss of signal within each voxel. Watery tissues that have mobile molecules give low signal intensity whilst more solid and static tissues give a stronger signal. This signal is more attenuated when diffusion is fast or at large b-values. Restricted diffusion is often seen in cancers where cells are denser and so appear bright on DW images (44). DW-images are also sensitive to T1 and T2 contrast effects. The signal strength of a DW-image is described by the following monoexponential;

$$S_b = S_0 e^{-b.D}$$

Equation 3.2

where *D* is the self-diffusion constant for that tissue, S_0 is the signal intensity at an initial b-value, for example b = 0 *s/mm*^{2}, and S_b is the signal intensity at an arbitrary higher b-value chosen, usually around 1000 *s/mm*^{2} in breast.

In practise, what is measured by a PGSE sequence is related to the actual diffusion coefficient, *D*, but may contain movement from other sources. Therefore, what is referred to is the apparent diffusion coefficient (ADC), is calculated from two images, one being diffusion-weighted and the other not (S_0). Sometimes, a low b-value may be used to avoid movement from other sources that occur at lower b-values. The ADC can be displayed as a map on a

voxel-by-voxel basis, and is calculated by rearranging Equation 3.2 and replacing *D* with the ADC;

$$ADC = \frac{-1}{b} \ln \frac{S_b}{S_0}$$

Equation 3.3

A high ADC implies high motion and results in low signal – the corresponding ADC map would be bright. The ADC and D are measured in mm^2/s. At room temperature, water has a value of $D = 2.2 \times 10^{-3}\ mm^2/s$. With a weighting of b = 1000 s/mm^2, the water signal would be reduced to 11% of its non-weighted value.

DWI is appealing as an imaging biomarker for cancer because it is noninvasive, non-ionising and no contrast agents are needed.

3.2. Intravoxel Incoherent Motion Imaging – Beyond DWI

One source of signal in DW-images that contributes towards what is calculated by the ADC is that from microcirculation systems in pseudo-random capillary networks (36, 45). These extra sources of signal are known as Intravoxel Incoherent Motion (IVIM). Due to improvements in MRI technology and the mathematical models to quantify IVIM, these additional sources can now be imaged with quantifiable parameters (46). Consequently, there is an emerging popularity of IVIM in cancer imaging (47).

The molecular random motion of water, known as diffusion, and the microcirculation of blood in the capillaries, known as perfusion, are both important physiologic parameters in oncological MRI. The motion of water molecules is more restricted in tissues with higher cellular density (e.g. tumours) and perfusion of tumours can be higher than in normal tissue due to increased vascularity. These two parameters are therefore potentially useful in detection, diagnosis, treatment planning and monitoring of various cancers (36). Diffusion and perfusion MR-images are usually acquired as separate sequences, using different techniques. Diffusion imaging is explained in detail in the previous section. MR perfusion measurements determine tissue vascularisation and blood flow using techniques such as arterial spin tagging or contrast enhanced imaging (48). The two techniques, diffusion and perfusion imaging, are routinely used in clinic and give essential information about tumours and treatment. Therefore, an MRI technique in which these two parameter measurements could be acquired and

quantified simultaneously would be advantageous in an oncological setting. In fact, scans quantifying several parameters, as part of multiparameteric MRI, and their use in personalised medicine is currently one of the forefronts of MR research (49-51). There is a need to find techniques that give useful information and employ these in a standardised way, routinely, to enable the best possible care for patients.

In simple terms, molecular diffusion of water involves molecules travelling and colliding with each other because of their own thermal energy. Each collision results in a change of direction for individual molecules and the overall process is described by a random walk. This fundamental concept of Brownian motion was described by Brown and subsequently explained by Einstein (52). The macroscopic model of blood capillaries can be compared to this phenomenon; with the water molecules in blood flowing and changing direction between pseudo-randomly distributed capillary segments. So, the random walk mathematical model for nanoscale-diffusion should be applicable to microscale-perfusion, too. Figure 3.1 shows an illustration of a microcapillary random walk in the tissue microenvironment.

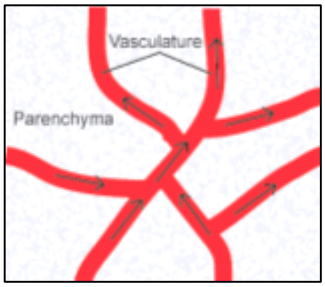

Figure 3.1: Microcapillary random walk in the tissue microenvironment.

This leads to the introduction of Intravoxel Incoherent Motion Imaging (IVIM), a theory and MRI technique that enables the measurement of both the cellularity and vascularity using DW-imaging in one protocol. This analytical model was formally presented in 1988 by Le Bihan (41), who concluded that MR diffusion measurements were also sensitive to microcirculation of blood in capillary networks. He presented the following IVIM biexponential model;

$$S = S_0[(1-f)e^{-bD} + fe^{-bD^*}]$$

Equation 3.4

where S is the diffusion-weighted signal, f is the perfusion fraction, D is the diffusion coefficient and D^* is the pseudodiffusion coefficient. There are five orders of magnitude between the molecular diffusion and micro capillary perfusion models but the model's diffusion and pseudodiffusion parameters differ by only one order of magnitude. Diffusion, D, is about 1×10^{-3} mm^2/s and pseudodiffusion, D^*, is about 1 to 10×10^{-3} mm^2/s - depending on the body part imaged. This counterintuitive difference is explained by particle velocity and distance; molecular diffusion happens very fast over short distances and blood flow happens more slowly over larger distances.

The three IVIM parameters can be described by their underlying physiological processes, their corresponding tumour physiognomy, and their application in breast cancer imaging. The diffusion coefficient, D, is the tissue diffusivity, which corresponds to cell density (higher in cancers than normal tissue) and proliferation (the exponential cell multiplication of the cancer). The perfusion fraction, f, corresponds to the blood volume and angiogenesis of new vessels in the tissue being imaged. Higher angiogenesis has been shown to be indicative of cancer (53-55). The pseudo diffusion, D^*, corresponds to blood velocity and flow, and is therefore useful in measuring a cancers susceptibility to drug delivery. Figure 3.2 below shows these parameters and their applications summarised.

Diffusion	Perfusion fraction	Pseudo diffusion
D	***f***	***D****
Cell density	Blood volume	Blood velocity
Proliferation	Angiogenesis	Drug delivery
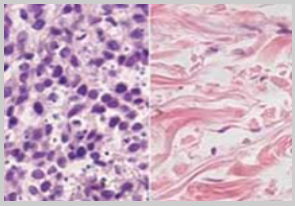	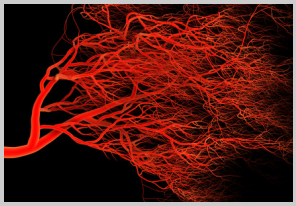	

Figure 3.2: IVIM parameters, their underlying physiological processes and their application in understanding cancer. Images: (56-58)

The IVIM model is an elegant synthesis of diffusion and perfusion, which promised great potential at publication in the 1980s. However, images in these initial IVIM studies were obtained at 0.5 *T*, the gradient hardware only allowed strengths up to 10 *mT/m* and b-values of only up to 100 s/mm^2 were achievable. Thankfully, due to MRI benefitting from significant technological advances in the last couple of decades, DW-imaging is now of much better quality; and consequently IVIM has recently undergone a revival. IVIM is now more accessible hardware-wise, and the increase in published literature has shown its popularity. The problem is, is that there is no clear standardisation and rationale behind the building of IVIM protocols at institutions around the world. Le Bihan himself wrote an editorial in 2008 saying that IVIM had 'woken up after some time of hibernation' and to 'let us further explore its potential' (59). A more recent IVIM review by Iima, who works closely with Le Bihan's research group, states that in breast cancer, the choice of b-values, acquisition methods, data analysis approaches, and differences in patient population were the main problems in this body part to be addressed (47). Thus, there is much work to be done in applying IVIM in cancer imaging, and especially in breast cancer which is one of the newest areas to be explored in regards to IVIM.

3.3. IVIM Fitting Methods

Currently, most DW-imaging studies are described using the well-established monoexponential model (Equation 3.2) to calculate the apparent diffusion coefficient (ADC). As described in more detail in Section 3.2, IVIM imaging relies on a more advanced model to describe microperfusion and molecular diffusion. The signal attenuation from microcirculation-induced spin dephasing effects can be separated from that of normal restricted passive diffusion by the biexponential IVIM model (Equation 3.4).

Figure 3.3 demonstrates a typical monoexponential fit (dashed line) and a typical biexponential fit (solid line) of the decay of signal values (circles) as a function of increasing b-value. It can be seen that if ADC is calculated with low b-values, as it routinely is, then microperfusion effects will influence this and so the ADC may not be accurate. Rectangle A shows the exponential decay from unity of the perfusion based parameters, f and D^*. Rectangle B shows the monoexponential tail allowing D to be calculated.

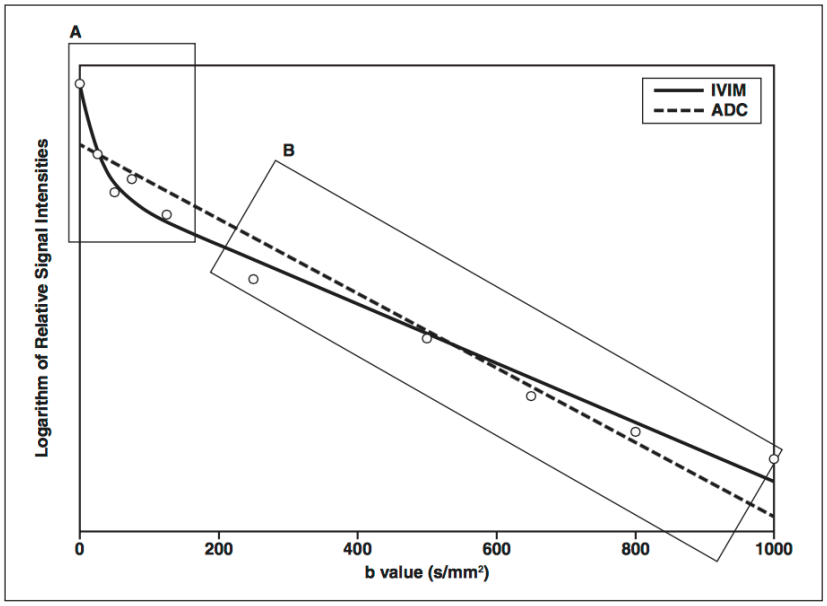

Figure 3.3: Mono- (dashed line) and biexponential (solid line) fits of IVIM signal data (circles) as a function of increasing b-value, with Rectangle A showing where both perfusion and diffusion effects reside, and Rectangle B showing where purely diffusion effects reside (60).

Fitting data to these models when imaging biological tissue can be problematic due to finite signal-to-noise (SNR). Signal data can be gathered through standard ROI analysis –

whole tumour, or sectional, for example, in the most malignant part of the tumour. From there, an average of pixel values can be taken, or parametric maps can be generated allowing voxel-by-voxel analysis to produce histograms. Once signal values have been collected from IVIM images, there are several fitting methods that allow extraction of the IVIM parameters. Common fitting methods are outlined below (61).

Fitting Method 1: Monoexponential fit

The ADC is calculated using the monoexponential fit (Equation 3.3), shown in Figure 3.3 by the dashed line. This method does not account for perfusion effects but can be used on IVIM scans as they are simply just diffusion scans with multiple b-values i.e. pick two suitable b-values to analyse.

Fitting Method 2: Stretched-exponential fit

The stretched-exponential model (62) improves upon Method 1;

$$S_b = S_0 e^{-b.DDC^{\alpha}}$$

Equation 3.5

where DDC is the distributed diffusion coefficient and α is the heterogeneity index ranging from 0 to 1. If $\alpha = 1$, the model simplifies to Method 1. Lower values of α result from nonexponential behaviour caused by the addition of 'proton pools' with a range of diffusion rates within the imaged voxel or from a process where the motion is intermittent (63).

Fitting Method 3: Free biexponential fit

The signal decay data is fitted to Equation 3.4 using an unconstrained biexponential fit. This can be computed using a nonlinear fitting algorithm, such as nonlinear least squares or damped least squares (Levenberg-Marquardt). This method is sensitive to outliers and can lead to misleading results if underlying assumptions are not true.

Fitting Method 4: Constrained biexponential fit

The signal decay data is fitted to Equation 3.4 using a biexponential fit, using a nonlinear fitting algorithm with bound constraints, for example: $0 < f < 10\%$, $0 < D < 0.001\ mm^2/s$, $0 < D^* < 0.01\ mm^2/s$, $D < D^*$. These limits filter spurious and physiologically meaningless results.

Fitting Method 5: Segmented fit

Assuming that *D** is significantly greater than *D* (at least by an order of 10), and its influence on diffusion-weighted signal is weak when the b-value is large enough (typically > 200 *s/mm*^{2}), then in this higher b-value regime the pseudodiffusion component *D** can be neglected and *D* can be obtained by a simplified monoexponential fit as in Method 1. Then, *D** and *f* can be calculated using a biexponential fit as in Methods 3 or 4.

Fitting Method 6: Over-segmented fit

High b-value data is fitted using the monoexponential fit to obtain *D* as in Method 5, and then a monoexponential fit is extrapolated back to zero to calculate *f* using;

$$f = (S_0 - intercept)/S_0$$

Equation 3.6

D and *f* are then used to constrain a biexponential fit to obtain *D** as in Methods 3 or 4.

Fitting Method 7: Triexponential

A tri-exponential model can be applied, where f_n represents the perfusion fraction of each compartment (these sum to 1) and D_n represents the joint diffusion and pseudodiffusion coefficients of each compartment;

$$S = S_0[f_1 e^{-bD_1} + f_2 e^{-bD_2} + f_3 e^{-bD_3}]$$

Equation 3.7

The most commonly utilised methods are Fitting Methods 5 and 6 – the segmented and over-segmented fits, as shown in Table 4.1 in the literature review summary.

4. Intravoxel Incoherent Motion Imaging: Literature Review

4.1. Introduction

IVIM has recently been applied to various tissue and cancer types including breast, but not extensively. IVIM effects have been observed in a variety of both poorly- and well-vascularised tissues. Measurements in malignant lesions have been reported in the liver, prostate, brain, kidney, head and neck, pancreas, and breast (64-70). Often the driving force behind the investigation into IVIM parameters is that the perfusion effect may reduce the accuracy of cancer differentiation using the widely applied ADC value by introducing a positive bias proportional to the perfusion fraction into the ADC values (71) thus increasing their variability and dependence on the choice of the diffusion-weighting (44, 72-74). The b-value scheme also strongly affects the calculated IVIM parameters and the separation between their values in cancer and normal tissue, especially when a small number of b-values are implemented (75). Also, the allure of a '2-in-1 scan', without the need for contrast for perfusion quantification, is attractive.

4.2. Breast IVIM Imaging

Several key research groups have investigated IVIM parameters and their clinical significance in malignant and benign breast lesions, as well as in healthy breast parenchyma.

Baron *et al* (76) scanned 7 healthy volunteers (14 normal breasts) with a well-sampled b-value scheme of 16 b-values: 0, 20, 40, 60, 80, 100, 150, 200, 300, 400, 500, 600, 800, 1000, 1300, 1600 s/mm^2. Different fat suppression techniques were investigated, but the relevant conclusion here is that in these volunteers perfusion effects did not exist in normal fibroglandular tissue. Baron stated that this fitted with the physiologic knowledge that the mammary gland is not a highly vascular organ. However, this is a small cohort, and the use of IVIM in normal individuals has little clinical utility. High risk cohorts or the contralateral normal breast of breast cancer patients may serve as a more useful test set whilst investigating IVIM effects since its clinical utility ultimately lies in cancer. These findings may be due to perfusion only being detected once various limits have been reached due to lesion formation. Fitting was implemented by checking if the data could be fitted using a 'free' approach, using an unconstrained biexponential fit. If not, then a monoexponential fit was used.

Tamura *et al* (77) reported that a monoexponential diffusion model best described normal tissue, as in the Baron *et al* study, and that malignancies were best described by the biexponential model (fast and slow component fraction model as opposed to standard IVIM). However, they could not prove a significant difference between benign and malignant lesions. For malignant tumour subtypes, D^* of non-invasive ductal carcinoma was found to be greater than that of invasive ductal carcinoma. Eight healthy women were scanned with 12 b-values: 0, 318, 636, 954, 1272, 1590, 1908, 2226, 2544, 2862, 3180, 3498 s/mm^2 to investigate normal tissue, and 100 breast tumours were analysed from 80 women with 6 b-values: 0, 700, 1400, 2100, 2800, 3500 s/mm^2. The normal and malignant sub-type cohorts were small for statistical analysis. This group highlighted the fact that their pathological diagnosis was performed with an emphasis on cell configuration and shape rather than tumour cellularity meaning the IVIM parameters were not directly comparable to their pathology data. The biexponential analysis on b-values of 0, 700 and 3500 s/mm^2 (repeated twice to give 6 b-values) meant that the curve was not sampled well at low b-values, where the IVIM model assumes perfusion effects lie. The Levenberg-Marquardt algorithm, a nonlinear damped least squares fitting approach, was used to fit data using the biexponential model.

Sigmund *et al* (78) demonstrated significant differences between normal fibroglandular tissue and malignant lesions in ADC and D values. DW-response curves in lesions were found to be biexponential in comparison with the monoexponential response in parenchyma in this cohort of 34 breast patients. There was some differentiation of lesion subtypes (invasive ductal carcinoma vs. other malignant lesions). It was concluded that there was a moderate correlation between IVIM parameters and contrast enhancement. It was suggested that further work should be done to support the notion of IVIM parameters as biomarkers for initial grading, progression monitoring, or treatment assessment of breast tumours. Limitations that should be noted are that the cohort analysed was biased to malignant lesions as opposed to benign lesions, most benign lesions were small, the b-value scheme was not optimised and the number of b-values used was reduced due to time constraints. Ten b-values: 0, 30, 70, 100, 150, 200, 300, 400, 500, 800 s/mm^2 were planned and used on most patients. When calculating the IVIM parameters, a segmented approach was used where D was calculated using the monoexponential diffusion model for b-values above 200 s/mm^2, and extrapolated backwards to 0 to calculate *f*. D^* was calculated using the IVIM model as in Equation 3.4 for b-values

less than 200 *s/mm*^{2}, fixing *D* and *f*. This is an over-segmented nonlinear fit, and works on the assumption that *D** is significantly larger than *D* and the effects of *D** on *D* at large b-values can be neglected

From the same research group, a study by Cho *et al* (79) continuing this work with the same cohort as in Sigmund *et al* and data gathered more recently was published. This time, histogram analysis was used to assess breast tumour heterogeneity to look at malignant subtypes of breast cancer. Fifty malignant lesions and 12 benign lesions were assessed. Ten b-values: 0, 30, 70, 100, 150, 200, 300, 400, 500, 800 *s/mm*^{2} were used. Significant differences among tumour subtypes were only found when comparing *ADC* and *D*, which were lower in invasive cancers that DCIS. Significant differences for *ADC*, *D* and *f* were found between malignant and benign lesions. IVIM was also shown to have the potential to discriminate between molecular subtypes, with several statistically significant results involving IVIM perfusion parameters. The over-segmented approach was used again as described by Sigmund *et al*. Cho *et al* have also compared fitting methods in 14 breast cancer patients (80). Free versus over-segmented fitting were compared, in the same b-values as used above plus another set optimised for liver by the same research group: 0, 70 (x3 NEX), 300 (x3 NEX), 800 (x3 NEX) *s/mm*^{2}. Experimentally, for each IVIM parameter, the lowest relative error was found for segmented fitting of the conventional protocol. This trend mirrored simulations at different SNRs.

Another key breast IVIM paper is by Liu *et al* (81). This study obtained perfusion as well as diffusion information in parenchyma and breast lesions using IVIM imaging with biexponential analysis and compared these parameters to the ADC with monoexponential analysis in their ability to discriminate benign lesions and malignant tumours. Eighty-four patients were imaged at 1.5 T using 12 b-values: 0, 20, 30, 40, 50, 70, 100, 150, 200, 400, 600, 1000 *s/mm*^{2}. All IVIM parameters and ADC values were significantly different among malignant tumours, benign lesions, simple cysts and normal breast tissues. All comparisons were statistically significant with $P < 0.001$. The *f* of malignant tumours was significantly higher than that of benign lesions, simple cysts and normal breast tissues. DWI response curves in malignant tumours, benign lesions and normal fibroglandular tissues were found to be biexponential fit in comparison with the monoexponential fit for simple cysts. It was concluded that IVIM provides separate quantitative measurement of *D* for diffusion and *f* and

*D** for perfusion and is helpful for differentiation between benign and malignant breast lesions. An interesting change in this paper was that the IVIM model had an extra term on the second exponential (See Equation 3.4) as below;

$$S = S_0[(1-f)e^{-bD} + fe^{-b(D^*+D)}]$$

Equation 4.1

A segmented fit was applied to this data. It was not clear why a modified IVIM equation was used instead of the original model (apart from obviously including diffusion signal in the second exponential, but there was no evidence or rationale this was better or correct) and it was not compared to the standard model of IVIM.

Liu *et al* (82) has also investigated the correlation of IVIM parameters with pharmacokinetic modelling parameters of dynamic contrast-enhanced MR imaging. In theory, perfusion parameters should have some correlation between the two types of MRI scan and would strengthen the feasibility of IVIM in breast. They found that *f* was moderately correlated with the blood volume fraction, V_p, but not with volume transfer constant, K_{trans}. Thirty-six breast cancers and 23 benign lesions were evaluated. This study did show that *D* was significantly lower in breast cancers than in benign lesions, which is consistent with other studies and DWI studies. A segmented fit was utilised. The discussion stated that the way *f* is fitted may give it large variability, as well as if the edges of the tumour are not taken into account with ROI analysis - the edges of a tumour may have higher blood flow and thus *f* will be determined by this inclusion or exclusion. *D** was stated as being generally unreliable if SNR is not good.

Bokacheva *et al* (83) demonstrated that the IVIM effect is significantly larger in malignant breast lesions than in benign lesions and normal breast parenchyma. The results of this research support the idea that IVIM parameters may improve the accuracy of malignant breast cancer differentiation from benign lesions. Nine b-values were used: 0, 30, 60, 90, 120, 400, 600, 800, 1000 s/mm^2. Limitations included the fact that the study was retrospective and the acquisition parameters and the b-values were not optimised or standardised, which provides a possible source of bias and variability in the IVIM parameter values. The patient cohort was 35, and each sub-cohort of malignant and benign lesions were therefore smaller. Furthermore, even though ROI analysis is standard in MRI research, it limits parameter values

to a particular area and is not a full representation of the lesion, especially since the heterogeneity of a lesion is important in characterisation. A segmented approach to fitting was used as detailed by Sigmund *et al*.

Iima *et al* (84), a team who works closely with Le Bihan, compared non-Gaussian diffusion models to IVIM. Twenty-six women were scanned using 16 b-values: 3 (Not 0), 5, 10, 20, 30, 50, 70, 100, 200, 400, 600, 800, 1000, 1500, 2000, 2500 s/mm^2. This study did not find a statistical difference in D^* between tissue types. It also highlighted the problem of T_1- and T_2 weighting effects on IVIM images when converting f to blood flow volume. This study also suggested refining the IVIM model by comparing IVIM parameters to quantitative dynamic contrast-enhanced perfusion MR-imaging to explore the underlying vascular functional architecture. This study used a kurtosis diffusion model to fit D and the IVIM model for f and D^*. This was to account for non-Gaussian diffusion of water at high b-values.

Three fitting methods: monoexponential, segmented and over-segmented, were compared in a study by Suo *et al* (85). Thirty patients were scanned using b-values: 0, 50, 100, 150, 200, 500, 800 s/mm^2. Segmented approaches fitted D^* and f best, whilst the monoexponential model fitted the most pixels. Statistically significant differences were found for all parameters between all three fitting methods. Only the segmented fit produced parameters correlating with the Dynamic Contrast Enhanced (DCE) relative enhancement ratio.

Validation of the IVIM model in breast has been explored. Liu *et al* (86) scanned 36 breast cancers and compared quantitative diagnostic performance of DCE imaging with IVIM. Significant correlations were found between perfusion-related parameters from IVIM and DCE MRI. Twelve b-values up: 0, 20, 30, 40, 50, 70, 100, 150, 200, 400, 600, 1000 s/mm^2 were used, and a segmented fit was used as before.

Cho *et al* (87) explored the IVIM response in a versatile flow phantom on a clinical MRI scanner at 3T. Eighteen b-values up to 500 s/mm^2 were acquired. Configurations were explored to represent what might be expected in a clinical setting: healthy tissue with low pressure and normal flow, and malignant with restricted flow and higher pressures. The flow speed was controlled in various directions. D^* and f showed strong increases with pressure, decreases with impedance, and high anisotropy in the direction of flow. D was largely

independent of the flow speed and direction. This informs the in-vivo IVIM behaviour, to an extent.

From the breast literature it is clear that IVIM has the potential to improve the specificity and sensitivity of breast MRI. IVIM would be particularly interesting as an adjunct to other MR-imaging protocols in multiparameteric MRI, just as its ADC-yielding counterpart is, in breast imaging now. Further, it has potential to be used in lieu of invasive contrast agent screening scans such as DCE, where there is much discussion in light of recent findings that substances like gadolinium reside on the lining of the brain and can cause adverse side affects (88, 89). There is excitement in the literature at the prospect of differentiating tumour subtypes via quantifying tumour physiognomies and predicting treatment response but first an agreement on how to build IVIM protocols is needed. Further work in larger patient populations and comparison with quantitative pathology may demonstrate diagnostic ability for grading of lesions of various sub-types of malignancies. The most obvious finding from surveying the literature was that IVIM b-value protocols are heuristic and differ between research groups – this is a major, rectifiable problem in which upon its solution, the literature would hopefully be more coherent in its findings and move to put IVIM at the forefront of diffusion imaging. Fitting methods were also variable between studies, and this is a factor that can affect the IVIM parameters.

4.3. Optimisation of IVIM Imaging

Optimisation for IVIM imaging protocols has been carried out in several body parts, to a certain degree. Lemke *et al* (73) published a paper in 2011 toward an optimal distribution of b-values. Brain, kidney and liver estimated values for *f, D* and *D** were used as inputs to the optimisation- named low, medium and high, respectively. Monte Carlo simulations were carried out to determine the optimal set of b-values from these different input parameter sets. Signal and noise were generated using the initial estimates and b-values starting from an initial b-value distribution of 0, 40 and 1000 s/mm^2. The relative overall error of each b-value distribution was tested with the addition of one b-value at a time from 0 to 1000 s/mm^2 in steps of 10 s/mm^2. The b-value distribution with the smallest overall error was then said to be optimal for that initial estimate set. Up to 100 b-values could be in a set. The optimal number of b-values was found to be 26 for low, 36 for medium and 20 for high. The relative overall errors for the three optimal sets of b-values were summed and a b-value set ‘sum’ was

produced. The first 16 of this 'sum' set are said to be optimal and appropriate for all three IVIM regimes: 0, 40, 1000, 240, 10, 750, 90, 390, 170, 10, 620, 210, 100, 0, 530, 970 *s/mm*^{2}. This paper recommends using a minimum of 10 b-values. Limitations were that the algorithm consecutively added b-values and so it could not be certain that the distribution is optimal. A better optimisation would require the consideration of any possible distribution of b-values but would lead to extensive computation time. This study focused on the precision and accuracy of parameter calculation. Systematic errors from movement were not considered. It was shown that the 'sum' b-values outperformed existing literature b-values with respect to standard deviation and image quality.

Next, Zhang *et al* (74) optimised b-value sampling in the kidney using the error propagation factor – the minimum of the sum of the squared residuals between the data and the model fit indicated the optimal sampling strategy. The range of b-values tested was from 0 to 800 *s/mm*^{2}, for 4, 6, 8, and 10 b-values. The optimal set with the lowest average propagation error at 10 b-values was 0, 59 (x3 NEX), 263 (x3 NEX), 800 (x3 NEX) *s/mm*^{2}. This was not validated in a clinical setting, but tested on 4 healthy volunteers. Monte Carlo simulations were computed showing that the optimised scheme lowered estimation error by up to 30% compared to literature.

Jambor *et al* (90) optimised b-value selection for imaging of normal prostate tissue using computer modeling and in vivo measurement. Four modeling approaches were used to generate b-values. The first method added b-values to three initial b-values of 0, 50, and 100 *s/mm*^{2}. All possible new combinations were examined and the combination with the smallest convergent mean was chosen. The second method started with 41 evenly distributed b-values and the number of b-values was consecutively decreased. In a similar manner to the first method, each new combination was assessed and the combination that increased the convergent mean the least was chosen as optimal. The third method used the optimal set of b-values from the first method and assessed the convergent mean as b-values were removed in a step-wise manner. The fourth method was to generate 13,000 random distributions of 16 b-values and the convergent mean was assessed. The maximum b-value was always 2000 *s/mm*^{2} and the minimum between b-value was always 50 *s/mm*^{2}. Clusters of b-values were consistent with all 4 optimisation methods, which were 0-400 *s/mm*^{2}, 650-1200 *s/mm*^{2} and 1700-2000 *s/mm*^{2} – 16 b-values were recommended: 0, 50, 100, 200, 350, 500, 650, 800, 950, 1100, 1250,

1400, 1550, 1700, 1850, 2000 *s/mm*^{2}. The optimised b-value protocol had better repeatability when compared to an equal distribution of b-values in 8 healthy volunteers.

Leporq *et al* (91) presented their optimisation of IVIM in the liver using the Cramer-Rao Lower Bound theory to determine the lowest optimum number of b-values and corresponding b-values needed to calculate IVIM parameters. Four, 6 and 8 b-values were explored – it was not stated how many sets of b-values were tested, but the values came from commonly used IVIM protocols in the liver literature. Four b-values 0, 12, 82, 1210 *s/mm*^{2} were found to produce the minimum standard deviation from expected calculated IVIM parameters using an input of physiological values for perfusion and diffusion in the liver from the literature. Twenty-five healthy volunteers and 12 patients with liver disease were retrospectively evaluated, originally scanned with 4 different IVIM protocols using the same b-values: 0, 20, 40, 60, 80, 100, 200, 300, 400, 600, 800 *s/mm*^{2}, but varying free-breathing, respiratory triggering, NEX, echo time, and the gradient scheme. The nearest 4 b-values to the optimised scheme were used for IVIM analysis: 0, 10, 80, 800 *s/mm*^{2}. The protocol was shown to be feasible in detecting non-advanced and advanced liver fibrosis – however this was a small cohort, and the exact optimised b-values were not actually used.

Dyvorne *et al* (92) also optimised for IVIM in liver. This study took Lemke *et al*'s 16 b-values and explored all possible subsets from 4 to 15 b-values (64,838 subsets were assessed) by finding the minimum global parameter error, indicating the best sampling strategy. Fifty-three subjects who had had IVIM MR scans (7 healthy and 46 with liver disease) were retrospectively analysed; 14 subjects had been scanned twice to test reproducibility. An optimal set of b-values was chosen such that the error lay within the test-retest reproducibility at 16 b-values. The minimal number of b-values that lay within this range was 4 at: 0, 15, 150, 800 *s/mm*^{2}, reducing the scan time up to 75%.

Liao *et al* (93) investigated a non-gaussian IVIM model to generate IVIM signals. There were three conditions of b-values: (1) 0–500 *s/mm*^{2} (2) 0–1000 *s/mm*^{2} (3) 0–2500 *s/mm*^{2}. For analysis, the Gaussian and the Non-Gaussian models were used for both full-fitting and asymptotic methods. The IVIM images were obtained with the following b values: 0, 5, 10, 20, 30, 50, 70, 100, 200, 400, 600, 800, 1000, 1500, 2000, 2500 *s/mm*^{2}. The mean errors and coefficient of variation were calculated. Compared with the full-fitting methods, the asymptotic methods provided better precision for IVIM analysis. However, the asymptotic

methods were sensitive to the weighting of perfusion component. The minimum b-value set for asymptotic methods should be larger than 500 *s/mm*^{2} and 767 *s/mm*^{2} for 5% and 1% residual perfusion component, respectively. In addition, the Gaussian models were sensitive to the non-Gaussian effects. This is interesting as it suggests a larger cut-off than 200 *s/mm*^{2} to use in a segmented fitting model. Rather than an optimisation, it was more comparing three regimes.

The first optimised protocol applied in breast (actually optimised for liver) was by Cho *et al* (80), from the same research group as Zhang *et al* (74) and Sigmund *et al* (94), comparing a conventional protocol: 0, 30, 70, 100, 150, 200, 300, 400, 500, 800 *s/mm*^{2} (as used in the clinical studies (95)) and a protocol similar to the optimised protocol for liver presented by Zhang: 0, 70 (x3 NEX), 300 (x3 NEX), 800 (x3 NEX) *s/mm*^{2}. Fourteen breast cancer patients were scanned, and simulations were carried out to support this data. Free and segmented approaches to fitting data were also compared. Experimentally, for each IVIM parameter, the lowest relative error was found for segmented fitting of the conventional protocol. The optimised scan did not outperform the standard protocol, due to segmented fitting breaking down due to not enough b-values below the cut-off. This trend mirrored simulations at different SNRs. Accuracy and reproducibility were not explored using the optimised protocol.

4.4. Literature Review Summary

Table 4.1 shows the relevant breast literature discussed in this chapter in summary form, detailing the first author, year, number of lesions scanned, magnetic field strength, DWI sequence used, b-values used, curve fitting method employed, and the calculated IVIM parameters as mean ± standard deviation or median (range).

Author, year	Number of malignant lesions	Magnetic field strength	DWI sequence	B-values (*s/mm²*)	Curve fitting method(s)	*D* (10^{-3} mm²/s)	*D** (10^{-3} mm²/s)	*f* (%)
Tamura et al, 2010	58	3.0 T	Single shot spin-echo EPI	0, 700, 1400, 2100, 2800, 3500 *s/mm²*	Method 3	0.18 ±0.09	2.10 ±0.68	0.67±0.13
Sigmund et al, 2011	24	3.0 T	Single shot spin-echo EPI	0, 30, 70, 100, 150, 200, 300, 400, 500, 800 *s/mm²*	Method 6	1.15 ±0.35	15.1 ±10.4	9.8 ±4.8
Iima et al, 2013	16	3.0 T	Single shot spin-echo EPI	0, 3, 5, 10, 20, 30, 50, 70, 100, 200, 400, 600, 800, 1000, 1500, 2000, 2500 *s/mm²*	Method 5 (Using kurtosis for D)	0.98 ±0.22	6.8 ±1.2	13.6 ±2.2
Bokacheva et al, 2013	26	3.0 T	Single shot spin-echo TSE	0, 30, 60, 90, 120, 400, 600, 800, 1000 *s/mm²*	Method 6	1.29 ±0.28	21.7 ±11.0	6.4 ±3.1
Liu et al, 2013	40	1.5 T	Single shot spin-echo EPI	0, 20, 30, 40, 50, 70, 100, 150, 200, 400, 600, 1000 s/mm²	Method 5	0.85 (0.77, 0.98)	94.71 (70.33, 113.23)	10.34 (7.68, 11.88)
Cho et al, 2014 (Conventional)	14	3.0 T	Single shot spin-echo TSE	0, 30, 70, 100, 150, 200, 300, 400, 500, 800 *s/mm²*	Method 3 Method 6	1.01±0.397 1.323 ±0.472	8.97 ±4.258 15.31 ±9.634	28.40 ±15.99 13.31 ±5.05
Cho et al, 2014 (Optimised)	14	3.0 T	Single shot spin-echo TSE	0, 70, 300, 800 *s/mm²*	Method 3 Method 6	1.088 ±0.390 1.195 ±0.471	11.028 ±7.981 13.183 ±6.529	24.89 ±11.39 16.83 ±9.06
Suo et al., 2014	30	3.0 T	Single shot spin-echo EPI	0, 50, 100, 150, 200, 500, 800 *s/mm²*	Method 1 Method 5 Method 6	0.70 ±0.11 0.83 ±0.19 0.77 ±0.15	98.24 ±59.25 159.50 ±90.32 69.28 46.19	16.33 ±5.21 7.61 ±2.33 6.10 ±3.19
Cho et al., 2015	50	3.0 T	Single shot spin-echo TSE	0, 30, 70, 100, 150, 200, 300, 400, 500, 800 *s/mm²*	Method 6	1.32 (0.65)	17.73 (4.45)	9.1 (5.1)

Table 4.1: Summary of b-values, fitting methods used and IVIM parameters calculated in the reviewed breast literature. EPI, echo planar imaging; TSE; turbo spin echo; parameters expressed as mean ±standard deviation or median (interquartile range) as reported.

4.5. Future IVIM Work

A consensus statement (96) was recently published on diffusion imaging outside of the brain; and in it were recommendations by world leaders in DW-imaging on what research is needed to improve DWI, and also IVIM specifically. It was said that IVIM should be utilised now technical advances allowed, and that IVIM should be investigated to see if it is as good as or better than standard DWI and ADC analysis. Main areas of research encouraged in IVIM research are; 1) Optimisation of protocols for better image quality (SNR) and parameter calculation; 2) B-value selection needs to be standardised and appropriate (number and choice of b-values for body part, accurate sampling of curve, and acceptable scan time); 3) Reliable methods to calculate parameters are needed (post processing robustness); and 4) Further IVIM model validation to confirm IVIM corresponds to actual tumour physiognomies.

Optimisations have been carried out for several organs – but mainly in the liver. A protocol developed for the liver has been applied in breast with the indication that a body part-specific optimisation is needed. Several different statistical methods were used for these limited optimisations, concentrating on minimising errors when calculating the IVIM parameters. There are various parameters that can be adjusted in DW-imaging, but the main parameters affecting the accuracy of f, D and D^* using the IVIM model are the b-values. That is, the number of b-values, the values of these applied gradients, and the range of b-values. The choice of b-values also affects the SNR and scan time – two important factors in clinical imaging with repercussions ranging from post processing ability to patient comfort and cost of imaging. In using different protocols, data acquired and analysis methods cannot be accurately compared, and so a consensus on IVIM has not been reached thus far. It also means that some patient cohorts get better quality scans than others, which could affect their diagnosis and treatment in the clinic. There is a clear motive in standardising an IVIM protocol. The clinical literature suggests that the heuristic (but logical) b-value choices concentrate on the usual cut-off for particular body parts (e.g. around 1000 s/mm^2 for breast (97)) and the decay curve is sampled well at low b-values to assess perfusion effects. An optimal set of b-values ideally creates good quality images for viewing a lesion, for post processing and will be able to be part of a clinically feasible protocol i.e. usable on the majority of MR scanners and in a short enough scan time. A protocol that generates IVIM parameters with minimal errors is also of importance.

So, it can be seen from the literature reviews of breast, optimisation, and the consensus recommendations that there are several directions in which research should be undertaken for IVIM. Firstly, an optimisation and standardisation of the IVIM protocol that is body part specific and able to be used clinically in terms of scan time and hardware needs to be carried out. Then, fitting methods to yield *f, D* and *D** need to be further explored and a robust method confirmed. Further, the presence of IVIM effects in normal tissue needs to be confirmed or rejected. The repeatability and reproducibility of IVIM measurements with an optimised protocol needs to be explored. Clinically, the presence of and accurate measurement of IVIM effects in different lesion types and subtypes needs to be properly established. The clinical utility of distinguishing malignancy (and tumour sub groups) versus benign and normal tissue with an optimal protocol needs to be explored. If this can be proven, then the implementation and exploration of IVIM into a clinical multiparametric MR exam is justifiable. The potential for IVIM parameters to correlate with, characterise, and quantify cancer physiognomies will be even more so once these aims have been met.

The aims of the main body of this thesis (Chapters 5 to 9), using advanced diffusion imaging, were therefore: 1) to develop software to allow an optimised IVIM protocol to be established for any body part with inputs of estimated perfusion and diffusion, scan time and other limitations, evaluating an exhaustive range of b-values considered in the literature; 2) to present an acceptable optimised IVIM protocol leading to standardisation of this type of imaging in breast tissue and malignancies; 3) to investigate IVIM effects, repeatability and reproducibility in normal healthy tissue and malignant lesions in breast; 4) to investigate the robustness of fitting methods for IVIM data in breast; 5) to investigate the clinical utility of an optimised protocol in breast cancer patients; 6) to support these with statistical simulations; and 7) to allow clinicians to keep qualitative evaluation preferences by creating a computed DWI tool to calculate DW-images of any b-value if the optimised protocol did not suit preferences.

5. Optimisation of Intravoxel Incoherent Motion Imaging

5.1. Introduction

There lies an impotency in the application of IVIM imaging due to a lack of standardisation. The main parameters affecting the calculation of the IVIM parameters *f, D* and *D** are the b-values and NEX (number of excitations) - the signal from these diffusion-weighted images is used to calculate the parameters. The b-value protocol can be broken down into;

- The number of b-values, *nb* (e.g. 4 b-values)
- The values of the specific weightings (e.g. 0, 50, 700, 1000 mm/s^2)
- The range (minimum and maximum cut-offs) of the protocol (e.g. 0 and 1000 mm/s^2)
- The spacing – i.e. how best to sample the signal curve

The choice of b-values affects the SNR and scan time. These are two important factors in clinical imaging that are constraints in terms of time because of patient comfort and resources. There is a clear motive in optimising and standardising an IVIM protocol from both an exciting scientific and sensible clinical perspective. Implementing this can further the potential of IVIM itself as a biomarker in diagnosis and treatment response assessment.

The literature suggests that the heuristic (but logical) b-value choices concentrate on a common cut-off for particular body parts (e.g. about 1000 s/mm^2 for breast (44, 97)) and the decay curve is sampled well at low b-values to assess perfusion effects.

An optimal set of b-values ideally creates good quality images for viewing a lesion, post processing, and will be part of a clinically feasible protocol i.e. usable on the majority of MR scanners and in a short scan time. A protocol that generates IVIM parameters with minimal errors is also of importance - see Monte Carlo Simulations in Chapter 8, which looks at the mean squared errors given by different protocols.

A robust, statistical approach to the analysis of a wide range of b-values is needed, which is body-part specific and accounts for scan time. Optimisation of IVIM in breast cancer is needed with its popularity and potential in the clinical setting becoming clear. The application of these optimised protocols is explored in healthy volunteers in Chapter 6, and as part of a clinical MR protocol for lesion detection and characterisation in Chapter 7.

The aim of the work in this chapter was to develop software to allow an optimised IVIM protocol to be established for breast cancer with inputs of estimated perfusion and diffusion parameters, scan time, and any other limitations such as NEX. This was done evaluating an exhaustive number of sets of b-values, surpassing work carried out in the literature. Several different methods were used in the literature for optimisation and some of these have been combined, implemented and improved on, here. Optimisation in the literature was not specifically for breast, but an optimised protocol for the kidney was applied and assessed in breast (80). A statistical approach to selection of b-values is described, which was an iterative process with a final protocol proposed and applied clinically in breast cancer in Chapter 7, after assessing data from healthy volunteers in Chapter 6. Optimisation iterations and scanning volunteers were done in parallel and so the two chapters tie in together with the latter investigating post-processing analysis of the images. The protocols used in each chapter have been named identically and clearly to cross-reference (Protocols C-F). The final program was implemented in breast but could be used on any body part with different initial inputs (e.g. higher perfusion in the kidney or lower in the brain).

5.2. Optimisation Software

Optimisation was carried out using in-house developed software written and computed in MATLAB (MathWorks, Massachusetts, USA). Several programs were implemented, computing the calculations in Sections 5.2.1-5.2.3 separately at first. The iterations of optimisation outlined throughout Sections 5.3 promoted code improvements. Upon the fourth iteration a final program was written condensing all parts of the optimisation into one and allowing the user to explore all of the options needed to generate an optimised b-value scheme for a specific body part.

5.2.1. Generating Sets of b-values to be Analysed: Exponential and Power Law Spacing

The program allows the user to generate any number of b-value sets for analysis of optimality using two regimes; power law spacing and exponential spacing. Both spacing types embody the intuitively reasonable requirement that b-values need to be sampled more frequently at low values to pick up perfusion effects, as this signal drops much faster exponentially (98). Clearly, there are a near infinite number of ways b-values could be sampled between a lower and upper limit. Therefore, the use of power law and exponential spacing methods is a more

pragmatic approach to reduce calculation burden. The scanner used only allowed whole numbers to be entered into the protocol. These approaches were thought to be the next best solution to an infinite analysis as thousands of sets of b-values can be generated within seconds.

The user chooses a minimum b-value, for example, b = 0 *s/mm*^{2}. The user also needs to choose a maximum b-value, for example, b = 2000 *s/mm*^{2}. These are the minimum and maximum b-values of the protocol. NB: In the final program the maximum b-value could be any multiple of 100 up to the maximum inputted, 2000 *s/mm*^{2} in this example. The number of b-values also needs to be chosen by the user. In the final program, as for the cut-off b-value, variation in the number of b-values was allowed, for example up to and including 20 b-values in increments of 1. Power law spacing and exponential spacing are established methods to generate non-linear spacing, and work well in this scenario of assuming the curve needs to be better sampled at lower values. The exponent, *r*, is entered into the program and this affects how extreme the spacing will be, which is sampled in increments. These mathematical models are presented below.

Equation 5.1 shows Exponential spacing;

$$b_i = b_{min} + (b_{max} - b_{min})\left(\frac{1 - r^{i-1}}{1 - r^{nb-1}}\right)$$

Equation 5.1

Equation 5.2 shows Power Law spacing;

$$b_i = b_{min} + (b_{max} - b_{min})\left(\frac{i - 1}{nb - 1}\right)^r$$

Equation 5.2

where b_{min} is the lowest b-value, b_{max} is the highest b-value, b_i is the b-value for *i*th iteration, *nb* is the number of b-values, and *r* is the exponent. An *r* of 5 would not sample low b-values as well as that of an *r* of 8, for example. The increments of *r* affect how many sets of b-values will be generated. An increment of 1 will generate fewer sets of b-values than 0.1, and so on. To achieve uniform spacing, *r*, must be 1 for power law spacing and *r* must take the limit towards 1 for exponential spacing. As a result of this, in exponential spacing, at 1 the program failed. To alleviate this, optimisations were carried out with an exponent starting at 1.01 or the

exponent increments were modified to skip over 1 (eg. use 0.11 instead of 0.1). This was not a problem in the end as the optimal set of b-values was never at or near $r = 1$.

5.2.2. Cramer-Rao Lower Bound Theory

In estimation theory and statistics, the Cramér–Rao lower bound (CRLB), named after Cramér and Rao who were the first to report it (99, 100), expresses a lower limit to the accuracy with which a parameter can be determined from experimental data. It is the lower limit of the variance, with units of those of the parameter, squared. This theory can be applied to a multitude of physical problems and has been used in MRI in biexponential problems such as T_2 relaxation and multi b-value sequences in the liver (98, 101, 102), but not to the extent presented in this chapter in regards to the number and breadth of sets of b-values analysed (73, 91, 103). A Gaussian distribution of noise should be assumed when applying this theory to MR images.

In terms of statistical analysis, an estimator calculates a parameter. The estimator is the method used to calculate the IVIM parameters from the experimental data i.e. the fitting of the experimental data acquired from the MR protocol. An estimator may be unbiased (accurate to the true value), or biased if otherwise. A bias may occur due to random or systematic error, or indeed due to randomness, especially due to noise in MR images. A biased parameter can have a low mean squared error (MSE) or CRLB of variance – sometimes even lower than unbiased estimators. That is because it is describing the precision in which the data can be fit, not the true accuracy of the parameter. The CRLB theory and calculation is valid for both biased and unbiased estimators. The efficiency of an estimator can be measured by setting a measure of optimality, in this case, the CRLB. The MSE is also commonly used. If an estimator is efficient, the performance target is met from real data. So, if the fitting method and b-value protocol was efficient, then the CRLB or low MSE would be met and indicate it was as precise as possible. We can only know if something is accurate and therefore unbiased if there is a true value to compare it with – something that IVIM does not have. It must be noted that bias can mean the experimental data gives a lower MSE or CRLB than expected. Using the CRLB calculation, optimisation is done by calculating the CRLB for variations of the b-value protocol, using Fitting Method 5 (Segmented Fit – the gold standard as described in the literature but also tested against other fitting methods in Chapter 6) to fit data simulated from

initial inputs into the program. The protocol with the lowest CRLB is thus the most precise way to acquire data and calculate IVIM parameters.

The IVIM model, described in Equation 3.4, yields four parameters to precisely determine; S_0, the diffusion-weighted signal; f, the perfusion fraction; D, the diffusion coefficient and D^*; the pseudodiffusion coefficient. These parameters are normally calculated from MR-images via post-processing in MATLAB using signal values acquired via ROIs or full tumour segmentation. The b-values from which the parameters are calculated are to be optimised.

In order to determine the optimal set of b-values for IVIM in the breast, the CRLBs of the standard deviations (SD) of the IVIM equation parameters were calculated. The user enters literature values (or values calculated from non-optimised scans) of the model's parameters into the program. The program uses these to calculate the CRLB for each set of b-values generated from Section 5.2.1. Throughout the iterations of optimisation, these parameter values were taken from the literature and from data obtained in healthy volunteers. The following equations were coded into the program to calculate the CRLB for each set of b-values in question.

The CRLB of the SD of the kth of these parameters, $s(\theta_k)$, was calculated using;

$$s(\theta_k) = \sqrt{(\mathbf{F}^{-1})_{kk}}$$

Equation 5.3

for the kkth element of the Fisher Information Matrix, $\mathbf{F}$, given by the partial derivative summations;

$$\mathbf{F}_{jk} = \sum_{b's} \left(\frac{\partial s}{\partial \emptyset_j} \frac{\partial s}{\partial \emptyset_k}\right)$$

Equation 5.4

where j and k correspond to pairs of parameters ($S_0 = 1$, $f = 2$, $D = 3$, $D^* = 4$) as in the completed Fisher Information Matrix;

$$\mathbf{F} = \begin{bmatrix} F_{11} & F_{12} & F_{13} & F_{14} \\ F_{21} & F_{22} & F_{23} & F_{24} \\ F_{31} & F_{32} & F_{33} & F_{34} \\ F_{41} & F_{42} & F_{43} & F_{44} \end{bmatrix}$$

Equation 5.5

The partial derivatives are as follows;

$$\frac{\partial S}{\partial S_0} = (1-f)e^{-bD} + fe^{-bD^*}$$

Equation 5.6

$$\frac{\partial S}{\partial f} = -S_0 e^{-bD} + S_0 e^{-bD^*} = S_0(e^{-bD^*} - e^{-bD})$$

Equation 5.7

$$\frac{\partial S}{\partial D} = -b.S_0(1-f)e^{-bD}$$

Equation 5.8

$$\frac{\partial S}{\partial D^*} = -b.S_0 f e^{-bD^*}$$

Equation 5.9

which are used to construct the Fisher Information Matrix elements shown below. Partial derivatives are commutative, so $F_{21} = F_{12}$, etc. meaning only half of the calculations need to be carried out. These are as follows;

$$F_{11} = \sum_{nb}^{0} \frac{\partial S}{\partial S_0} \frac{\partial S}{\partial S_0}$$

$$F_{12} = \sum_{nb}^{0} \frac{\partial S}{\partial S_0} \frac{\partial S}{\partial f}$$

$$F_{13} = \sum_{nb}^{0} \frac{\partial S}{\partial S_0} \frac{\partial S}{\partial D}$$

$$F_{14} = \sum_{nb}^{0} \frac{\partial S}{\partial S_0} \frac{\partial S}{\partial D^*}$$

$$F_{22} = \sum_{nb}^{0} \frac{\partial S}{\partial f} \frac{\partial S}{\partial f}$$

$$F_{23} = \sum_{nb}^{0} \frac{\partial S}{\partial f} \frac{\partial S}{\partial D}$$

$$F_{24} = \sum_{nb}^{0} \frac{\partial S}{\partial f} \frac{\partial S}{\partial D^*}$$

$$F_{33} = \sum_{nb}^{0} \frac{\partial S}{\partial D} \frac{\partial S}{\partial D}$$

$$F_{34} = \sum_{nb}^{0} \frac{\partial S}{\partial D} \frac{\partial S}{\partial D^*}$$

$$F_{44} = \sum_{nb}^{0} \frac{\partial S}{\partial D^*} \frac{\partial S}{\partial D^*}$$

Equations 5.10

and so **F** can be constructed. Each b-value in a set is evaluated for each pair of partial derivatives and are summed to give that Fisher matrix element. The main diagonal of the

inverse matrix represents the $s(\theta_k)$ for each of the four parameters. Plotting $s(\theta_k)$ versus r and finding the minimum indicates the best sampling strategy for that parameter.

When investigating the alternative IVIM model (Equation 4.1) with an extra term as mentioned in the breast literature review (86), the following partial derivatives were used in lieu to construct **F**;

$$\frac{\partial S}{\partial S_0} = (1-f)e^{-bD} + fe^{-b(D^*+D)}$$

Equation 5.11

$$\frac{\partial S}{\partial f} = S_0(e^{-b(D^*+D)} - e^{-bD})$$

Equation 5.12

$$\frac{\partial S}{\partial D} = -b.S_0(1-f)e^{-bD} - b.S_0.fe^{-b(D^*+D)}$$

Equation 5.13

$$\frac{\partial S}{\partial D^*} = -b.S_0.fe^{-b(D^*+D)}$$

Equation 5.14

5.2.3. Figure of Merit

An optimised b-value scheme was chosen based on a figure of merit (FoM), Γ, which balances the relative errors of the parameters of interest by taking the square root of the sum of each CRLB over the corresponding initial parameter value inputted by the user, as shown below;

$$\Gamma = \sqrt{\frac{s(\theta_f)}{f} + \frac{s(\theta_{fD})}{D} + \frac{s(\theta_{fD^*})}{D^*}}$$

Equation 5.15

The lowest Γ out of a set of generated b-values meant the optimal choice. Comparing the minima of *r* versus Γ, gave a value for the optimal r and thus the corresponding optimal set of b-values from those generated. S_0 is not accounted for here as we are not interested in

measuring S_0 as it is not an IVIM potential biomarker with underlying physiological importance, so there is no need to take into account in figure of merit calculation.

5.2.4. MATLAB Output

On execution prompts for the input parameters will appear. The program is coded to run through Sections 5.2.1 – 5.2.3. Once the program has run, two spread sheets are generated. The first, 'PowerLawResults' or 'ExponentialResults', details the sets of b-values generated, with each *nb* on a different sheet within the document, along with the corresponding *r*, the exponent, '*SD S0*', the CRLB of the SD of the signal, '*SD f*', the CRLB of the SD of the perfusion fraction parameter, '*SD D*', the CRLB of the SD of the diffusion parameter, '*SD Dstar*', the CRLB of the SD of the pseudo diffusion parameter, and '*FofM*', the figure of merit. The second excel spreadsheet, '*FoM results min10Dstar*'*, details the figure of merit only for each b-value cutoff and *nb*. This allows a quick comparison of the FOMs, their corresponding *r*, and so enables the user to find the optimal set of b-values quickly. *Subject to change depending on regime used.

Figure 5.1 shows the optimisation program running in MATLAB for the case of '*CRTmin10Dstar*', with *'min10*' referring to the second b-value being constrained to 10 (see later optimisations) and '*Dstar*' referring to using the original IVIM equation for calculations.

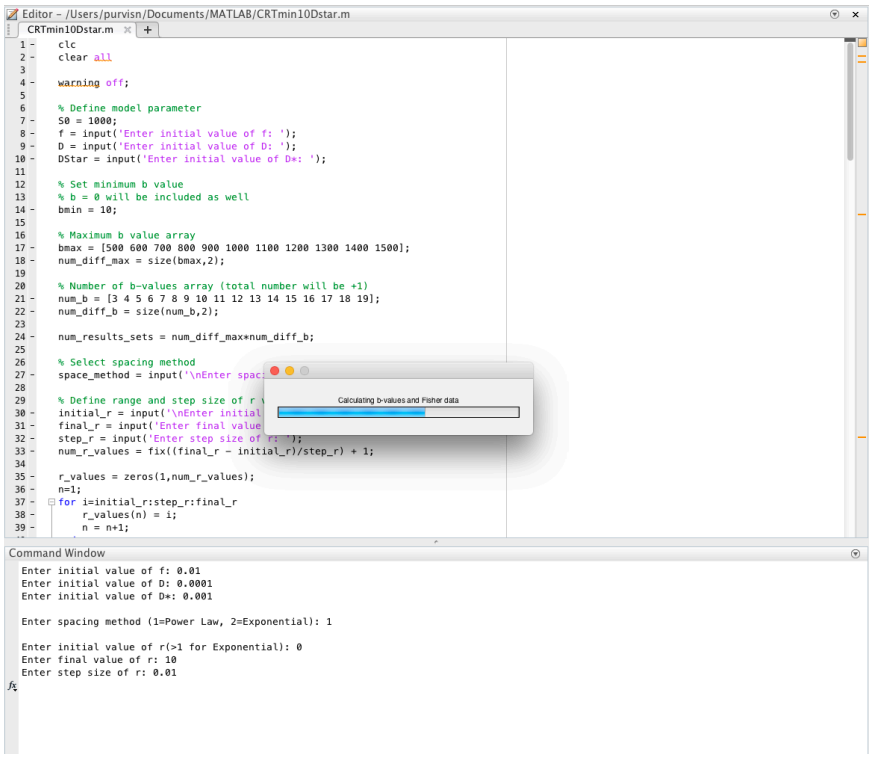

Figure 5.1: Screen shot of the optimisation program running in MATLAB ('CRTmin10Dstar' refers to the second b-value being constrained to 10 and to using the original IVIM model).

5.3. Breast Optimisation Iterations

5.3.1. Method: Breast First Iteration

The first iteration of optimisation was carried out to investigate the extremes of user inputs *f, D* and *D** to see if there were differences between the produced optimal sets of b-values. The optimisation was carried out with initial inputs of *f, D* and *D** from the literature (at date of optimisation) for malignant highest value found, malignant lowest value found and for normal tissue (81, 83, 94). This was done for both exponential and power law spacing. This yielded 6 optimisations. The minimum b-value, maximum b-value, exponent minimum, exponent maximum and exponent increment were all kept consistent for the 6 optimisations. The number of b-values in a set ranged from 10 up to 20 in increments of 1. After scanning healthy volunteers with heuristic protocols (see Chapter 6), it was decided that a clinical constraint of 5 minutes for scan time was needed for IVIM if it was to be implemented in clinic; this was encouraged by feedback from radiologists and volunteers - considering comfort, financial implications and time limits for breast exams. This meant that a maximum of 10 b-values with

4 NEX per b-value could only be used, which ranged from 4m20s to 5m depending on breast size. Less NEX may result in inadequate SNR to calculate IVIM parameters. The optimal set of 10 b-values is referred to as ‘clinically optimal’ from here on, and the actual optimal set with none of these limitations is referred to as ‘optimal’. Obviously, sampling the curve in excess would give better calculations but there may be a saturation point. It would never be practical to do this, however. Below in Tables 5.1 are the summarised inputs to the MATLAB program for this iteration.

Input parameter	Malignant lowest Exponential/Power	Malignant highest Exponential/Power	Normal Exponential/Power
f	0.06400	0.1034	0.0110
D	0.000850 mm^2/s	0.00129 mm^2/s	0.00216 mm^2/s
D^*	0.0151 mm^2/s	0.0947 mm^2/s	0.00970 mm^2/s
B_{min}	0 s/mm^2	0 s/mm^2	0 s/mm^2
B_{max}	1000 s/mm^2	1000 s/mm^2	1000 s/mm^2
Nb	10-20	10-20	10-20
r_{min}	1	1	1
r_{max}	10	10	10
r_{step}	0.01	0.01	0.01

Table 5.1: Input parameters for the first iteration of optimisation into the program for malignant lesions and normal tissue.

5.3.2. Results: Breast First Iteration

The figure of merit, Γ, versus the exponent, *r,* was graphed to find the minimum figure of merit and its corresponding exponent. Graphs 5.1-12 show this for the 6 optimisations carried out. This value of *r* corresponded to an optimal set of b-values, which could be looked up from the spread sheets produced by the software. This was also done for the clinically optimal (10) b-values. These outputs are detailed below in Table 5.2 for malignant lesions and in Table 5.3 for normal tissue. The lower the figure of merit, the more optimal that corresponding set of b-values. The most optimal out of the 4 sets for malignant tissue is shown in bold, with the same for normal tissue, comparing the two sampling strategies (exponential and power law). All b-values were rounded to the nearest whole number, since MRI scanners currently do not allow b-values with decimal places clinically.

Output parameter	Malignant lowest Exponential	Malignant highest Exponential	Malignant lowest Power Law	Malignant highest Power Law
Optimal *nb*	**20**	20	20	20
Optimal *r*	**1.18**	1.38	1.96	3.65
Optimal Γ	**0.102971**	0.135084	0.106589	0.151030
Clinically optimal *nb*	**10**	10	10	10
Clinically optimal *r*	**1.44**	1.99	2.06	4.04
Clinically optimal *Γ*	**0.122087**	0.162233	0.127083	0.178925
B-values optimal	**0, 0, 0, 0, 0, 0, 0, 0, 0, 0, 1, 2, 4, 9, 20, 44, 97, 210, 458, 1000 *s/mm²***	0, 0, 0, 0, 1, 2, 3, 5, 8, 12, 17, 25, 35, 50, 70, 98, 137, 517, 719, 1000 *s/mm²*	0, 0, 0, 0, 1, 2, 5, 10, 18, 31, 51, 79, 119, 172, 242, 334, 451, 597, 778, 1000 *s/mm²*	0, 0, 0, 0, 0, 1, 2, 4, 8, 15, 27, 46, 75, 118, 179, 264, 379, 534, 737, 1000 *s/mm²*
B-values clinically optimal	**0, 0, 2, 4, 11, 28, 69, 168, 410, 1000 *s/mm²***	0, 2, 6, 14, 29, 61, 123, 249, 499, 1000 *s/mm²*	0, 1, 10, 35, 84, 167, 290, 465, 698, 1000 *s/mm²*	0, 0, 2, 12, 38, 93, 194, 362, 621, 1000 *s/mm²*

Table 5.2: Output parameters for the first iteration of optimisation for malignant lesions.

Output parameter	Normal Exponential	Normal Power Law
Optimal *nb*	**20**	20
Optimal *r*	**1.15**	1.86
Optimal Γ	**0.098857**	0.103919
Clinically optimal *nb*	**10**	10
Clinically optimal *r*	**1.34**	1.86
Clinically optimal *Γ*	**0.119133**	0.125396
B-values optimal	**0, 0, 0, 0, 0, 0, 0, 0, 0, 0, 0, 0, 0, 1, 3, 10, 32, 101, 318, 1000 *s/mm²***	0, 4, 16, 33, 56, 85, 119, 158, 202, 251, 305, 364, 427, 496, 568, 646, 728, 814, 905, 1000 *s/mm²*
B-values clinically optimal	**0, 0, 0, 0, 2, 8, 27, 90, 300, 1000 *s/mm²***	0, 17, 61, 131, 223, 337, 472, 628, 804, 1000 *s/mm²*

Table 5.3: Output parameters for the first iteration of optimisation for normal tissue.

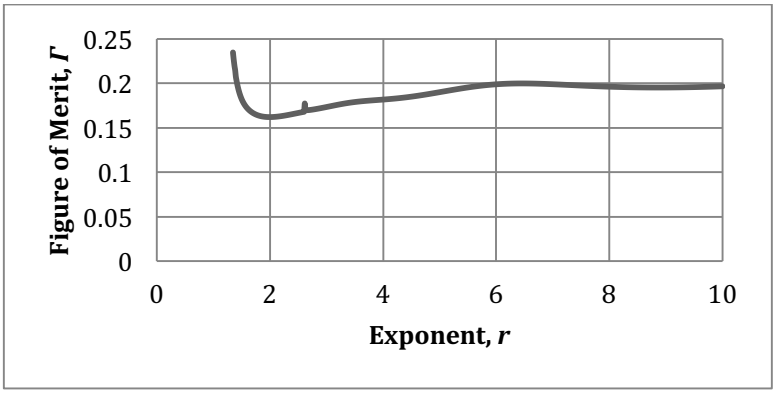

Graph 5.1: Figure of merit versus exponent for malignant highest, exponential spacing, clinically optimal number of b-values (10).

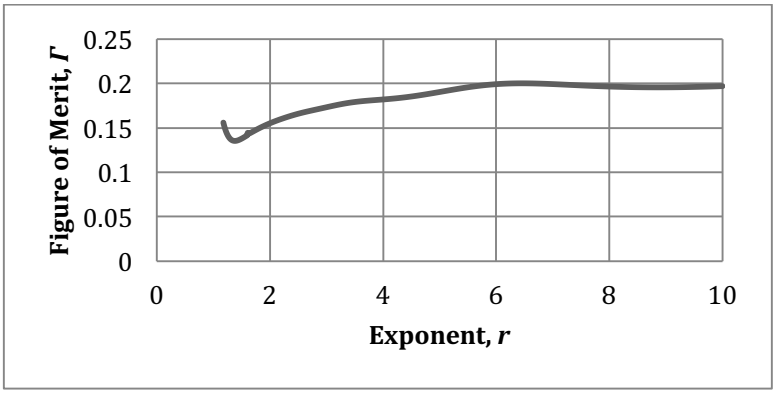

Graph 5.2: Figure of merit versus exponent for malignant highest, exponential spacing, optimal number of b-values (20).

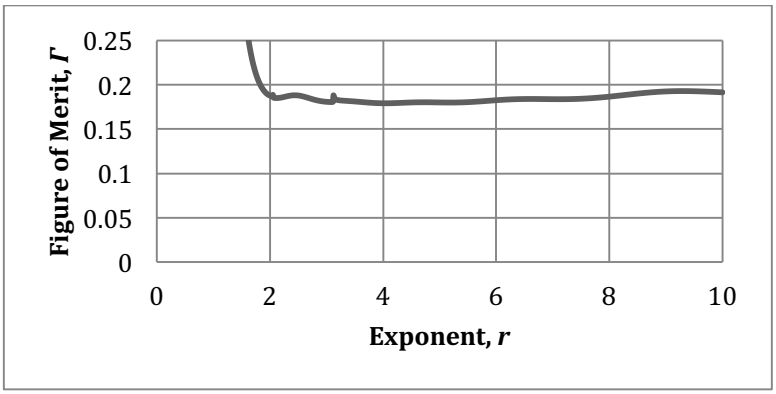

Graph 5.3: Figure of merit versus exponent for malignant highest, power law spacing, clinically optimal number of b-values (10).

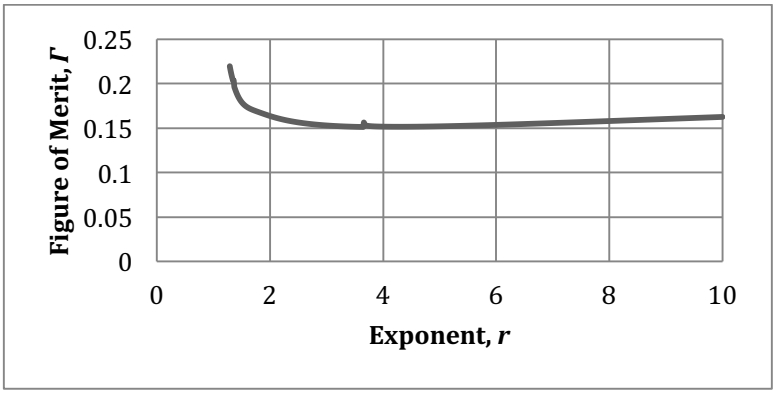

Graph 5.4: Figure of merit versus exponent for malignant highest, power law spacing, optimal number of b-values (20).

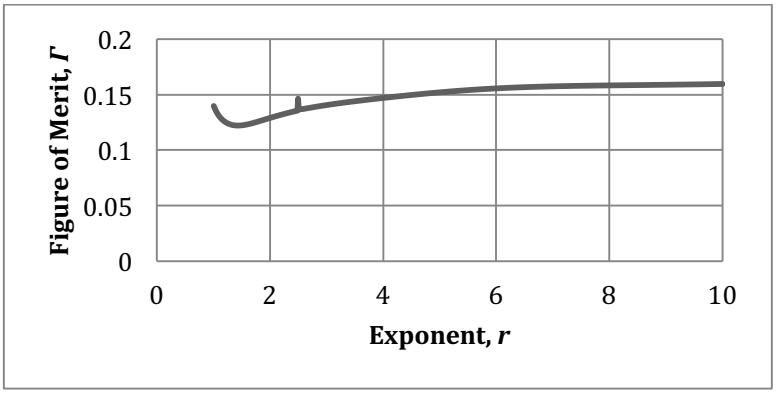

Graph 5.5: Figure of merit versus exponent for malignant lowest, exponential spacing, clinically optimal number of b-values (10).

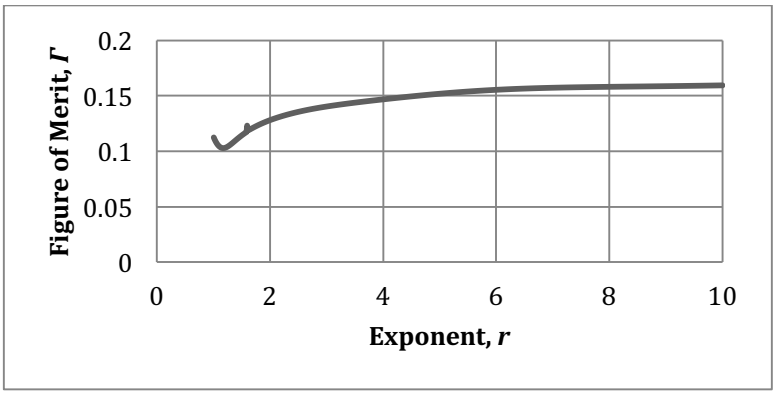

Graph 5.6: Figure of merit versus exponent for malignant lowest, exponential spacing, optimal number of b-values (20).

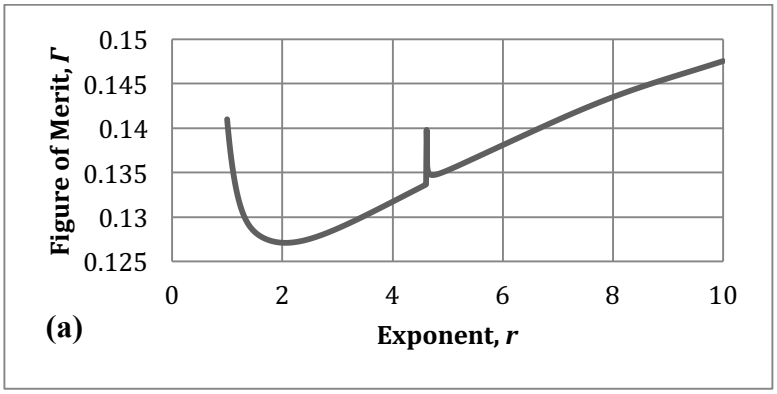

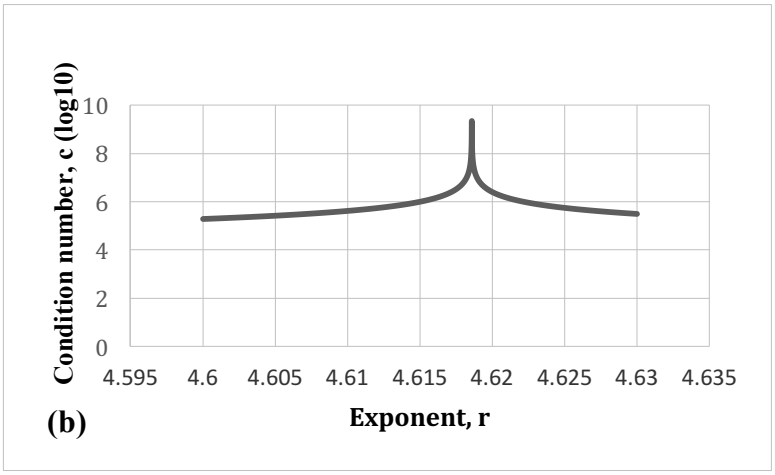

Graphs 5.7a and 5.7b: (a) Figure of merit versus exponent for malignant lowest, power law spacing, clinically optimal number of b-values (10). (b) The relation between the exponent, r, and the condition number of the matrix, c.

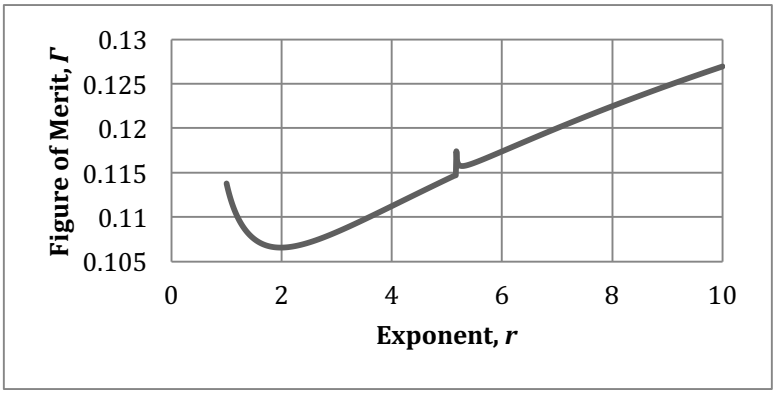

Graph 5.8: Figure of merit versus exponent for malignant lowest, power law spacing, optimal number of b-values (20).

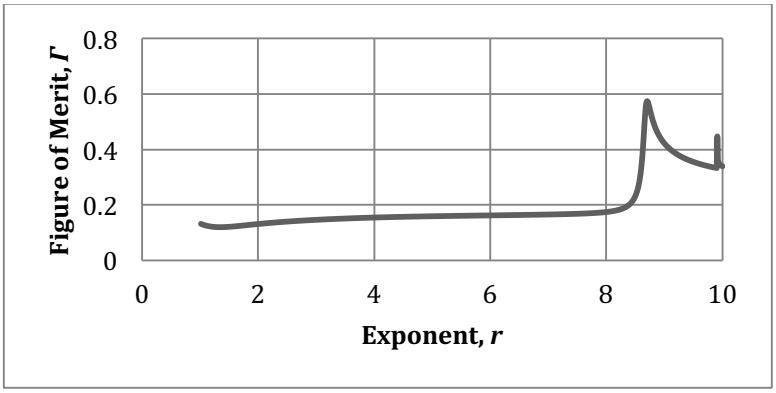

Graph 5.9: Figure of merit versus exponent for normal tissue, exponential spacing, clinically optimal number of b-values (10).

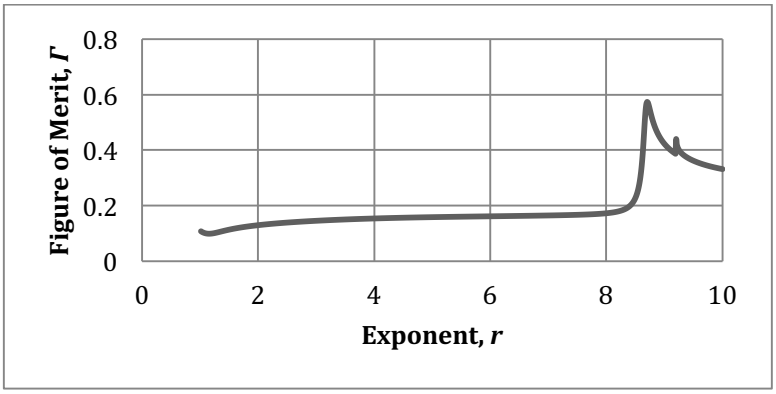

Graph 5.10: Figure of merit versus exponent for normal tissue, exponential spacing, optimal number of b-values (20).

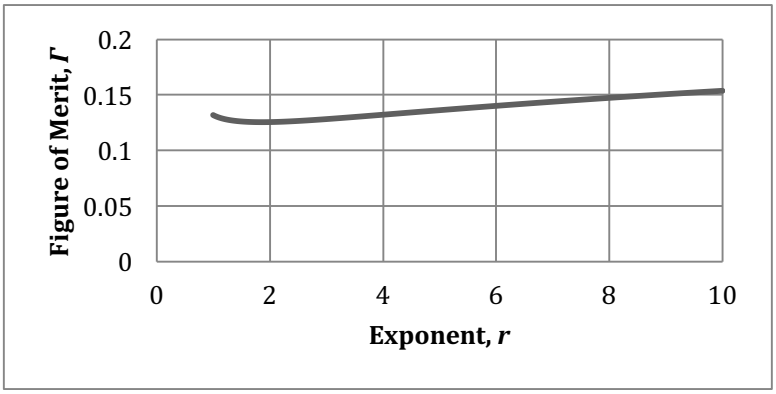

Graph 5.11: Figure of merit versus exponent for normal tissue, power law spacing, clinically optimal number of b-values (10).

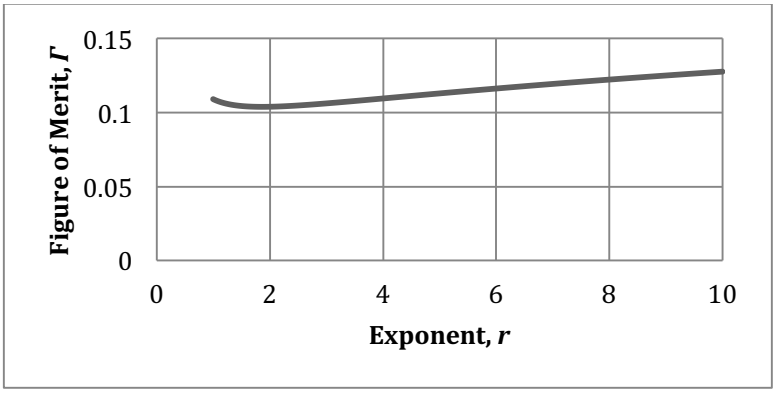

Graph 5.12: Figure of merit versus exponent for normal tissue, power law spacing, optimal number of b-values (20).

5.3.3. Discussion: Breast First Iteration

Six optimisations were carried out, for initial inputs of *f, D* and *D** from the literature for malignant highest value found, malignant lowest value found and for normal tissue values using both exponential spacing and power law spacing to generate sets of b-values. Nine-hundred sets of b-values were generated for each *nb* (10 up to 20 in increments of 1) for each of the 6 optimisations and so 59,400 sets of b-values were analysed in this iteration in total. Making the increment of *r* smaller would generate more sets of b-values. It appears that increasing *r* beyond the current limit of 10 would have no beneficial effect since the optimal b-values lie below this limit for all optimisations. Decreasing r is difficult using this increment due to the program failing at the limit of 1 for exponential spacing, but this is also not problematic as the *r* values corresponding to minimum FoMs are higher than 1. This is due to the solution of the equation tending towards infinity at unity. Skipping 1 and values close to one would allow lower values to be investigated.

For malignant lowest with exponential spacing the zero values, except for the first zero, were decimals of the order ranging from 10^{-6} to 10^{-2} before rounding. The optimisation procedure has determined that many near zero values are necessary. Owing to the fact that non-integer values cannot be inputted into the scanner, the benefit of this cannot be realised. The other b-values do sample the curve well at low b-values to calculate *f* and *D**, in comparison to literature. To calculate *D*, which is monoexponential, there are higher b-values, but only two (assuming high is accepted as well over 200 s/mm^2). This was the most optimal scheme overall, mathematically. Upping the NEX by 9 times for 0 s/mm^2 would improve image quality, but so many 0 s/mm^2 do not indicate the best sampling strategy as they are not the true values from the optimisation.

The malignant highest with exponential spacing scheme is reasonably comparable to literature schemes. It samples low b-values well and allows *D* to be calculated, uninfluenced by the perfusive component, with 3 higher b-values. Compared to its malignant lowest counterpart, it makes more sense as a sampling strategy. A trade off between the two by using an average of the input parameters may be a good compromise, reflecting the fact that clinical values obtained will probably fall between the two extremes of high and low literature values.

The malignant lowest with exponential spacing regime fulfils the criteria of needing to sample lower b-values well and enables calculation of the diffusion parameter with higher b-

values, though there is a large gap between the penultimate and last b-value. Two 0 s/mm^2 are not necessary as previously explained. This is the third most optimal scheme overall, and the best clinically optimal scheme. Malignant highest with power law spacing is the least optimal scheme overall.

From this assessment of malignant optimisation, it can be seen that the most optimal scheme is found when modelling malignant lowest input values according to the program. However, from visually inspecting the b-value sets, the malignant highest offers schemes that are more practical to implement. Therefore it seems prudent to investigate the use of average values for the malignant parameters next. Having 20 b-values is more optimal according to the MATLAB program but clearly some user consideration is needed. The program will need to be improved to overcome this, perhaps by using constraints. If 20 b-values cannot be used because of time, financial and comfort constraints then a limit on the number of b-values could be used. For identical input parameters, exponential spacing always produces lower figure of merits. Therefore exponential spacing will be utilised next, too.

Exponential spacing produces more optimal results for identical input parameters in normal tissue. It appears that lower b-values are sampled more frequently, which corresponds to the input parameters representing low perfusion.

The figure of merit versus the exponent for all malignant optimisations show a clear minimum and follow approximately the same shape. It would be interesting to see what the graphs do below $r = 1$, but avoiding 1, for exponential spacing as it can be seen that they tend to infinity approaching 1. The graphs for normal tissue follow a different shape from malignant initial inputs, indicating the sensitivity of the software to tissue type.

The spikes in graphs 5.5 to 5.10 indicate ill-conditioning of the matrix calculation in MATLAB. A command to calculate the condition number of a matrix (cond) was used to investigate the spikes. The higher the condition number, c, the more ill-conditioned the matrix is. An ill-conditioned matrix is almost singular and the computation of its inverse is prone to large numerical errors. A singular matrix has a determinant of 0 and can't be inverted. For example, a simple matrix [0 0; 0 0] has a determinant of zero and can't be inverted. Graph 5.7b shows r against condition number, and clearly shows the rapid increase at the same point as the spike in graph 5.7a. Thus, in these cases the Fisher matrix was ill-conditioned leading to

numerical errors. These spikes do not appear near the minimum and so are not thought to have affected the results of optimisation.

Salient points to consider from these optimisations are; exponential spacing is always better; and 20 b-values are always better than 10 (although not clinically appropriate). Many values close to zero are indicated when it is more difficult to tease out D^* from D i.e. normal values and lowest malignant.

The optimisation results in this iteration show that there are differences in the calculated optimal b-values when considering differing inputs of f, D and D^*. This is encouraging as it means the program can tailor optimisation for different body parts with different physiological perfusion and diffusion rates. However, it means that the parameter inputs (corresponding to expected accurate values) for one body part need to be as accurate and precise as possible – this is difficult considering all tumours, and indeed breasts, have differing perfusion and diffusion rates depending on the individual's biology and tumour biology. The next best solution is to simply take an average of all of the values available from literature for specific tissue types. Once clinical results are obtained, another optimisation could be carried out tailoring b-values to those tissue types of interest in a final post-clinical optimisation.

5.3.4. Method: Breast Second Iteration (Protocols C and D)

The second iteration of optimisation was carried out using an average (mean) of malignant values from the literature (81, 83, 94) for user inputs f, D and D^*. Protocols C and D are the names given to the optimised scans from this section in Chapter 6 when scanning volunteers. It was established that exponential spacing was superior previously and so power law spacing was discarded in this iteration. The exponent minimum is now 0, with increments of 0.011 to step over 1 up to a maximum of 10 due to the equation tending to infinity at unity. The number of b-values in a set range from 10 up to 20 in increments of 1. This yielded 11 sets of optimisation results. Below in Table 5.4 are the summarised inputs to the MATLAB program.

Input parameter	Malignant average Exponential
f	0.0885
D	0.001097 mm^2/s
D^*	0.04384 mm^2/s
B_{min}	0 s/mm^2
B_{max}	1000 s/mm^2
Nb	10-20
r_{min}	0
r_{max}	10
r_{step}	0.011
Spacing	Exponential

Table 5.4: Input parameters for the second iteration of optimisation.

5.3.5. Results: Second Iteration (Protocols C and D)

Following the methodology described in Section 5.3.2, the results shown in Table 5.5 were obtained. All b-values were again rounded to the nearest whole number. The graphs did not indicate any change in shape in comparison to the malignant graphs from the first iteration of optimisation.

Output parameter	Malignant average
Optimal *nb*	20
Optimal *r*	1.59
Optimal *Γ*	0.143054
Clinically optimal *nb*	10
Clinically optimal *r*	1.24
Clinically optimal *Γ*	0.210541
B-values optimal (Protocol D)	0, 4, 8, 14, 21, 30, 41, 55, 73, 94, 122, 156, 198, 251, 318, 401, 505, 635, 797, 1000 *s/mm²*
B-values clinically optimal (Protocol C)	0, 9, 23, 46, 82, 140, 233, 382, 619, 1000 *s/mm²*

Table 5.5: Output values for the second iteration of optimisation.

5.3.6. Discussion: Breast Second Iteration (Protocols C and D)

An optimisation was carried out, for average initial inputs of *f, D* and *D** from the literature for malignant lesions using exponential spacing to generate sets of b-values. One thousand sets of b-values were generated for each *nb* (10 up to 20 in increments of 1) and so 11,000 sets of b-values were analysed in this iteration in total. Making the increment of *r* smaller would generate more sets of b-values. Increasing *r* beyond the defined maximum of 10 would have no beneficial effect since the optimal b-values lie below this limit for all optimisations.

For average malignant with exponential spacing the clinically optimal $\Gamma = 0.210541$ (to 6dp). This occurs at $r = 1.24$, corresponding to 10 b-values of 0, 9, 23, 46, 82, 140, 233, 382, 619, 1000 *s/mm²* (Protocol C). For average malignant with exponential spacing the optimal $\Gamma = 0.143054$ (to 6dp). This occurs at $r = 1.59$, corresponding to 20 b-values of 0, 4, 8, 14, 21, 30, 41, 55, 73, 94, 122, 156, 198, 251, 318, 401, 505, 635, 797, 1000 *s/mm²* (Protocol D). These sets of b-values are much more acceptable in terms of implementation than the protocols presented in the first iteration. There are no repeats of b-values in the protocols

discussed here. These schemes are more comparable to literature schemes, too. They both sample low b-values well and allow *D* to be calculated with higher b-values.

The optimisation results in this iteration show that average values of *f, D* and *D** from the literature for the input parameters gave more suitable optimal b-values, as hypothesised. Next it was envisioned to widen the input parameter investigations, especially the final b-value, to see if a different protocol would be proposed.

These protocols are investigated in healthy volunteers and in a clinical pilot study in Chapters 6 and 7, respectively.

5.3.7. Method: Breast Third Iteration (Protocol E)

The third iteration of optimisation was carried out using average malignant values from the literature as before for user inputs *f, D* and *D**. The resulting optimised protocol from this iteration is named Protocol E in Chapter 6 when scanning volunteers. Exponential spacing was used to generate b-values to be tested. The exponent minimum was 0, with increments of 0.011 to step over 1 up to a maximum of 10. The maximum b-value was now iterated from 500 s/mm^2 through to 1500 s/mm^2 in increments of 100 to see if the final b-value of 1000 s/mm^2 was actually optimal, as previously utilised in the first and second iterations. The number of b-values in a set was constrained to 10 since this was clinically optimal. This yielded 1 set of optimisation results. Below in Table 5.6 are the summarised inputs to the MATLAB program.

Input parameter	Malignant average Exponential
f	0.0885
D	0.001097 mm/s^2
D^*	0.04384 mm/s^2
B_{min}	0 s/mm^2
B_{max}	500-1000 s/mm^2
nb	10
r_{min}	0
r_{max}	10
r_{step}	0.011

Table 5.6: Input parameters for third iteration of optimisation.

5.3.8. Results: Breast Third Iteration (Protocol E)

Following the methodology described in Section 5.3.2, the results shown in Table 5.7 were obtained. All b-values were again rounded to the nearest whole number.

Output parameter	Malignant average
Clinically optimal *nb*	10
Clinically optimal *r*	1.68
Clinically optimal *Γ*	0.172882
B-values clinically optimal	*0, 4, 12, 24, 45, 80, 140, 241, 412, 700 s/mm^2*
Spacing	Exponential

Table 5.7: Output parameters for the third iteration of optimisation.

The figure of merit versus the exponent was graphed to find the minimum figure of merit and its corresponding exponent. Graph 5.16 shows this for this third optimisation. This

value of *r* corresponded to an optimal set of b-values, which could be looked up from the spread sheet produced by the software. The individual $s(\theta_k)$ versus *r* (Graphs 5.13-15) for each IVIM parameter are also shown to visually show how the three separate CRLBs for each parameter look and are merged via the figure of merit calculation to give Graph 5.16.

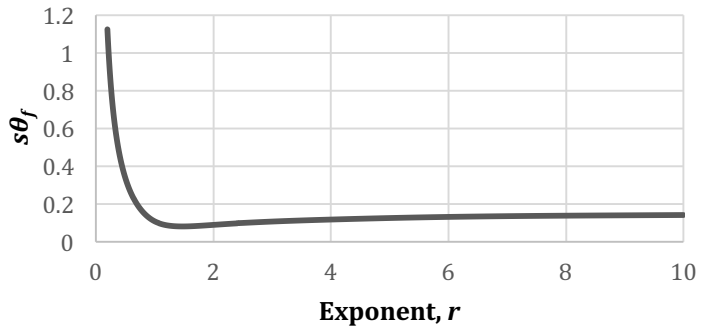

Graph 5.13: $s(\theta_f)$ versus the exponent for the third optimisation. r = 1.47 gives the lowest value for (θ_f).

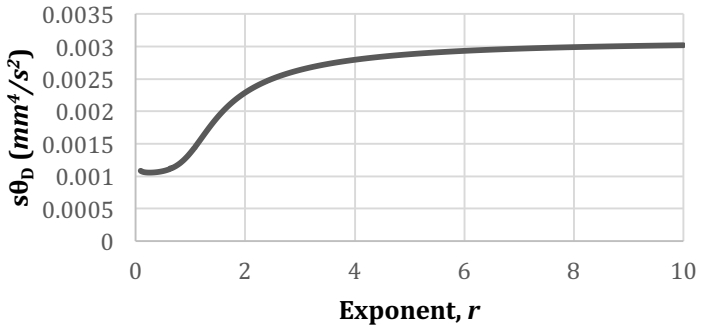

Graph 5.14: $s(\theta_D)$ versus the exponent for the third optimisation. r = 0.26 gives the lowest value for $s(\theta_D)$.

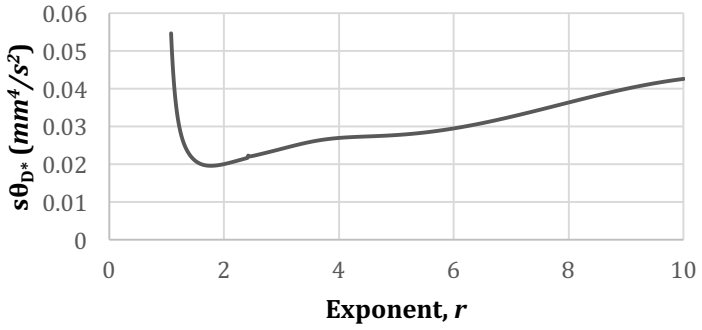

Graph 5.15: $s(\theta_{D*})$ versus the exponent for the third optimisation. r = 1.77 gives the lowest value for (θ_{D*}).

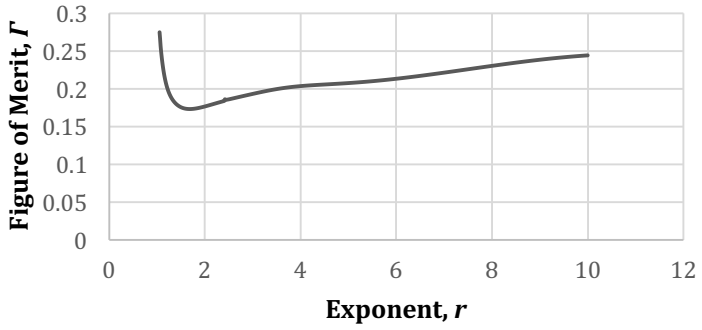

Graph 5.16: Figure of merit versus the exponent for the third optimisation. r = 1.68 gives the lowest figure of merit.

5.3.9. Discussion: Breast Third Iteration (Protocol E)

An optimisation was carried out for average initial inputs of *f, D* and *D** from the literature for malignant lesions using exponential spacing to generate sets of b-values. One thousand sets of b-values were generated for *nb* = 10, and there were 6 maximum b-values used (500-1000 in increments of 100) and so 6,000 sets of b-values were analysed in this iteration in total.

For average malignant values with exponential spacing the clinically optimal Γ = 0.172882 (to 6dp). This occurs at *r* = 1.68, corresponding to 10 b-values of 0, 4, 12, 24, 45, 80, 140, 241, 412, 700 *s/mm*^{2}. There are no repeats of b-values. This scheme is very comparable to literature schemes. It samples low b-values well and allows *D* to be calculated with higher b-values. The major difference to the second iteration is that the final b-value calculated to be optimal was 700 *s/mm*^{2}, as opposed to 1000 *s/mm*^{2} previously. Mathematically, this may be

optimal for calculating IVIM parameters, however clinicians routinely use high b-value images for qualitative assessment of lesions. Seven-hundred is still relatively high for breast, though higher is usually preferred.

The separate graphs for each IVIM parameter of $s(\theta_k)$ versus the exponent shows how the exponent changes for each parameter. *D** needs the highest *r* at 1.77, with *f* lower at 1.47 and then *D* with the lowest at 0.26. This is due to the spacing produced by the exponent. Values of *r* over 1 sample the curve well at low b-values and some high b-values, and *r* lower than 1 concentrates on higher b-values which *D* needs for monoexponential diffusion calculation. Using one set of *nb* was a clinical constraint, but of course the more b-values the better sampled the curve for calculating the IVIM parameters.

The optimisation results in this third iteration show that average values of *f, D* and *D** for these input parameters gave an even more suitable set of optimal b-values than in previous iterations, with the main finding being that the maximum b-value should be 700 *s/mm*^{2}, with these input parameters.

5.3.10. Method: Breast Fourth Iteration (Protocol F)

For this iteration, both types of spacing were explored again, along with the two variations of the IVIM equation described in Chapter 4. The two models are reshown below.

The standard IVIM model being;

$$S = S_0[(1-f)e^{-bD} + fe^{-bD^*}]$$

Equation 5.16

And the variation of the IVIM equation with an extra *D* term in the second exponential;

$$S = S_0[(1-f)e^{-bD} + fe^{-b(D^*+D)}]$$

Equation 5.17

A wider exploration of all models and parameters was undertaken in an attempt to find a protocol to use in clinic (Protocol F) on breast cancer patients for in-depth analysis in Chapter 7, after analysing data acquired from volunteers in Chapter 6 first. The input values of *f, D* and *D** were once again averages of calculated values presented in the literature for

malignant lesions. The minimum b-value was 0 s/mm^2, and the maximum b-value 2000 s/mm^2 sampled in increments of 100 s/mm^2 from 500-2000 s/mm^2. The exponent minimum was 0, exponent maximum 10, and exponent increment 0.01 for power law spacing and 0.011 for exponential spacing. The number of b-values in a set ranged from 4 up to 20 in increments of 1 but only 10 and 20 are reported since the maximum number is optimal, always, and 10 is the maximum allowed in clinic because of scan time constraints. This yielded 4 sets of optimisation results, and 8 protocols for comparison.

There was a significant drawback highlighted when scanning volunteers using protocols from iterations one to three, in Chapter 5, in that no b-value lower than 10 s/mm^2 (unless 0 s/mm^2) could be entered and used on the GE MRI scanner available at the CMRI. Therefore, a second set of optimisations were carried out with the second b-value constrained to be 10 s/mm^2. This yielded a further 4 sets of optimisation results. This yielded 8 sets of optimisation results, and 16 protocols for comparison, in total - exponential spacing and power law spacing for each variation of the IVIM model, for 10 and 20 b-values with the second b-value either constrained to 10 or not. Tables 5.8 and 5.9 are the summarised inputs to the MATLAB program for exponential and power law spacing, respectively.

Input parameter	Exponential min_0 D^*	Exponential min_0 D^*+D	Exponential min_{10} D^*	Exponential min_{10} D^*+D
f	0.00885	0.00885	0.00885	0.00885
D	0.001097 mm^2/s	0.001097 mm^2/s	0.001097 mm^2/s	0.001097 mm^2/s
D^*	0.004384 mm^2/s	0.004384 mm^2/s	0.004384 mm^2/s	0.004384 mm^2/s
B_{min}	0 s/mm^2	0 s/mm^2	0 s/mm^2	0 s/mm^2
B_{max}	500-2000 s/mm^2	500-2000 s/mm^2	500-2000 s/mm^2	500-2000 s/mm^2
Nb	4-20	4-20	4-20	4-20
r_{min}	0	0	0	0
r_{max}	10	10	10	10
r_{step}	0.011	0.011	0.011	0.011
Equation used	Standard	Variation	Standard	Variation

Table 5.8: Input parameters for the fourth iteration of optimisation for exponential spacing.

Input parameter	Power Law min_0 D^*	Power Law min_0 D^*+D	Power Law min_{10} D^*	Power Law min_{10} D^*+D
f	0.00885	0.00885	0.00885	0.00885
D	0.001097 mm^2/s	0.001097 mm^2/s	0.001097 mm^2/s	0.001097 mm^2/s
D^*	0.004384 mm^2/s	0.004384 mm^2/s	0.004384 mm^2/s	0.004384 mm^2/s
B_{min}	0 s/mm^2	0 s/mm^2	0 s/mm^2	0 s/mm^2
B_{max}	500-2000 s/mm^2	500-2000 s/mm^2	500-2000 s/mm^2	500-2000 s/mm^2
Nb	4-20	4-20	4-20	4-20
r_{min}	0	0	0	0
r_{max}	10	10	10	10
r_{step}	0.01	0.01	0.01	0.01
Equation used	Standard	Variation	Standard	Variation

Table 5.9: Input parameters for the fourth iteration of optimisation for power law spacing.

5.3.11. Results: Breast Fourth Iteration (Protocol F)

The results from the fourth iteration of optimisation generated from the two types of spacing, constraints and IVIM models were exported from MATLAB as spread sheets detailing all of the sets of b-values, the CRLB Fisher Matrix main diagonal values for each b-value set ($s(\theta_k)$ for each of the 4 parameters from the IVIM model), and the figure of merit corresponding to each b-value set. The most optimal out of the 8 protocols for exponential spacing is shown in bold, with the same for power law spacing. All b-values were rounded to the nearest whole number, since MRI scanners currently do not allow b-values with decimal places clinically. These outputs are detailed in Tables 5.10 and 5.11.

Output parameter	Exponential min_0 D^*	Exponential min_0 D^*+D	Exponential min_{10} D^*	Exponential min_{10} D^*+D
Optimal *nb*	20	20	**20**	20
Optimal *r*	1.287	1.298	**2.783**	1.595
Optimal Γ	0.144393	0.145617	**0.132817**	0.133507
Clinically optimal *nb*	10	10	**10**	10
Clinically optimal *r*	1.68	1.69	**2.89**	1.57
Clinically optimal *Γ*	0.172882	0.174339	**0.160077**	0.160860
B-values optimal	0, 2, 4, 8, 12, 17, 24, 32, 44, 58, 77, 100, 131, 171, 222, 287, 372, 480, 620, 800 *s/mm²*	0, 2, 4, 7, 10, 15, 21, 30, 40, 54, 71, 94, 124, 163, 213, 278, 363, 471, 615, 800 *s/mm²*	**0, 10, 10, 10, 10, 10, 10, 10, 10, 10, 10, 10, 10, 10, 12, 17, 28, 61, 151, 402, 1100 *s/mm²***	0, 10, 10, 10, 10, 10, 10, 10, 10, 10, 10, 10, 10, 10, 12, 17, 28, 61, 151, 402, 1100 *s/mm²*
B-values clinically optimal	0, 4, 12, 25, 46, 82, 142, 243, 413, 700 *s/mm²* (Previous clinically optimal)	0, 4, 11, 24, 44, 80, 139, 240, 411, 700 *s/mm²*	**0, 10, 24, 46, 71, 135, 221, 355, 567, 900 *s/mm²*** (Protocol F)	0, 10, 10, 11, 14, 23, 47, 116, 318, 900 *s/mm²*

Table 5.10: Output parameters for fourth iteration of optimisation for exponential spacing.

Output parameter	Power Law min_0 D^*	Power Law min_0 D^*+D	Power Law min_{10} D^*	Power Law min_{10} D^*+D
Optimal *nb*	**20**	20	20	20
Optimal *r*	**2.68**	2.77	2.71	2.78
Optimal Γ	**0.154986**	0.156368	0.152583	0.155634
Clinically optimal *nb*	**10**	10	10	10
Clinically optimal *r*	**2.69**	2.76	2.74	2.79
Clinically optimal *Γ*	**0.185651**	0.187320	0.181775	0.185671
B-values optimal	**0, 0, 1, 4, 8, 14, 23, 34, 49, 67, 90, 116, 146, 181, 221, 265, 315, 371, 433, 500 *s/mm²***	0, 0, 1, 3, 7, 12, 21, 31, 46, 63, 84, 110, 140, 175, 215, 260, 311, 367, 430, 500 *s/mm²*	0, 10, 10, 10, 10, 10, 10, 10, 10, 10, 10, 11, 14, 18, 29, 50, 89, 161, 287, 500 *s/mm²*	0 10, 10, 10, 10, 10, 10, 10, 10, 10, 10, 10, 11, 16, 18, 29, 50, 89, 161, 287, 500 *s/mm²*
B-values clinically optimal	**0, 1, 8, 25, 54, 100, 165, 251, 362, 500 *s/mm²***	0, 1, 9, 26, 56, 102, 167, 254, 364, 500 *s/mm²*	0, 10, 10, 10, 10, 11, 18, 60, 244, 900 *s/mm²*	0, 10, 10, 10, 10, 11, 17, 54, 218, 800 *s/mm²*

Table 5.11: Output parameters for fourth iteration of optimisation for power law spacing.

The figure of merit versus the exponent was graphed to find the minimum figure of merit and its corresponding exponent for all optimisations. Graphs 5.17 and 5.18 show this for the most optimal and most clinically optimal protocols out of all 16 protocols, highlighted in bold in Table 5.10 (exponential spacing).

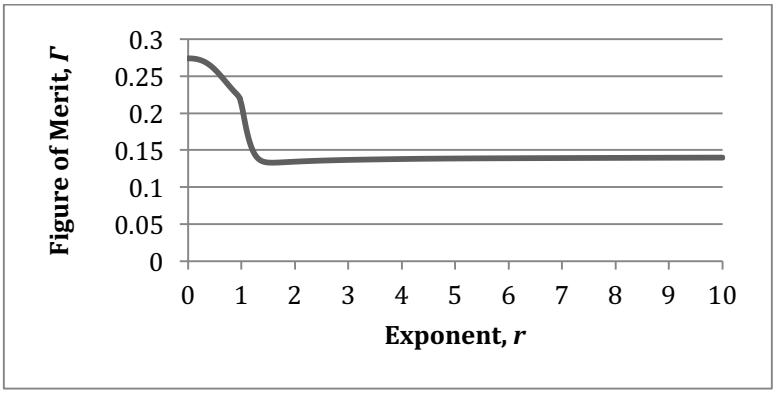

Graph 5.17: Figure of merit versus the exponent for malignant average, second b-value 10 s/mm^2, exponential spacing, standard IVIM model, optimal number of b-values (20).

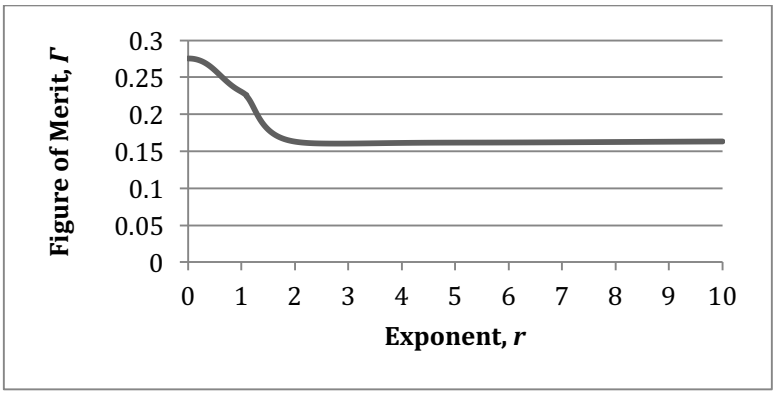

Graph 5.18: Figure of merit versus the exponent for malignant average, second b-value 10 s/mm^2, exponential spacing, standard IVIM model, clinically optimal number of b-values (10).

5.3.12. Discussion: Breast Fourth Iteration (Protocol F)

Eight optimisations were carried out for malignant average initial inputs of *f, D* and *D** from the literature with exponential and power law spacing to generate sets of b-values. Two forms of the IVIM model were investigated along with constraints on the second b-value due to scanner limitations. One thousand sets of b-values were generated for each *nb* (4-20) for power law spacing and 900 for exponential spacing, and there were 16 maximum b-values used (500-2000 *s/mm^2* in increments of 100 *s/mm^2*) and so 4,134,400 sets of b-values were analysed in this iteration in total. 16 protocols were presented – 20 b-values being optimal as the more b-values sampled, the better. Then 10 b-values, termed clinically optimal, being the most b-values able to be acquired in a total scan time of five minutes.

Incidentally, the most optimal and most clinically optimal schemes, with the constraint of the second b-value being 10 s/mm^2, both had exponential spacing, implementing the standard IVIM equation as highlighted in Table 5.10, and shown in Graphs 5.17-18. This is different to the third iteration of optimisation, which yielded a final b-value of 700 s/mm^2 without constraining the second b-value. It was expected that this constraint would influence the optimal b-value scheme – it raised the final cut-off by 200 s/mm^2. It seems to have pushed values larger, with the larger the b-value being, then the larger the 'push'. The final clinically optimal scheme is 0, 10, 24, 46, 71, 135, 221, 355, 567, 900 s/mm^2. This will be investigated in healthy tissue and implemented clinically (Protocol F, volunteers in Chapters 6 and patients in Chapter 7). This scheme is particularly comparable to literature schemes. It samples low b-values well and allows *D* to be calculated with higher b-values. Mathematically, this may be assumed to be optimal for calculating IVIM parameters, and also allows clinicians to use a higher b-value for qualitative assessment of lesions (the lesion signal remains in the image whilst background parenchyma loses signal at higher b-values, making the lesion less occult to see on DW MR images).

The optimisation results in this fourth iteration gave an even more suitable set of optimal b-values than in previous iterations, evaluating more variations of input parameters into the MATLAB programs over the 4 iterations of optimisation, with the main finding being that the maximum b-value should be 900 s/mm^2, with a constrained second b-value due to scanner limitations. Interestingly, the standard IVIM model performed better through CRLB and figure of merit calculations.

5.3.13. Method: Breast Post-clinical Application Iteration

The average values of *f, D,* and *D** for all malignancies calculated from clinical data in Chapter 7 were used as inputs into the optimisation program to get a final optimised protocol based on that patient cohort of pre neoadjuvant breast cancers. It should be noted that this cohort is less than the collective cohort used to take an average from malignant cases in the literature. The aim was to find a protocol that was optimised for malignant breast lesions, in a cohort of age representative patients in the UK, before chemotherapy treatment, for this particular scanner. The program is quick to implement and so any institution or hospital could carry this out if implementing IVIM already. One drawback is that this protocol presented is not tailored to a specific subtype of malignancy – this was due to the small numbers in sub

cohorts. That statistical power would be small. Exponential spacing was used to generate b-values to be tested with the program. The exponent minimum was 0; the exponent maximum was 10 with increments of 0.011 to step over unity. The maximum b-value was iterated from 500 s/mm^2 through to 1500 s/mm^2 in increments of 100 s/mm^2. The number of b-values in a set ranged from 4-20. The second b-value was constrained to 10 s/mm^2, once more. The original IVIM model was used. This yielded 1 optimisation. Below in Table 5.12 are the summarised inputs to the MATLAB program.

Input parameter	Value
f	0.072
D	0.00081 mm^2/s
D^*	0.0073 mm^2/s
B_{min}	0 s/mm^2
B_{max}	500-1500 s/mm^2
Nb	4-20
r_{min}	0
r_{max}	10
r step	0.011
Spacing	Exponential

Table 5.12: Input parameters for breast post-clinical application optimisation.

5.3.14. Results: Breast Post-clinical Application Iteration

The results from the breast post-clinical optimisation were exported from MATLAB as spread sheets detailing all of the sets of b-values generated, the CRLB main diagonal values for each b-value set ($s(\theta_k)$ for each of the 4 parameters from the IVIM model), and the figure of merit corresponding to each b-value set. The minimum figure of merit was found and its corresponding exponent. This value of r corresponded to an optimal set of b-values that could be looked up from the spread sheet. The optimal and clinically optimal protocols are detailed

below in Table 5.13. All b-values were rounded to the nearest whole number, since MRI scanners currently do not allow b-values with decimal places clinically.

Output parameter	Value
Optimal *nb*	20
Optimal *r*	0.979
Optimal *Γ*	0.153610
Clinically optimal *nb*	10
Clinically optimal *r*	0.979
Clinically optimal *Γ*	0.186958
B-values optimal	0, 10, 42, 74, 105, 136, 165, 195, 223, 251, 278, 305, 331, 357, 382, 407, 431, 454, 477, 500 s/mm^2
B-values clinically optimal	0, 10, 76, 140, 204, 265, 326, 385, 443, 500 s/mm^2

Table 5.13: Output parameters for breast post-clinical application optimisation.

Graphs 5.19 and 5.20 show the figure of merit versus the exponent for the optimal and clinically optimal results for this optimisation.

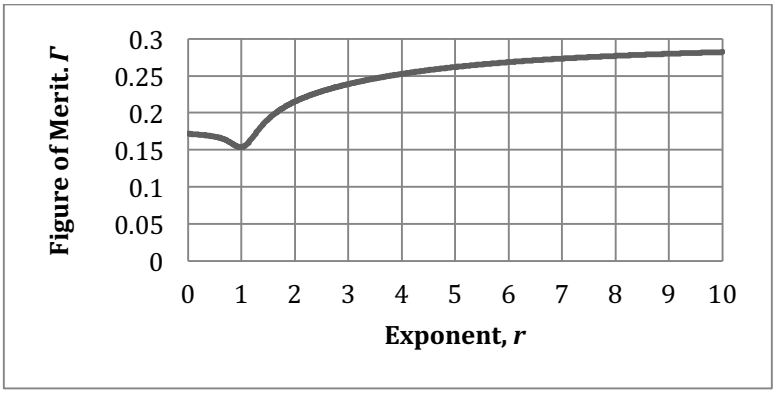

Graph 5.19: Figure of merit versus the exponent for post-clinical average of malignancies, second b-value 10 s/mm^2, exponential spacing, optimal number of b-values (20).

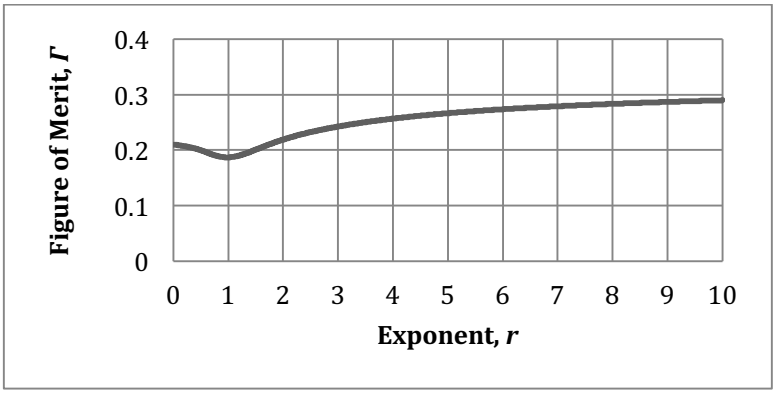

Graph 5.20: Figure of merit versus the exponent for post-clinical average of malignancies, second b-value 10 s/mm^2, exponential spacing, clinically optimal number of b-values (10).

5.3.15. Discussion: Breast Post-clinical Application Iteration

The Γ versus r graphs for both the optimal and clinically optimal regimes have the same shape and clearly show the minimum that indicates the best b-value sampling scheme for these initial inputs calculated from the patient cohort in Chapter 7. As expected, the optimal protocol had 20 b-values, as the curve is sampled more, and so the more precise and accurate the calculated IVIM parameters will be. The clinically optimal protocol was at the same r, with a different Γ. This was triple checked and the inputs did give these results. Surprisingly, the cut-off b-value of 500 *s/mm*^{2} is lower than expected. This indicates that the curve is sampled enough up to 500 *s/mm*^{2} to calculate D. This is, however, a drawback for qualitative lesion characterisation as the signal from FGT may still be apparent. It could eradicate any potential non-Gaussian (not free) water diffusion effects seen at higher b-values (26), however, which is useful. The graph below shows how the b-values are spaced in relation to incidence. There are 4 b-values up to 200 *s/mm*^{2}, agreeing with the consensus being that these lower b-values need to be sampled well. This graph shows that after about 76 the b-values increase linearly (monoexponential to calculate D). This does make sense in terms of calculating the three IVIM parameters. One cause for these interesting changes in r and the final cut-off b-value could be that the cohort of patients was smaller than those used in the four previous optimisations as inputs and so the mean would not be as reliable as an accurate representation of f, D and D*. These differences are outlined in Table 5.14. All parameters are smaller for the post clinical cohort compared to the mean taken from the literature.

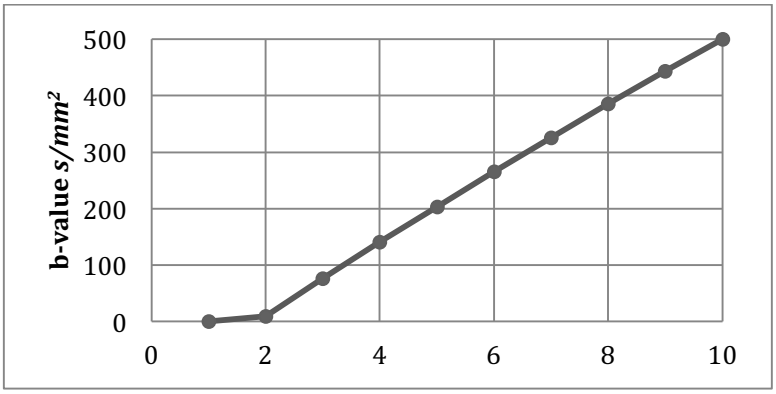

Graph 5.21: Clinically optimal b-values as a function of incidence.

Input parameter	Iterations 1-4	Post-clinical
f	0.0885	0.072
D	0.001097 mm^2/s	0.00081 mm^2/s
D*	0.04384 mm^2/s	0.0073 mm^2/s
Number of lesions	90	44

Table 5.14: Comparison of f, D and D* inputs into program between pre and post clinical results optimisations.

5.3.16. Method: Comparing b-value Protocols

After findings in the first optimisation that the inputs to the program dictated greatly the b-value protocol that was optimal, the literature that produced these inputs were investigated along with others that were cited as optimal for other body parts. The variation of b-values utilised in the literature to calculate average malignant values were investigated to see how optimal they were compared to those produced in this chapter.

The $s(\theta_k)$ of *f, D* and *D** for several literature protocols and volunteer non-optimised heuristic protocols scanned in Chapter 6 were calculated. The figure of merit was also calculated, to show the difference in what this could be for the various protocols. These were tabulated and compared to the protocols produced in this chapter.

Only one set of b-values was entered into the optimisation program each time, forcing it to perform CRLB analysis on only that set of b-values. This gave the CRLB of the SD of each parameter for each of the b-value sets, and the figure of merit.

A study by Lemke *et al* (73) was used to pick b-value sets to compare. The study was 'toward an optimal distribution of b-values for IVIM' in the liver. This study presented a range of 'optimal' b-value protocols to fit the purpose of this analysis. The CRLB theory was not used in this optimisation; instead another method utilising error calculation was implemented and b-values were generated (not in ascending order) as to which gave the lowest errors in Monte Carlo simulations. The Monte Carlo simulation was performed on three input parameter regimes, namely low, medium, and high (corresponding to the level of perfusion expected). This study presented 6 b-value regimes, the three previously mentioned, and then a sum set of the most optimal values, and a set that allowed choice in order of importance depending on how many b-values the user wanted. A sample literature-like set was also presented for comparison in this study. Three other heuristic protocols from the literature (used to calculate the average malignant values) were also surveyed alongside Lemke's protocols, the ones used to calculate the original means of *f, D* and *D** as inputs, along with the volunteer protocols used at the CMRI in Chapter 6. These b-values and the optimisation input parameters were as in the Tables 5.15-16 below.

Input parameter	Malignant average
f	0.0885
D	0.001097 mm/s^2
D^*	0.04384 mm/s^2
B_{min}	0 s/mm^2
B_{max}	Dependant on set
Nb	Dependant on set

Table 5.15: Input parameters for b-value set CRLB calculations.

Set name	B-values
Volunteer 10s	0, 10, 20, 30, 40, 50, 60, 70, 80, 90, 100, 200, 300, 400, 500, 600, 700, 800, 900, 1000 *s/mm²*
Volunteer 25s	0, 10, 25, 50, 75, 100, 125, 150, 175, 200, 225, 250, 275, 300, 400, 500, 600, 700, 800, 900, 1000 *s/mm²*
Volunteer 50s	0, 50, 100, 150, 200, 250, 300, 350, 400, 450, 500, 550, 600, 650, 700, 750, 800, 850, 900, 950, 1000 *s/mm²*
Lemke optimal	0, 40, 1000, 240, 10, 750, 90, 390, 170, 10, 620, 210, 100, 0, 530, 970 *s/mm²*
Lemke low	0, 40, 1000, 260, 560, 190, 160, 40, 170, 560, 190, 980, 40, 150, 440, 700, 180, 0, 710, 860, 40, 580, 1000, 250, 0, 150, *s/mm²*
Lemke medium	0, 40, 1000, 160, 150, 40, 680, 150, 200, 940, 170, 990 440, 740, 40, 230, 360, 0, 270, 70, 270, 870, 0, 40, 940, 60, 320, 240, 0, 260, 60, 1000, 920, 310 1000, 50 *s/mm²*
Lemke high	0, 40, 1000, 10, 130, 10, 70, 980, 190, 10, 740, 170, 200, 0, 830, 240, 80, 20, 1000, 680, 10, 190, 0, 170, 880 *s/mm²*
Lemke sum	0, 40, 1000, 240, 10, 750, 90, 390, 170, 10, 620, 210, 100, 0, 530, 970, 350, 40, 990, 50, 30, 100, 970, 70, 390, 290, 120, 1000, 520, 0, 60, 260, 240, 10, 0 *s/mm²*
Lemke lit	0, 10, 20, 30, 40, 50, 60, 70, 80, 90, 100, 150, 200, 400, 800, 1000 *s/mm²*
Liu	0, 10, 20, 30, 50, 70, 100, 150, 200, 400, 600, 1000 *s/mm²*
Bokacheva	0, 30, 60, 90, 120, 400, 600, 800, 1000 *s/mm²*
Sigmund	0, 30, 70, 100, 150, 200, 300, 400, 500, 800 *s/mm²*

Table 5.16: B-value sets for CRLB calculations.

5.3.17. Results: Comparing b-value Protocols

The bar charts in Graphs 5.22-25 demonstrate the variation in the lower bounds of the standard deviations for each IVIM parameter and the figure of merit for the analysed protocols. Table 5.16 shows a summary of the figure of merits calculated from the protocols in Table 5.16 compared to the figure of merit calculated from protocols from optimisations presented in this chapter.

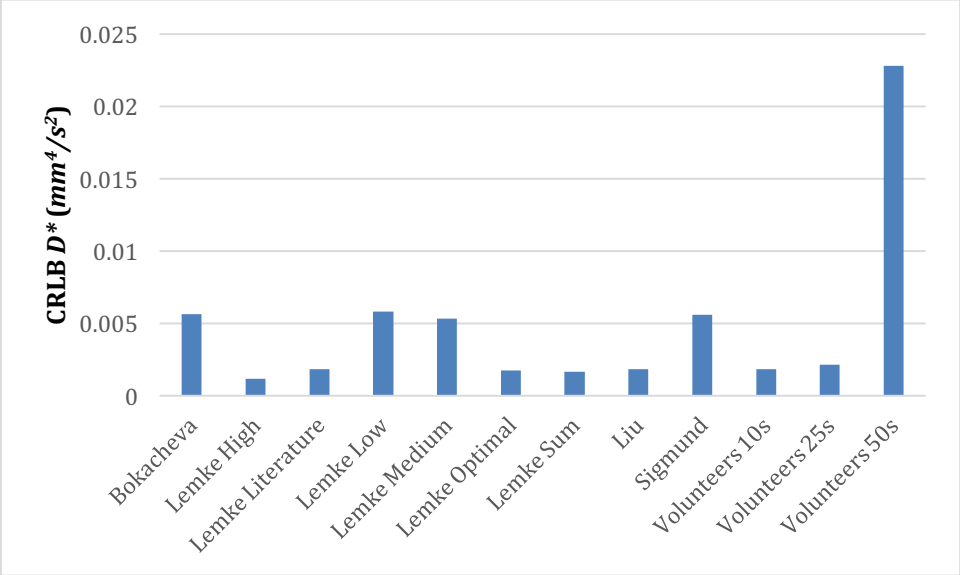

Graph 5.22: CRLB of the SD for D* (mm^4/s^2).

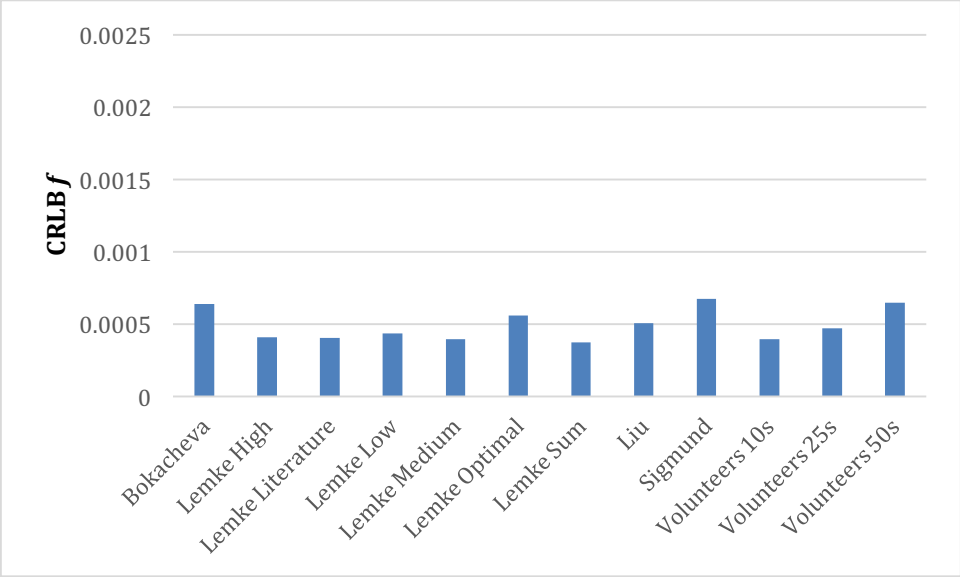

Graph 5.23: CRLB of the SD for f (no units).

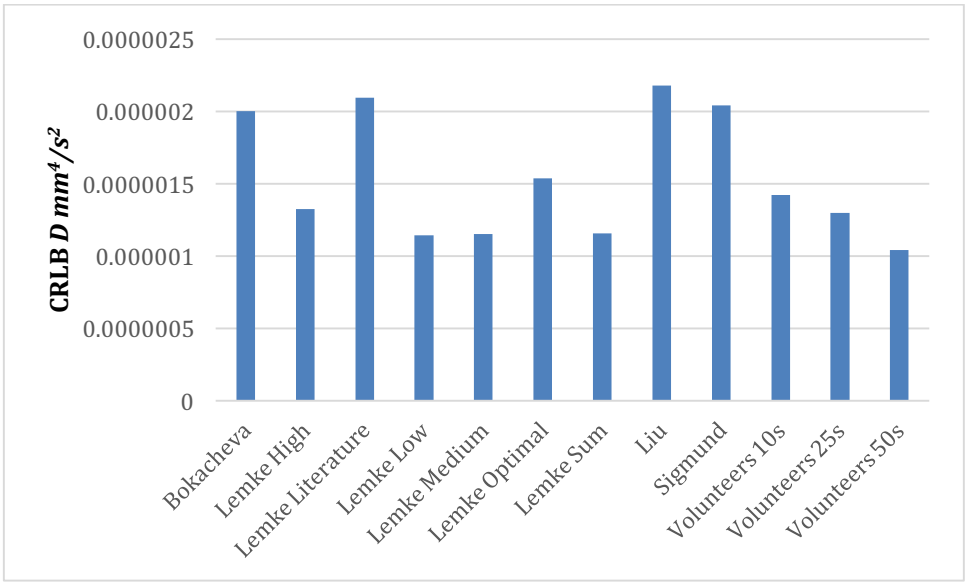

Graph 5.24: CRLB of the SD for D (mm^4/s^2).

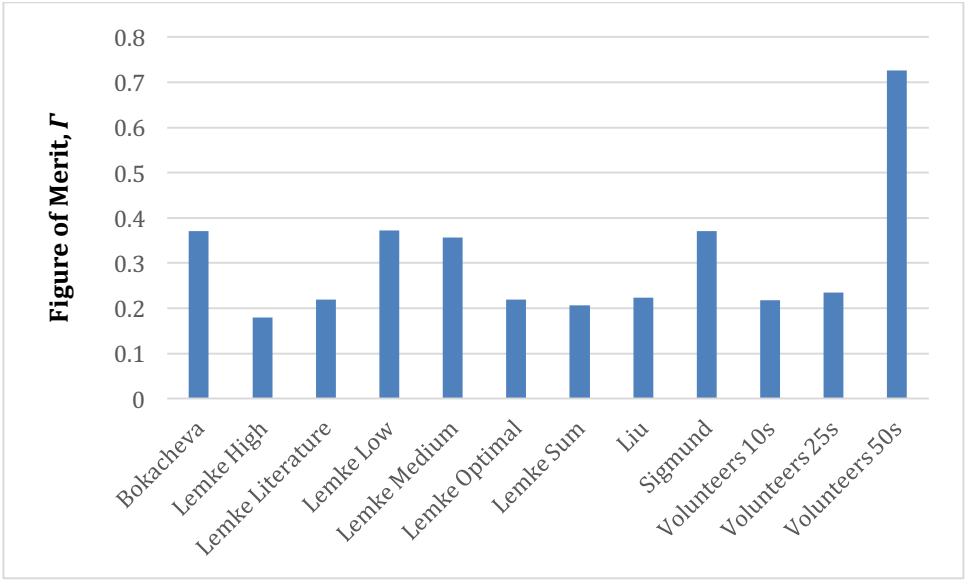

Graph 5.25: Figure of Merit for each b-value protocol.

Protocol	FoM, Γ	Iteration of Optimisation (or other)
Volunteer 10s	0.217690	Volunteer scans pre optimisation
Volunteer 25s	0.234610	Volunteer scans pre optimisation
Volunteer 50s	0.726670	Volunteer scans pre optimisation
Lemke optimal	0.218670	Literature
Lemke low	0.372730	Literature
Lemke medium	0.356830	Literature
Lemke high	0.179470	Literature
Lemke sum	0.206440	Literature
Lemke lit	0.219640	Literature
Liu	0.223730	Literature
Bokacheva	0.370730	Literature
Sigmund	0.370610	Literature
Mal high optimal exponential	0.135084	First
Mal low optimal exponential	0.102971	First
Mal high clinically optimal exponential	0.162233	First
Mal low clinically optimal exponential	0.135084	First
Protocol C	0.210541	Second
Protocol D	0.143054	Second
Protocol E	0.172882	Third
Protocol F	0.160077	Fourth
Post-clinical	0.186958	Post

Table 5.17: Comparison of figure of merits for literature protocols, volunteer protocols pre optimisation, and optimised protocols from Chapter 5.

5.3.18. Discussion: Comparing b-value Protocols

The CRLB and FoM for each b-value protocol in Table 5.16 were successfully calculated. A lower CRLB is better; as this is the lowest variance we would expect to see when calculating that parameter efficiently. When calculating parameters from data, if that bound (and/or MSE) is achieved, then the estimator (method of calculation/b-values) is said to be efficient.

For D^*, the CRLBs are significantly higher than those for f and D (note scales on vertical axes of graphs 5.22-5.24). Since the perfusion parameters are often the hardest to fit, this explains their larger CRLBs. D has the lowest CRLB, meaning the calculations are more likely to be precise.

The CRLBs for D^* show that Volunteers 50s is dramatically high compared to the rest. This is a linear protocol with the second b-value of 50 s/mm^2 and does not sample lower b-values as well as some of the other protocols, including the post-clinical clinically optimised protocol, therefore this higher CRLB makes sense.

The CRLBs for f have limited variation, but do demonstrate differences between the sets with the Sum optimised protocol by Lemke and Volunteer 10s showing the lowest CRLBs.

The CRLBs for D show that Volunteers 50s (linear) and the optimal sets presented by Lemke (Low, Medium and Sum) have the lowest CRLBs. The combination of these two being the lowest for this parameter sheds some light on the surprisingly linear protocol produced by the post-clinical optimisation in Section 5.3.14.

In respect to the FoM, the Lemke optimised protocols and Volunteers 10s and 25s perform the best. The FoM calculation gives equal importance to all three parameters. To even out the disparities of lowers bounds between parameters, more weighting could be given to perfusion parameters if needed in the figure of merit calculation. Until the clinical utility of perfusion parameters is proven more important than D, though, there is no justification in this.

A comparison of the FoMs can be made between b-value protocols from the literature, heuristic protocols from scanning volunteers (beginning of Chapter 5) and optimised protocols produced in this chapter by looking at Table 5.17. Considering the heuristic volunteer protocols, Volunteer 50s is the worst, and is in fact the worst when comparing all protocols. This may be due to being fully linear and not calculating perfusion parameters well, which

account for two thirds of the FoM calculation. From the literature, Sigmund and Bokacheva, which are non-optimised protocols, present protocols with relatively high FoMs when compared to the optimised literature b-value protocols by Lemke. The lowest FoMs appear when considering optimised protocols produced in this chapter. Considering constraints and trade-offs such as the second b-value having to be 10 mm/s^2 and a scan time limit, Protocol F is a good compromise of FoM– the only protocols lower are those with double the number of b-values (disallowed due to scan time) and those that do not take a proper average of initial inputs presented in the literature (that is mal high, mal low, Protocol D, Protocol E). Since actual accurate physiological values are unknown for IVIM, an average has to be taken and not particular values assumed.

As expected the existing protocols to date of analysis in the literature are not optimal, or at least more optimal than in this chapter, due to not have the lowest CRLB for any of the three parameters or FoM. It should be noted that the low figure of merits achieved with 10 b-values outperform many of the longer protocols in the literature and so a non-optimised protocol with many b-values is not better than an optimised, shorter one.

Points to take from this analysis are that; the b-value protocol influences the CRLB and FoM; the protocols produced in this chapter are, on a whole, at least more optimal than those in the literature, especially Protocol F used in the clinical study in Chapter 7; D^* has the highest CRLB, then f, then D and so the perfusion parameters may have a higher variance.

5.4. Breast Optimisation Iterations: Overall Conclusions

The aim of the work in this chapter was to develop software to allow an optimised IVIM protocol to be established for malignant breast cancer, in this case, with inputs of perfusion and diffusion parameters from previous studies, scan time, and any other limitations such as NEX. To date, such an optimisation of breast IVIM has not been published. Several studies have optimised IVIM in other body parts using various measures of optimality such as the minimum relative overall error for ‘high’, ‘medium’ and ‘low’ perfused organs (70); the smallest error propagation factor in kidney (74), the previous applied in breast (80); the smallest convergent mean in prostate (90); the minimum Cramer-Rao Lower Bound in liver (91); and the minimum global parameter error in liver (92). All of these optimisations yielded very different results in respect to the b-value protocol established. Also, the number of sets of b-values analysed were not as extensive as those presented here.

The optimisations carried out in this chapter were done using a robust statistical approach. For each optimisation, sets of b-values were produced using two spacing methods; exponential spacing and power law spacing (found to be inferior so not implemented in some cases). In the fourth iteration of optimisation, over 4 million b-value sets were analysed, with thousands more b-value sets analysed in optimisations one to three, and more so when considering the post optimisation, and literature, and heuristic protocols investigated.

The software computes the Cramer-Rao Lower Bound of each the IVIM models parameters, *f*, *D* and *D** from initial inputs of what the accurate real-life values should be. This CRLB is at least as high as the variance will be for that parameter. It therefore tells us within what preciseness that parameter can be measured using that estimator (the b-values, which sample the curve, from which the IVIM model biexponential is fitted). The variance is also related to the mean squared error. The MSEs we would expect to see from calculating these parameters in the linear protocol used to scan volunteers, Volunteer 50s in Chapter 6, is explored using Monte Carlo simulations in Chapter 8. A figure of merit is then produced by the program to quantify, which b-value set is best – that b-value set corresponds to a particular exponent (*r* in the spacing equations), which is found from plotting a graph of the figure of merit versus the exponent.

The optimal protocols from the 5 iterations are shown at the end of this chapter in summary in Table 5.18. To recap, the first iteration looked at various input parameters of *f, D* and *D** into the optimisation software, trying different combinations from the literature including malignant lowest and malignant highest. Normal tissue was also investigated. This was done for both types of spacing. The most optimal scheme was found when modelling malignant lowest input values according to the program. However, from visually inspecting the b-value sets, the malignant highest offers schemes that are more practical to implement. It was decided a trade of between the two would be sensible going forward onto the next optimisation, and so the mean of some literature values published by that date were calculated. Exponential spacing was also seen to perform better overall than power law spacing. Normal tissue and lowest malignant inputs suggested that if the perfusion parameters are more difficult to tease out, because there is not much perfusion in normal breast tissue, then low b-values were repeated to reflect this. This optimisation also showed the sensitivity of the program for

differing levels of perfusion and its suitability for use in producing protocols for other body parts.

The second iteration produced Protocols C and D. This optimisation used malignant average values as inputs to the program implementing exponential spacing from 0 to 10 for r (instead of 1 to 10 as before), 10 to 20 b-values, first b-value 0 s/mm^2 and last 1000 s/mm^2. The exponent was changed from 0.01 to 0.011 to step over unity and allow values lower than 1 to be probed. This did not make a difference, as all best figure of merits were larger than 1 from results. These optimised protocols did not have repeat b-values, which was the aim of using malignant average inputs into the program. It was concluded more b-values were always going to give lower CRLBs but a constraint of scan time had to be implemented after volunteers were scanned in Chapter 6. Thus, the clinically optimal protocols were deemed best with 10 b-values to scan in under five minutes with a suitable amount of NEX.

The third iteration of optimisation yielded Protocol E and explored different final b-values. The maximum b-value was now iterated from 500 s/mm^2 through to 1500 s/mm^2 in increments of 100 to see if the final b-value of 1000 s/mm^2 was actually optimal, as previously utilised in the first and second iterations. The number of b-values in a set was constrained to 10 since this was clinically optimal. This b-value scheme was comparable to literature, sampled low b-values well to calculate perfusion and showed that a different cut-off was indeed more optimal.

The fourth iteration culminated all explorations into a comprehensive analysis to find a Protocol F, suitable for clinical use with a constraint on scan time. Both the standard IVIM model and the variation presented with an extra D term in the second exponential were explored. After scanning volunteers, investigating fitting methods and repeatability in Chapter 6 in parallel with optimising protocols, it was found that no b-value lower than 10 s/mm^2 (unless 0 s/mm^2) could be entered and used on the 3.0 T MRI scanner available at the CMRI. Therefore, a second set of optimisations was carried out with the second b-value constrained to be 10 s/mm^2. The two types of spacing, time and value constraints, and IVIM models produced 16 protocols with 10 or 20 b-values. Over 4 million b-value sets were analysed for optimality. The standard IVIM model and exponential spacing were both optimal. The optimisation with the constraint of 10 did not underperform compared to its unconstrained

counterpart, with the clinically optimal and optimal schemes both being the most optimal over all others. The min_0 figure of merit being 0.172882 and the min_{10} figure of merit being 0.160077. Protocol F is particularly comparable to literature schemes. It samples low b-values well and allows *D* to be calculated with higher b-values. Mathematically, this may be assumed to be optimal for calculating IVIM parameters, and also allows clinicians to use a higher b-value for qualitative assessment of lesions.

Finally, the post clinical iteration of optimisation produced an incongruent result. Using inputs of *f*, *D* and *D** which were means of the IVIM parameters calculated from the 44 malignant lesions in Chapter 7, a protocol was produced which had a much lower cut-off than previously. This was scrutinised and everything was done correctly as in previous optimisations. The graphs were not incoherent with previous results, either. The exponent for the most optimal and clinically optimal protocols were also identical. Perhaps this is coincidence. Quantitative characterisation using IVIM could be carried out with such a protocol successfully. It was noted that 44 lesions were used to find the mean of the IVIM parameters in comparison to the 90 taken from literature.

After findings in the first optimisation that the inputs to the program dictated greatly the b-value protocol that was optimal, the literature b-value protocols that produced these were investigated. 'Optimal' b-value protocols for liver were also analysed. The $s(\theta_k)$, which is the CRLB of the SD for any parameter *k*, of *f, D* and *D** for several literature protocols and volunteer non-optimised heuristic protocols scanned in Chapter 6 were calculated. The figure of merit was also calculated, to show the difference in what this could be for the various protocols. These were compared to the protocols produced in this chapter. It was found that the b-value protocol influences the CRLB and FoM, especially for the perfusion parameters. It was also concluded that the protocols produced in this chapter are, on a whole, at least more optimal than those in the literature, especially Protocol F used in the clinical study in Chapter 7. In terms of fitting data, *D** has the highest CRLB, then *f*, then *D* and so the perfusion parameters may have a higher variance. This is seen in the literature that the perfusion parameters are difficult to fit and so is not unexpected.

Overall, the use of the Cramer-Rao Lower Bound theory to optimise IVIM has been successful. The program was built over the 5 iterations and is applicable to any body part.

There were some problems along the way, including b-value constraints, which have been accounted for within the optimisations.

The aim of the work in this chapter was to develop software to allow an optimised IVIM protocol to be established for breast cancer. This was done evaluating an exhaustive number of sets of b-values, surpassing work carried out in the literature. Several different methods were used in the literature for optimisation and some of these have been combined, implemented and improved on, here.

The first two aims outlined for the IVIM work in this thesis have been achieved: 1) To develop software to allow an optimised IVIM protocol to be established for any body part with inputs of estimated perfusion and diffusion, scan time and other limitations, evaluating an exhaustive range of b-values considered in the literature; and 2) To present an acceptable optimised IVIM protocol leading to standardisation of this type of imaging in breast tissue and malignancies.

An optimal set of b-values ideally creates good quality images for viewing a lesion, post processing, and will be part of a clinically feasible protocol i.e. usable on the majority of MR scanners and in a short scan time. A protocol that generates IVIM parameters with minimal errors is also of importance - see Monte Carlo Simulations in Chapter 8, which looks at the mean squared errors given by different protocols. In the next chapter, Protocols C-F are tested in healthy volunteers, along with other non-optimised protocols, to assess image quality and post-processing methods.

Optimal Protocols	B-values
First (clinically optimal)	0, 0, 0, 0, 2, 8, 27, 90, 300, 1000 *s/mm²*
First (optimal)	0, 0, 0, 0, 0, 0, 0, 0, 0, 0, 0, 0, 0, 1, 3, 10, 32, 101, 318, 1000 *s/mm²*
Second (C, clinically optimal)	0, 9, 23, 46, 82, 140, 233, 382, 619, 1000 *s/mm²*
Third (D, optimal)	0, 4, 8, 14, 21, 30, 41, 55, 73, 94, 122, 156, 198, 251, 318, 401, 505, 635, 797, 1000 *s/mm²*
Third (E, clinically optimal)	0, 4, 12, 24, 45, 80, 140, 241, 412, 700 *s/mm²*
Fourth (F, clinically optimal)	0, 10, 24, 46, 71, 135, 221, 355, 567, 900 *s/mm²*
Post (clinically optimal)	0, 10, 76, 140, 204, 265, 326, 385, 443, 500 *s/mm²*

Table 5.18: Comparison of the most optimal and most clinically optimal protocols produced in the 5 iterations of optimisation.

6. Presence and Repeatability of IVIM in Healthy Tissue: Comparing Different Fitting Methods in Heuristic and Optimised Protocols

6.1. Introduction

The work in this chapter was carried out to confirm or reject the presence of IVIM (in particular perfusion) effects in healthy breast parenchyma, as this has been contested in the literature (76, 83). The repeatability of IVIM measurements was also calculated to give a sense of whether IVIM is a reliable tool before undertaking a clinical trial. In the literature, and as explained in Chapter 3, there are many fitting methods implemented. These were investigated to see which one was more successful and precise in fitting IVIM signal data. Several protocols (A to F) were tested; heuristic protocols (A and B), and protocols from optimisation iterations (C-F) with the final protocol being implemented clinically after all work in this chapter was considered to make a decision on how best to acquire and analyse IVIM data.

6.2. Heuristic Protocols in Healthy Breast Tissue (Protocols A and B)

Heuristic IVIM protocols (Protocols A and B) were taken with inspiration from the breast literature to investigate the presence of perfusion effects in healthy breast parenchyma, quantify repeatability of IVIM parameters, to investigate different fitting methods and to calculate values for *f, D,* and *D** as possible inputs into the IVIM optimisation program (Chapter 5).

6.2.1. Volunteer subjects

Ten healthy volunteers were consented to take part in this pilot study at the Centre for Magnetic Resonance Investigations (CMRI), Hull Royal Infirmary in May 2014. Volunteers had a mean age of 24 years (range 21 - 54 years). Informed consent was obtained and MR safety screening forms were completed prior to imaging.

6.2.2. MRI scans

Volunteers underwent a bilateral MRI breast examination on a 3.0 T MR750 scanner using the body coil as a transmitter and an 8-channel breast receiver coil (GE Healthcare, Milwaukee, WI).

A general 3-plane T1-weighted localiser was acquired to set up slice locations and shim volumes. A T2-weighted anatomical scan was acquired for guiding ROI placement.

IVIM images were acquired axially using diffusion weighted single-shot echo planar imaging (EPI) with the following parameters: repetition time/echo time (TR/TE), 6366 *ms*/54.4 *ms*; field of view, 34x34cm; matrix, 128x128; slice thickness 4mm; slice spacing 1mm; 42 slices (variable with breast size); Bandwidth, ±250Hz; frequency direction, right to left; diffusion direction, 3 in 1; NEX, 2; bi-lateral shimming; scan duration 6.10min; with water only excitation. Four IVIM series were acquired per volunteer, two repeats of the 'Equal 50s' protocol (named Protocol A) and two of the '10s up to 100' protocol (named Protocol B). Protocol A had the following 21 diffusion weightings, b = 0, 50, 100, 150, 200, 250, 300, 350, 400, 450, 500, 550, 600, 650, 700, 750, 800, 850, 900, 950, 1000 s/mm^2. Protocol B had the following 20 diffusion weightings, b = 0, 10, 20, 30, 40, 50, 60, 70, 80, 90, 100, 200, 300, 400, 500, 600, 700, 800, 900, 1000 s/mm^2. Total scan time including volunteer positioning on the scanner bed was 30 minutes.

6.2.3. ROIs and SNR

A region of interest (ROI) was drawn on the largest cross-section of parenchyma seen on DW-images in whichever breast was more suitable (where the most parenchyma was). The ROI was then copied onto its repeated counterpart series since each scan was repeated twice. This was done for both protocols, Protocol A and Protocol B. This produced signal values to fit as a function of the corresponding b-values in the IVIM protocol. The average size of the ROIs was 290mm^2 for Protocol A and 288mm^2 for Protocol B.

The SNR was calculated as the mean signal intensity of the ROI minus the mean signal of background noise divided by the standard deviation of the mean of the background noise, multiplied by 0.655. The 0.655 factor arises because the Gaussian noise present on the raw data is centered about zero (104).

6.2.4. Fitting of data

All fitting of data was coded and computed in MATLAB (MathWorks, Massachusetts, USA).

(i) 'Free fit' of data

Firstly, the data was fitted using a 'free fit' (Method 3, Chapter 3) by applying the Levenberg-Marquardt algorithm using the standard biexponential IVIM model (Equation 6.1 below). This damped least squares approach finds a local minimum to fit data and so needs initial inputs

from the user to start the search for said local minima. The initial inputs used were $f = 0.3$, $D = 0.001$ and $D^* = 0.01$, chosen by examining literature reported values for the IVIM parameters.

$$S = S_0[(1 - f)e^{-bD} + fe^{-bD^*}]$$

Equation 6.1

where S is the diffusion-weighted signal, f is the perfusion fraction, D is the diffusion coefficient and D^* is the pseudodiffusion coefficient. The mean square error (MSE) for each fit was reported. In statistics, the mean squared error (MSE) of an estimator measures the average of the squares of the errors between the estimator and what is estimated. This allows quantification of how 'good' the fit is. This is related to the variance, which was the main concern of goodness of fit of IVIM parameters in Chapter 5 when optimising b-value protocols.

(ii) 'Constrained biexponential fit' of data

Secondly, a 'constrained biexponential' fit (Method 4, Chapter 3) was applied using the cf tool graphical user interface (GUI) function in MATLAB, which allows the user to input custom equations and constraints for parameters. Equation 6.1 was entered and constraints were explored if the data was nonsensical using a 'free fit' (e.g. negative or physiologically illogical). The constraints used were $0 < f < 0.30$, $0.0001 < D < 0.01$, $0.001 < D^* < 0.1$, and $D < D^*$. The mean square error (MSE) for each fit was reported.

(iii) Segmented fit of data

Finally, a segmented fit (Method 5, Chapter 3) was applied assuming that D^* is significantly greater than D (at least by an order of 10), and its influence on diffusion-weighted signal is weak when the b-value is large enough. In this higher b-value regime the pseudodiffusion component D^* can be neglected and D can be obtained by a simple monoexponential fit. Instead of crude initial inputs to find the local minima for the Levenberg-Marquardt algorithm, initial estimates were calculated as follows.

For high b-values it can be assumed that signal decay is monoexponential;

$$S = S_{mono}e^{-bD}$$

Equation 6.2

Fitting of high b-value data to this equation reveals estimates of D and S_{mono} which can subsequently be used to estimate f. Equating S_{mono} to S_0 modified by the perfusion fraction and rearranging reveals an expression for f;

$$f = \frac{S_0 - S_{mono}}{S_0}$$

Equation 6.3

Inserting values for D and f back into Equation 6.1 and rearranging allows a calculation of the initial D^* estimate in Equation 6.4. However, after comparing this method to simply multiplying D by 10, it was found that the latter method was a more pragmatic (and numerically indistinguishable) approach and so was used in the MATLAB program.

$$D^* = \frac{ln\frac{S_{high} - S_0(1-f)e^{-bD}}{S_0 . f}}{-b}$$

Equation 6.4

A cut-off to fit D monoexponentially (Method 1) was set as 200 s/mm^2. All data was then fitted using the biexponential model (Equation 6.1) by implementing the Levenberg-Marquardt algorithm to calculate S_0, f and D^* over all b-values whilst utilising calculated D as a constraint from the monoexponential model. Constraints to disallow any parameter to be negative were coded, and f was constrained to be between 5% and 30% for initial estimates, as anything else is deemed physiologically impossible in the breast. This increased robustness of the fit. The mean square error (MSE) for each fit was reported.

6.2.5. *D** versus *D*+D* in the IVIM Equation

The segmented fit was also carried out to compare the D^* and D^*+D variations of the IVIM equation, the latter described below. Equation 6.5 states there is a component of both pseudodiffusion and molecular diffusion in the perfusion regime.

$$S = S_0[(1-f)e^{-bD} + fe^{-b(D^*+D)}]$$

Equation 6.5

6.2.6. Repeatability of IVIM Parameters

Repeatability is something that needs to be quantified in IVIM. The lack of consistency in literature is due to several factors, for example b-value selection, but other reasons may be a lack of consistency in the measuring process such as fitting methodology. The question needing to be answered is, 'How variable is IVIM parameter measurement?' Repeatability is important to know because it gives some indication as to how much change in a parameter (on treatment for example) is required to be confident it is a true effect and not just the limitations of the experiment involved. The methodology for calculating repeatability in this instance is outlined below (105).

1st measurement	2nd measurement
A1	A2
B1	B2
C1	C2
D1	D2
E1	E2

Table 6.1: Example measurements for calculating repeatability.

Considering Table 6.1, the differences between the 1st and 2nd measurements (A1-A2, B1-B2, etc.) are calculated. Then the mean and standard deviation (SD) of these differences are calculated. If the mean -2SD through to mean +2SD spans zero then there is no evidence of bias between the two measurements. The SD of the differences divided by $\sqrt{2}$ is then calculated. This multiplied by 2.77 is the repeatability. This can then be converted to a percentage by dividing by the mean of all of the measurements and multiplying by 100.

Assessing repeatability from two measurements is not ideal but was dictated by constraints on volunteer comfort and scan time available.

6.2.7. Results: MR images

For qualitative purposes, the heuristic scans for the highest and lowest b-values are shown in Figures 6.2-3, for both repeats of Protocol A and Protocol B. At low b-values, there is

attenuation of signal. In higher b-value images, the signal drops off and SNR is more influential– but this is the 'monoexponential tail' and so is theoretically easier to fit. SNR needs to be good in the low b-value range so that perfusion effects can be teased out of the biexponential. An anatomical T2-weighted scan shows the breast parenchyma (dark) and fat (bright) for comparison in Figure 6.1.

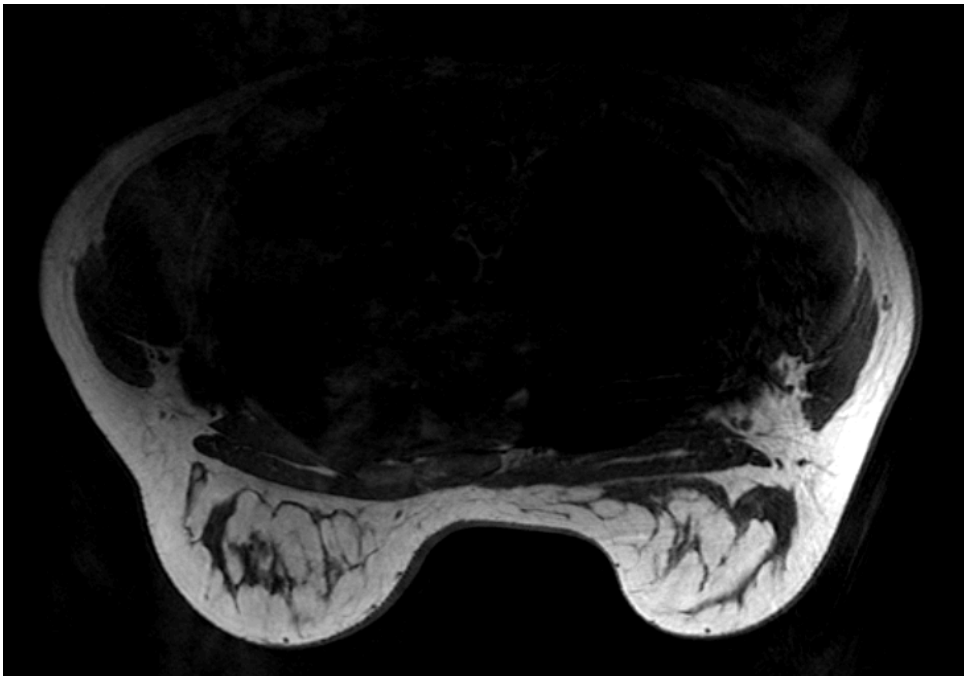

Figure 6.1: T2-weighted axial anatomical scan showing breast parenchyma (dark) and fat (bright).

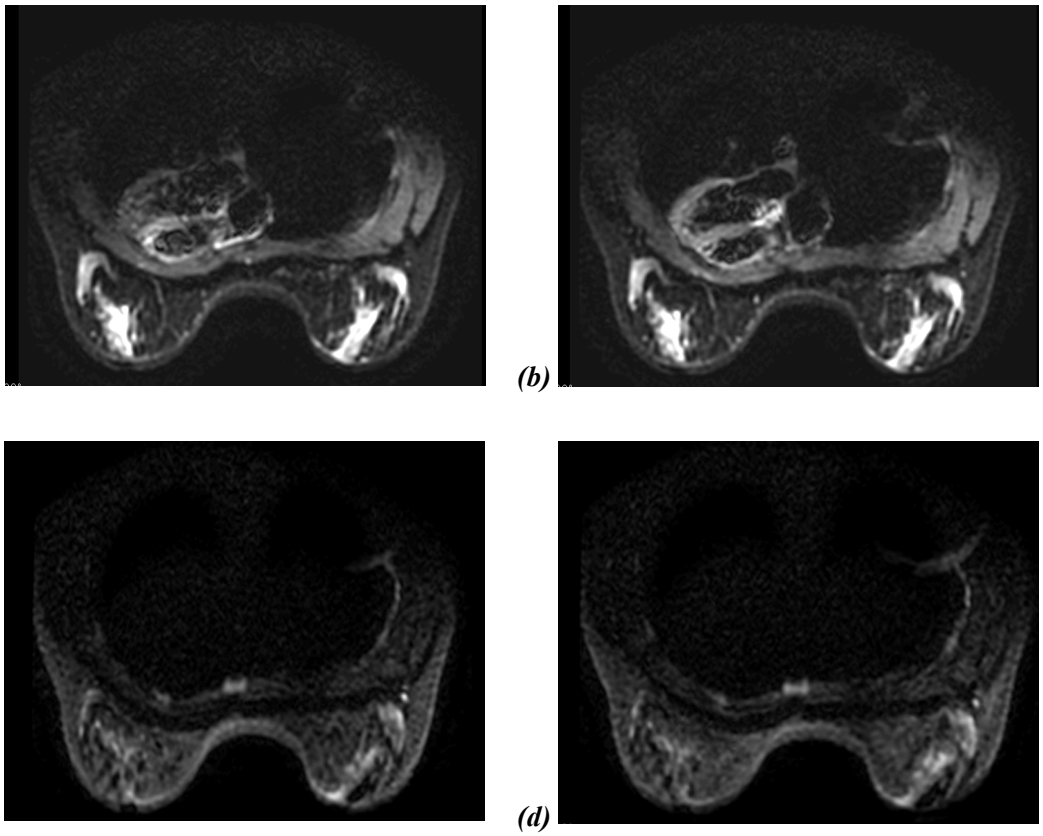

Figure 6.2: Protocol A: b = 0 s/mm2 (a, b) and b = 1000 s/mm2 (c, d) for repeats 1 (a, c) and 2 (b, d).

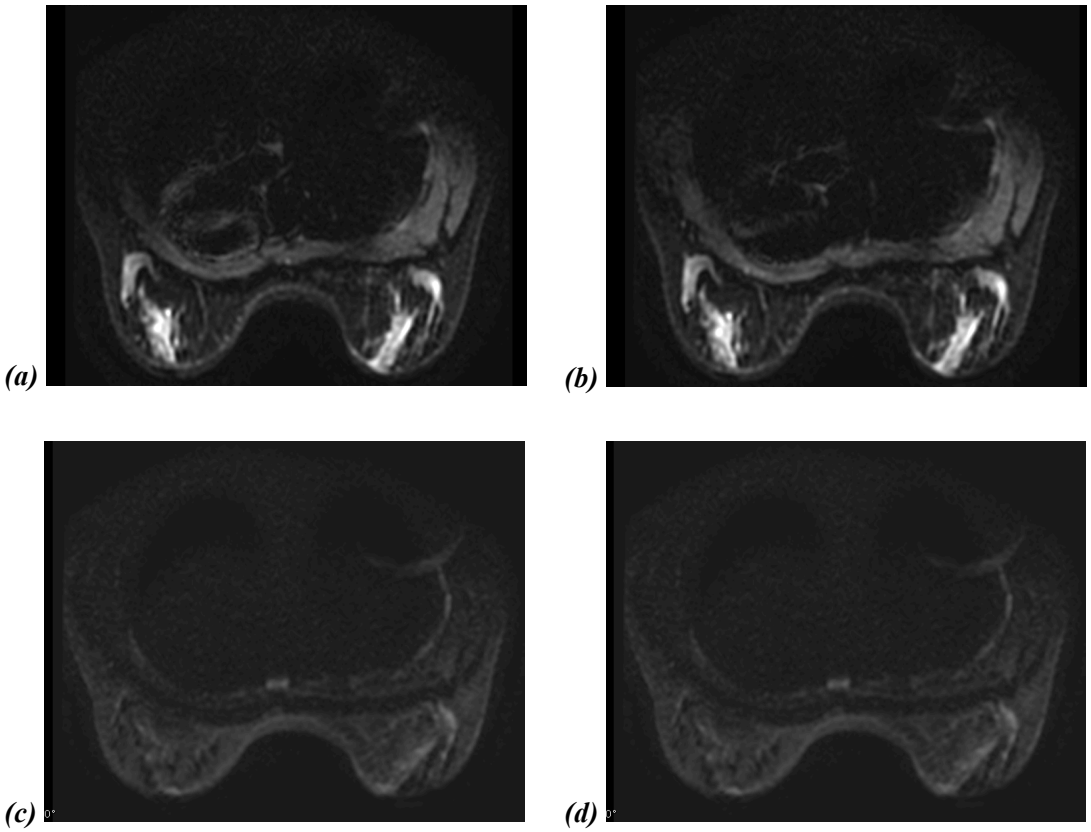

Figure 6.3: Protocol B: b = 0 s/mm2 (a, b) and b = 1000 s/mm2 (c, d) for repeats 1 (a, c) and 2 (b, d).

The average SNR in parenchyma for Protocol A was 14, and 16 for Protocol B.

6.2.8. Results: Fitting Data

(i) 'Free Fit' of Data

Table 6.2 shows the results for the 'free fit' of the IVIM signal data as a function of b-value using the standard IVIM model. The number of data points that did not fit is shown in brackets (i.e. were a nonsensical negative or large value).

Protocol	*f*	*D* mm^2/s	*D** mm^2/s	MSE
Protocol A (repeat 1)	0.117 (4/10 did not fit)	0.00124	0.007422 (4/10 did not fit)	325
Protocol A (repeat 2)	0.120 (4/10 did not fit)	0.00125	0.00684 (4/10 did not fit)	336
Protocol B (repeat 1)	0.118 (4/10 did not fit)	0.00123	0.00714 (4/10 did not fit)	267
Protocol B (repeat 2)	0.146 (3/10 did not fit)	0.00122	0.00589 (3/10 did not fit)	276

Table 6.2: Free fit for Protocol A and Protocol B for both repeats showing average f, D, D*, and the MSE.

Graphs 6.1-2 show example 'free fits' for both protocols scanned, for both repeats for one volunteer.

(a)

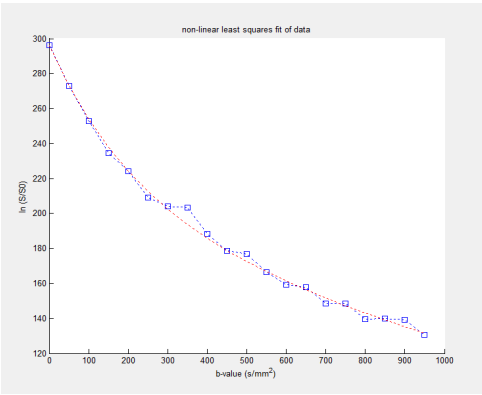

(b)

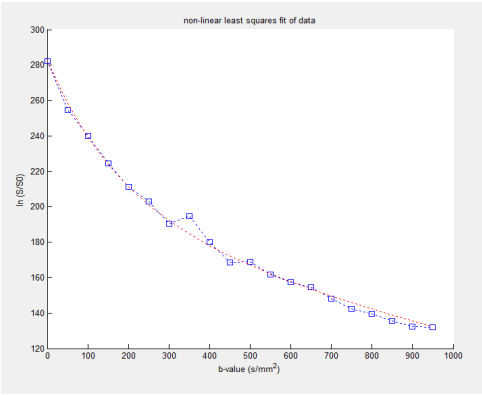

Graph 6.1: (a) and (b) example fits of Protocol A for both repeats.

(a) 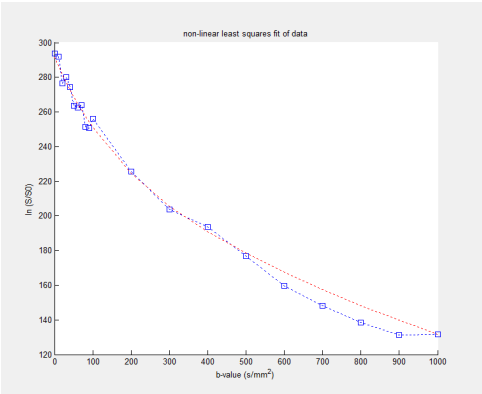

(b) 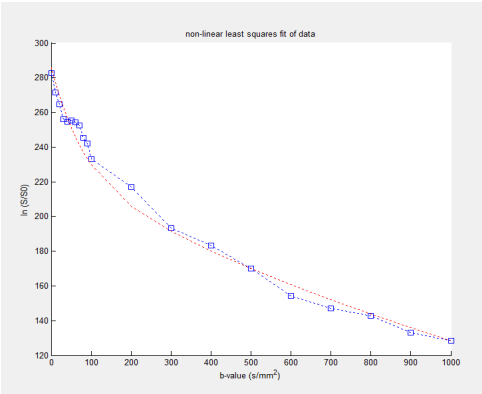

Graph 6.2: (a) and (b) example fits of Protocol B for both repeats.

(ii) 'Constrained Biexponential Fit'

Table 6.3 shows the results for the 'constrained biexponential fit' of the IVIM signal data as a function of b-value using the standard IVIM model. The number of data points that were at the boundaries of the constraints is shown in brackets.

Protocol	***f* (constraint 0<*f*<0.30)**	***D* mm²/s (constraint 0.0001<*D*<0.01)**	***D** mm²/s (constraint 0.001<*D**<0.1)**	**MSE**
Protocol A (1)	0.192 (4/10 at boundary)	0.00124	0.0440 (4/10 at boundary)	325
Protocol A (2)	0.192 (4/10 at boundary)	0.00125	0.0440 (4/10 at boundary)	336
Protocol B (1)	0.191 (4/10 at boundary)	0.00123	0.0440 (4/10 at boundary)	267
Protocol B (2)	0.192 (3/10 at boundary)	0.00122	0.0440 (3/10 at boundary)	276

Table 6.3: 'Constrained biexponential fit' for Protocol A and Protocol B for both repeats showing average f, D, D*, and the MSE for the fit.

(iii) Segmented Fit Using Both Variations of the IVIM Equation

Table 6.4 shows the results for the segmented fit of the IVIM signal data as a function of b-value using both variations of the IVIM model. The repeatability for measurements over both repeats is shown for each IVIM parameter and the monoexponential diffusion. Monoexponential diffusion is also shown (D_m), calculated using the monoexponential ADC model outlined in Chapter 3 using a free fit.

Protocol	D_m mm^2/s	± Repeatability	MSE	D mm^2/s	± Repeatability	f	± Repeatability	D^* mm^2/s	± Repeatability	MSE
D*										
Protocol A (1)	0.00125	0.000151 12%	151	0.00114	0.000583 51%	0.119	0.0588 49%	0.00742	0.0212 286%	52
Protocol A (2)	0.00127		156	0.00113		0.118		0.00741		60
Protocol B (1)	0.00139	0.000222 16%	125	0.00123	0.000554 45%	0.118	0.0955 81%	0.00713	0.00508 71%	38
Protocol B (2)	0.00139		119	0.00124		0.103		0.00721		42
D*+*D*										
Protocol A (1)	0.00125	0.000151 12%	151	0.00114	0.000583 51%	0.119	0.0588 49%	0.00742	0.0212 286%	52
Protocol A (2)	0.00127		156	0.00113		0.118		0.00741		60
Protocol B (1)	0.00139	0.000222 16%	125	0.00123	0.000554 45%	0.118	0.0955 81%	0.00712	0.00508 71%	38
Protocol B (2)	0.00139		119	0.00124		0.103		0.00709		42

Table 6.4: Segmented fit for Protocol A and Protocol B for both repeats for both variations of the IVIM equation showing average D_m, f, D, D*, repeatability and the MSE for the fit.

6.2.9. Discussion: Heuristic Protocols A and B

First of all, this application of heuristic protocols has shown that both perfusion and diffusion effects are quantifiable in breast parenchyma in this healthy volunteer cohort. The presence of such has been argued in the literature (76, 83), but different and more reliable fitting methods have been explored here. Using all fitting methods, it is clear that Protocol B samples the data better in both the perfusion and diffusion regimes, with lower MSEs in general. *f* and *D** are

better calculated using this protocol in comparison to evenly distributed sampling. This was expected and the literature also supports this (106).

Free fitting did not fit up to 4 data sets per protocol repeat, shown in table 6.2. This is a success rate of 60% using this particular fitting regime. The MSE was large for both protocols (ranging from 267 to 336), but was less for Protocol B than for Protocol A. The values for *f, D* and *D** are on the order of what would physiologically be expected, but are variable for both protocols and repeats. Graphs 6.1-2 show example fits for one volunteer for both protocols and repeats. Outliers affecting the fitting of signal data are probably due to patient movement, or artefacts. These are minimised using technical skills and patient comfort but are sometimes inexorable.

The constrained biexponential fit was similar to the free fit in that the MSEs were the same; but constrained IVIM parameters made the average IVIM parameter values increase, and so all values for the IVIM parameters are alike across all repeats and protocols because of averaging. It is possible that the data sets with constrained parameters are in fact monoexponential but here a biexponential fit is forced giving unreasonable values for *f* and *D**. Constraining calculations is therefore not an ideal solution to data that cannot be fitted well using a free fit, though it is potentially useful when dealing with noisy data. Filtering noise may be a better approach.

The segmented fit of this data, shown in Table 6.4, yielded the lowest MSEs. Protocol B had lower MSEs than Protocol A. This indicates that applying the biexponential fit whilst sampling the curve well at lower b-values works better. Using the segmented fit, there is a higher *f* when using Protocol B than Protocol A, this suggests that sampling the curve well at low b-values allows perfusion effects to be calculated more accurately. *D** is less for Protocol B, with a much better repeatability than Protocol A, too. The better estimation of IVIM parameters using segmented fitting is due to the initial estimates of the method to find local minimums, and also due to calculating *D* first monoexponentially and then using this value to guide the calculation of *f* and *D**. The repeatability for the IVIM parameters was better in general for Protocol B. The repeatability of *D* was better than that of *f* and *D**. The repeatability of D_m was better than the IVIM parameters, which was expected as it is simpler to fit and had many data points for one parameter. The perfusion parameters have proven

difficult to calculate here as well as in the literature. To improve this, an optimised protocol needs to be applied in breast.

Using the variation of the IVIM model which incorporates D and D^* into the second exponential of the model, the fit is almost identical but with D^* being very slightly less for this variation of the IVIM model. Otherwise, the two equations calculate IVIM parameters with the same MSEs and repeatability.

It can be seen that the two protocols yield different calculated IVIM parameters, and that the more sophisticated the fitting method, the better the fit in respect to MSE and residuals. By taking into account the physiological meaning of the parameters, and logically applying this as an adjunct to mathematical consideration, the best way to calculate parameters seems to be; 1) have a suitable protocol that samples the curve adequately at low b-values for perfusion parameters and high b-values for monoexponential diffusion; 2) use a sophisticated fitting method to calculate the IVIM parameters from the average signal of the ROI; 3) take into account SNR, patient set up to prevent movement, and suitable shimming.

This goal of this study was to find the best fitting strategy to improve the precision and accuracy of IVIM biexponential. Comparison of the different analysis methods showed that the segmented analysis had higher precision. There was no effective difference found between the two IVIM models used in the literature. When the signal curve was sampled more at lower b-values, perfusion parameters f and D^* were able to be calculated better, as shown by the lower MSEs. The repeatability using a segmented fit was calculated and can be compared to future optimised protocols. The next step in healthy volunteers is to test optimised protocols (Chapter 5) using the segmented fitting method.

6.3. Optimised Protocols: Breast Second Iteration (Protocols C and D)

The optimised and clinically optimised protocols generated from the second iteration of optimisation (Protocols C and D, Chapter 5) were investigated in healthy volunteers to assess image quality, fitting of the data, presence of perfusion effects in healthy breast parenchyma, repeatability of IVIM parameters, and to calculate values for f, D, and D^* as possible inputs into future optimisations. The clinically optimal protocol was the maximum number of optimal b-values with suitable NEX scanned in under 5 minutes as part of a multiparameteric MR breast exam (Protocol C). The optimal protocol had half the amount of NEX than that of

the clinically optimal protocol (Protocol D), to see if the postulation of taking 10 b-values with suitable NEX was definitely better than 20 optimal b-values with low NEX.

6.3.1. Volunteer subjects

Eleven healthy volunteers were consented to take part in this study at the Centre of Magnetic Resonance Investigations, Hull Royal Infirmary in October 2014. Volunteers had a mean age of 26 years (range 20 - 34 years). Informed consent was obtained and MR safety screening forms were completed prior to imaging.

6.3.2. MRI Scans

Volunteers underwent a bilateral MRI breast examination on a 3.0 T MR750 scanner using the body coil as a transmitter and an 8-channel breast receiver coil (GE Healthcare, Milwaukee, WI).

A general 3-plane T1-weighted localiser was acquired to set up slice locations and shim volumes. A T2-weighted anatomical scan was acquired for guiding ROI placement. IVIM images were acquired axially using diffusion weighted single-shot echo planar imaging (EPI) with identical parameters to those detailed in Section 6.2.2 apart from NEX, 2 for 20 b-values, 4 for 10 b-values; scan duration 4.20min; with water only excitation. Four IVIM series were acquired per volunteer, two repeats of Protocol C and two of Protocol D. Protocol C had the following 10 diffusion weightings, b = 0, 9 (10), 23, 46, 82, 140, 233, 382, 619, 1000 *s/mm*^{2}. Protocol D had the following 20 diffusion weightings, b = 0, 4 (10), 8 (10), 14, 21, 30, 41, 55, 73, 94, 122, 156, 198, 251, 318, 401, 505, 635, 797, 1000 *s/mm*^{2}. Total scan time including volunteer positioning on the scanner bed was 25 minutes. Note the MR system would not allow 4 *s/mm*^{2}, 8 *s/mm*^{2} and 9 *s/mm*^{2} as stated in the optimisation so 10 s/mm^2 was used instead.

6.3.3. ROIs and SNR

A region of interest (ROI) was drawn on the largest cross-section of parenchyma seen on DW-images in whichever breast was more suitable. The ROI was then copied onto its repeated counterpart series. This was done for both protocols. The average size of the ROIs were 250 *mm*^{2}.

The SNR was calculated as in Section 6.2.3.

6.3.4. Fitting of Data

All fitting was coded and computed in MATLAB (MathWorks, Massachusetts, USA). A segmented fit was applied as described in Section 6.2.4. A lower cut-off to fit D monoexponentially was set as 200 s/mm^2. Constraints to disallow any parameter to be negative were coded, and f was constrained to be between 5% and 30% for initial estimates, as anything else is deemed physiologically impossible in that breast. The segmented fit was also carried out to compare the D^* and D^*+D variation of the IVIM equation. The mean square error for each fit was reported.

6.3.5. Repeatability of IVIM Parameters

Repeatability was calculated as in Section 6.2.6, with the hypothesis that since the protocols were optimised, and segmented fitting was implemented, then they should have better repeatability.

6.3.6. Results: MRI Scans

For qualitative purposes, examples of the Protocols C and D scans for the highest and lowest b-values are shown in Figures 6.4-5, for both repeats.

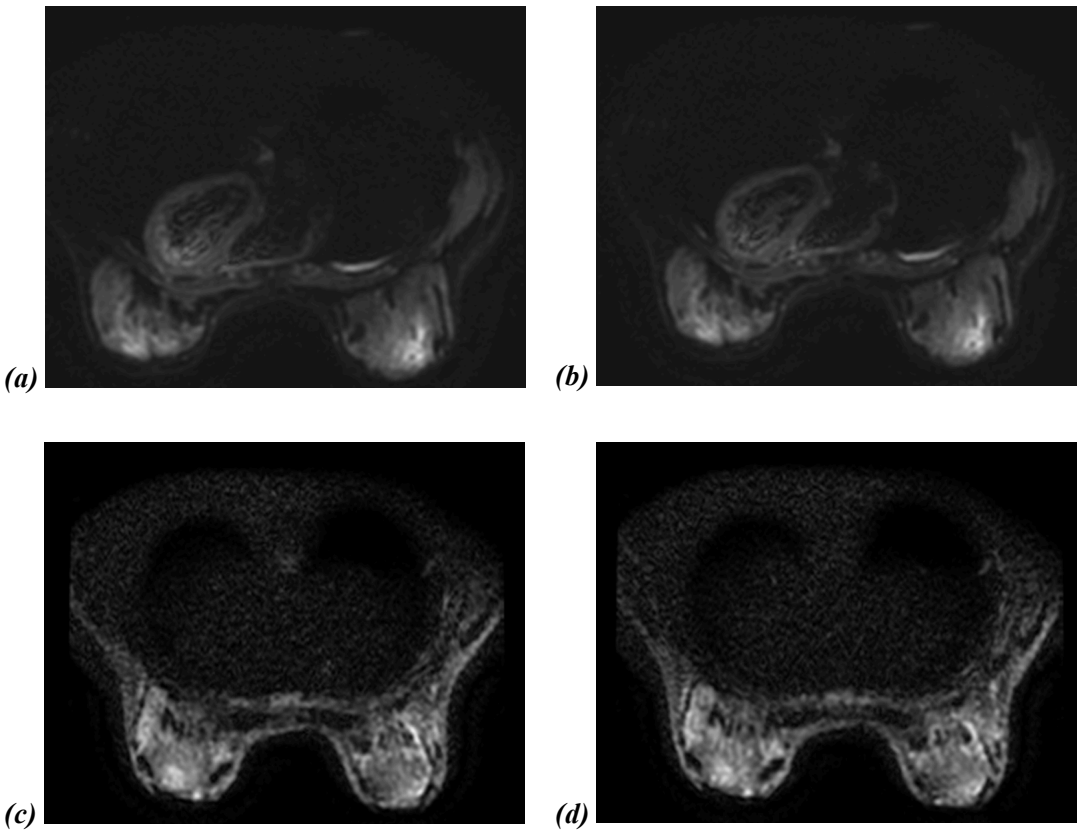

Figure 6.4: Protocol C: b = 0 s/mm^2 (a, b) and b = 1000 s/mm^2 (c, d) for repeats 1 (a, c) and 2 (b, d).

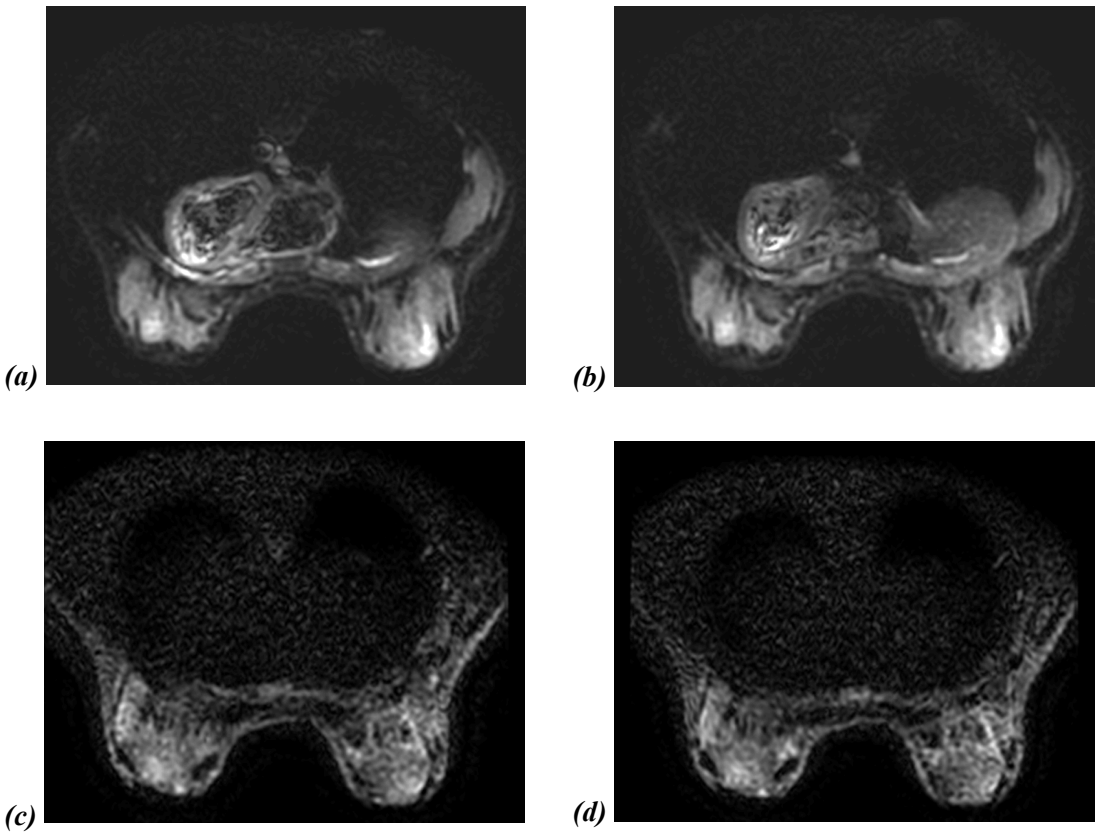

Figure 6.5: Protocol D: b = 0 s/mm2 (a, b) and b = 1000 s/mm2 (c, d) for repeats 1 (a, c) and 2 (b, d).

The average SNR for the Protocol C was 23 and for Protocol D was 18.

6.3.7. Results: Segmented Fit *D** and *D**+*D*

Table 6.5 shows the results for the segmented fit of the IVIM signal data as a function of b-value using both variations of the IVIM model for Protocol C and Protocol D. The repeatability for measurements over both repeats is shown for each IVIM parameter and the monoexponential diffusion.

Protocol	D_m mm^2/s	± Repeatability	MSE	D mm^2/s	± Repeatability	f	± Repeatability	D^* mm^2/s	± Repeatability	MSE
D*										
Protocol C (1)	0.00188	0.00015 8%	546	0.00180	0.00016 9%	0.0560	0.084 105%	0.00851	0.0216 108%	76
Protocol C (2)	0.00187		291	0.00180		0.103		0.0194		110
Protocol D (1)	0.00205	0.00033 17%	193	0.00180	0.00035 20%	0.0630	0.12 171%	0.0104	0.039 195%	113
Protocol D (2)	0.00187		268	0.00170		0.0789		0.0223		160
D+D*										
Protocol C (1)	0.00188	0.00015 8%	546	0.00180	0.00016 9%	0.0560	0.084 105%	0.00850	0.0216 108%	76
Protocol C (2)	0.00187		291	0.0018		0.103		0.0193		110
Protocol D (1)	0.00205	0.00033 17%	193	0.0018	0.00035 20%	0.063	0.12 171%	0.0100	0.039 195%	113
Protocol D (2)	0.00187		268	0.0017		0.0789		0.0220		160

Table 6.5: Segmented fit for Protocol C and Protocol D for both repeats for both variations of the IVIM equation showing average D_m, f, D, D*, repeatability and the MSE for the fit.

6.3.8. Discussion

The image quality of both IVIM protocols was suitable enough in that an anatomical scan was not needed to guide ROI placement. The parenchyma was clearly distinguishable from fat. Perfusion and diffusion effects were calculated to be present in healthy breast parenchyma in this cohort of volunteers using optimised protocols. The repeatability of Protocol C is better

than Protocol D for all IVIM parameters. This may be due to higher NEX, despite more b-values being implemented in Protocol D. All volunteer data sets fitted successfully, yielding calculations of *f, D* and *D** as physiologically expected and comparable to literature. The MSEs for Protocol C were all lower than that of Protocol D. Since less b-values are used in Protocol C, this enabled the number of NEX to be increased and thus SNR to be improved – this perhaps explains why this protocol was fitted better than Protocol D. As before, with heuristic protocols, there is no significant difference between the two variations of the IVIM model. The repeatability of Protocol C was better than that of Protocol D, in general. Perfusion parameters displayed the worst repeatability, with mono- and biexponential fitted diffusion both performing best and similarly. The repeatability for these optimised protocols are better than the repeatability for the heuristic protocols (Compare Tables 6.4 and 6.5). A factor adding to this huge difference in repeatability could be that the investigator had now scanned volunteers before and was better at both scanning and making sure the volunteer was both comfortable and knew they had to stay as still as possible.

6.4. Optimised protocol: Breast Third Iteration (Protocol E)

The clinically optimised protocol generated from the third iteration of optimisation (Protocol E, Chapter 5) was investigated in healthy volunteers to assess image quality, fitting of the data, presence of perfusion effects in healthy breast parenchyma, repeatability of IVIM, and to calculate values for *f, D,* and *D** as possible inputs into future optimisations.

6.4.1. Volunteer subjects

Six healthy volunteers were consented to take part in this study at the Centre of Magnetic Resonance Investigations, Hull Royal Infirmary in January 2015. Volunteers had a mean age of 28 years (range 23 - 50 years). Informed consent was obtained and MR safety screening forms were completed prior to imaging.

6.4.2. MRI scans

Volunteers underwent a bilateral MRI breast examination on a 3.0 T MR750 scanner using the body coil as a transmitter and an 8-channel breast receiver coil (GE Healthcare, Milwaukee, WI).

A general 3-plane T1-weighted localiser was acquired to set up slice locations and shims. A T2-weighted anatomical scan was acquired for guiding ROI placement. IVIM images

were acquired axially using diffusion weighted single-shot echo planar imaging (EPI) with identical parameters to those detailed in Section 6.1.2 apart from NEX, 4 for the 10 b-values. Two IVIM series were acquired per volunteer, two repeats of Protocol E to assess repeatability. Protocol E had the following 10 diffusion weightings, b = 0, 9 (10), 12, 24, 45, 80, 140, 241, 421, 700 s/mm^2 (Note that the second b-value had to be 10 s/mm^2 due to scanner limitations; this was accounted for in the fourth iteration of optimisation but iterations 2 and 3 were done prior to scanning). Total scan time including volunteer positioning on the scanner bed was 15 minutes.

6.4.3. ROIs

A region of interest (ROI) was drawn on the largest cross-section of parenchyma seen on DW-images in whichever breast was more suitable. The ROI was then copied onto its repeated counterpart series. This produced signal values to fit for the corresponding b-values in the IVIM protocol. The average size of the ROIs was 210 mm^2.

The SNR was calculated as in Section 6.2.3.

6.4.4. Fitting

All fitting was coded and computed in MATLAB (MathWorks, Massachusetts, USA). A segmented fit was applied as described in Section 6.1.4. A cut-off to fit D monoexponentially was set as 200 s/mm^2. Constraints to disallow any parameter to be negative were coded, and f was constrained to be between 5% and 30% for initial estimates, as anything else is deemed physiologically impossible in that breast. This increased robustness of the fit. The segmented fit was also carried out to compare the D^* and D^*+D variation of the IVIM equation. The mean square error (MSE) for each fit was reported.

6.4.5. Repeatability

Repeatability was calculated as in Section 6.1.6, with the hypothesis that since this protocol was optimised, and segmented fitting was implemented, then it should have better repeatability than previous protocols.

6.4.6. Results: MRI Scans

For qualitative purposes, example scans for the highest and lowest b-values are shown in Figure 6.6, for both repeats of Protocol E.

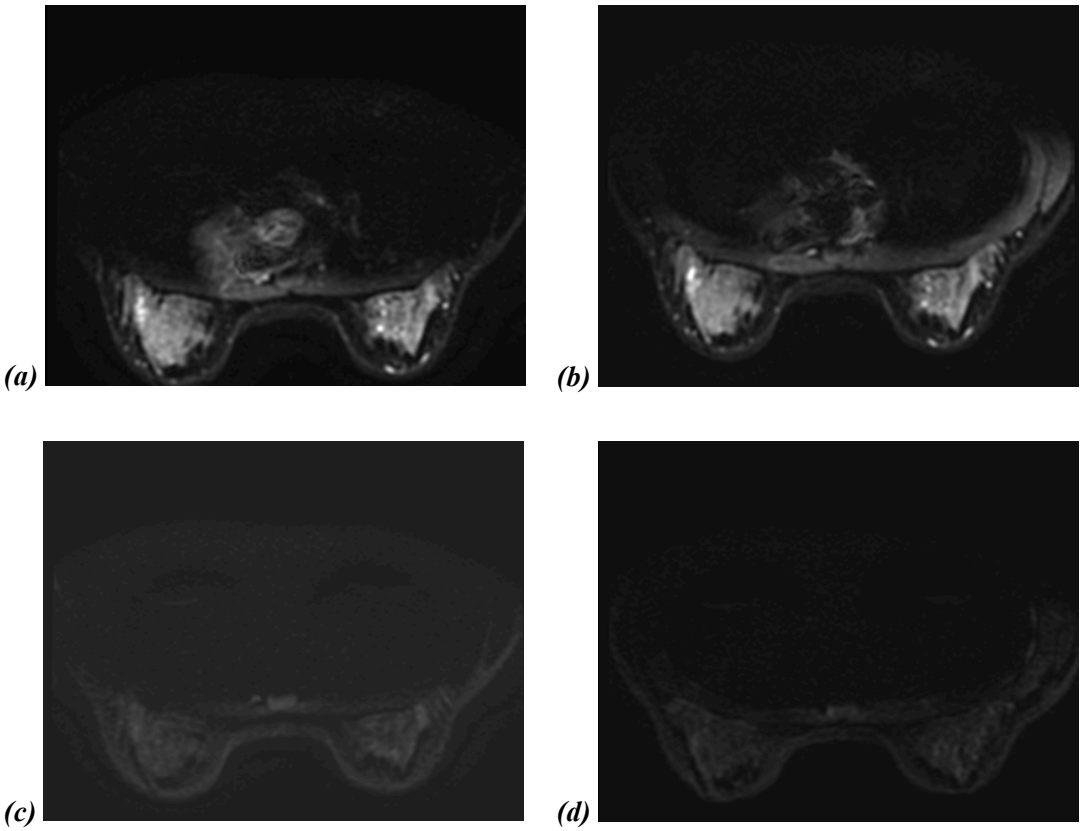

Figure 6.6: Protocol E: b = 0 s/mm2 (top) and b = 700 s/mm2 (bottom) for repeats 1 (a, b) and 2 (c, d).

The average SNR for this protocol was 25.

6.4.7. Results: Fitting

Figures 6.7-8 show the segmented fit for both repeats of one volunteer using the standard IVIM model, scanned using Protocol E. The residuals of the fit are also shown in red underneath the fit.

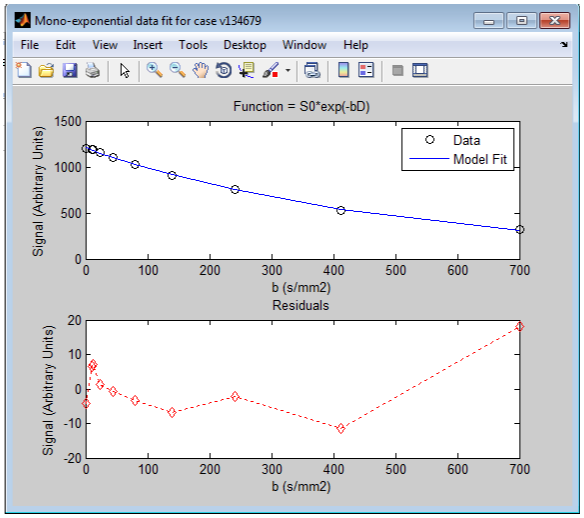

(a)

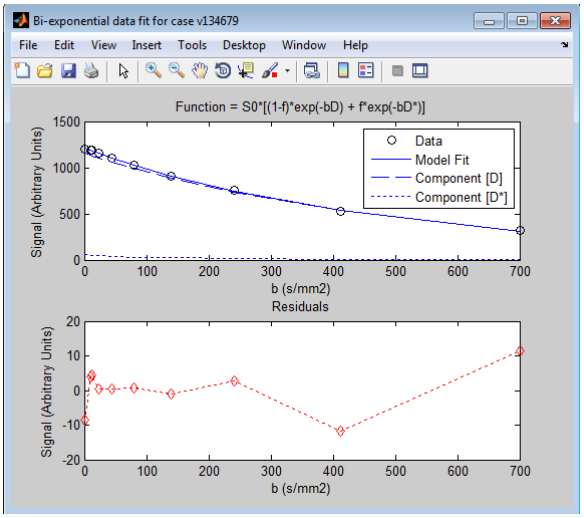

(b)

Figure 6.7: (a) Monoexponential fit and (b) biexponential fit of a volunteer using the standard IVIM model (repeat 1).

(a)

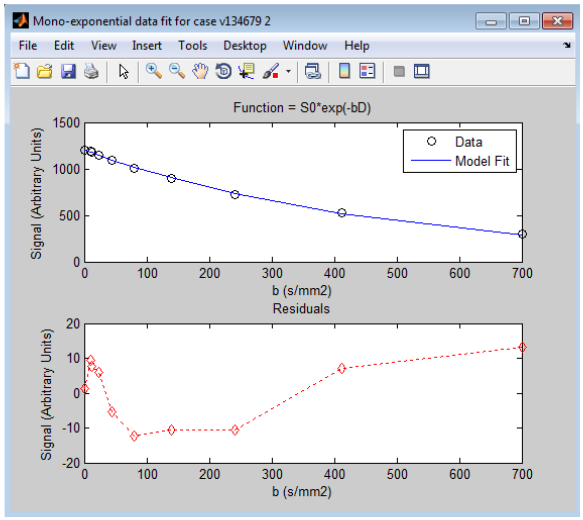

(b)

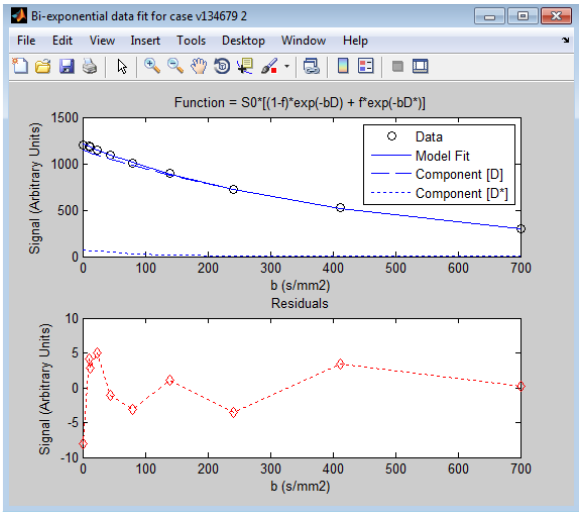

Figure 6.8: (a) Monoexponential fit and (b) biexponential fit of a volunteer using the standard IVIM model (repeat 2).

Table 6.6 shows the results for the segmented fit of the IVIM signal data as a function of b-value using both variations of the IVIM model. The repeatability for measurements over both repeats is shown for each IVIM parameter and monoexponential diffusion.

Protocol	D_m mm^2/s	± Repeatability	MSE	*D* mm^2/s	± Repeatability	*f*	± Repeatability	*D** mm^2/s	± Repeatability	MSE
D*										
Protocol E (1)	0.00167	0.000164 10%	68	0.00154	0.000159 10%	0.0834	0.0450 60%	0.0445	0.0500 90%	60
Protocol E (2)	0.00165		64	0.00153		0.0677		0.0672		67
D*+D										
Protocol E (1)	0.00167	0.000164 10%	68	0.00154	0.000159 10%	0.0834	0.0450 60%	0.0445	0.0500 90%	60
Protocol E (2)	0.00165		64	0.00153		0.0677		0.0673		67

Table 6.6: Segmented fit for Protocol E for both repeats for both variations of the IVIM equation showing average D_m, f, D, D*, repeatability and the MSE for the fit.

6.4.8. Discussion

The main difference with this clinically optimised protocol is that the final b-value is not 1000 s/mm^2 as used previously. This does not seem to have affected the calculation of *D*, and has, in fact, improved the MSE of this parameter. This could be due to eliminating non-Gaussian diffusion that appears at high b-values. The repeatability for D_m, *f, D,* and *D** is better than that for the second iteration b-value schemes. *D** is the least precise of the three IVIM parameters, which is a theme recurrent in the literature. This has been suggested to be due to a bias arising from using the segmented approach, and is also due to pseudo diffusion composing the smallest fraction of the decay signal and so is inherently difficult to estimate. The mono- and biexponential fitting of diffusion have similar repeatability once more. The MSEs are also all lower for this protocol than previous ones. Biexponentially fitted *D* is lower than D_m as expected, and all IVIM parameters agree with physiologically expected and literature values. All 6 volunteer data sets fitted without the need for any parameter to be bound by the inputted constraints. Once again, there is no difference between the two

variations of the IVIM model, which can be seen by the calculated parameters in Table 6.6. The residuals are graphed in red and the main variations seem to be at lower b-values.

6.5. Optimised protocol: Breast Fourth Iteration (Protocol F)

The clinically optimised protocol generated from the fourth iteration of optimisation (Protocol F, Chapter 5) was investigated in healthy volunteers to assess image quality, fitting of the data, presence of perfusion effects in healthy breast parenchyma, repeatability of IVIM parameters, and to calculate values for *f, D,* and *D** as inputs into a post-clinical optimisation using the Hull and East Riding patient cohort. This scan was consequently implemented in breast cancer patients (Chapter 7), as it was the most extensive optimisation after iterated learning outcomes in Chapter 5. It also performs well in this chapter.

6.5.1. Volunteer subjects

Six healthy volunteers were consented to take part in this study at the Centre of Magnetic Resonance Investigations, Hull Royal Infirmary in March 2015. Volunteers had a mean age of 31 years (range 20 - 64 years). Informed consent was obtained and MR safety screening forms were completed prior to imaging.

6.5.2. MRI scans

Volunteers underwent a bilateral MRI breast examination on a 3.0 T MR750 scanner using the body coil as a transmitter and an 8-channel breast receiver coil (GE Healthcare, Milwaukee, WI). A general 3-plane T1-weighted localiser was acquired to set up slice locations and shims. A T2-weighted anatomical scan was acquired for guiding ROI placement. IVIM images were acquired axially using diffusion weighted single-shot echo planar imaging (EPI) with the identical parameters to those detailed in Section 6.2.2 apart from NEX, 4 and 10 b-values. Two repeats of this protocol were acquired per volunteer. Protocol F had the following 10 diffusion weightings, b = 0, 10, 24, 46, 71, 135, 221, 355, 567, 900 s/mm^2. Total scan time including volunteer positioning on the scanner bed was 15 minutes.

6.5.3. ROIs

A region of interest (ROI) was drawn on the largest cross-section of parenchyma seen on DW-images in whichever breast was more suitable. The ROI was then copied onto its repeated counterpart series. The average size of the ROIs were 285 mm^2.

The SNR was calculated as in Section 6.2.3.

6.5.4. Fitting

All fitting was coded and computed in MATLAB (MathWorks, Massachusetts, USA). A segmented fit was applied as described in Section 6.2.4. A cut-off to fit D monoexponentially was set as 200 s/mm^2. Constraints to disallow any parameter to be negative were coded, and f was constrained to be between 5% and 30% for initial estimates, as anything else is deemed physiologically impossible in the breast. The segmented fit was also carried out to compare the D^* and D^*+D variation of the IVIM equation.

6.5.5. Repeatability

Repeatability was calculated as in Section 6.2.6, with the hypothesis that since the protocol was optimised, and segmented fitting was implemented, then it should have better repeatability than previous protocols.

6.5.6. Results: MRI Scans

For qualitative purposes, examples of Protocol F scans for the highest and lowest b-values are shown in Figure 6.9, for both repeats.

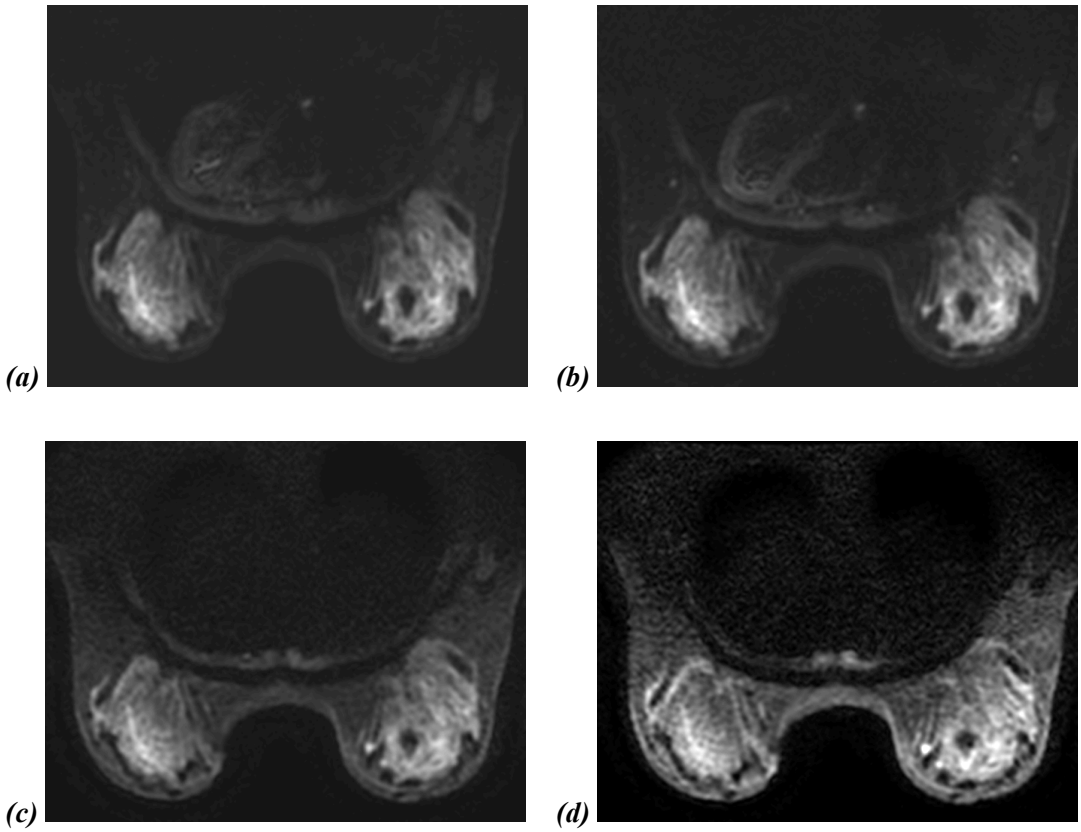

Figure 6.9: Protocol F: b = 0 s/mm^2 (top) and b = 900 s/mm^2 (bottom) for repeats 1 (a, b) and 2 (c, d).

The average SNR for Protocol F was 25.

6.5.7. Results: Segmented Fit for *D** and *D*+D*

Table 6.7 shows the results for the segmented fit of the IVIM signal data as a function of b-value using both variations of the IVIM model for this protocol. The repeatability for measurements over both repeats is shown for each IVIM parameter and monoexponential diffusion.

Protocol	D_m mm^2/s	± Repeatability	MSE	D mm^2/s	± Repeatability	f	± Repeatability	D* mm^2/s	± Repeatability	MSE
D*										
Protocol F (1)	0.00185	0.000151 8%	115	0.00176	0.000146 8%	0.0505	0.0449 74%	0.0414	0.0351 85%	55
Protocol F (2)	0.00181		79	0.00173		0.0716		0.0456		54
D*+D										
Protocol F (1)	0.00185	0.000151 8%	115	0.00176	0.000146 9.5%	0.0505	0.0449 74%	0.0413	0351 85%	55
Protocol F (2)	0.00181		79	0.00173		0.0716		0.0456		54

Table 6.7: Segmented fit for Protocol F for both repeats for both variations of the IVIM equation showing average D_m, f, D, D*, repeatability and the MSE for the fit.

6.5.8. Discussion

The differences between this clinically optimised protocol (Protocol F) and that of the previous third iteration of optimisation (Protocol E) are that the final b-value is now 900 s/mm^2 and the second b-value is constrained to be 10 s/mm^2 in the optimisation procedure due to scanner limitations rather than changing this second b-value post-optimisation, as described previously. This optimisation was also more far-reaching and explored millions of sets of b-values. Together with this rationalisation, and the fact that the repeatability for all IVIM parameters and the MSEs are similar to the third iteration of optimisation, then this protocol appears to be the most optimal produced thus far. Naturally, the next step is to investigate this protocol in breast cancer patients.

6.6. Volunteer Studies: Overall Conclusions

Table 6.8 shows a summary of the protocols scanned in this chapter. Heuristic and optimised protocols were used to establish the presence of IVIM effects in healthy breast parenchyma. Microperfusion has been observed in several tissues at low b-values in the liver and kidneys (107), but it has been argued that this effect is negligible in the breast (76) using non-optimal protocols. It is well known that the breast is not a highly vascular organ, however with optimised scans and advanced fitting strategies, the perfusion effects have been drawn out of the signal decay.

Varied fitting methodologies have been used in the literature, and here the best technique to calculate IVIM parameters was established using the MSE of residuals as a measure of goodness of fit. This involved investigating several fitting methods and IVIM models. It was found that the segmented approach yielded the lowest MSEs, as expected, due to its popularity in the literature and agreeing with studies comparing fitting methods in whole tumour analysis as opposed to ROI analysis here (80, 85).

Here, healthy volunteers were employed to enable repeat scans. From evaluation of Protocols A and B, Protocol B (where b-values were sampled well at lower values) was best for calculating f, D and D^*, impelling the use of exponential and power law sampling strategies in Chapter 5. No significant difference between the two IVIM models explored was found in these heuristic protocols.

Despite an optimal protocol having 20 b-values (Protocol D) in the second iteration of optimisation, it was shown that clinical time constraints meant that 10-b-values with more NEX (Protocol C) yielded lower MSEs and better repeatability.

Further optimisations varying the final b-value (Protocol E) and considering scanner limitations (Protocol F) also improved the accuracy, precision and repeatability of IVIM parameters. The best repeatability was for the fourth iteration of the optimisation (Protocol F). This was intuitively expected. D^* had the worst repeatability, then f, and then D/D_m, in general.

It should be noted that despite more b-values being present in Protocols A and B, that D (comparable because it also had 2 NEX) shows a great improvement in repeatability and MSEs. A conclusion could be drawn that an optimised protocol is better. Protocols C, E and F

had double the NEX, and ‘more’ optimal b-values through further iterations and constraints. They were better, sill, despite having less b-values.

Several limitations to these volunteer studies should be noted. Firstly, a small number of volunteers were scanned and any statistics would therefore not necessarily be calculated as statistically significant, even if true. We were unable to observe true accuracy in volunteers due to the inaccessibility of measured physiological values, but comparison to literature and previous calculated values allowed for reasonable acceptance. Initial estimates for fitting used universal parameter input from literature rather than healthy parenchyma specific values – this was due to patients having not been scanned before. Scanning the same cohort for each iteration of optimisation would have negated this, but this is difficult when recruiting over a large span of time.

A robust protocol (Protocol F) has been developed and tested in healthy volunteers, which has a reasonable SNR in a clinically acceptable time. This will be subsequently investigated in detail for clinical scanning of breast cancer patients in Chapter 7 using the segmented fit.

Two more aims of those outlined at the end of Chapter 4 have now been met; 3) to investigate IVIM effects, repeatability and reproducibility in normal healthy tissue; 4) to investigate the robustness of fitting methods for IVIM data in breast tissue.

Optimal Protocols	B-values
Protocol A (Heuristic)	00, 50, 100, 150, 200, 250, 300, 350, 400, 450, 500, 550, 600, 650, 700, 750, 800, 850, 900, 950, 1000 s/mm^2
Protocol B (Heuristic)	0, 10, 20, 30, 40, 50, 60, 70, 80, 90, 100, 200, 300, 400, 500, 600, 700, 800, 900, 1000s/mm^2
Protocol C (Clinically optimal)	0, 9, 23, 46, 82, 140, 233, 382, 619, 1000 s/mm^2
Protocol D (Optimal)	0, 4, 8, 14, 21, 30, 41, 55, 73, 94, 122, 156, 198, 251, 318, 401, 505, 635, 797, 1000 s/mm^2
Protocol E (Clinically optimal)	0, 4, 12, 24, 45, 80, 140, 241, 412, 700 s/mm^2
Protocol F (Clinically optimal)	0, 10, 24, 46, 71, 135, 221, 355, 567, 900 s/mm^2

Table 6.8: Summary of protocols investigated in healthy volunteers.

7. IVIM for Malignant Lesion Subtype Classification in Pre Neoadjuvant Chemotherapy Breast Cancer Patients

7.1. Introduction

Several groups have demonstrated the feasibility of IVIM in clinical oncological studies (108-111), especially in breast (78-83, 112), as outlined in the IVIM literature review in Chapter 4. The potential as a biomarker for malignancy, and further, subtypes has been suggested (22). IVIM imaging can probe vascularity and the complex heterogeneity and cell structure of tumours. However, breasts have been assumed to have a relatively low blood volume in normal fibroglandular tissue and so it has previously been anticipated that perfusion effects measured from IVIM may be negligible (76). In Chapter 6, it was demonstrated that healthy volunteers had perfusion effects quantifiable by the IVIM model in normal tissue. It is also now known that several types of breast cancers have a high rate of angiogenesis and are aggressive (9, 54), which indicates that a technique such as IVIM would be useful in detecting and classifying breast cancers. Breast is therefore one of the most novel anatomies of interest in IVIM. Studies thus far mainly evaluate the potential for IVIM parameters to differentiate between malignant and benign lesions, as well as normal tissue, using heuristic protocols and several different fitting methodologies. Some studies have gone further, not using optimised schemes, to try and classify histological types and molecular subtypes with a good degree of statistical significance (79).

This chapter will elaborate on healthy volunteer breast tissue studies in Chapter 6, using protocols generated through optimisation in Chapter 5, initially in a clinical pilot study, and then in a full clinical study. These are logical steps after optimising and validating IVIM protocols, fitting methods, and IVIM models in healthy volunteers. The clinically optimised protocol (Protocol F) from the fourth IVIM optimisation for breast cancer is employed in attempting to classify malignant lesions into histopathologic subtype and molecular subtype using IVIM parameters, which have been shown to have potential as promising biomarkers for diagnosis and monitoring response to treatment.

7.2. Second Iteration of Optimisation (Protocol C): Initial Clinical Pilot Study in Breast Cancer Patients

7.2.1. Pilot Study Patient Cohort

This initial pilot study observed nineteen patients with biopsy proven malignant breast cancer (any type and subtype for the pilot study) at the Centre for Magnetic Resonance Investigations, Hull Royal Infirmary from October 2014 to January 2015. Patients had a mean age of 53 years (range of 37–81 years). MR safety screening forms were completed prior to imaging. An IVIM protocol was added to replace the standard DWI protocol. The multi b-value nature could be utilised for ADC assessment as standard of treatment, and also for IVIM biexponential fitting for this investigation.

MR scans were taken prior to any cancer treatment (pre neoadjuvant chemotherapy (NAC), surgery or radiotherapy). Patients were scanned for screening purposes, problem solving or pre-treatment planning. Cancer was confirmed via biopsy; stereotactic core biopsy, US-guided fine needle aspiration (FNA), or MRI guided core biopsy. Final histopathology diagnosis was confirmed through histology and/or surgical specimen analysis.

7.2.2. MRI Scans

Patients underwent a standard of care bilateral MRI breast examination on a 3.0 T MR750 scanner (GE Healthcare, Milwaukee, WI) using the body coil as a transmitter and an 8-channel breast receiver coil (GE Healthcare, Milwaukee, WI) with the substitution of a <5 minute IVIM series in place of standard DWI (2 b-values). These IVIM images were acquired axially using diffusion weighted single-shot echo planar imaging (EPI) with the following parameters: repetition time/echo time (TR/TE), 6366 *ms*/54.4 *ms*; field of view, 34x34cm; matrix, 128x128; slice thickness 4mm; slice spacing 1mm; 42 slices (variable with breast size if needed); Bandwidth ±250MHz; frequency direction, right to left; diffusion direction, 3 in 1; NEX, 4; bi-lateral shimming; scan duration 4.20min (variable with breast size); with water only excitation. Only one IVIM series was acquired per patient. Protocol C had the following 10 diffusion weightings: b = 0, 10 (9), 23, 46, 82, 140, 233, 382, 619, 1000 s/mm^2, in lieu of the conventional DWI scan at CMRI. Note 10 s/mm^2, as the MR system would not allow 9 s/mm^2 as stated in the optimisation results for the second iteration in Chapter 5.

7.2.3. ROIs and SNR

An experienced radiologist (Professor LW Turnbull) kindly drew regions of interest. Lesions were identified on a post-contrast T1-weighted anatomical image first for guidance (gadolinium contrast agent was given as part of the standard breast MR exam) and then a region of interest (ROI) was drawn on the most malignant part of the lesion as seen on DW-images. The most malignant part of the lesion was identified as having restricted diffusion (ADC) and strong signal intensity on DW-images. The ROI was drawn as large as possible using this criterion. This produced signal values to fit as a function of the corresponding b-values in the IVIM protocol. The average size of the ROIs was 45 mm^2. Figure 7.1 shows an example DCE image on the left and the placement (blue arrow) of an ROI (green) on the IVIM image on the right.

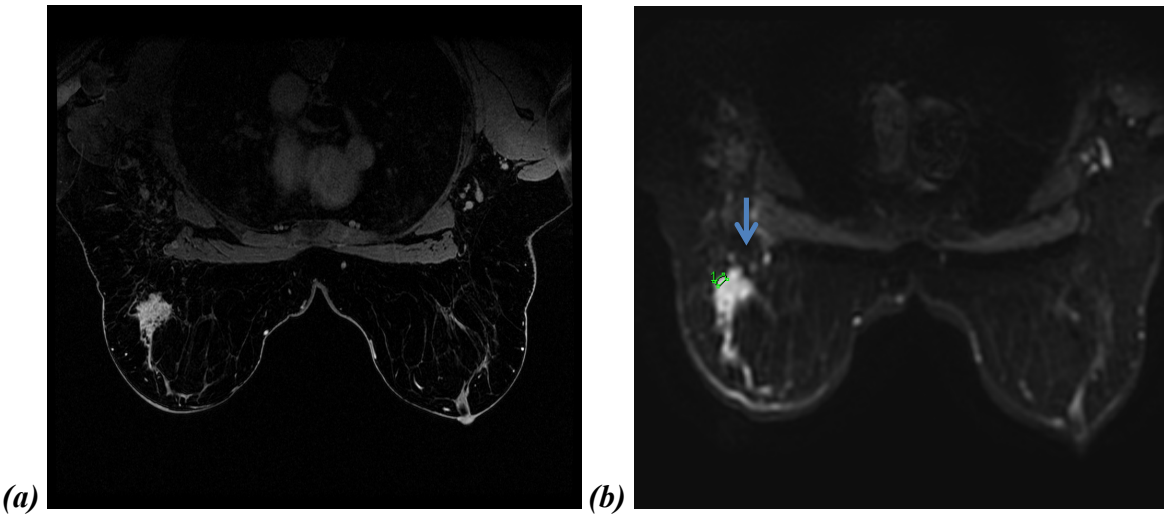

Figure 7.1: Lesion in the left breast on a) a post-contrast T1-weighted image; and b) an IVIM image b = 1000 s/mm^2 with an ROI in the most malignant region of the lesion.

The SNR was calculated as the mean signal intensity of the ROI minus the mean signal of background noise divided by the standard deviation of the mean of the background noise, multiplied by 0.655.

7.2.4. Fitting of Data

All fitting was coded and computed in MATLAB (MathWorks, Massachusetts, USA). A segmented fit was applied as described in Section 6.2.4 (*iii*) using Method 5, Chapter 3. A cut-off to fit D monoexponentially was set as 200 s/mm^2. Constraints to disallow any parameter to

be negative were coded, and f was constrained to be between 5% and 30% for initial estimates, as anything else is deemed physiologically impossible in that breast. The segmented fit was also carried out to compare the D^* and D^*+D variation of the IVIM equation. The mean square error (MSE) for each fit was reported.

7.2.5. Investigating Final Cut-offs for the Segmented Fit

The segmented fit was also carried out at various final b-value cut-offs after seeing that later optimisations (Chapter 5) generated protocols with a final b-value of less than 1000 s/mm^2. The final cut-offs evaluated were 382 s/mm^2, 619 s/mm^2, and 1000 s/mm^2.

7.2.6. Results: MRI Scans

To demonstrate image quality, IVIM scans using the clinically optimal protocol (second iteration, Protocol C) for the highest and lowest b-values are shown in Figure 7.2, along with a post contrast T1-weighted anatomical image of the same slice. For higher b-value images, the signal drops off and SNR is more influential– but this is the 'monoexponential tail' and so is theoretically easier to fit. SNR needs to be good in the low b-value range so that perfusion effects can be teased out of the biexponential.

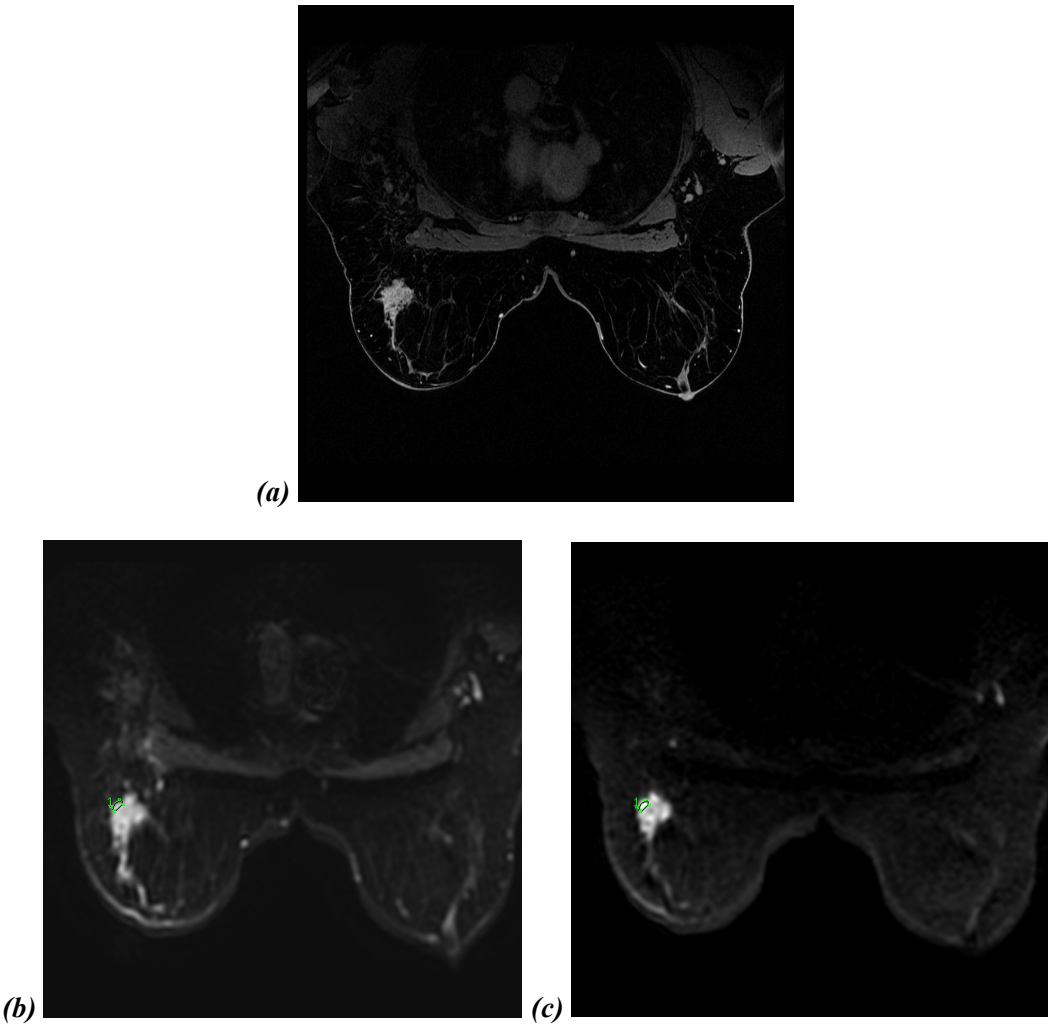

Figure 7.2: (a) Post contrast T1-weighted anatomical scan showing lesion in left breast and IVIM images (b) b = 0 s/mm^2 and (c) b = 1000 s/mm^2 with ROI placement in green. Example as in Figure 7.1: Age, 57 years; reason for scan, pre NAC staging; lesion type, IDC, grade 2, triple negative; treatment, NAC and breast conserving surgery (BCS). f = 0.15, D_m = 0.000541, D = 0.000647 , D* = 0.00475.

The average SNR was 22.

7.2.7. Results: Segmented Fit

Two example fits are shown in Figures 7.3 (standard IVIM model) and 7.4 (variation of IVIM model). On the top the monoexponential fit is shown. On the bottom, the segmented biexponential fit is shown. Residuals are shown below each fit in red.

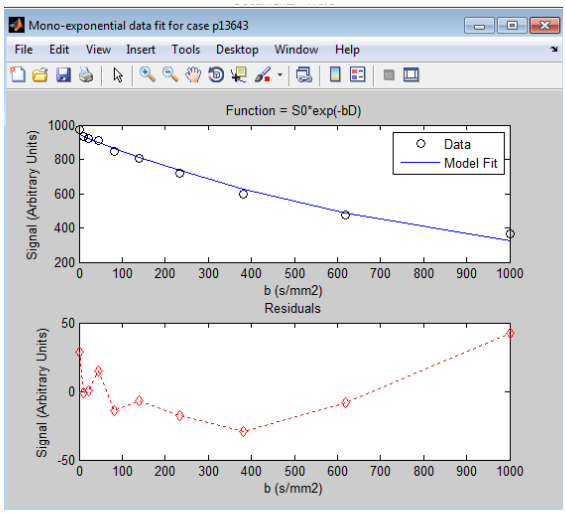

(a)

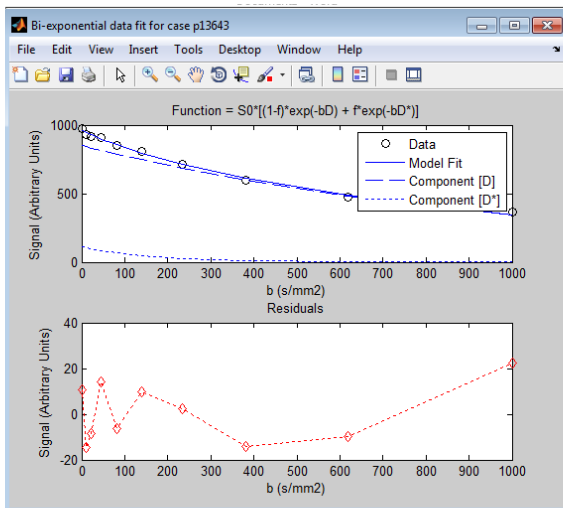

(b)

Figure 7.3: (a) Monoexponential and (b) biexponential fits of IVIM signal data with residuals of fit. Example as in Figures 7.1 and 7.2.

(a)

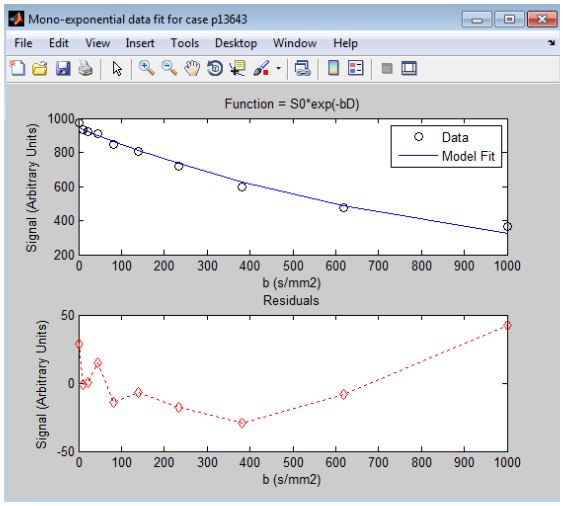

(b)

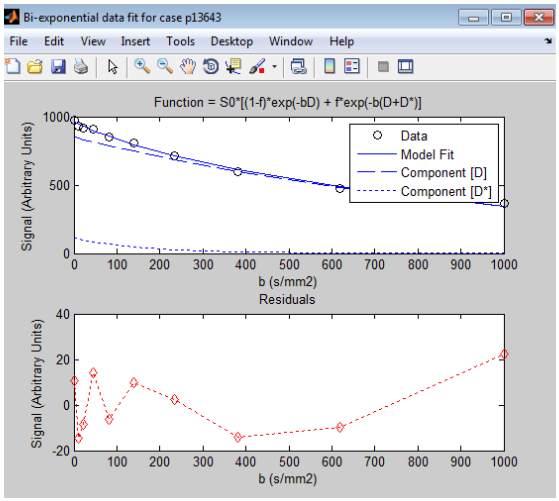

Figure 7.4: (a) Monoexponential and (b) biexponential fits of IVIM signal data with residuals of fit for variation of IVIM equation (D*+D). Example as in Figures 7.1 and 7.2.

Figure 7.5 shows an unsuccessful biexponential fit using the variation of the IVIM model.

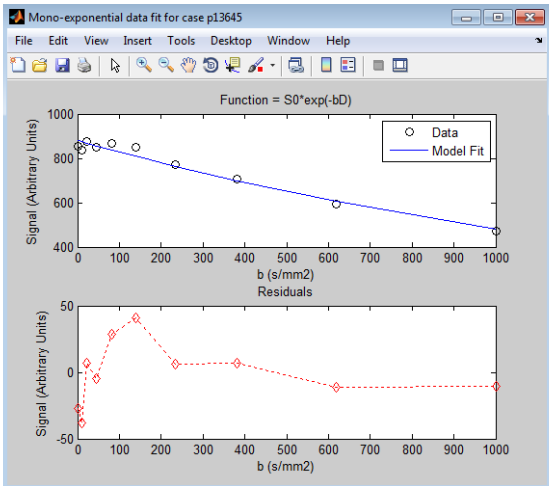

(a)

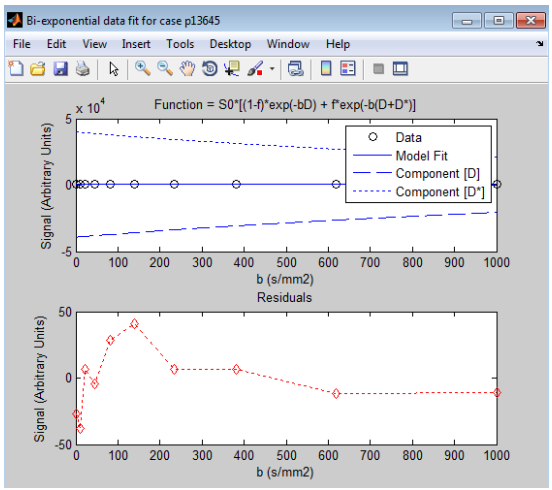

(b)

Figure 7.5: (a) Successful monoexponential fit and (b) unsuccessful biexponential fit of IVIM signal data with residuals of fit for variation of IVIM equation (D*+D).

Table 7.1 shows the calculated IVIM parameters (mean) for both IVIM equation variations with 3 different cut-offs for the standard IVIM equation.

Parameter	D_m mm^2/s	MSE	*D* mm^2/s	*f*	*D** mm^2/s	MSE
Standard equation (D*)						
Cut-off 1000 s/mm^2	0.000922	162	0.000829	0.0815	0.00613	126
Cut-off 619 s/mm^2	0.000922	393	0.000829	0.0815	0.00613	126
Cut-off 382 s/mm^2	0.00101	638	0.000930	0.0815	0.00613	312
Variation of IVIM equation (D*+D) (1 case did not fit)						
Cut-off 1000 s/mm^2	0.000922	175	0.000829	0.0815	0.00672	126

Table 7.1: IVIM parameters for both IVIM equation variations with 3 different cut-offs for calculating D using the standard IVIM equation.

7.2.8. Discussion

The aims of this pilot study were to assess the image quality of an optimised protocol (Protocol C) in malignant tissue, to make sure fitting using the segmented fit was suitable, and to evaluate different cut-offs for this segmented fit when calculating *D* monoexponentially (i.e. the fitting of *D* would be from 200 s/mm^2 to the cut-off).

All 19 lesions fitted successfully using the standard IVIM model but one failed for the variation of the IVIM model (Figure 7.5). This variation of the model was further tested here as it had not been investigated in this thesis in malignancy thus far. It was again shown to not be dissimilar to the standard model in terms of values calculated, but it did fail in one instance. This could be due to *D* and *D** being so close together that the fitting method set them both to be asymptotes in the second term as neither could be separated from the other. The results for *f*, *D* and *D** agree well with previously reported values in the literature. Considering Table 4.1 which summarises relevant breast IVIM literature; *D* is of the order of 0.001 to 0.0001 mm^2/s; *D** is of the order of 0.01 to 0.001 mm^2/s; and *f* ranges up to 30% (0.30). Table 7.1 shows that all IVIM parameters are physiologically acceptable for malignant lesions. D_m is larger than *D*, in general, and thus supports the IVIM model that *D* (or ADC) is an overestimation of

diffusion measured using diffusion-weighted imaging. This is obviously due to the perfusion effects, which can be measured at lower b-values, because of better SNR.

The segmented fit is being used to fit clinical data as that was shown to have the lowest MSE, and best repeatability, in Chapter 6. One concern, after further iterations of optimisations in Chapter 5 was that the final b-value was lower than 1000 s/mm^2. The fitting of D from 200 s/mm^2 to the cut-off was then going to be less. Protocol E produced a cut-off of 700 s/mm^2 and Protocols F a cut-off of 900 s/mm^2. Thus, the 3 final b-values in Protocol C were examined to see the effect of a lower cut-off. A low cut-off of 382 s/mm^2 increased D_m, and D. f and D* were left unchanged as expected. The MSE increased with the lowest cut-off, too. A cut-off of 619 s/mm^2 left calculated values unchanged when compared with a cut-off of 1000 s/mm^2, but did increase the MSE of D_m. The reason for the poor fit using 382 s/mm^2 is obviously because of there being less data points to fit and also because the range of data was not as large.

Clinically this protocol has proved useful thus far, especially after receiving feedback from clinicians, where visualising the lesion when contrast could not be given was made easier with multiple b-values and better image quality. No contrast was given in some cases because of problems such as breast implants, unable to cannulise, patient anxiety, or breast feeding.

7.3. Fourth Iteration of Optimisation (Protocol F): IVIM for Malignant Lesion Subtype Classification in Pre Neoadjuvant Chemotherapy Breast Cancer Patients

After the pilot study in breast cancer patients and further optimisation of the IVIM protocol leading to Protocol F, auspicious results were obtained that were worthy of further pursuit. The patient population was expanded to explore the use of IVIM in breast cancer imaging in more detail; by examining the diversity of the patient population and choosing a suitable clinical cohort to analyse; and by increasing the analysis to correlation of IVIM parameters with grade, histological subtype, hormonal status, and molecular subtype. This expanded study on IVIM in breast cancer follows the principal goal of trying to effectively develop and standardise IVIM as a diagnostic tool for clinical use.

Using IVIM to quantitatively identify tumour subtypes has the potential to add specificity to multiparameteric MRI exams, enable diagnosis through imaging, benefit therapy

making it tailored and earlier, and could even minimise the need for biopsies and pathological diagnosis. Heterogeneity, angiogenesis and cell proliferation are all tumour characteristics that could be correlated with the perfusion and diffusion IVIM parameters. These can classify, predict response to therapy and characterise aggressiveness of tumours (65, 66, 79, 113). MRI research in a clinical setting has now evolved from the need for just improved morphological imaging to quantitative imaging that can facilitate detection, diagnosis and monitoring.

The clinically optimised protocol generated from the fourth iteration of optimisation (Protocol F) was applied in pre neoadjuvant breast cancer patients to assess image quality, fitting of the data, presence of perfusion effects in normal breast parenchyma in the contralateral breast, and to calculate values for IVIM parameters *f, D,* and *D** to use as biomarkers to classify malignant tumours according to grade, hormonal status, histological subtype and molecular subtype.

7.3.1. Patient Cohort

Two-hundred and seven patients were scanned in this clinical study at the Centre of Magnetic Resonance Investigations, Hull Royal Infirmary from March 2015 – September 2015. MR safety screening forms were completed prior to imaging. The IVIM protocol was added to the standard of care breast MR exam for all breast cancer patients, at the request of the consultant radiologist who found the scan qualitatively useful in the first instance in place of standard DWI (See pilot study). IVIM as an adjunct to the multiparametric MR protocol already in place at Hull Royal Infirmary allowed standard ADC calculation carried out on DW-imaging plus the added benefits of better image quality, and more b-value images, in a similar scan time. IVIM parameters were not used in standard of care MR reporting. For analysis of this cohort in September 2015, unfortunately, the consultant radiologist was not available but an experienced breast MR researcher (and previously a radiographer) helped with acquiring data and depicted ROIs.

From this cohort of 207 patients, a sub-cohort for IVIM analysis was selected. Patients of interest received their MR scans prior to any breast cancer treatment (pre neoadjuvant chemotherapy (NAC), surgery or radiotherapy). Patients were therefore scanned for screening purposes, problem-solving or for pre-treatment planning. Patients were diagnosed with breast cancer through MR reporting by a radiologist, leading to a biopsy; stereotactic core biopsy,

US-guided fine needle aspiration (FNA), or MRI guided core biopsy. Final histopathology diagnosis was confirmed through histology and/or surgical specimen analysis.

Inclusion criteria comprised; invasive malignant breast cancer of any grade, type, and molecular subtype; and/or pre-treatment of any form.

Exclusion criteria comprised; metastatic disease; prior breast cancer treatment (NAC, surgery, radiotherapy prior to MR); and/or if tumour grading and/or pathology were not available (due to information held elsewhere outside of HEY NHS trust).

Exclusion criteria for normal tissue analysis were as above, and also; bilateral disease; mastectomy in contralateral breast; and/or little or no visible parenchyma on MR images.

After these criteria had been applied, 60 patients remained for analysis. Patients had a mean age of 52 years (range 31 - 79 years). Information on tumour grade, histological subtype, hormonal receptor status, molecular subtype, and subsequent treatment were collected for these 60 patients. Due to image artifacts, probably due to movement, 2 further patients were excluded. Fifty-eight patients were therefore analysed.

Tumour grade was classified as low grade (grades 1 and 2) or high grade (grade 3). There were low numbers of grade 1 tumours, so grades 1 & 2 were pragmatically grouped together and then compared to 3. The tumor histological subtype breakdown was as follows; ductal carcinoma in situ (DCIS); invasive lobular carcinoma (ILC); or invasive ductal carcinoma (IDC). The tumour molecular subtype was classified using hormonal receptor status as; Luminal A (ER+ and/or PR+, HER2-); Luminal B (ER+ and/or PR+, HER2+); triple negative or basal-like (ER-, PR-, HER2-); or HER2 type (ER-, PR-, HER2+). These classifications are outlined in Chapter 2 in more detail.

7.3.2. MRI Scans

Patients underwent a standard of care bilateral MRI breast examination on a 3.0 T MR750 scanner (GE Healthcare, Milwaukee, WI) using the body coil as a transmitter and an 8-channel breast receiver coil (GE Healthcare, Milwaukee, WI) with the substitution of a <5m IVIM series in place of standard DWI. IVIM images were acquired axially using diffusion-weighted single-shot echo planar imaging (EPI) with the following parameters: repetition time/echo time (TR/TE), 6366 *ms*/54.4 *ms*; field of view, 34x34cm; matrix, 128x128; slice thickness 4mm; slice spacing 1mm; 42 slices (variable with breast size if required); Bandwidth, ±250Hz

frequency direction, right to left; diffusion direction, 3 in 1; NEX, 4; bi-lateral shimming; scan duration 4 minutes 20 seconds (variable with breast size if needed up to 5 minutes); with water only excitation. Only one IVIM series was acquired per patient. The clinically optimal protocol (Protocol F) had the following 10 diffusion weightings, b = 0, 10, 24, 46, 71, 135, 221, 355, 567, 900 s/mm^2 sometimes with an extra b-value of 1000 s/mm^2, 1250 s/mm^2 or 1500 s/mm^2 depending on radiologist preference. This extra b-value was for visualising the lesion and was not included in IVIM analysis, but was used in computed-DWI analysis (see Chapter 9). Total scan time including volunteer positioning on the scanner bed was approximately 40 minutes in total.

7.3.3. ROIs and SNR

An experienced breast MR researcher kindly drew the regions of interest. Lesions were identified on a post-contrast T1-weighted anatomical image first, and then a region of interest was drawn on the most malignant part of the lesion (area of highest signal intensity/restricted ADC in lesion) as seen on DW-images. An ROI was also drawn over normal parenchyma in the contralateral breast. This produced signal values to fit as a function of the corresponding b-values in the IVIM protocol. The average size of the ROIs was 52 mm^2 for malignant lesions and 65 mm^2 for normal tissue. This was single slice analysis. Figure 7.6 shows an example of ROI placement, pink in the malignant lesion and green in normal tissue.

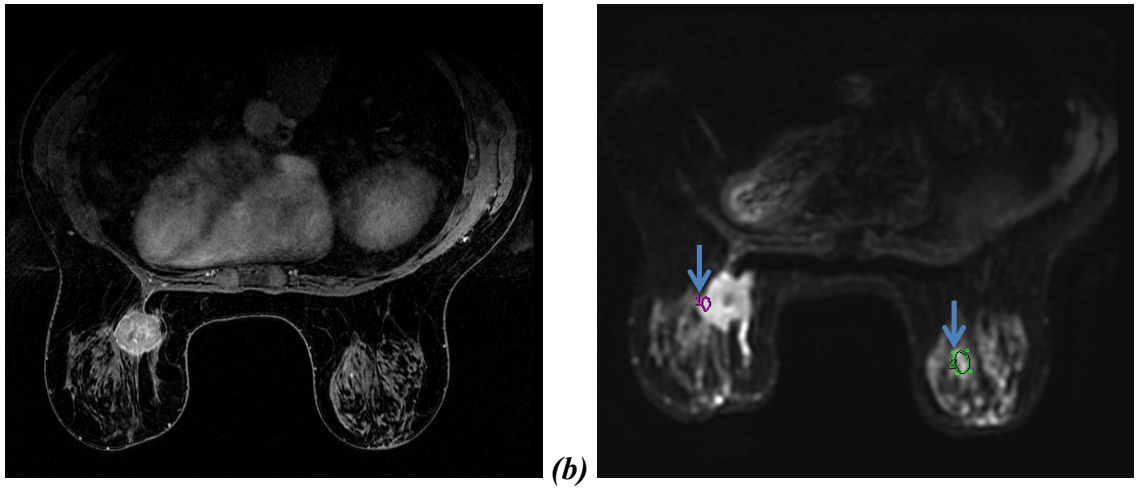

Figure 7.6: (a) Lesion in the left breast on a post-contrast T1-weighted image and (b) an IVIM image b = 900 s/mm^2 with an ROI in the most malignant region of the lesion (pink) and an ROI in the contralateral breast in normal parenchyma (green) indicated with blue arrows.

The SNR was calculated as in Section 7.2.3.

ROI analysis was used to ensure only malignant tissue or fibroglandular tissue was analysed (excluding necrosis, clips, etc.). Histogram analysis of the whole tumour (as used with ADC) is advantageous and would be the next step after confirming the utility of IVIM parameters using ROI analysis.

7.3.4. Fitting

All fitting was coded and computed in MATLAB (MathWorks, Massachusetts, USA). A segmented fit was applied as described in Section 6.2.4 (*iii*) using Method 5, Chapter 3. A cut-off to fit D monoexponentially was set as 200 s/mm^2. Constraints to disallow any parameter to be negative were coded, and f was constrained to be between 5% and 30% for initial estimates, as anything else is deemed physiologically impossible in the breast. Monoexponential diffusion (the ADC), D_m, was also calculated. The standard IVIM model was used.

7.3.5. Statistical Analysis

All malignant lesions were classified by histopathology and these results were used to group data for statistical analysis. Grade was classified as either low grade (1 and 2) or high grade (3 and 4). Lesion type was classified as IDC or ILC (No DCIS cases). Both ductal and lobular carcinomas were considered despite ILC representing only 10% of breast cancer cases as the

tumour microenvironment was hoping to be probed and exploring all options was cogitated important and novel in this instance. ER, PR and HER2 were scored from 0 to 8, with 0-2 being negative 3-8 being positive. The molecular subtype was determined as one of the 4 molecular subtypes from the ER, PR and HER2 scores; Luminal A, Luminal B, Triple Negative or HER2 type.

The purpose of this statistical analysis was to investigate possible correlations between the IVIM parameters, f, D, and D^*, the apparent diffusion coefficient, D_m, between types and subtypes of malignant breast tumours. Normal tissue values in the contralateral breast versus all malignant lesion values were also compared. SAMPL guidelines (114) were adhered to throughout statistical analysis.

Descriptive statistics were calculated using SPSS (IBM, New York, USA). The mean, lower and upper bounds of the 95% confidence internal, 5% trimmed mean, median, variance, standard deviation, minimum, maximum, range, interquartile range, skewness and kurtosis were reported for each breakdown of analysis and reported accordingly after normality tests.

First, an unpaired analysis was considered. Comparisons were made between malignant and normal tissue for each IVIM parameter and D_m. Then the grade, histological subtype, hormonal status (positive and negative) and molecular subtype for each IVIM parameter were compared for malignant lesions.

Next, a paired statistical analysis of the 30 lesions paired with normal tissue in the contralateral breast from the same patient is presented. Comparisons were made between malignant and normal tissue for each IVIM parameter and D_m. Then the grade, histological subtype and molecular subtype for each IVIM parameter were compared for both malignant lesions and normal tissue.

Unpaired results are in a way more powerful as in an ideal world you could then say, for example, that a D^* of above X mm^2/s indicates grade III. However, this is very rarely possible and these results demonstrate this (due to large overlaps on box-plots, for example). Paired results are potentially important. Paired tests enable comparison with that patients own normative values so for example if D* is 20% higher in suspicious area compared to normal tissue this is indicative of grade III. This approach is not as powerful as is relies on getting a good measure from normal tissue, which can be problematic as there is no accurate value of

normal tissue for comparison, but still has value. This is the rationale for doing both kinds of tests.

Test for normality were carious out on all 4 parameters for normal and malignant tissue. The Shapiro-Wilk test was chosen, not only for its robustness as compared to other normality tests, but also for its suitability for smaller sample sizes. The Komogoriv- Smirnov test was also computed and results agreed with the preferred normality test. The alpha value was taken to be 0.1. A higher p-value accepts the null hypothesis that the data is normally distributed (115).

If normally distributed, parametric statistics were reported as the mean ± standard deviation. The student's t-test was computed to determine if the results were statistically significant. An alpha level of 0.05 was used. The null hypothesis was that there was no difference between the groups.

If not normally distributed, or if subgroups were very small (as unfortunately so), then nonparametric tests were used. The median (range) was reported. To determine if results were statistically significant, the Mann-Whitney U test was computed. The null hypothesis was that two samples come from the same population against an alternative hypothesis, that a particular population tends to have larger values than the other. An alpha level of 0.05 was used.

The Kruskal-Wallis one-way analysis of variance (ANOVA) was used to compare the 4 molecular subtypes with each other, and to calculate the statistical significance. Again an alpha level of 0.05 was used.

Boxplots were used to depict results graphically.

7.3.6. Results: MRI scans

To demonstrate image quality, IVIM scans using the clinically optimal protocol (Protocol F) for the highest and lowest b-values are shown in Figure 7.7, along with a post contrast T1-weighted anatomical image of the same slice.

(a)

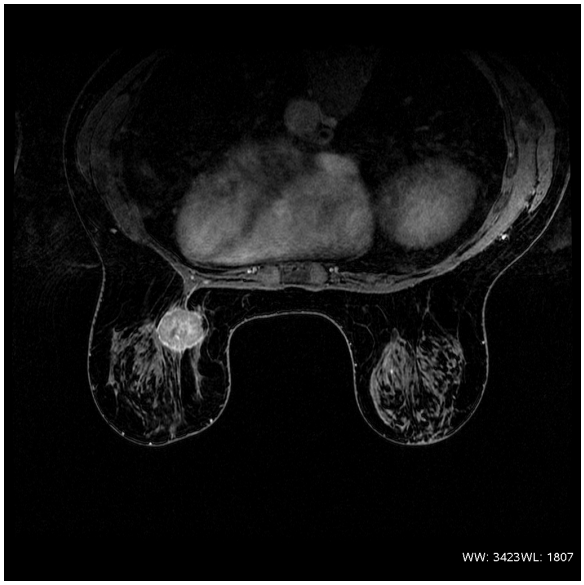

(b)

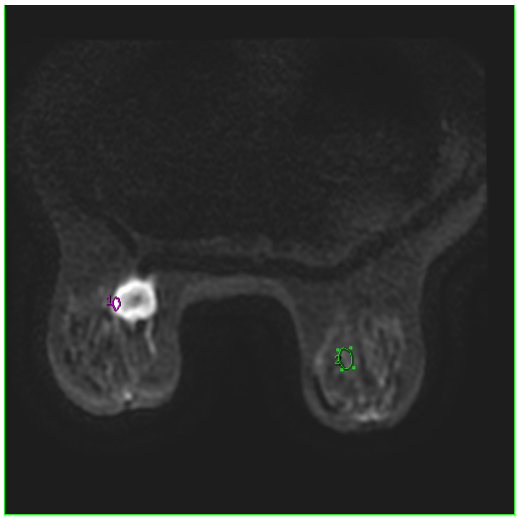

(c)

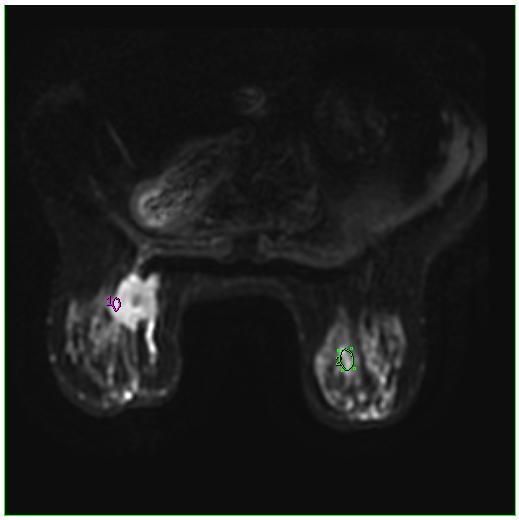

Figure 7.7: (a) Post contrast T1-weighted anatomical scan showing lesion in left breast (bright) and IVIM images (b) b = 0 s/mm^2 and (c) b = 900 s/mm^2 with ROIs in the malignant lesion (pink) and normal parenchyma (green). Age, 45 years; reason for scan, pre NAC staging; lesion type, IDC, grade 3, triple negative; treatment, NAC. f = 0.0661, D_m = 0.000613, D = 0.000552 , D* = 0.00549.

The average SNR was 23.

7.3.7. Results: Fitting

Example fits using the standard IVIM equation are shown in Figure 7.8. On the top the monoexponential fit is shown. On the bottom, the segmented biexponential fit is shown. Residuals are shown below each fit in red.

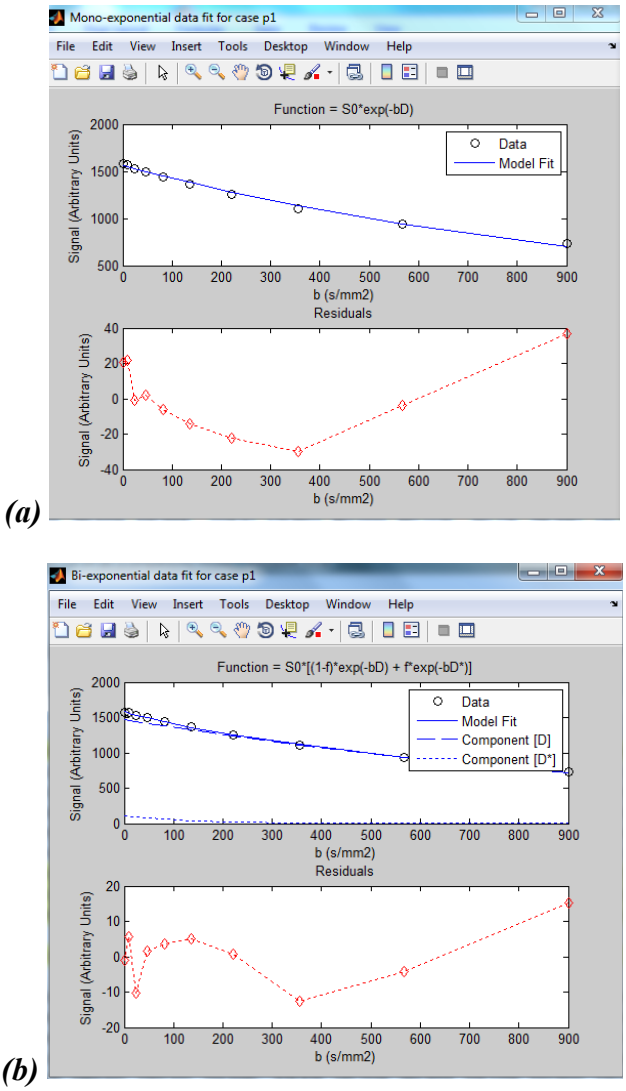

Figure 7.8: (a) Monoexponential and (b) biexponential fit of IVIM signal data with residuals of fit in red.

An example unsuccessful biexponential fit using the standard IVIM equation is shown in Figure 7.9.

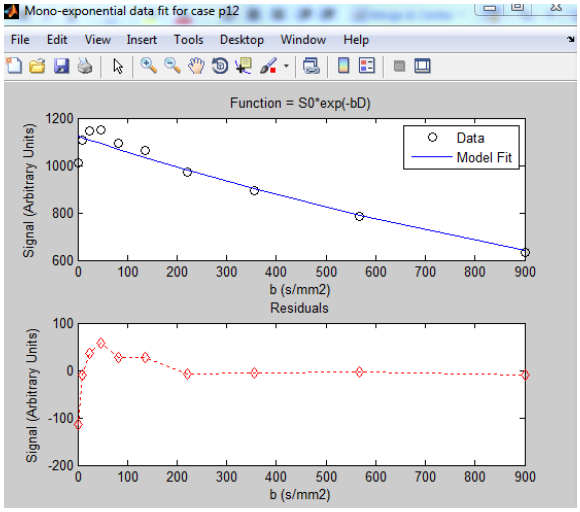

(a)

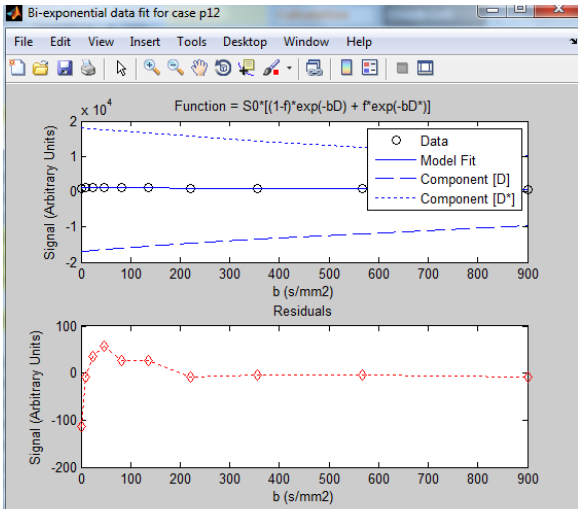

(b)

Figure 7.9: (a) Successful monoexponential and (b) unsuccessful biexponential fit of IVIM signal data with residuals of fit in red.

An example successful fit using the standard IVIM equation in normal tissue is shown in Figure 7.10. An example unsuccessful fit using the standard IVIM equation in normal tissue is shown in Figure 7.11.

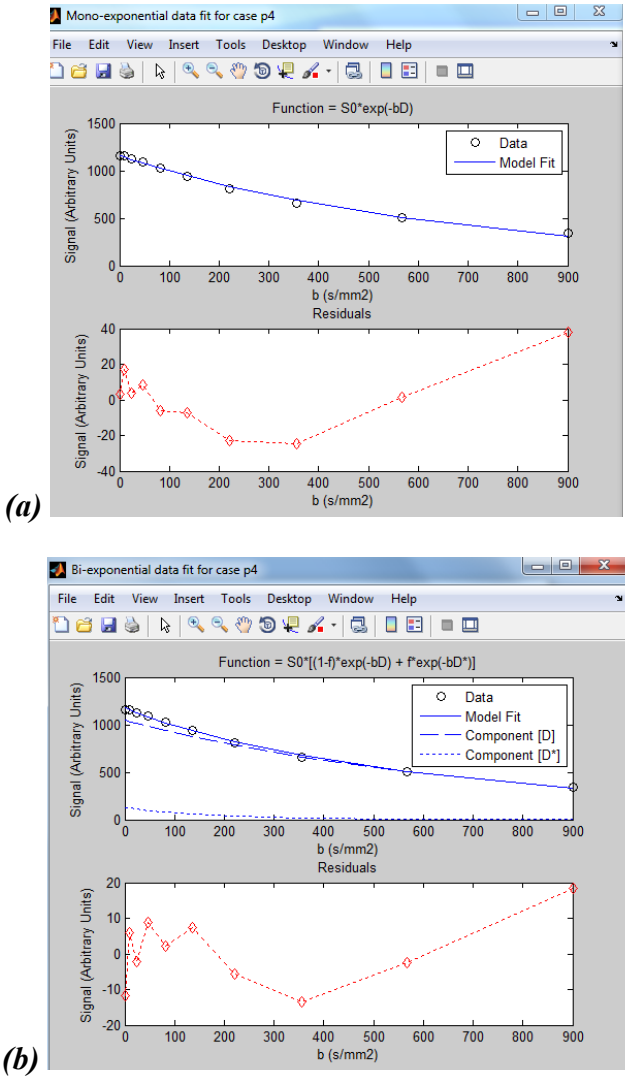

Figure 7.10: (a) Monoexponential and (b) biexponential fit of IVIM signal data in normal tissue with residuals of fit in red.

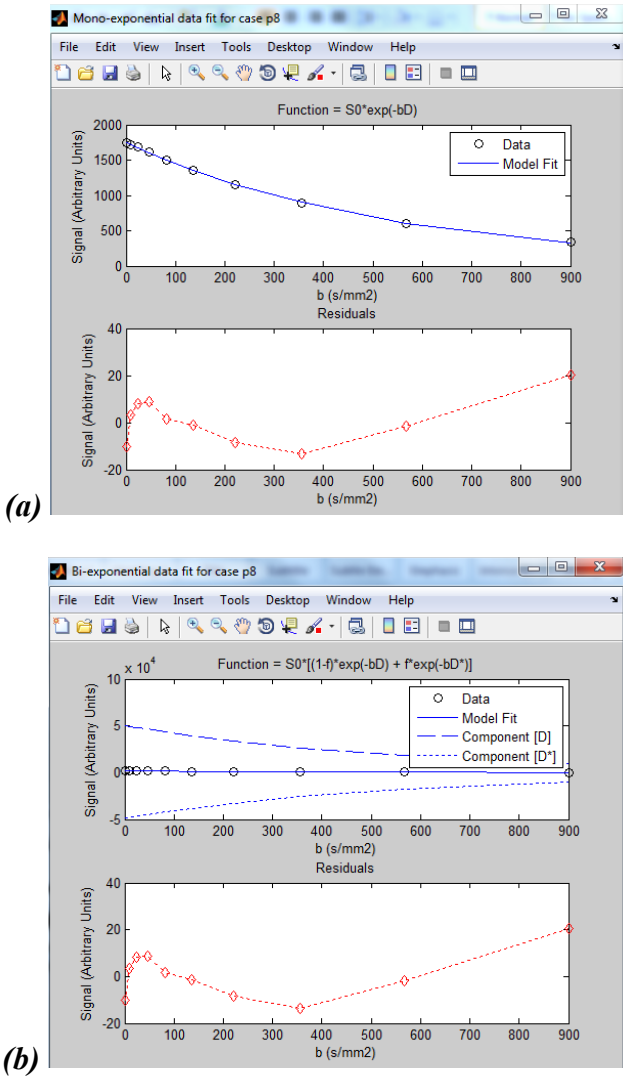

Figure 7.11: (a) Monoexponential and (b) unsuccessful biexponential fit of IVIM signal data in normal tissue with residuals of fit in red.

The grade, type, histological type and molecular subtype breakdowns are shown in Table 7.2. Among the 58 lesions assessed, 44 malignant cancers fitted successfully, equating to a success rate of 76%. Among the 44 contralateral breasts assessed, 42 contralateral breasts fitted successfully, this equates to a 95% success rate. Of these successful fits, 30 lesions paired up to normal tissue in the contralateral breast from the same patient. The average MSE of the fits for the 44 malignant lesions was 360 (mean). This was reported when the data was fitted using MATLAB as part of the program's analysis, but MSEs are not further used in in-depth statistical analysis as the fit was not of concern, rather the parameter values (mean ± SD, or the median (range)).

IDC is more common than ILC, and this is as much due to the difficulty in detecting ILCs especially in the early stages. This bias of IDC may affect results, with lower numbers for ILC meaning statistics would not be as strong for ILC.

Characteristic	**N**
Total number of malignant lesions	44 (30 paired)
Histological type	
IDC	33
ILC	11
Grade	
Low (1 and 2)	30
High (3)	14
Molecular subtype	
Luminal A	27
Luminal B	5
Triple negative	6
Basal-like	6
Normal tissue	42 (30 paired)

Table 7.2: Histological type and molecular subtype break down of malignant lesions from the 44 successful fits of the 3 IVIM parameters and D_m.

7.3.8. Unpaired Statistical Analysis

Here, a statistical analysis of ROIs from 44 lesions, and ROIs from normal tissue in 42 contralateral breasts is presented. Data is considered in an unpaired fashion. Comparisons were made between malignant and normal tissue for each IVIM parameter. Then the grade, histological subtype, hormonal status (positive versus negative) and molecular subtype for each IVIM parameter and D_m were compared for malignant lesions.

7.3.9. Results: Unpaired Test Comparison between Malignancy and Parenchyma

Table 7.3 shows the results for the Shapiro-Wilk normality test of all malignant lesions and all normal tissue ROIs.

Parameter	*p*-value (malignant tissue N = 44)	*p*-value (parenchyma N = 42)
D_m	0.004	0.000
D	0.000	0.604 *
f	0.123 *	0.304 *
D^*	0.049	0.000

Table 7.3: Results of normality tests (Shapiro-Wilk) for the 44 malignant lesions and 42 normal tissue ROIs data. * = Normally distributed.

Table 7.3 shows that D_m, D and D^* need to be compared using non-parametric tests and that f can be compared using a parametric test.

Table 7.4 shows the average IVIM parameters and D_m for malignant tissue and parenchyma with p-value from the corresponding parametric or non-parametric test for significance.

Parameter	Malignant tissue (N = 44)	Parenchyma (N = 42)	*p*-value
D_m	0.000902 (0.00107)	0.00152 (0.00119)	0.000 †
D	0.000811 (0.00115)	0.00134 (0.00126)	0.000 †
f	0.0727 ± 0.0378	0.0988 ± 0.0483	0.004 †
D^*	0.00736 (0.0177)	0.00738 (0.0603)	0.557

Table 7.4: IVIM parameters and D_m for malignant and normal tissue. † = Statistically significant.

Figure 7.12 shows box-plots for all four parameters, demonstrating significant differences (but large overlap) for D_m, D, and f. No significant difference for D^*.

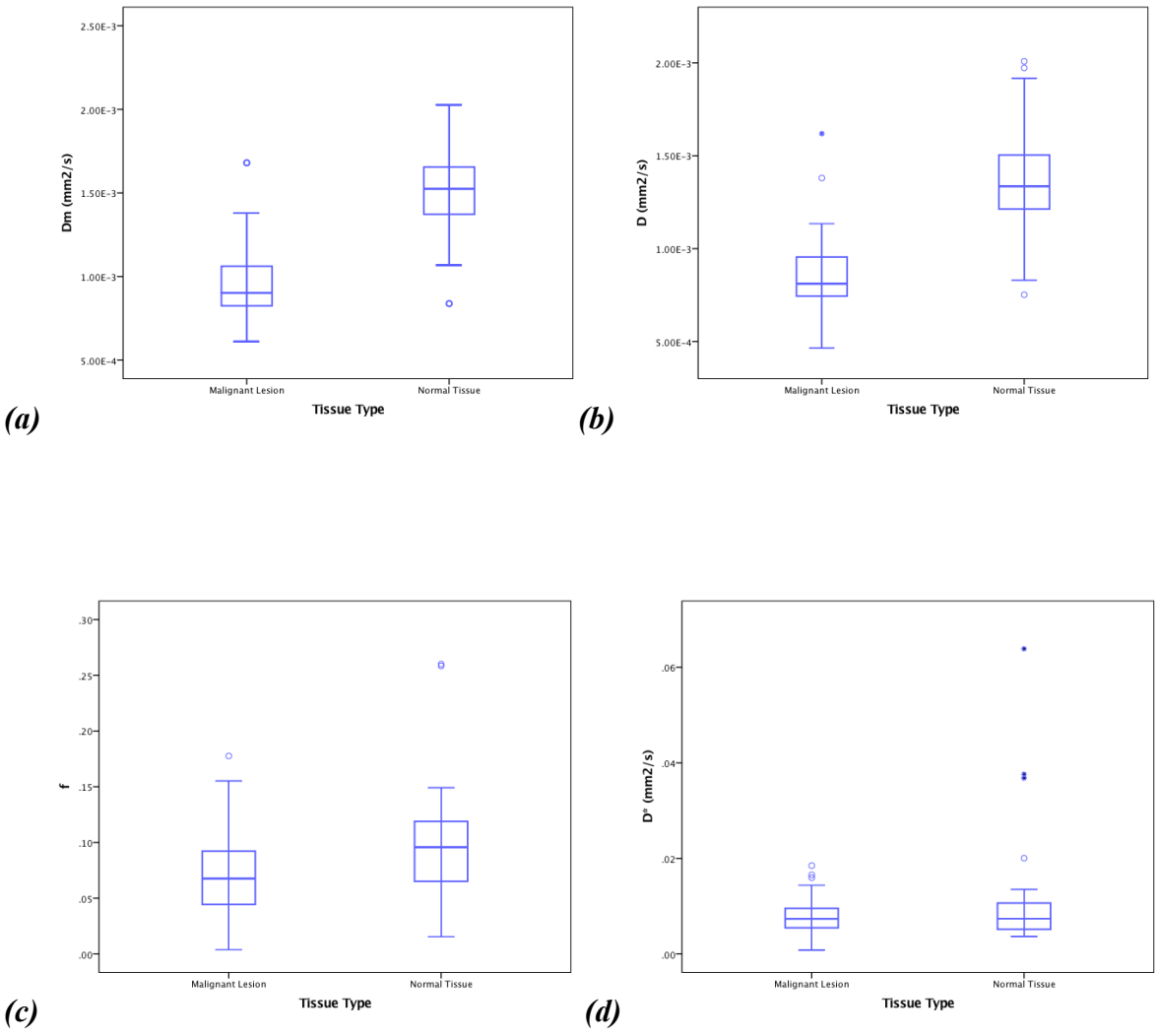

Figure 7.12: Boxplots for comparison of malignant lesion and normal tissue for all four parameters. (a) D_m, (b) D, (c) f, and (d) D*.

7.3.10. Results: Unpaired Test Comparisons between Types and Subtypes

There is always at least one group with low numbers (i.e. only 14 high grade lesions) so this is justification for using non-parametric tests for all of the following subtype comparisons and therefore there is no need to include Shapiro-Wilk tests for normal distribution.

7.3.11. Low Grade versus High Grade

Table 7.5 shows the median (range) for all four parameters for low grade and high grade.

Parameter	Malignant tissue (Low Grade, N = 30)	Malignant tissue (High Grade, N = 14)	*p*-value
D_m	0.000916 (0.000768)	0.000864 (0.00101)	0.480
D	0.000834 (0.000916)	0.000780 (0.000992)	0.226
f	0.0676 (0.174)	0.0686 (0.123)	0.743
D^*	0.00691 (0.0151)	0.00934 (0.0152)	0.027 †

Table 7.5: IVIM parameters and D_m for low grade = 1 and 2, and high grade = 3. † = Statistically significant.

Figures 7.13 and 7.14 are box-plots showing D_m as it is not significant, and D^* because it is significant.

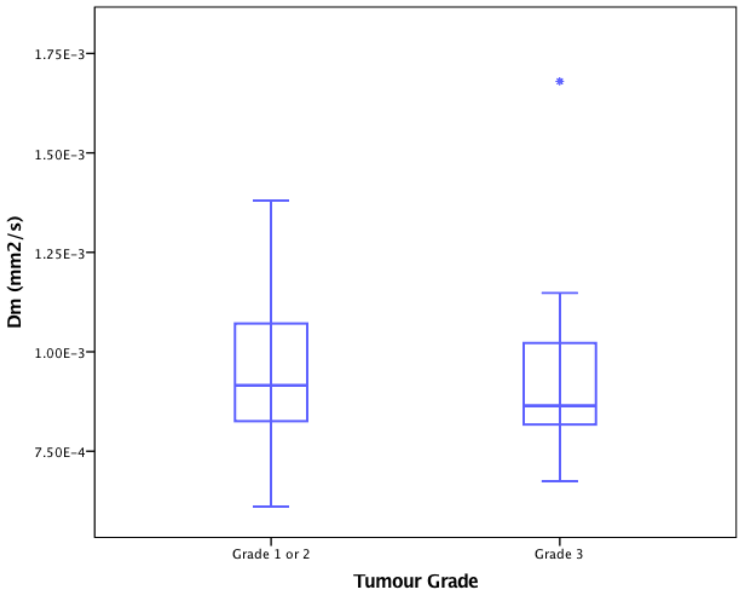

Figure 7.13: Boxplot for comparison of low grade and high grade for D_m.

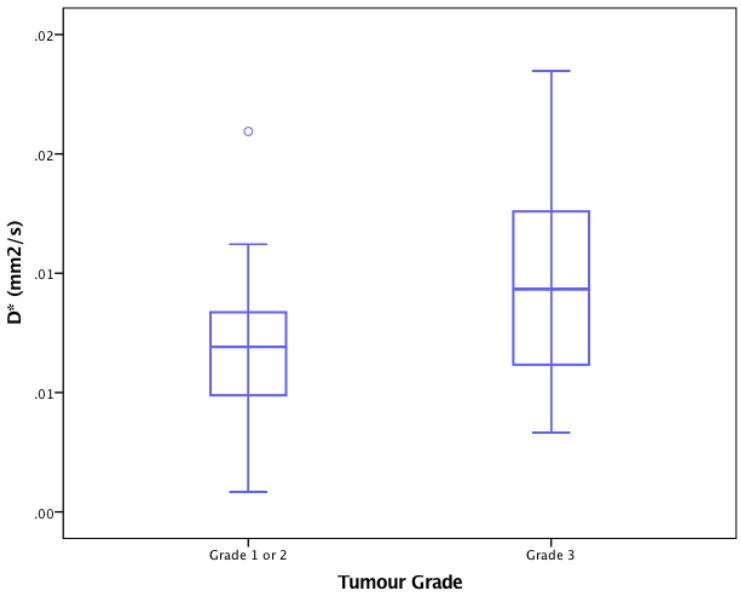

Figure 7.14: Boxplot for comparison of low grade and high grade for D*.

Figure 7.15 displays IVIM images for an example low grade lesion, in comparison to Figure 7.16, an example high grade lesion, with values of the four parameters in the figure legend. A significant result for *D** means the differences between grade in this parameter may be assumed to be true.

(a)

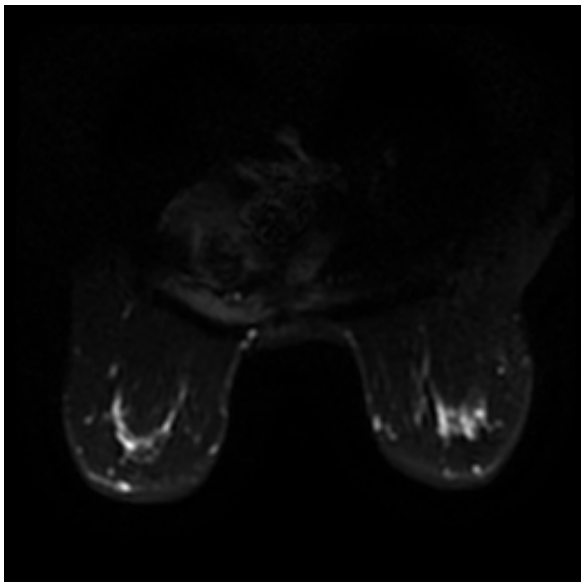

(b)

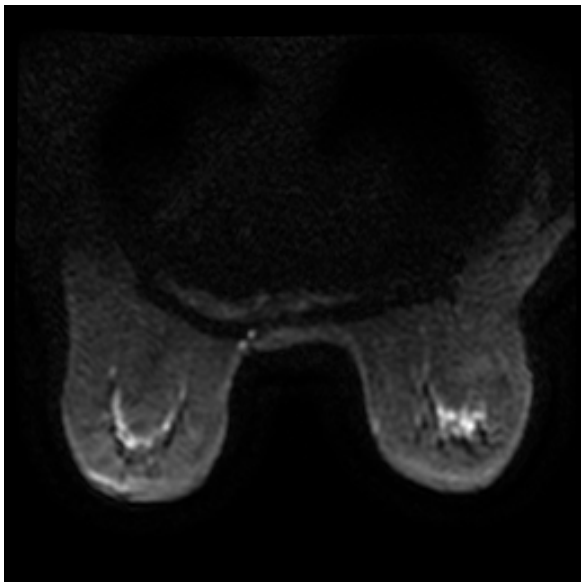

Figure 7.15: IVIM images (a) b = 0 s/mm^2 and (b) b = 900 s/mm^2. 54 years, lesion in right breast, grade 1 (low), ILC, ER/PR +ive, HER2 –ive. f = 0.0899, D_m = 0.00117, D = 0.00103 , D* = 0.00721.

(a)

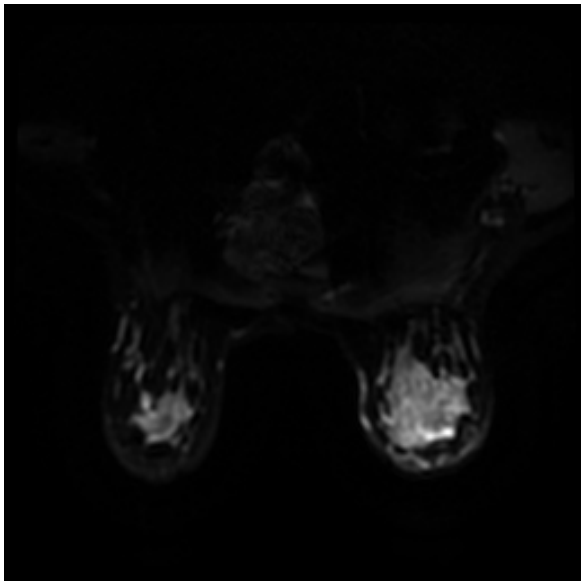

(b)

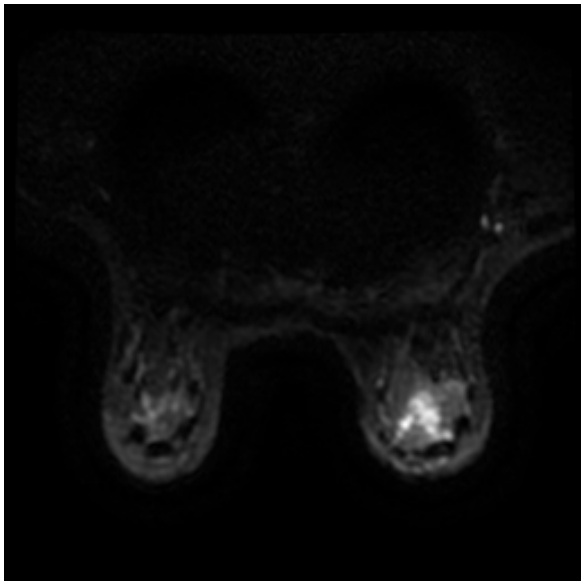

Figure 7.16: IVIM images (a) b = 0 s/mm^2 and (b) b = 900 s/mm^2. 41 years, lesion in right breast, grade 3 (high), ILC, triple negative. f = 0.0656, D_m = 0.000846, D = 0.000752, D* = 0.00866.

7.3.12. Invasive Ductal Carcinoma versus Invasive Lobular Carcinoma

Table 7.6 shows the median (range) for all four parameters for IDC in comparison to ILC.

Parameter	Malignant tissue (IDC, N = 33)	Malignant tissue (ILC, N = 11)	*p*-value
D_m	0.000893 (0.00107)	0.000978 (0.000662)	0.041†
D	0.000825 (0.00105)	0.000798 (0.000916)	0.957
f	0.06503 (0.121)	0.0899 (0.174)	0.187
D^*	0.00740 (0.0177)	0.00678 (0.0112)	0.831

Table 7.6: IVIM parameters and D_m for IDC and ILC. † = Statistically significant.

Figures 7.17 and 7.18 are box-plots showing D_m as it is significant, and D^* because it is not significant and thus there is no improvement with biexponential fitting in this tumour type cohort.

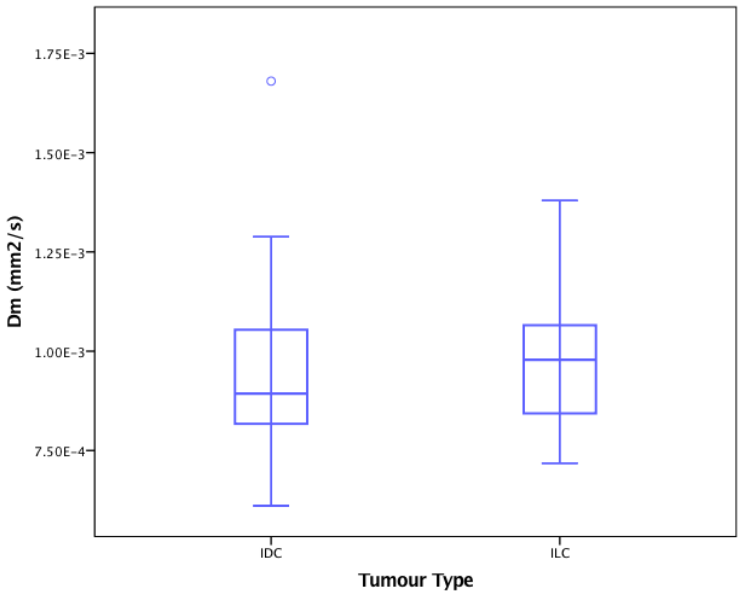

Figure 7.17: Boxplot for comparison of tumour type for D_m.

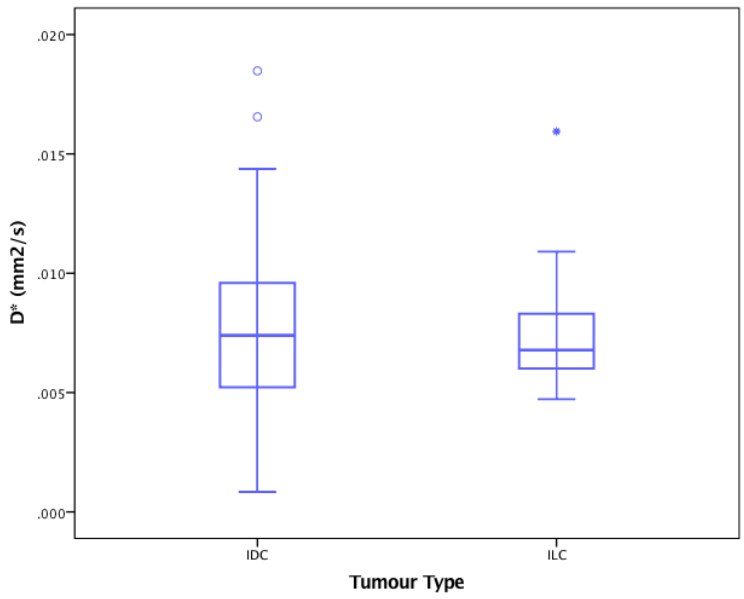

Figure 7.18: Boxplot for comparison of tumour type for D^*.

7.3.13. Comparison of Molecular Subtypes

Tables 7.7-9 show positive versus negative status for ER, PR and HER2 test results. These have been reported in this way using non-optimised IVIM protocols (79). Molecular sub-typing is then compared in Table 7.10 using the Kruskal-Wallis ANOVA.

Parameter	ER+ (N = 32)	ER- (N = 12)	*p*-value
D_m	0.000896 (0.00107)	0.000947 (0.000476)	0.612
D	0.000811 (0.00115)	0.000819 (0.000345)	0.785
f	0.0664 (0.174)	0.0676 (0.0998)	0.845
D^*	0.00653 (0.0177)	0.00872 (0.00916)	0.084

Table 7.7: IVIM parameters and D_m for ER status. † = Statistically significant.

Parameter	PR+ (N = 27)	PR- (N = 17)	*p*-value
D_m	0.000893 (0.00107)	0.000939 (0.000475)	0.638
D	0.000798 (0.00115)	0.000843 (0.000345)	0.673
f	0.0678 (0.174)	0.0675 (0.0998)	0.990
*D**	0.00627 (0.0177)	0.00866 (0.00931)	0.114

Table 7.8: IVIM parameters and D_m for PR status. † = Statistically significant.

Parameter	HER2+ (N = 11)	HER2- (N = 33)	*p*-value
D_m	0.000851 (0.000581)	0.000905 (0.00101)	0.689
D	0.000796 (0.00049817)	0.000825 (0.00115)	0.769
f	0.0624 (0.10206937)	0.0678 (0.174)	0.487
*D**	0.00738 (0.0124)	0.00721 (0.0177)	0.979

Table 7.9: IVIM parameters and D_m for HER2 status. † = Statistically significant.

Box plots are not shown for ER, PR or HER2 status as no significant results were found.

Parameter	Luminal A (N = 27)	Luminal B (N = 5)	TNEG (N = 6)	HER2 (N = 6)	p-value
D_m	0.000905 (0.00100)	0.000844 (0.000581)	0.000911 (0.000476)	0.000989 (0.000391)	0.704
D	0.000824 (0.00115)	0.000757 (0.000498)	0.000810 (0.000345)	.000851 (0.000278)	0.893
f	0.0720 (0.174)	0.0624 (0.102)	0.0675 (0.077)	0.0741 (0.0849)	0.566
*D**	0.00627 (0.0177)	0.00734 (0.00763)	0.00872 (0.00555)	0.00828 (0.00916)	0.329

Table 7.10: IVIM parameters and D_m for the four 4 molecular subtypes.* † = *Statistically significant.

Figures 7.19 and 7.20 show 2 box-plots as examples (D_m and D) for these 4 molecular subtypes showing no improvement in discriminating subtype using bi-exponential fitting.

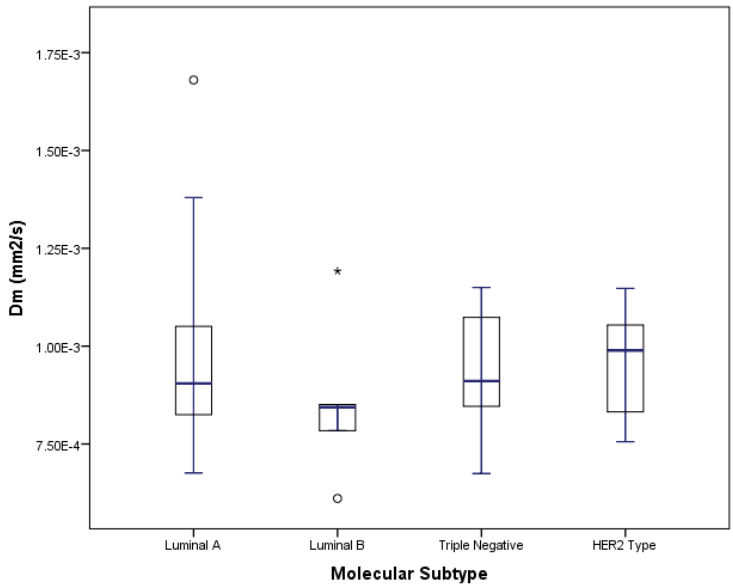

Figure 7.19: Boxplot for comparison of molecular subtypes for D_m.

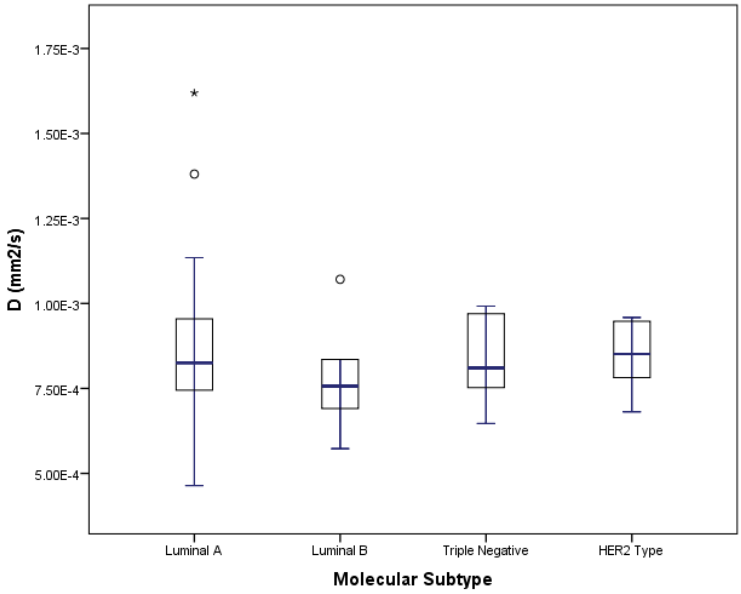

Figure 7.20: Boxplot for comparison of molecular subtypes for D.

7.3.14. Discussion: Unpaired Test Comparisons

For unpaired consideration, there were 44 malignant lesion regions of interest and 42 normal regions of interest in the contralateral breast analysed. This analysis firstly looked at malignancy versus normal tissue values. These normal tissue values can also be compared to the same protocol (Protocol F) used in scanning healthy volunteers in Chapter 6, Table 6.7.

The cohort was then divided into grade, histological type, immunohistochemistry status, and molecular subtype; and statistics were computed to compare the groups within these divisions respectively.

This unpaired analysis shows that there is a significant difference between malignant and normal tissue for D_m, D and f. Non-optimised protocols have shown this significant difference, also (78, 81, 83, 84). Referring to Table 7.4, D_m and D both show restricted diffusion in the malignant tissue. This makes physiological sense as the proliferation rate is higher in cancers and thus the cells are bunched together in a random manner, not allowing water molecules to flow as they usually would via the laws of Brownian motion. f shows a 2.61% decrease in micro capillary perfusion fraction, which is thought to correlate with blood volume within the tumour. It has been suggested that f should increase in malignancy so the apparent reduction noted in these results is surprising. Less than 10% for f is more than acceptable in breast as it is not a highly perfused anatomical structure. Figure 7.12 shows boxplots for the four parameters supporting and visualising these findings. D^* shows no significant difference; this is a difficult parameter to fit and has much variation in previous studies. The reason for no significant difference between tumour and parenchyma may at least be partially attributed to the difficulty in fitting this parameter well. This is reflected in the large range of values compared to the other parameters (See Table 7.4). There is contradicting evidence in the literature that a) a perfusion effect exists in parenchyma, and that b) the IVIM model is complete to calculate such perfusion effects. Outliers appear to be far out in this data set, however the numbers dealt with are very small and so any relative difference is quite large. This does not necessarily mean the results are anomalies but rather extremes. Reasons for such extremes could be noise on the MR scans, ROI placement, fitting methods used and the robustness of these. Therefore because of the nature of outliers they are not to be excluded. In malignancy, low D_m, D, and D^* would be expected due to restricted diffusion and blood flow due to proliferation, but high f due to increased angiogenesis. Even though f is not higher than in normal tissue in this case, this does not mean that this is not true in the case of breast cancer in a stand-alone analysis rather than in comparison to normal tissue. It could be that the normal tissue looked at here is variable and the malignancy value for f is acceptable. Liu found a small but non-negligible f whilst Baron and Tamura did not (76, 77, 86).

The IVIM parameters calculated in normal tissue in Table 7.4 can be compared to those in healthy volunteers in Chapter 6 using the same protocol (Table 6.7). f is lower in healthy volunteers than in cancer patients, and D^* is higher. D and D_m are more comparable between healthy volunteers and the normal tissue in cancer patients. The repeatability of these diffusion parameters were found to be much better, too. The repeatability of f and D^* actually show that values from both normal tissue cohorts lie within the calculated ranges. Therefore, these findings are not surprising.

Comparing low grade versus high grade gave one significant result – unexpectedly D^*. Figures 7.13 and 7.14 are box plots showing D_{m} as it is not significant, and D^* because it is significant. This is a notable result as it shows IVIM may have added value. D^* is higher in high grade tumours than in low grade tumours. D^* is considered proportional to the mean capillary segment length and average blood velocity. For capillaries to be longer and blood to travel faster in higher grade tumours, this could be interpreted to some extent that the tumour has more nutrients to grow and thus can mutate and become more heterogeneous and thus higher grade. It is acknowledged that the fact that D* cannot separate benign and malignant lesions but appears to separate grades of malignancy may be a spurious result.

For invasive ductal carcinoma versus invasive lobular carcinoma, the monoexponential diffusion, D_m, has a significant difference with invasive lobular carcinoma having a higher value. When looking at the Boxplots in Figure 7.17 and 7.18 it can be seen that D^* has complete overlap whilst D_m is slightly higher for ILC. Less restricted diffusion means the cells may not be packed as close together or the rate of proliferation is not as high. This would be sensible as invasive ductal carcinoma is more mass like and would restrict diffusion more, while the histology of many invasive lobular cancers are more organised and less clumped together. Aggressive cancers with low cell density have been reported. An inverse correlation between the cellularity and the ADC has been reported (7,15,17). This is thought to be due to changes in cellularity, fluid viscosity and cell permeability. The proliferation of cells generally reduces the extracellular space. Because ADC is an overestimation, due to contributions of signal from micro capillary networks, it is thought that IVIM parameters may give more insight into this tumour microenvironment, however the IVIM parameters were not significant in this instance.

The comparisons of receptor status for immunohistochemical tests gave no significant results. Cho *et al* (79) did show significant differences for a cohort of 50 patients, comparing negative or positive receptor status of ER, PR and HER2. However, the significant differences were not found in the mean or median (as are reported here), but through histogram analysis calculating the minimum, maximum, standard deviation, kurtosis and skewness of some IVIM parameters. In this study, these histogram parameters were not evaluated, as the starting point of ROI analysis and taking a simple average (mean or median) was thought to be principal. Comparison of the 4 molecular subtypes did not yield significant results but this is not surprising as the cohort numbers were very small for these subgroups. It can be noted that for triple negative, the perfusion fraction is lower than all other subtypes, and this is the subtype that is reported to respond the least well to therapy.

It cannot be said that monoexponential analysis has prevailed over biexponential, in this analysis. Mixes of both sets of parameters have shown significant results. This protocol implements b-values very near to the reported best 2 values for ADC calculation in breast cancer; 50 and 850 s/mm^2 (44), and so it would be expected that the monoexponential diffusion would perform very well if not better than IVIM paramaters. That was not the case.

Better estimation of vascular diffusion effects can be made when sampling lower b-values and even though this protocol is optimised, the figure of merit that sampled this protocol gave equal value to each of the three IVIM parameters. Perhaps weighting perfusion parameters more would mean they were sampled better as they are clearly difficult to calculate. Fitting only ever failed because of the perfusion parameters, not monoexponential diffusion.

Non-Gaussian diffusion effects at higher b-values can affect quantification of both IVIM paramaters and the monoexponential diffusion. It has been reported that f is actually influenced by higher b values if there is non-Gaussian diffusion present. In prostate, f was significantly increased in tumours with the final b-value below 750 s/mm^2, and was indistinguishable from normal tissue in cancer patients at higher cut offs (116). Tamura *et al* (77) concluded f was not significant in the differentiation between benign and malignant disease because of the high cut off of 3500 s/mm^2 used. f can also be influenced by T2 contributions. A shortened TE may result in lower f values.

ROI analysis has been carried out by taking the average signal value of that region, however this does not consider the whole tumour slice and results may be skewed upon ROI placement. ROIs excluded tumour edges, which have also been shown to skew averages. The ROI method was done to minimise partial volume and motion artefacts, also. A full histogram and volumetric analysis would definitely have the potential to give better insight into the tumour microenvironment but this also has its disadvantages in skewing values of the IVIM parameters unless filtering or constraints are used. The perfusion fraction may be lower from this analysis as the tumour periphery is usually more vascularised.

This analysis supports the hypothesis that diffusion and perfusion via IVIM can provide information to help assess and characterise the tumour microenvironment.

7.3.15. Statistical Analysis: Paired Test Comparisons

Here, a statistical analysis of 30 lesions paired with normal tissue in the contralateral breast from the same patient is presented. Comparisons were made between malignant and normal tissue for each IVIM parameter.

7.3.16. Results: Paired Test Comparison between Malignancy and Parenchyma (in the Contralateral Breast)

This paired analysis is not as powerful as unpaired analysis as it relies on getting a good measure from normal tissue and there is no reference true value to compare to for accuracy. This is problematic but still has value. Therefore, there is rationale for doing both kinds of tests on this data.

Parameter	*p*-value (malignant tissue)	*p*-value (parenchyma)
D_m	0.980 *	0.208 *
D	0.870 *	0.262 *
f	0.137	0.003
*D**	0.000	0.000

Table 7.11: Results of normality tests (Shapiro-Wilk) for the 30 paired data sets of malignant lesions and normal tissue. * = Normally distributed.

Table 7.11 shows that D_m, and D can be compared using a parametric test (t-test) whilst f and D^* have to be analysed using a non-parametric test. Table 7.12 shows the IVIM parameters for malignant and normal paired data.

Parameter	Malignant tissue	Parenchyma	p-value
D_m	0.000937 ±0.000162	0.001521 ±0.000275	0.045 †
D	0.000839 ±0.000140	0.001385 ±0.000289	0.000 †
f	0.0676 (0.136)	0.0937 (0.243)	0.000 †
D^*	0.00770 (0.0807)	0.00841 (0.0603)	0.405

Table 7.12: IVIM parameters and D_m for malignant and normal tissue, N = 30.* † = *Statistically significant.

Figure 7.21 shows the boxplots for all four IVIM parameters. D_m, D and f are statistically significant.

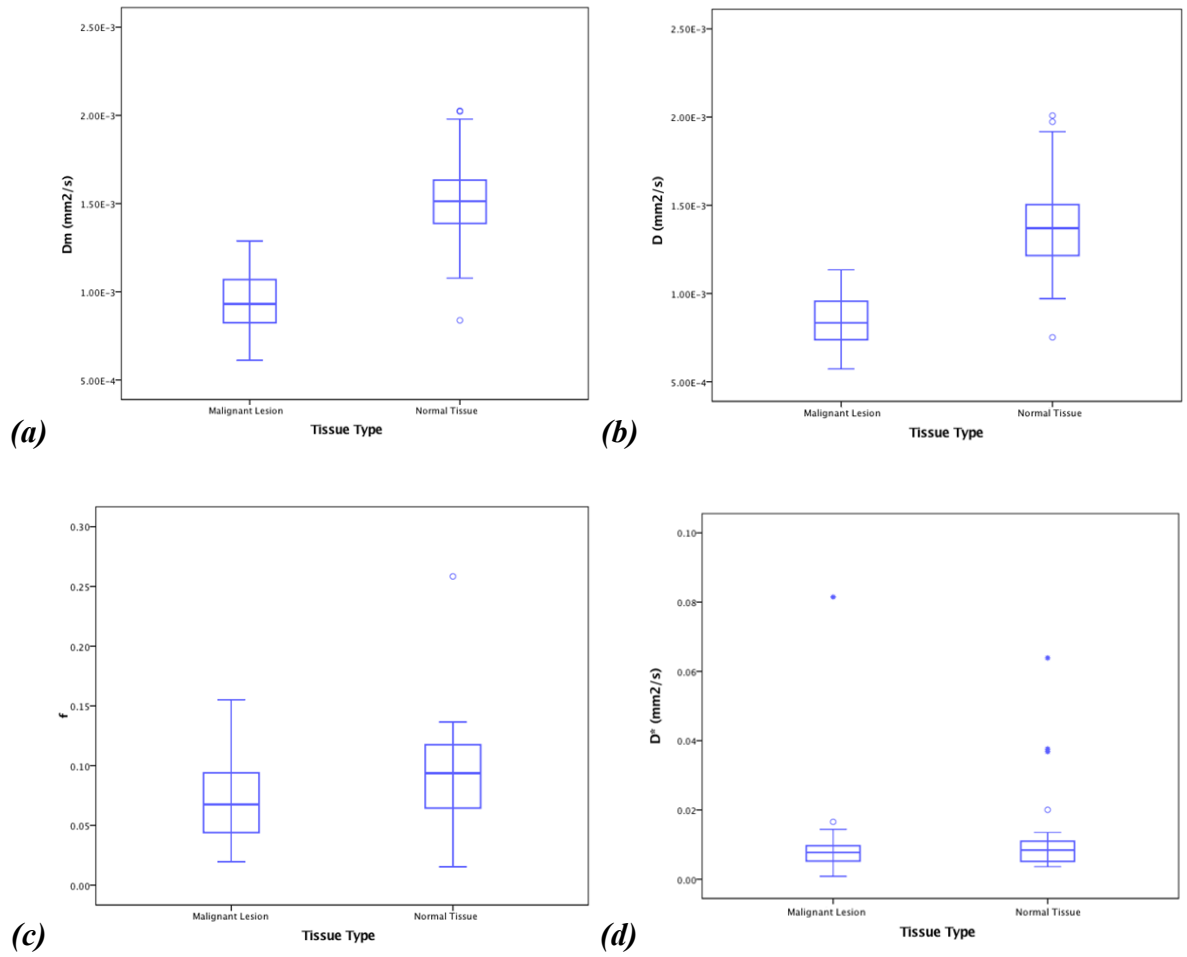

Figure 7.21: Boxplots for paired comparison of malignant lesion and normal tissue for all four parameters. (a) D_m, (b) D, (c) f, and (d) D*.

7.3.17. Discussion: Paired Test Comparisons

Paired tests were carried out to see if these supported or contrasted the unpaired tests, as much overlap between histological types and molecular subtypes was found, particularly due to small cohorts and other factors outlined in the unpaired discussion. One factor that can be addressed with paired tests is that each patients biology is different to start with and thus normalising these results with the contralateral breast may bring about undiscovered findings.

Lesions were clearly differentiated from normal fibroglandular tissue except for with *D**, echoing the unpaired test comparison.

A paired comparison between histological types and molecular subtypes was not reported, as these would not be valid when comparing differing types and subtypes with each other between different patients.

Paired tests at least supported findings from unpaired analysis.

7.4. Clinical Studies: Overall Conclusions

The clinical studies in this chapter, in pre neoadjuvant breast cancer patients, show the feasibility to quantify malignancy and parenchymal properties using biexponential IVIM and monoexponential diffusion analysis of the breast. IVIM MRI can be used as a possible biomarker of cellularity and proliferation (D), vascular blood perfusion fraction (f), and micro capillary blood velocity (D^*).

A pilot cohort of patients with malignant lesions (pre treatment but any type) was analysed and proved the image quality and utility of calculating parameters using the segmented fitting method in a clinical setting had potential.

A full clinical study was then implemented. This included the analysis of normal tissue in the contralateral breast. For unpaired consideration, there were 44 malignant lesion regions of interest and 42 normal regions of interest in the contralateral breast analysed. For paired consideration there were 30 pairs. This analysis firstly looked at malignancy versus normal tissue values. These normal tissue values were compared to the same protocol (Protocol F) used in scanning healthy volunteers in Chapter 6, Table 6.7. Then the cohort was divided into grade, histological type, immunohistochemistry status, and molecular subtype; and statistics were computed to compare the groups within these divisions respectively and to find correlations of parameters with these divisions.

A patient population was chosen for the main clinical study, consisting of various histological types and molecular subtypes. Unfortunately, numbers were not large at 58 patients after exclusions, but this is not the smallest IVIM cohort in the literature and so was deemed worthy of pursuit. However, molecular subtype groups were as low as N = 5 and that is not a large enough cohort to assume a significant or insignificant result is true. Thus, an increase in patient numbers for each subtype is warranted. This expanded study on IVIM in breast cancer follows the principal objective of trying to successfully develop and standardise IVIM as a diagnostic tool for clinical use.

Examining Figure 7.7, it can be seen that the IVIM images are of good quality. Almost all morphology can be seen, including the tumour demonstrating restricted diffusion and thus low signal attenuation.

Segmented fitting was implemented, which was deemed the most robust and precise method of calculating IVIM parameters from Chapter 6. Among the 58 lesions assessed, 44 malignant cancers fitted successfully, equating to a success rate of 76%. Among the 44 contralateral breasts assessed, 42 contralateral breasts fitted successfully, this equates to a 95% success rate. This was using the standard IVIM model. The lower rate of fitting in malignancy was unexpected – in healthy volunteers in Chapter 6 there were almost no unsuccessful fits, supported by the 95% fitting rate in normal tissue in the contralateral breast. One reason for this is that the fitting method, the non-linear least squares algorithm, may not be able to separate D and D^* if they are essentially just monoexponential. So rather than failing the fit, the tumour should be treated as a monoexponential candidate only and that parameter calculated. In retrospect, this may have shown differences in D_m – it did not behave as well as expected and certainly did not surpass the IVIM parameters in terms of number of significant results. The residuals shown in the example fits always seem to be larger for lower b-values. The perfusion parameters that are calculated from the higher b-values are always more difficult to quantify, this is also evident in the literature, as well as in this thesis. Larger residuals mean they are perhaps not fitted as well as the later b-values producing their monoexponential and biexponential diffusion counterparts.

The results for f, D and D^* agree well with previously reported values in the literature. Considering Table 4.1 which summarises relevant breast IVIM literature; D is of the order of 0.001 to 0.0001 mm^2/s; D^* is of the order of 0.01 to 0.001 mm^2/s; and f ranges up to 30% (0.30). All values calculated are physiologically acceptable when looking at previous studies.

Statistical analysis, both unpaired and paired, supported each other's findings. This was that significant differences were found for IVIM parameters in distinguishing malignancy from normal tissue (*f, D*), in categorising tumour grade (D^*), but not in categorising histological type, molecular subtype, or immunohistochemical status. Some differences were suggested but the cohort numbers did not enable a statistical result to be proven. This does not mean that a larger cohort would not prove this and further research should be done.

Monoexponential diffusion (D_m) did not out perform IVIM. It could, however, characterise histological type, IDC from ILC, with IDC being lower. D_m could not distinguish between high and low grade, or between any further molecular subtypes. However, the treatment pathways for both ILC and IDC do not differ on their classification clinically and so clinically there may not be a need to classify the two using imaging.

Areas of improvement for the main clinical study include implementing this analysis in a larger cohort. Significant differences trailed off as the cohorts were divided further.

Histogram and parameter mapping analysis could give further insight into how these parameters fare in different types of tumour. ROI single slice analysis could be considered a limitation but it also has advantages. ROI analysis has been carried out by taking the average signal value of that region, however with no constraints which skews values. ROIs excluded tumour edges, which have also been shown to skew averages. The ROI method was done to minimise partial volume and motion artefacts, also. A full histogram and volumetric analysis would definitely have the potential to give better insight into the tumour microenvironment but this also has its disadvantages in skewing values of the IVIM parameters unless filtering or constraints are used – which then induces bias.

The main conclusions from this clinical study are; that an optimised protocol allows IVIM parameters to be correlated with malignancy and these are significantly different from normal tissue; that D^* demonstrates significant differences between high and low grade; that monoexponential diffusion does not outperform IVIM analysis; and finally that this optimised protocol has performed just as well as non-optimised protocols in the literature.

On a tumour physiology note, the IVIM and monoexponential diffusion parameters have raised some interesting questions and possible mechanisms for the values calculated. Restricted diffusion in invasive ductal carcinoma in comparison with freer diffusion in invasive lobular carcinoma gives insight into the cellularity and proliferation of these two histological types. Higher grade tumours had higher pseudo diffusion indicating more blood flow in micro capillary networks. f was found to be lower (although not significantly) in triple negative cancers that respond worse to treatment which could mean less efficient drug delivery. The question of what is an acceptable value for perfusion in normal tissue is still debatable as on one hand it is shown that perfusion exists in healthy or normal parenchyma,

but that the malignancies show insignificant differences when they are assumed to have higher angiogenesis and blood volume.

The clinical aim from Chapter 4 has been achieved; 5) to investigate the clinical utility of an optimised protocol in breast cancer patients.

8. Monte Carlo Simulations of IVIM Protocols

8.1. Introduction

The Monte Carlo method is a broad class of computational algorithm that relies on repeated random sampling to obtain numerical results. This approach is especially useful in testing and analysing optimised and probabilistic physical problems.

In principle, Monte Carlo methods can be used to solve any problem that has a probabilistic interpretation. By the law of large numbers, outcomes can be modelled on probability distributions. Monte Carlo simulations were implemented to predict the expected mean squared errors (MSE) when fitting MRI signal data from ROIs drawn in breast tissue, to calculate IVIM parameters. These predicted MSEs were then used to compare actual MSEs from volunteer and clinical signal data to ensure variance in values for *f*, *D* and *D** were within statistical limits. Two protocols were investigated; Protocol A (heuristic representing non-optimised protocols), and Protocol F (optimised protocol applied clinically in Chapter 7).

8.2. Fitting Algorithm

The Monte Carlo simulations were carried out using an in-house developed program written and computed in MATLAB (MathWorks, Massachusetts, USA). The program allows the user to input values for the IVIM equation parameters *f*, *D* and *D** from the biexponential IVIM equation (117);

$$S = S_0[(1-f)e^{-bD} + fe^{-bD^*}]$$

Equation 8.1

where *S* is the diffusion-weighted signal, *f* is the perfusion fraction, *D* is the diffusion coefficient and *D** is the pseudodiffusion coefficient. The initial signal, S_0, was chosen to be the arbitrary value of 1000 as this is simply a starting point for the fit and irrelevant to the outcome of the simulation.

The signal was calculated using these user inputted parameter values. Random noise was added to the signal based on a Gaussian distribution. High b-value signal data (over 200 s/mm^2) was extracted. For high b-values a monoexponential model can be used to calculate the estimated signal, S_{0est}, and *D,* assuming that *D** is negligible. This is because *D** is significantly greater than *D* (approximately 10 times larger) and its influence on diffusion-

weighted signal is weak when b-values are over 200 s/mm^2 (85). The monoexponential diffusion model (Equation 8.1) was consequently used to calculate S_{0est} and D using the high b-value signal data, implementing the non-linear least squares fit, the Levenberg-Marquardt algorithm.

$$S = S_{0est}e^{-bD}$$

Equation 8.2

Using simultaneous equations, D can be calculated through Equations 8.3-5; however, the monoexponential model was utilised so that fitting did not fail. For mathematical purposes, equating S_{0est} from Equation 8.2 and Equation 8.1, and using high b-values in simultaneous equations, allows D to be calculated to give Equation 8.5;

$$S_1 = S_0[(1-f)e^{-b1D}]$$

Equation 8.3

$$S_2 = S_0[(1-f)e^{-b2D}]$$

Equation 8.4

$$D = \frac{ln\frac{S_1}{S_2}}{b_2 - b_1}$$

Equation 8.5

Initial estimates for the remaining IVIM parameters (f and D*) were calculated by equating S_{0est} and Equation 8.1; which allowed for the rearrangement for f;

$$f = \frac{S_0 - S_{0est}}{S_0}$$

Equation 8.6

Inserting values for D and f back into Equation 8.1 and rearranging allows a calculation of D*. However, after comparing this method to simply multiplying D by 10, it was found that the latter method was a more pragmatic (and numerically indistinguishable) approach and so was used in this program. Equation 8.7 shows the rearrangement of Equation 8.1 for completeness.

$$D^* = \frac{ln\frac{S_{high} - S_0(1-f)e^{-bD}}{S_0.f}}{-b}$$

Equation 8.7

Finally, the data was fitted using the biexponential model (Equation 8.1) by implementing the Levenberg-Marquardt algorithm to calculate S_0, f and D^* over all b-values whilst utilising calculated D from the monoexponential model. This increased robustness of the fit (85). The mean square error (MSE) for each fit was reported. f was constrained to be between 5% and 30% for initial estimates as anything else is deemed physiologically impossible in that body part. The results for the Monte Carlo simulations were written to a spread sheet where whole data lines were filtered if f was negative or more than 50%, or if D^* was negative or greater than 0.3.

Histograms of the MSEs were generated in SPSS (IBM, New York, USA) for the 8 Monte Carlo simulations.

8.3. Breast Simulations

Values for f, D and D^* for breast were chosen based on taking an average for tumour values from surveyed literature. For breast the average values used were; f = 0.0885, D = 0.0011 mm^2/s, D^* = 0.04384 mm^2/s (78, 81, 83). The user then inputs the SNR calculated as the mean signal intensity of malignant tissue minus the mean signal of background noise divided by the standard deviation of the mean of the background noise as a percentage. This was calculated for the breast by taking 12 clinical IVIM scans at random (Chapter 7) and taking an average percentage. For breast the SNR percentage was 0.68%. This was rounded to 1%. The simulations were run for 1% (clinical scan average), 2%, 5% and 10% for breast. The simulations were run 50,000 times each, which took approximately 15 minutes per simulation. The simulations were run for a standard, heuristic IVIM protocol (named 'linear sampling'): b = 0, 100, 200, 300, 400, 500, 600, 700, 800, 900, 1000 s/mm^2, of which similar forms are commonly used throughout the literature. The simulations were then run for the optimised b-value protocols for breast (Protocol F), being: b = 0, 10, 24, 46, 71, 135, 221, 355, 567, 900 s/mm^2. The results for the Monte Carlo simulations were written to a spread sheet where whole data lines were filtered if f was negative or more than 50%, or if D^* was negative or greater

than 0.3. Histograms of the MSEs were generated in SPSS (IBM, New York, USA) for the 8 breast Monte Carlo simulations.

8.4. Results: Breast Simulations

8.4.1. Results: Linear Sampling

The results of the Monte Carlo simulations for the linear sampling breast protocol are presented in Figure 8.1 and Table 8.1. Figure 8.1 describes the spread of MSEs produced for calculated values of f, D and D^*. Table 8.1 summarises the average MSE, number of successful simulations, and the average f, D and D^* calculated for each percentage of added noise for the linear sampling breast protocol.

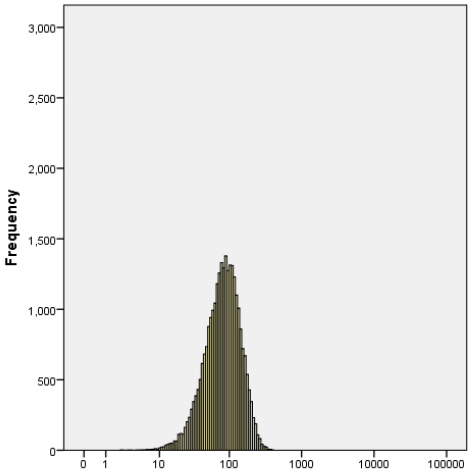

a) *Log_{10} (MSE) for breast linear protocol 1% noise*

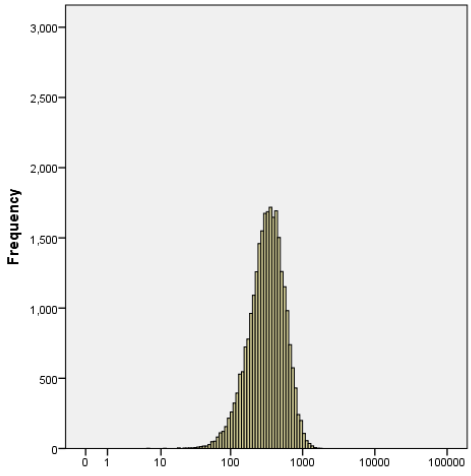

b) *Log_{10} (MSE) for breast linear protocol 2% noise*

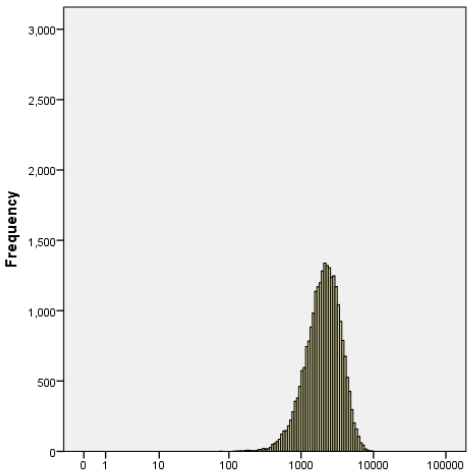

c) *Log_{10} (MSE) for breast linear protocol 5% noise*

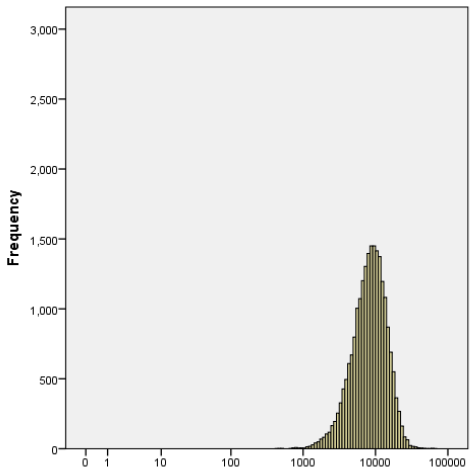

d) *Log_{10} (MSE) for breast linear protocol 10% noise*

Figure 8.1: Histograms of Monte Carlo generated MSEs for the linear sampling breast protocol with a) 1% added noise, b) 2% added noise, c) 5% added noise and d) 10% added noise.

Added noise, *%*	**Average MSE**	**Number of successful simulations, *N* (out of 50,000)**	**Average *f***	**Average *D* (*mm²/s*)**	**Average *D** (*mm²/s*)**
1	92	27189	0.07	0.0010	0.031
2	365	26509	0.11	0.0010	0.025
5	2311	24985	0.16	0.0010	0.017
10	9372	21578	0.25	0.00089	0.012

Table 8.1: Summary of average MSEs, number of successful simulations, and average f, D, and D* for each percentage of added noise for the linear sampling breast protocol.

8.4.2. Results: Optimised (Protocol F)

The results of the Monte Carlo simulations for optimised breast protocol (Protocol F) are presented in Figure 8.2 and Table 8.2. Figure 8.2 describes the spread of MSEs produced for calculated values of *f*, *D* and *D**. Table 8.2 summarises the average MSE, number of successful simulations, and the average *f, D* and *D** calculated for each percentage of added noise for the optimised breast protocol.

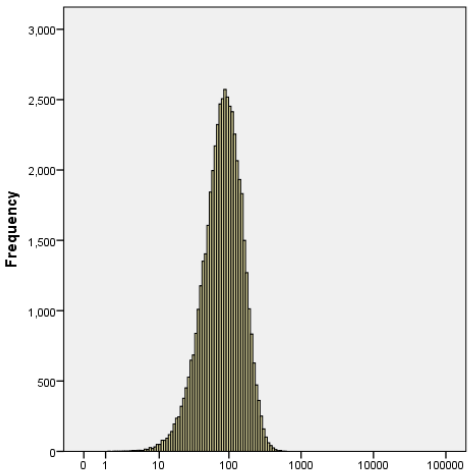

a) *Log_{10} (MSE) for breast optimised protocol 1% noise*

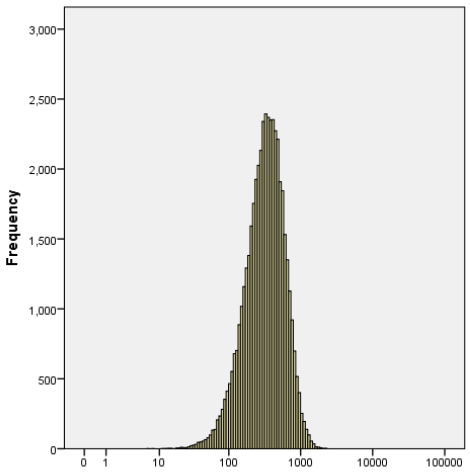

b) *Log_{10} (MSE) for breast optimised protocol 2% noise*

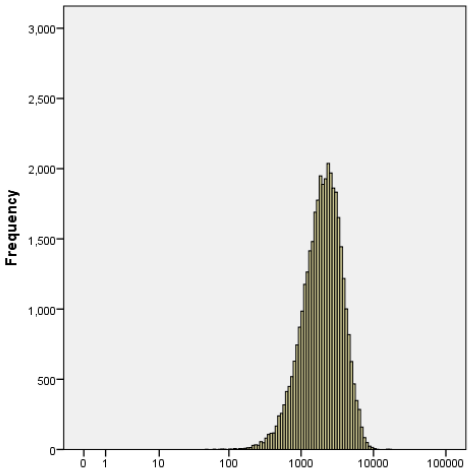

c) *Log_{10} (MSE) for breast optimised protocol 5% noise*

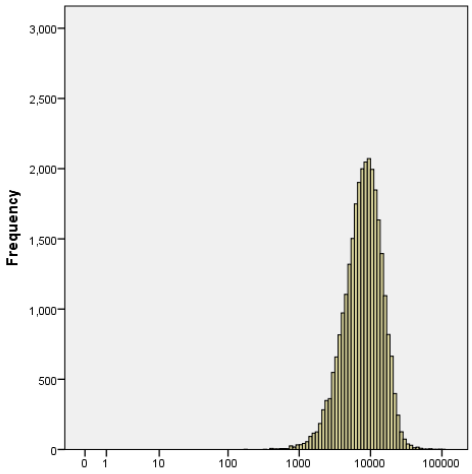

d) *Log_{10} (MSE) for breast optimised protocol 10% noise*

Figure 8.2: Histograms of Monte Carlo generated MSEs for the optimised breast protocol (Protocol F) with a) 1% added noise, b) 2% added noise, c) 5% added noise and d) 10% added noise.

Added noise, %	Average MSE	Number of successful simulations, *N* (out of 50,000)	Average *f*	Average *D* (mm^2/s)	Average *D** (mm^2/s)
1	96	49946	0.090	0.0011	0.047
2	375	47264	0.095	0.0011	0.052
5	2312	36751	0.14	0.0010	0.041
10	9211	28872	0.22	0.00092	0.032

Table 8.2: Summary of average MSE, number of successful simulations, average f, D and D* for each percentage of added noise for the optimised breast protocol.

8.5. Discussion and Conclusions

The results for both the linear sampling and optimised protocol (Protocol F) MSE histograms are as expected. Figures 8.1 and 8.2 show that the lower the percentage of added noise, the lower the average MSE. The average MSEs for linear sampling at 1%, 2%, 5% and 10% are 92, 365, 2,311, and 9,372 respectively. The average MSEs for the optimised protocol at 1%, 2%, 5% and 10% are 96, 375, 2,312, 9,211 respectively. The average MSEs for both linear sampling and the optimised protocol are very similar. The lower the MSE the better; a lower MSE implies that the data has been fitted better. The average fitted D^* at 5% shows the MSEs are similar but the optimised protocol values are much closer to the initial inputs (0.041 mm^2/s and 0.017 mm^2/s with 0.04384 mm^2/s). This is presumably because the linear protocol does not sample the D^* component very well so the fitting is good on the data it has got but the lack of low b-values means it is never going to do well at calculating the D^* and f components of the equation. Less noise therefore indicates a better fit of signal data to Equation 8.1 utilising a suitable fitting method. The segmented fit was utilised in these simulations, shown to be superior in Chapter 6. The MSEs appear to be normally distributed with slight tails to lower values, which is encouraging, as more MSEs are lower with suspected anomalies being at high

values. A lower percentage of noise also indicates a better fit to Equation 8.1 due to N, the number of Monte Carlo data sets left after being filtered at the end of the MATLAB program, being much higher for lower added noises. There are also more acceptable values for the IVIM parameters *f*, *D* and *D** at lower percentages of noise. This makes sense as signal data will be fitted better the more accurate the signal. N is 27,189, 26,509, 24,985, 21,578 out of 50,000 for linear sampling at 1%, 2%, 5% and 10% added noise respectively. N is 49,946, 47,264, 36,751, 28,872 out of 50,000 for Protocol F at 1%, 2%, 5% and 10% added noise respectively. N is higher in general for the optimised protocol which indicates that this protocol is more likely to fit data better than the linear protocol. All average values for calculated *f*, *D* and *D** for both linear and optimised breast are comparable to expected values as seen in the literature (Tables 8.1-2). The average *f*, *D* and *D** for lower percentages of added noise are more comparable to the initial inputs of *f*, *D* and *D**, with the optimised protocol producing the closest values. This makes it the preferred protocol. As noise increases, *f* appears to increase. *D* shows little variation even with a higher percentage of added noise due to the robustness of the fitting algorithm when calculating *D*. For linear, *D** decreases with noise and for optimised it increases slightly. This may be due to the sampling of the perfusion component of the biexponential via choice of b-values (i.e. 0, 100, 200 for linear sampling and 0, 10, 24, 46, 71, 135 for Protocol F). The optimised protocol allows for better sampling at low b-values therefore picks up pseudo perfusion better. Since optimised has a higher N, it can be concluded that the values calculated are more representative of actual values.

From Chapter 7, after fitting and omissions due to anomalous fits, an average MSE was taken from 44 sets of fitted data in malignant lesions. The average MSE was 360. This corresponds to the 1-2% noise bracket. This means that the fitting of clinical data is acceptable when comparing the MSEs to the simulated MSEs calculated from Monte Carlo simulations. The MSE was reported when the data was fitted using MATLAB as part of the program analysis, but MSEs are not further used in in-depth statistical analysis in Chapter 7 as the fit was not under investigation, rather the mean plus or minus the standard deviation, or the median and range of IVIM parameters were reported and correlated with tumour subtype.

A further aim from those outlined at the end of Chapter 4 has been met; 6) to support these (investigations in healthy and malignant tissue) with statistical simulations.

9. Computed Diffusion-Weighted Imaging

9.1. Background and Literature Review

Computed Diffusion-Weighted Imaging (cDWI) is a mathematical computational technique, which calculates a user defined b-value image from MR DW-images acquired with at least two b-values (for the monoexponential diffusion model) or multiple b-values (for the IVIM biexponential model). The technique can be employed using IVIM images to calculate the simple apparent diffusion coefficient (ADC), since there are at least two b-values. The motivation for this chapter is that because a post clinical optimisation in Chapter 5, Section 5.3.13 yielded a b-value protocol with a low final b-value (traditional opinion), then cDWI would be useful for clinicians if qualitative and morphological DWI were important to them in visualising lesions at high b-values. Adding extra high b-values to the protocol means extra scan time, but cDWI is a post-processing method that extends the fit to predict what the signal values, and thus quantitative parameters, would be. Lesions show restricted diffusion, and thus lesions have a lower ADC than normal tissue so the signal will take longer to decay, leaving them bright at high b-values, whilst normal tissue signal will reduced more quickly. At higher b-values, lesions are often clearly differentiated with other tissues having lost signal. The protocol produced in the post clinical optimisation was; 0, 10, 76, 140, 204, 265, 326, 385, 443, 500 s/mm^2. In breast, a final b-value of around 1000 s/mm^2 is common (44, 97).

Having acquired DWI data using Protocol F in Chapter 7 in a clinical study, this data was available for cDWI analysis. Some of these patients had a higher b-value added to their IVIM protocol (but not used in IVIM analysis) and this gave a real DW-image to compare to cDWI-generated images in this chapter. Acquired images and computed images could be compared using images from Protocol F to calculate the computed images.

The novelty of this work is that; 1) the IVIM protocol used in scanning breast cancer patients is optimised for calculating diffusion and perfusion parameters; and 2) multiple data points will allow a more accurate calculation of computed images as the computer generated maps need to be extrapolated from a well sampled curve. cDWI as an adjunct to optimised IVIM means that there is no disadvantage of not scanning high b-values since they can be generated if needed.

From the consensus statement on diffusion published in 2016 (96), summarising the current state of affairs in diffusion imaging outside of the brain, there are recommendations of what research is needed to improve diffusion MR imaging. Some clear points were that protocols needed to be optimised for better image quality, b-value selection needed to be appropriate, reliable methods to produce ADC maps were needed, accurate sampling of signal decay was needed and radiologist/analysts needed a clear definition of regions of interest. These points can all be addressed by cDWI, as a tool that allows the scan to do more than what it would have originally been utilised for before cDWI. In other words, cDWI is a solution to many of the problems faced in DW-imaging today with a lack of standardisation between institutions. For example, if one study concentrated on a particular cut-off, and the data available did not scan that b-value, then cDWI could generate this and this could be used in analysis.

Computed DWI is an innovative and relatively new technique made popular by Blackledge *et al* (118). It was originally explored in 1984 by Ortendahl (119, 120) and Riederer (121) and has since had a revival due to improvements in computation and MR hardware.

Technical developments in MRI have encouraged the implementation of DW-imaging outside of the brain to be routine. However, there is still not a consensus to which b-values should be used, how many should be used and what the optimal b-value for the detection of malignancy is. DW-imaging is used for detection, characterisation and assessment of treatment response. There are a multitude of incentives to favour DWI, including its ability to maximise contrast between lesions and normal tissue without the need for invasive contrast agent and a unique insight into the microscopic cellular environment. These features depend on the intrinsic tissue Brownian motion of water molecules, T_2 of the tissue, and the b-value (diffusion weighting of the motion probing gradients that are applied). High b-values (over 1000 s/mm^2) have been shown to improve visualisation and detection (122). The low apparent diffusion coefficient (ADC) and longer T_2 values make lesions visible at high b-values in comparison to surrounding parenchyma and fat. The use of longer echo times (TE) reduces the signal to noise ratio (SNR) and therefore leads to poorer image resolution. It also, obviously, takes longer to scan more b-values.

From this, there is a clear advantage to computing high b-value images. cDWI has been investigated using the monoexponential and biexponential models in various body parts including the breast and prostate using full body imaging (118), in prostate (123, 124) and in the liver (125). This technique suppresses background noise, raises SNR and attenuates signal from lesions at high b-values making them easier to detect whilst avoiding image distortion and long scan times. It is possible to maximise the contrast without rescanning the patient and without intravenous contrast agent, which is a topic of debate currently (89, 126, 127) and alternatives to such contrast-enhanced imaging like cDWI are encouraged. The success of the technique depends on the accuracy of estimated ADC values, software and SNR of DW-images acquired. The model may be ineffective at fitting an ADC value to particular pixel locations. These pixel locations can be zero filled. However, there is potential of misidentification of smaller lesions; but this is minimal in comparison to potential misidentifications due to eddy current artefacts and distortions that real higher b-values can include.

There have been suggestions other than cDWI to solve these distortion problems. Bodammer (128) described that acquiring two images with identical diffusion direction and weighting but inverted polarity – known as Reverse Polar Gradient (RPG) DW-imaging - allows the diffusion contrast to remain unchanged given inverted polarity, but the inversion affects the distortion by a compression being produced from a stretching. In this method, two images must be acquired for each diffusion direction and for every diffusion weighting. Moreover, the signal-to-noise ratio in images with high b-values can be extremely low, which makes the precise determination of the correction parameters difficult. Furthermore, contrast differences due to directed movement (for example flow or pulsations) or patient movement can lead to an inadequate robustness of the method. Thus, cDWI appears to be an easier and more robust method.

In 2011, $CoSO_4$ phantom studies confirmed that cDW-images were reliable. They prevented image distortion, improved contrast, lessened scan times, and SNR improved when compared to a scanned image - especially at $b > 840$ s/mm^2 (118). The image quality and background suppression of 10 patients (whole body DW-imaging for metastases, primary malignancy of prostate and breast) were then rated on a qualitative scale from ‘unacceptable’ to ‘good’ by radiologists. The McNemar test was carried out to assess diagnostic performance,

where a computed b-value of 2000 *s/mm²* resulted in a higher specificity and sensitivity compared with the images acquired at b-values of b = 0 *s/mm²* and b = 900 *s/mm²*.

In 2014, a paper was published investigating the optimal b-value to detect breast tumours with DWI on a 1.5 T scanner (129). Sixty-four subjects with breast cancer underwent DWI using 6 b-values up to 3000 *s/mm²*. Both mono- and biexponential fits were applied. This group recommend an optimal high b-value in breast of 1400 s/mm^2 for detecting tumours. In the radiological community this is seen as high for breast and many institutions scan to 1000 *s/mm²*, as published in a meta-analysis comparing mean ADC with b_{max} choice (130). cDWI would allow these higher, optimal b-values to be calculated without compromising scan time. A similar study (131) reported the maximum contrast achieved in breast between a tumour and normal tissue was at 1500 s/mm^2. They also stated that since SNR is higher at 3.0 T then in order to remove background signal from parenchyma, thus just leaving signal from the lesion, higher b-values are required compared to 1.5 T, and so the ideal cut-off b-value would be higher for 3.0 T in this study than for 1.5 T as mentioned previously. Some literature suggests that even though the contrast difference between tumour and normal tissue is highest at high b-values such as 1500 *s/mm²*, that using 1000 *s/mm²* is actually optimal in detecting malignancy to prevent false positives (44, 97, 132). Consequently it may be the case that using more than two b-values is optimal, as in IVIM, and with cDWI higher b-values can be calculated if needed, so enhancing the capability of a single diffusion scan on a patient. This is a tool that allows; if you need it, higher b-values, and suggests the ability to produce better images than actually scanning at higher b-values. There is also the issue that DWI is rarely used on its own, and is almost always used as part of a multiparameteric exam. So even though these high b-values are reported to be needed to detect malignancy, the contrast enhanced imaged would allow guidance if the tumour was not obvious on DW-images.

The influence of combinations of b-values in calculating cDWI was investigated in prostate cancer (123). This group found that the contrast ratio of cDWI = 2000 *s/mm²* was always significantly better than the scanned images. They then went on to discuss that care should be taken when computing cDW-images with low b-values, and that combinations of b > 100 *s/mm²* and b > 500 *s/mm²* along with commonly used 0 *s/mm²* and 1000 *s/mm²* was optimal from their study. This indicates that a cut off to remove perfusion effects would be useful in calculating reliable cDW-images.

High b-value cDWI obtained using IVIM was shown to have the same lesion visibility as that of acquired DWI in the prostate by Grant *et al* (133). Seven b-values were used up to 2000 *s/mm*^{2}. Another prostate investigation was to compare acquired versus computed DW-images at 1400 *s/mm*^{2} (134) and more lesions were detected using cDWI. Again, in prostate, cDWI was investigated by comparing the contrast to noise ratio (CNR) of aquired DWI and cDWI. It was found these were comparable and also that the CNR in cDWI was better when calculated from acquired images between 0 *s/mm*^{2} and 800 *s/mm*^{2} (135).

The complexities of improving SNR in cDWI further to beat its DWI counterpart indefinitely, and reducing T_2 shine through effects, has been addressed (136). A voxel-wise approach was employed and tested using a phantom with variable T_2 and diffusivity and retrospectively applied to whole-body DWI data for 20 subjects with metastatic disease. Image quality, lesion detectability and lesion diffusivity assessment were all better in cDWI.

In this chapter, a cDWI graphical user interface is presented that was built in MATLAB (MathWorks, Massachusetts, USA). cDWI images can be produced as an adjunct to the post clinical IVIM protocol. The cDWI images were calculated from patients scanned with Protocol F. These computed images were scored in comparison to real high b-value DW-images acquired in the clinical study in Chapter 7 (sometimes a higher b-value was added to the protocol but this was not used in IVIM analysis, such as 1000 *s/mm*^{2}, 1250 *s/mm*^{2} or 1500 *s/mm*^{2}). In this Chapter 1250 *s/mm*^{2} was used as the high b-value for comparison. This program was designed to be quick and user friendly. IVIM images can be loaded into the program, a cDWI b-value is chosen, noise is thresholded, and the computed image and ADC map is calculated.

9.2. Cohort

Out of the 207 patients scanned, 60 patients were considered in the clinical study in Chapter 7. Twelve of these patients that were scanned with an extra b-value of 1250 *s/mm*^{2} are considered here, of random histological type and molecular subtype. MR safety screening forms were completed prior to imaging. The IVIM protocol was added to the standard of care breast MR exam for all breast cancer patients, at the request of the consultant radiologist who found the scan qualitatively useful in the first instance in place of standard DWI. IVIM as an adjunct to the multiparametric MR protocol already in place at Hull Royal Infirmary allowed standard ADC calculation carried out on DW-imaging plus the added benefits of better image quality,

and more b-value images, in a similar scan time. IVIM parameters were not used in standard of care MR reporting.

Patients of interest received their MR scans prior to any breast cancer treatment (pre neoadjuvant chemotherapy (NAC), surgery or radiotherapy). Patients were therefore scanned for screening purposes, problem-solving or for pre-treatment planning. Patients were diagnosed with breast cancer through MR reporting by a radiologist, leading to a biopsy; stereotactic core biopsy, US-guided fine needle aspiration (FNA), or MRI guided core biopsy. Final histopathology diagnosis was confirmed through histology and/or surgical specimen analysis.

Inclusion criteria comprised; invasive malignant breast cancer of any grade, type, and molecular subtype; pre-treatment of any form; high b-value added to scan of 1250 s/mm^2.

Exclusion criteria comprised; metastatic disease; prior breast cancer treatment (NAC, surgery, radiotherapy prior to MR); if tumour grading and/or pathology were not available (due to information held elsewhere outside of HEY NHS trust); no high b-value in protocol.

Exclusion criteria for normal tissue analysis were as above, and also; bilateral disease; mastectomy in contralateral breast; and/or little or no visible parenchyma on MR images.

Patients had a mean age of 59 years (range 45 - 74 years). Information on tumour grade, histological subtype, hormonal receptor status, molecular subtype, and subsequent treatment were collected for these 12 patients.

Tumour grade was classified as low grade (grades 1 and 2) or high grade (grade 3). The tumor histological subtype breakdown was as follows; ductal carcinoma in situ (DCIS); invasive lobular carcinoma (ILC); or invasive ductal carcinoma (IDC). The tumour molecular subtype was classified using hormonal receptor status as; Luminal A (ER+ and/or PR+, HER2-); Luminal B (ER+ and/or PR+, HER2+); triple negative or basal-like (ER-, PR-, HER2-); or HER2 type (ER-, PR-, HER2+). These classifications are outlined in Chapter 2 in more detail.

9.3. DW-imaging

Patients underwent a standard of care bilateral MRI breast examination on a 3.0 T MR750 scanner (GE Healthcare, Milwaukee, WI) using the body coil as a transmitter and an 8-channel

breast receiver coil (GE Healthcare, Milwaukee, WI) with the substitution of a <5m IVIM series in place of standard DWI. IVIM images were acquired axially using diffusion-weighted single-shot echo planar imaging (EPI) with the following parameters: repetition time/echo time (TR/TE), 6366 *ms*/54.4 *ms*; field of view, 34x34cm; matrix, 128x128; slice thickness 4mm; slice spacing 1mm; 42 slices (variable with breast size if required); Bandwidth, ±250Hz frequency direction, right to left; diffusion direction, 3 in 1; NEX, 4; bi-lateral shimming; scan duration 4 minutes 20 seconds (variable with breast size if needed up to 5 minutes); with water only excitation. Only one IVIM series was acquired per patient. The clinically optimal protocol (Protocol F) had the following 11 diffusion weightings, b = 0, 10, 24, 46, 71, 135, 221, 355, 567, 900, 1250 s/mm^2 - an extra b-value of 1250 s/mm^2 was added due to radiologist preference. This extra b-value was for visualising the lesion and was not included in IVIM analysis, but was used in this computed-DWI analysis. For cDWI analysis, to mimic the post clinical optimised protocol (cut-off 500 s/mm^2), 900 s/mm^2 was not used in cDWI analysis. Total scan time including volunteer positioning on the scanner bed was approximately 40 minutes in total.

9.3.1. ROIs and SNR

An experienced breast MR researcher kindly drew the regions of interest in the clinical study in chapter 7. These were used to guide identification of lesions on DWI and cDWI. Therefore, this study was biased in knowing where malignancies were so that is why it was not a comparison of which method could identify lesions best but rather an assessment of image quality, which could delineate better, and if cDWI was useful as an adjunct to DWI IVIM. Lesions were identified on a post-contrast T1-weighted anatomical image first, and then a region of interest was drawn on the most malignant part of the lesion (area of highest signal intensity/restricted ADC in lesion) as seen on DW-images. This was single slice analysis in the largest cross sectional area of the lesion.

9.4. cDWI

The computed DWI program is a graphical user interface built using MATLAB (MathWorks, Massachusetts, USA). cDWI images and ADC maps can be produced as an adjunct to the IVIM protocol. The cDWI images are calculated from patients scanned with Protocol F in this chapter, negating b = 900 s/mm^2 and 1250 s/mm^2 to mimic the post clinical application protocol as much as possible. A study by Ueno *et al* actually stated that cDWI

calculations were best when using 100 *s/mm²* and 500 *s/mm²* to fit the ADC monoexponentially (123). The segmented approach used in IVIM biexponential fitting is used to calculate D (ADC) here; low b-values are not implemented in fitting the data to negate perfusion effects. See Table 9.1 to compare the two protocols. The b-values in bold were not used to calculate cDWI images and ADC maps.

Protocols	**b-values**
Protocol F (used in clinical study)	**0, 10, 24, 46, 71,** 135, 221, 355, 567, **900, 1250** *s/mm²*
Post clinical optimised protocol (produced using inputs of *f, D, D to program from clinical study)**	0, 10, 76, 140, 204, 265, 326, 385, 443, 500 *s/*mm²

Table 9.1: The two protocols relevant to this feasibility study of cDWI as an adjunct to optimised IVIM.

This program was designed to be quick and user friendly. IVIM images can be loaded into the program, a cDWI b-value is chosen, noise is thresholded to a user-defined value, and the computed image and ADC map is calculated then displayed.

The apparent diffusion coefficient (ADC) of tissues is calculated on a voxel-by-voxel basis by using the following equation;

$$S_b = S_0 e^{-b.ADC}$$

Equation 9.1

where S_0 is the signal intensity at $b = 0$ *s/mm²*. Once the ADC is known it can be used to extrapolate the expected signal intensity for each image voxel to any computed b value, b_c, as shown below;

$$S_{b_c} = S_0^* e^{-b_c.ADC^*}$$

Equation 9.2

where S^*_0 and ADC^* are the per voxel estimates of S_0 and ADC, respectively. A computed DW MR image is thus generated.

These computed DW-images were scored and compared to high b-value DW-images acquired in the clinical study in Chapter 7 (a higher b-value of 1250 s/mm^2 was added to the protocol but this was not used in IVIM analysis).

9.4.1. Visual Assessment and Scoring of DWI/cDWI Images

For qualitative assessment, the computed images were visually compared to real acquired images of the same b-value (1250 s/mm^2).

Further, for quantitative assessment, cDWI images were scored in an analysis of DWI at b = 1250 s/mm^2 versus cDWI at b = 1250 s/mm^2. Table 9.2 shows the criteria and scoring scale. Comments were allowed as cases could have extra features or problems, and these were taken into consideration if image quality judgement was going to be affected.

Images were scored by the author, with 3 years of breast DW-MRI research experience and exposure to clinical DWI.

Scale: 1 – Poor, 2 – Moderate, 3 – Good, 4 – Excellent, 0 – Unable to score.		
Criteria:	**DWI Score**	**cDWI Score**
Overall image quality		
Background suppression		
Absence of geometric distortion		
Absence of blurring		
Absence of ghosting		
Ability of lesion demarcation		
Total:	**…….. /24**	**…….. /24**
Any other comments? …… …….....		

Table 9.2: Criteria and scoring sheet.

These scores were summed to a total out of 24, and the higher the score, the better the image quality. An average was taken over all images for each category and the average total score reported.

9.5. Results: Program and Interesting Examples

This first example demonstrates the utility of cDWI in reducing background signal to demarcate the tumour clearly. Figure 9.1 shows the T1-weighted post contrast anatomical scan and the IVIM images. Figure 9.2 shows the acquired b = 1250 s/mm^2. Figure 9.3 shows the computed b = 1250 s/mm^2. Figure 9.4 shows the program interface.

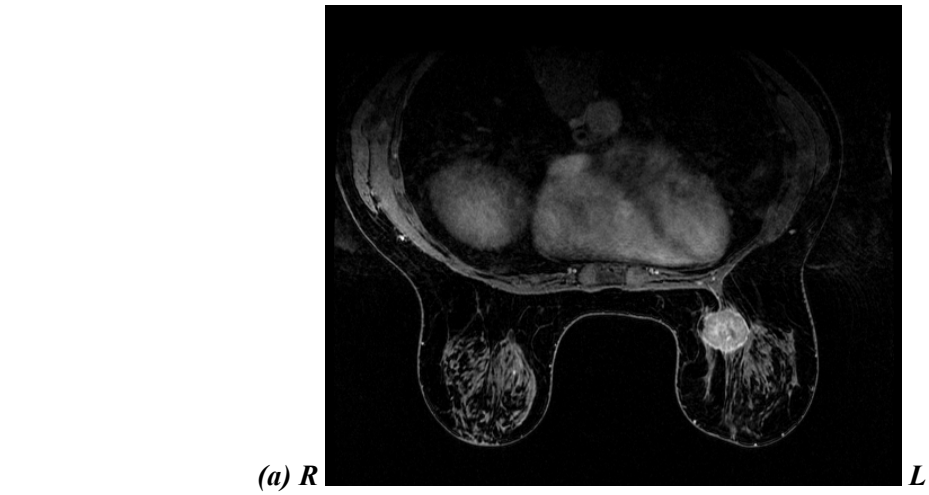

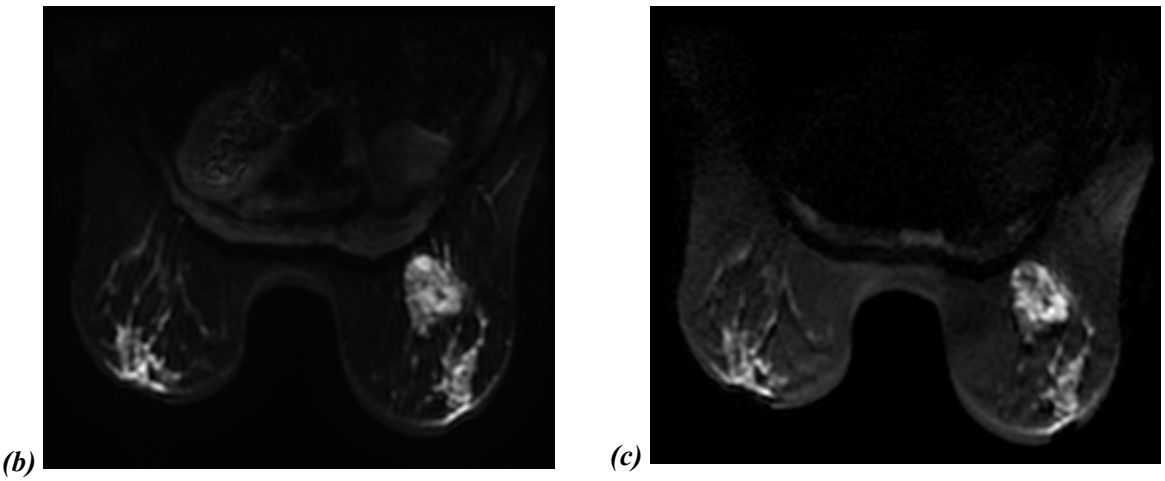

Figure 9.1: (a) Post contrast T1-weighted anatomical scan showing lesion in left breast (bright) and IVIM images (b) b = 0 s/mm^2 and (c) b = 900 s/mm^2. Age, 45 years; reason for scan, pre NAC staging; lesion type, IDC, grade 3, triple negative; treatment, NAC. f = 0.0661, D_m = 0.000613, D = 0.000552 , D* = 0.00549. Note example is used in Chapter 7 and is flipped due to the cDWI program reading in as such.

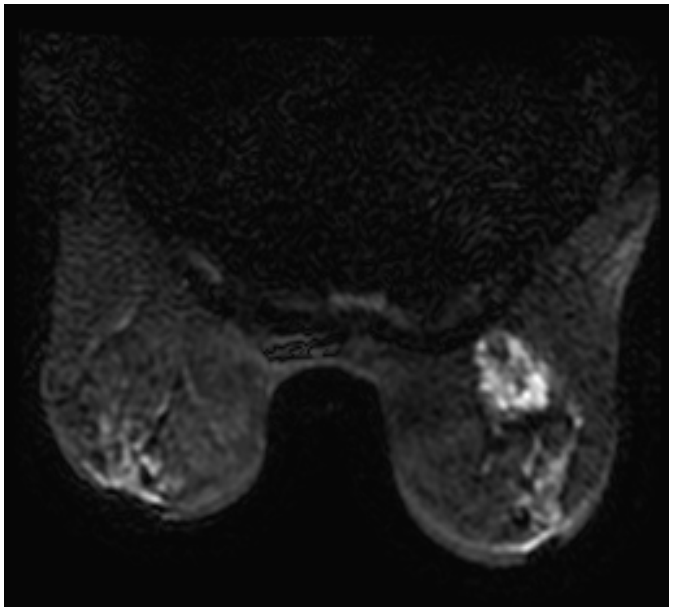

Figure 9.2: Acquired b = 1250 s/mm^2.

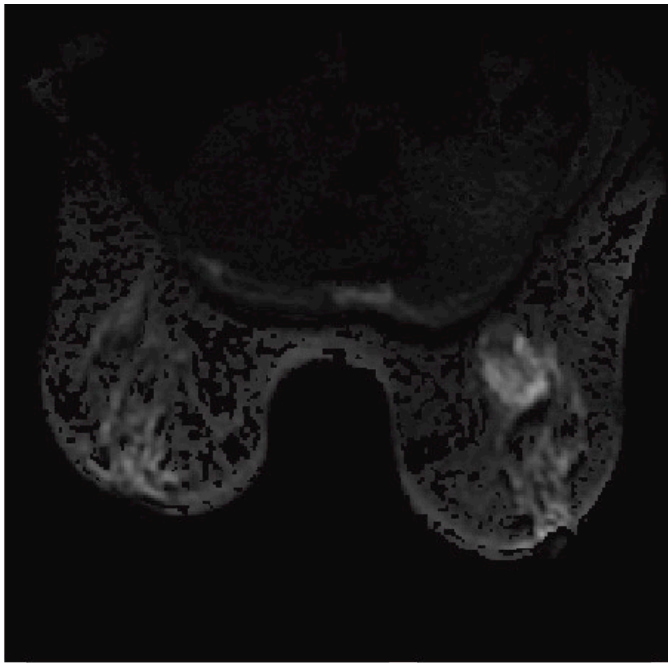

Figure 9.3: Computed b = 1250 s/mm^2.

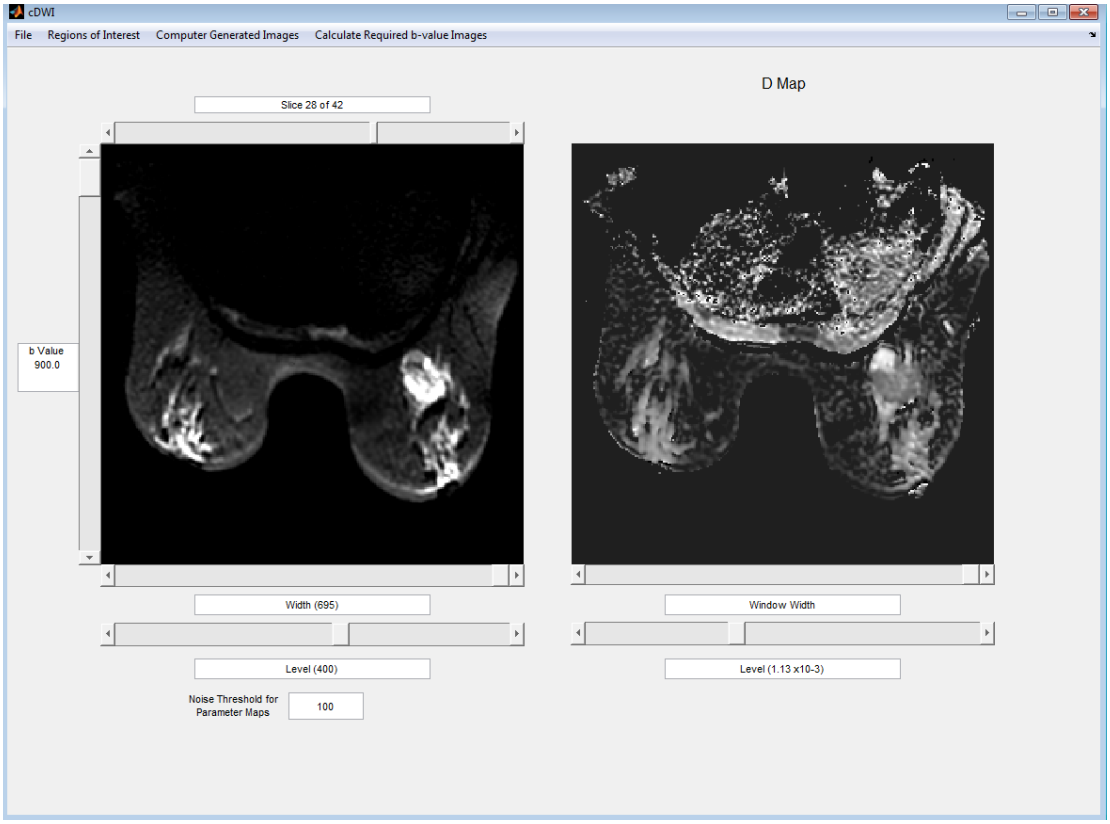

Figure 9.4: cDWI program showing user interface. The ADC map is calculated to extrapolate the signal.

This second example demonstrates the futility of cDWI as there is no improvement on lesion demarcation, but there is improvement in image quality. Figure 9.5 shows the T1-weighted post contrast anatomical scan and IVIM images. Figure 9.6 shows the acquired b = 1250 s/mm^2. Figure 9.7 shows the computed b = 1250 s/mm^2. Figure 9.8 shows the program interface.

(a) L

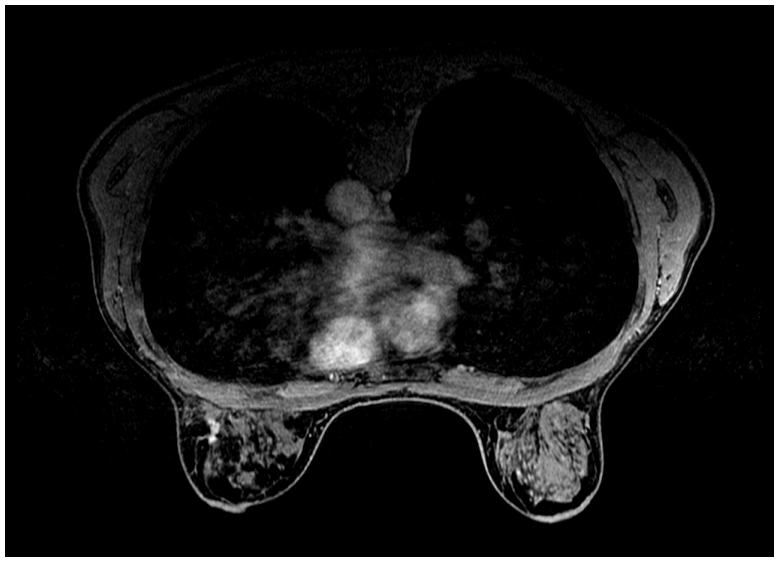

R

(b)

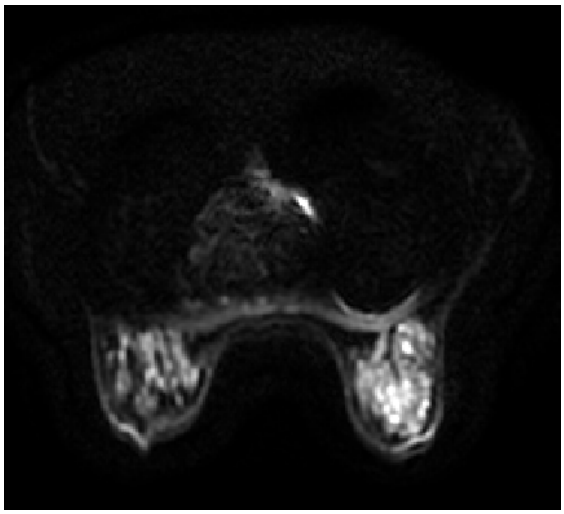

(c)

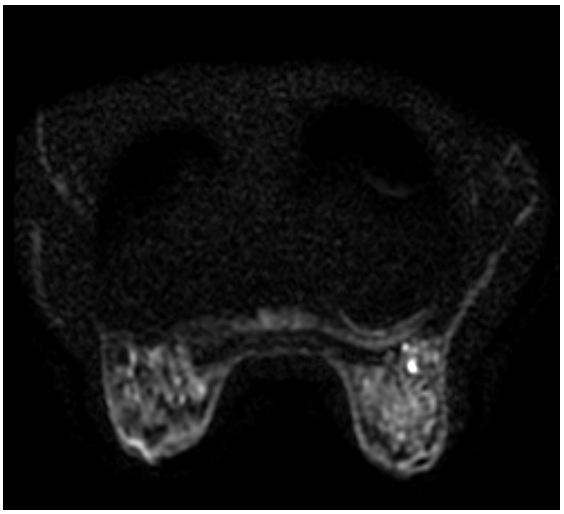

Figure 9.5: (a) Post contrast T1-weighted anatomical scan showing lesion in left breast (bright) and IVIM images (b) b = 0 s/mm^2 and (c) b = 900 s/mm^2. Age, 51 years; reason for scan, problem solving dense breasts; lesion type, ILC, grade 3, ER +/PR +, HER2 -; treatment, NAC and mastectomy. f = 0.0000100, D_m = 0.000679, D = 0.000700 , D* = 0.00700.

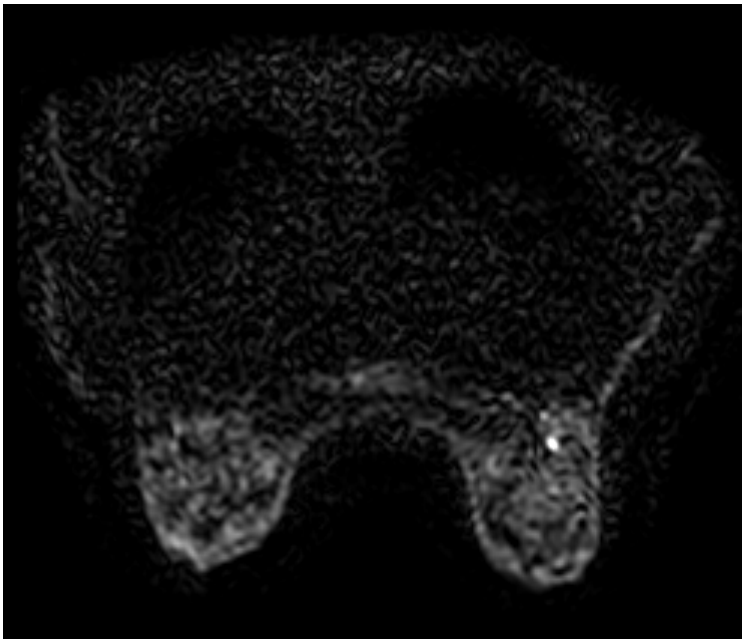

Figure 9.6: Acquired b = 1250 s/mm^2.

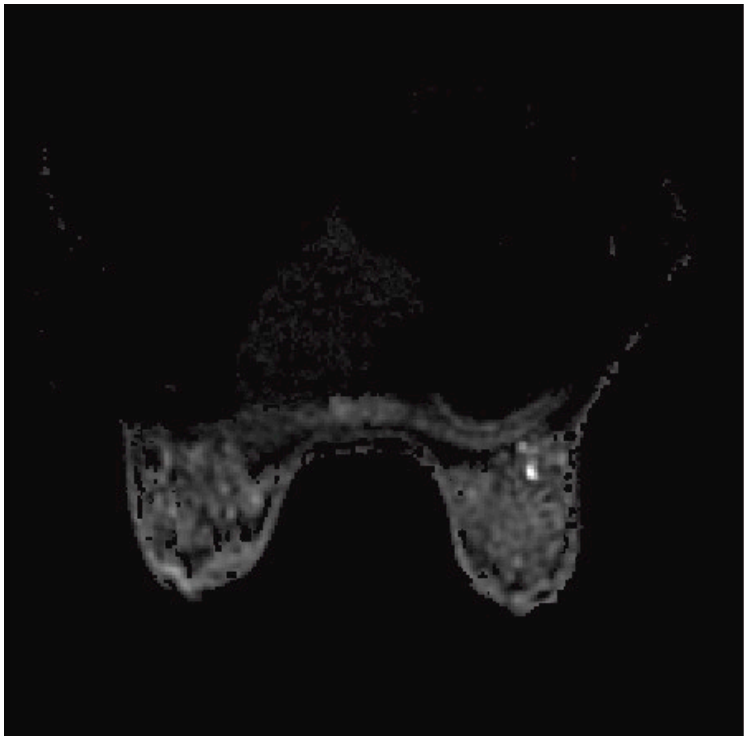

Figure 9.7: Computed b = 1250 s/mm^2.

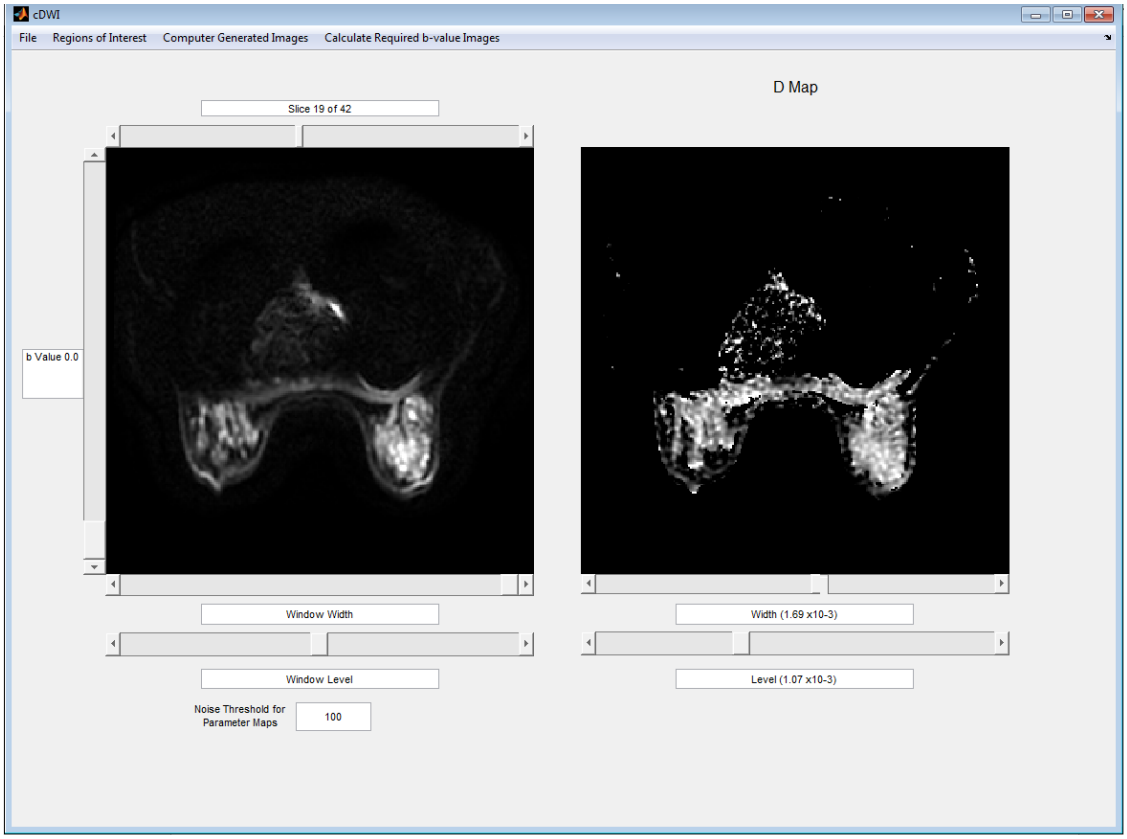

Figure 9.8: cDWI program showing user interface. The ADC map is calculated to extrapolate the signal.

9.6. Results: Visual Assessment and Scoring of DWI/cDWI Images

Table 9.3 outlines the average score (median) for each criterion, for both acquired DWI and cDWI. The average totals are also shown in the final row for the one dozen patients analysed.

N = 12.	*Scale: 1 – Poor, 2 – Moderate, 3 – Good, 4 – Excellent, 0 – Unable to score. Total out of 24.*	
Criteria:	**Average DWI Score**	**Average cDWI Score**
Overall image quality	2	2
Background suppression	3	4
Absence of geometric distortion	3	4
Absence of blurring	4	4
Absence of ghosting	4	4
Ability of lesion demarcation	3	4
Average Total	**19**	**22**
Comments	**If lesion cannot be seen at all here then cDWI would have no improvement.**	**Filtering of noise makes image look 'worse' even though this noise in real image is problematic.**

Table 9.3: Average score for each criterion, for both acquired DWI and cDWI. The average totals are also shown in the final row.

9.7. Discussion

Example 1 demonstrates a scenario where, on DW-images at final b-values lower than 1000 s/mm^2, the signal of background tissues around the tumour is still apparent and so delineating the tumour border is difficult. A higher b-value of 1250 s/mm^2 means the lesion attenuates the signal and background loses signal. However, the real acquired images suffer from noise and artefacts such as distortion. The computed image filters noise and shows the lesion-retaining signal only clearly. In this case, the cDWI program had practicality and value as an adjunct to IVIM with lower final cut-off b-values. It also shows a qualitative improvement in image quality, comparing Figures 9.2 and 9.3. The noise threshold was set to 100. This is where the equation either could not fit the signal data when the program was calculating ADC values, or the signal was noisy. Around the edges of anatomy in particular, these filtered pixels can be seen as darker spots. This looks anomalous but is actually an improvement as noise could give false positives on where parts of the lesion actually are. On a whole, equivalent information if

not more is obtained from cDWI in comparison to DWI at equal, high b-values. The issues of reduced SNR and thus image resolution are improved in cDWI, with a trade off of filtered pixels.

Example 2 is an illustration of where the lesion is occult on DWI even at lower b-values. There is no signal, or not enough, coming from it to delineate it and thus higher b-values show no lesion. Therefore, cDWI offers no improvement in that context but still shows general image quality improvement. Figure 9.7 actually shows a smoother and less noisy appearance of the dense breast tissue. This parenchymal density is probably why the lesion cannot be teased out of the DW-images.

Overall, the program is simple and quick to use. It computes the images within a minute, which is quicker than adding b-values to a scan. As clinical software, it would be accepted and useful especially if IVIM was part of the clinical exam. Many programs available at the moment have add-ons to do post-processing of images and this could be implemented as such.

Table 9.3 details the average scoring of acquired DWI b = 1250 s/mm^2 and computed b = 1250 s/mm^2, according to 6 criteria. An average total out of 24 was also reported. The overall image quality for the two data sets is moderate, cDWI is not worse than acquired, which is encouraging. Some cases were better than others, and this variability is obviously not shown through an average. The image quality of cDWI is going to be affected by the quality of the original DWI images to some extent. Background suppression is better using cDWI. This is because noise is filtered, and the mathematical model of calculating the diffusion is used to calculate the expected signal, thus without noise and artefacts. In general, cDWI has reduced artefacts and distortion compared to DWI. This was expected and is also encouraging. The ability to demarcate the lesion, using T1-weighted post contrast as gold standard, is better in cDWI. This was predicted and this small cohort shows that cDWI is a good alternative to scanning high b-values.

Comments about the DWI images included that if they were not good quality to start with, then cDWI would not be either. This was shown in example 2 to some extent as the lesion was not visible at all on DWI and thus could not be seen on cDWI. Comments about cDWI included that the filtering of pixels leaving darks spots made the image quality rating

instinctively worse, but on the contrary that if noise was gone then the existing information could be evaluated in a clearer manner.

9.8. Conclusions

The aims of this small proof of purpose study were to show that cDWI as an adjunct to optimised IVIM was an advantageous alternative to scanning high b-values. High b-value DWI has disadvantages of image artefacts and distortions, as well as being noisy and having low SNR. By calculating computed images, these drawbacks could be negated, as well as completing the possible need for high b-value images in an exam to show the attenuation of signal in a lesion when trying to demarcate it for ADC/IVIM analysis. The diffusion consensus in 2016 also encourages the use of cDWI in solving issues in the diffusion community.

A graphical user interface was built with the aim of clinical utility. Twelve patients who had IVIM scans with an added high b-value of 1250 *s/mm*^{2} in the clinical study in Chapter 7 using Protocol F were analysed using cDWI in this chapter. Therefore there was an acquired and computed image to compare at 1250 *s/mm*^{2}. The motivation for this chapter was that the post clinical optimisation yielded a low final cut-off of 500 *s/mm*^{2}. This protocol was not applied, Protocol F was, and so the b-values in Protocol F that did not correlate with the post clinical optimisation protocol were not used in analysis to calculate cDWI images. Table 9.1 shows that 135, 221, 355, 567 *s/mm*^{2} were used to calculate cDW-images to correlate with those of 204, 265, 326, 385, 443, 500 *s/*mm^2. It was reported in the literature that 100 *s/mm*^{2} and 500 *s/mm*^{2} to fit the ADC monoexponentially was optimal in cDWI (123). A b-value of 1000 *s/mm*^{2} has been reported to be optimal in detecting breast cancer on DWI, though is outperformed by having multiple b-values (129).

The novelty here is using an optimised protocol, and using cDWI as a tool to aid the qualitative analysis of such an optimised protocol. The ADC was also calculated using a partial segmented method (not utilising lower b-values containing intra voxel incoherent motions). Thus, the ADC in this case is actually D from the three IVIM parameters f, D and D*. This was shown to be a more accurate representation of ADC as monoexponential ADC from 0 to cut-off b-value contains perfusion effects.

Examples in Section 9.5 show that cDWI is useful on account of being able to view the lesion more clearly, and providing general improved image quality. The results of scoring image quality criteria shows cDWI outperforms DWI in several areas, and overall.

cDWI may contribute to an increase in diagnostic accuracy of DWI without increasing acquisition time. This is useful in prostate for guiding targeted biopsies and to improve multiparametric MRI. Especially taking into account financial aspects.

There were some drawbacks of this study. One reader assessed patients and so interobserver evaluation could not be assessed. The observer was also not a radiologist and was biased through knowing the case had a malignancy. Though, it was required to know where the malignancy was to assess images. A larger cohort could always be utilised, though the proof of concept of cDWI is demonstrated successfully here. The SNR was not compared numerically, or the contrast ratio. This could be done but because pixels are filtered then cDWI would perform better in such analysis, which is unfair. Protocol F was used as patients have not been scanned using the post clinical optimised protocol in this thesis. The data utilised from Protocol F was modified accordingly to be as similar as possible.

The final aim of DWI and IVIM related aims in this thesis has been achieved; 7) to allow clinicians to keep qualitative evaluation preferences by creating a computed DWI tool to calculate DW-images of any b-value if the optimised protocol did not suit preferences. And further, it has been proven that it outperforms high b-value acquired DWI.

Part 2: Magnetic Resonance-guided Focused Ultrasound as a Surgical Planning Tool

10. MR-guided Focused Ultrasound for Preoperative Localisation: Lesion Tattooing

10.1. Background and Literature Review

10.1.1. Breast Conserving Surgery

Positive tumour margin status remains a significant problem in breast conserving surgery often resulting in reoperation. MRI provides excellent delineation of a breast tumour's extent but translating this information into surgical practice can be problematic. By utilising MRgFUS to create a series of thermally induced lesions on the periphery of a tumour it is hoped the increased tissue stiffness produced, resulting in improved tumour palpation, will facilitate improved surgical outcome. The aim of this work is towards human application, by creating a clinical tool for planning lesion tattooing and by developing an animal model to carry out lesion tattooing experiments in.

The current clinical management for breast cancer includes surgical removal, either by mastectomy or breast conserving surgery (BCS). With improvements in early detection, breast-conserving therapies are becoming standard of care. It is well established that tumour margin positivity is the most important risk factor for recurrent disease post BCS, leading to reduced disease free survival intervals. Positive tumour margin status can also ultimately result in poor cosmetic effect, increased patient anxiety, delayed adjuvant therapy and increased treatment cost. In the UK up to 20% of cases (137) require reoperation, with higher rates reported globally. Therefore there is a clear need to improve breast tumour delineation prior to surgery to reduce reoperation rates.

Tumour localisation pre-surgery is usually performed with a single image-guided needle wire insertion, using ultrasound or mammography as guidance. This involves placing the wire within the centre of the lesion to be excised and providing a radiological size. MRI has been shown to provide the best delineation of tumour extent when compared with pathological samples. However, the addition of MRI to standard triple assessment in the COMICE trail (138) failed to reduce the reoperation rate, ostensibly due to difficulties in utilising the additional information that MR data provides within the surgical arena. Appropriate guide wire placement can also be problematic due to many factors including tissue stiffness, wire dislodgement or migration. Clearly there is a need for a robust methodology to provide clear demarcation of a lesion's boundaries.

10.1.2. MRgFUS

Therapeutic ultrasound integrated with imaging is now one of the most rapidly expanding techniques in image-guided therapy. It combines the expertise in imaging and various minimal and non-invasive procedures. Many traditional surgical procedures have been replaced by minimally invasive image-guided approaches such as biopsies, many vascular procedures, uterine artery embolization (UAE), and oncologic procedures such as radiofrequency ablation (RFA), microwave ablation, cryoablation, and irreversible electroporation (IRE). (139)

Magnetic Resonance guided Focused Ultrasound (MRgFUS) is a non-invasive surgical technique that focuses high intensity mechanical sound waves deep within the body. This focus of energy can be used to elevate the tissue temperature to such a degree that thermal ablation is achieved. This is carried out without damaging surrounding tissue as ultrasound can travel through the body at high intensities without causing enough heating to harm cells.

Thermal ablation occurs when the targeted delivery of heat causes a rapid change in temperature in the local tissue environment. At present, the Cumulative Equivalent Minutes (CEM) equation best describes the thermal dose needed to achieve desired results. Sapareto and Dewey (140) empirically showed that for most tissue types there is an exponential relationship between necessary treatment time and temperature needed to cause thermal damage. Above 43 degrees Celsius, with every increase in tissue temperature by one degree Celsius, treatment time to cause tissue damage is halved. The following equation shows this relationship, where t is the time of treatment in minutes, T is the average temperature over that time and $R = 2$ is a constant for temperatures above 43 degrees Celsius;

$$CEM43℃ = \int R^{43-T(t)}\, dt$$

Equation 10.1

MR imaging is used to localise and target the thermal effects to the tumour for treatment, control the energy deposition, and assess treatment response (141). Quantitative temperature measurements can be made in vivo through the temperature sensitivity of the water proton resonant frequency (142, 143), and there are other MR thermometry techniques available such as diffusion and T2 thermometry. The ability to use MR techniques to perform

real-time thermometry makes MR the most reliable and comprehensive modality available for real-time (non-invasive) temperature monitoring (139). Other monitoring techniques for FUS include B-mode ultrasound, however this method can traditionally only monitor below the achieved optimum temperatures of FUS.

MRgFUS has a variety of uses. It is currently CE and FDA approved for the treatment of uterine fibroids and bone metastases. It is CE marked for some neurological disorders (essential tremor, tremor-dominant idiopathic Parkinson's - unilateral and neuropathic pain) and various phases of clinical trials are being carried out for other applications such as the ablation of breast and prostate tumours. Other applications include targeted drug delivery and treatment of atrial fibrillation.

MRgFUS has been utilised in the ablation of breast tumours with regard to achieving complete tumour cell kill. Early studies involving complete tumour ablation followed by surgical excision have demonstrated the techniques potential. Clearly the ultimate goal is to achieve local tumour control in an excision-less manner followed by appropriate adjuvant therapy including radiotherapy, to ensure any microscopic disease is treated. However, MRgFUS is currently a multi hour procedure since the goal is total tumour cell kill. The requirement for 100% tumour control necessitates the use of a large number of overlapping sonications to ensure no region within the target zone is spared. As such, tumour size is realistically limited to around 2 *cm* in diameter for the foreseeable future. Clinically there are many breast tumours over 2 *cm* that ultimately proceed to surgery.

An alternative strategy is to utilise the excellent soft tissue delineation of MR alongside the therapeutic effects of MRgFUS to delineate the lesion boundary prior to surgery. Lesion tattooing using MRgFUS is a method of pre-surgical localisation of a tumour, creating sonicated spots of tissue around the tumour to be excised. These ablated spots create palpable and visual markers so that a surgeon may see or feel the boundaries of the malignant lesion. This technique could be used as pre-surgical localisation for many tumours, however tumours in the breast have been targeted since they are easily accessed by MRgFUS, are not close to major organs and because current methods of pre-surgical localisation of breast tumours could be improved upon.

With the arrival of screening mammography and other imaging modalities such as ultrasound and MRI, breast cancers are detected earlier and are therefore smaller and more likely nonpalpable (144, 145). The use of needle-wire localization (NWL) under image guidance is the standard method for the preoperative localisation of nonpalpable breast tumours (146-150). It is a relatively simple procedure but has its disadvantages. Although a needle can locate a tumour, it serves as an inexact and often inaccurate means for a surgeon to find the tumour and create an adequate margin of tissue around it. The objective of breast conservation is to remove the tumour and rim of normal tissue around it, leading to a cosmetically acceptable outcome. NWL frequently requires the patient to go through an additional procedure in a different hospital department, often remote from the surgery location, and frequently invokes patient discomfort and anxiety – though it is noted other alternatives also invoke patient anxiety including the proposed method in this work (150). NWL can add risks to the patient such as dislodgement of the wire and subsequent loss of localisation, displacement of the wire after the breast is out of compression leading to complications, and accidental transection of the wire during surgery resulting in loss of localisation (151). The presence of a NW may also limit surgical entry sites. Alternatives to NWL have been explored and include radioactive seeds (152), iatrogenically induced hematoma (153), cryoablation lesion marking (154) and the use of needle insertion devices. Currently surgeons are seeking better methods to identify and excise nonpalpable or poorly palpable lesions.

Previous work has compared the accuracy of MRgFUS with MR-guided needle wire placement for the preoperative localisation of non-palpable breast lesions in a turkey breast tissue model (155). Results comparing positive margin rates between the two groups were encouraging with no positive margins evident in the MRgFUS cohort. A surgeon did not perform dissection and manual palpation.

A second approach from the same research group has been described wherein cadaveric breast tissue was utilised and a series of palpable ablations created (156). However, no attempt was made to create artificial breast lesions and thus subsequently assess the excision accuracy when using ablation spots. Fixation of the cadaveric tissue in formaldehyde may also potentially alter its characteristics. Three breast specimens were used from two cadavers, absent the skin with no known breast pathology. Ablations were carried out to form

a square of 18 sonications, 4 sonications deep so that when the breast was cut in half all sonications would be shown easily. The palpability of the sonicated spots was assessed via two methods. The first was a remote palpation technique called Acoustic Radiation Force Imaging (ARFI), which provides a pushing pulse of acoustic energy allowing the measurement of displacement of tissue on MRI. ARFI was carried out pre and post ablation. The second method was gross dissection and manual palpation of the sonicated spots. ARFI data showed a collective post ablation reduction in displacement of tissue and increase in shear wave velocity, suggesting the tissue became stiffer at ablation locations after sonication. Manual palpation showed increased palpability and dissection showed that the sonication spots were visible in mixed adipose/fibroglandular tissue. This second study was useful as it used human breast tissue, helping erase doubts that sonications may not be palpated or seen in fatty breast tissue. The author did not state how long the cadavers had been deceased, and so the breast specimens may have started to produce gas, which can lead to cavitation. The cadaveric tissue would also have been fixed in formaldehyde that would make the tissue even more different to in vivo tissue.

A study by Hipp *et al* (157) quantitatively evaluated internal marks made by MRgFUS in rabbit thigh muscle using MRI, CT, US and digital colour images. Six thigh muscles were marked using a Philips system, and out of 19 marks made, 79% were visible on MRI T1- and T2-weighted images. The average temperature elevation was 39.7 degrees Celsius. This study was working toward these thermally induced markers to guide image-guided biopsies.

10.2. Aims

The aims of this work were; 1) to build a clinical tool to plan breast conserving surgery utilising MRgFUS as a means for creating non-invasive markers; 2) to optimise an animal breast tissue and pseudo tumour model; and 3) to carry out formal palpation tests as proof of feasibility. These aims pre-empt future work in humans in vivo, of which nothing has been reported to date of printing this thesis.

10.3. Lesion Tattooing Surgical Planning Program

A program was developed in MATLAB (MathWorks, Massachusetts, USA) with the potential of being a surgical planning tool, biopsy planning tool and/or radiotherapy planning tool. This simple user interface allowed the user to create a template of planned spots around an

automatically segmented lesion from an MR image of breast malignancy. These spots can then be used as a guide of where to sonicate using focused ultrasound to create thermally ablated lesions that should be visible and palpable. The program opens, sorts and displays DICOM images and allows the user to adjust window width and window level. The user may scroll through a series then choose an image and double click on an area of suspected malignancy. The program will segment the lesion using a threshold value chosen by the user. The convex hull of the outline of the segmented lesion is applied, and a margin width is chosen by the user (e.g. 10 *mm*). Along this outline, the user can choose how many sonication spots are required and these are plotted at equal distances apart. The user may also tell the program the radius of the required spots for visual purposes, since the FUS system has different protocols dictating the spot size. Spots may be deleted and added as appropriate. The overlay of spots is then imprinted onto the DICOM image as high intensity signal in the required places. The program also erases the series number and patient ID header tags so that the images may be transferred to the FUS system without the system knowing they are duplicate images of the FUS system MR images taken for planning. The images can then be saved as DICOM images and transferred to CD/USB. The program is simplistic and quick, as in practise a patient would be in the MRI scanner whilst these spots are planned, then sonication carried out once the plan images are loaded into the FUS system. Several studies have investigated the use of non-invasive marking for surgery, biopsy and radiotherapy as an alternative to invasive procedures such as needle wires and clips; however no group to date has presented a clinical tool to do so.

The program can segment and plan spot markers in 3D. After shadowing an experienced oncoplastic breast surgeon for several breast tumour resection operations, and talking through what a surgeon would want from such a clinical tool, it was decided that spot markers planned around one slice over the coronal largest cross sectional area would be sufficient. Lesions undergo convex hulling after segmentation to produce a purely convex representation of the lesion. This is to reflect surgical practise wherein during breast conserving procedures tissue excision does not generally conform to complex lesion shapes. During surgery an approximately cylindrical section of tissue is removed down to the chest wall, centred on the surgical guide wire and of an appropriate size informed by imaging. Figure 10.1 shows a plan of breast conserving surgery using sonicated spot markers as a template for avoiding positive tumour margin status. This method potentially has use in

replacing methods such as surgical clips and guide wires.

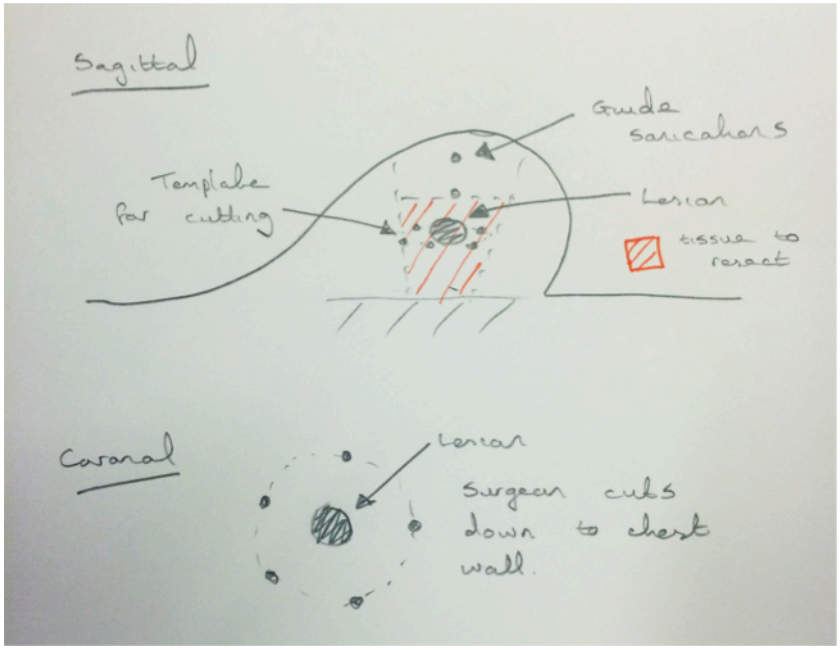

Figure 10.1: Sketch of sonicated template of spots as part of breast conserving surgery.

10.4. Focused Ultrasound System

The MRgFUS procedures were performed with an ExAblate 2100 system (InSightec, Haifa, Isreal). The ExAblate 2100 bed consists of a focused ultrasound transducer with mechanical positioning, which is immersed in an oil bath, covered by a mylar membrane. The lesion tattooing procedure was carried out on the FUS console workstation, while pre and post ablation images were taken using the MR workstation before and after the system was locked, respectively. Figure 10.2 shows the general set up for MRgFUS treatments.

Figure 10.2: MRgFUS system set up showing an MRI scanner, FUS bed containing an US transducer and the FUS workstation (158).

The transducer has a resonant frequency of 1 *MHz.* The transducer can be electronically steered to avoid certain areas that are undesirable to be in the ultrasound field.

10.5. Optimisation of Pseudo Lesion Generation in an Animal Model

10.5.1. Choosing a Breast Tissue Model

A variety of animal models have been used in the breast MRgFUS literature including goat, rabbit, sheep and turkey (155, 157, 159, 160). In this section, several animal tissues were investigated for their suitability to mimic the human breast tissue environment, and for their suitability to place a pseudo lesion in for lesion tattooing experiments. Both lactating and non-lactating animals have been used in HIFU studies. Reasons for using lactating animals include the mammary gland being larger and thus having more tissue for ablation.

10.5.2. Method: Tissue Investigation

Three tissues were investigated: turkey, sheep and goat. Fresh turkey was sourced from the supermarket, with the criteria of as little added water as possible. Fresh sheep and goat mammary glands were sourced from local abattoirs. The less time between slaughter and experiment was best to prevent air bubbles and cavitation during focused ultrasound sonication due to tissue degrading.

An artificial random-shaped non-palpable pseudo tumour was injected as in Schmitz *et al* into the centres of the animal models. This pseudo tumour was composed of agar, food colouring and gadolinium contrast agent.

A T1-weighted FSPGR (fast spoiled gradient-echo) anatomical scan was acquired to assess the tissue. T1-weighted images are used in the planning stage on the FUS system so this type of imaging was chosen in this investigation, also. Images were acquired axially with the following parameters: repetition time/echo time (TR/TE), 4.512 *ms*/2.1 *ms*; field of view, 32x32cm; matrix, 256x256; flip angle 15; slice thickness 2mm; slice spacing 1mm; 25-45 slices (variable with sample size); NEX 8; Bandwidth, ±244Hz; frequency direction, right to left. A breast coil within the FUS bed was used.

The T1-weighted images were then transferred to the lesion tattooing program and an arbitrary template of 6 sonications planned around the pseudo lesion. The series was saved to a USB to be transferred to the FUS system for ablation. It was problematic to get the images onto the MRgFUS/MRI system in real time due to the MRI system being locked when in use by the FUS system. This was worked around by putting the images with the planned spots onto a USB and loaded straight onto the FUS system as 'CT images' rather than onto the MRI system. The spots are not overlays, but pixels of high intensity to depict the location of where sonications should be made. Previously, no literature reports a clinically feasible tool to plan and implement this template in the MRgFUS system.

The 6 spots were sonicated in turn with a cooling period of 52 seconds between each sonication. The user must be alert and monitor the reflection, temperature and cavitation graphs. There is an emergency stop button if the user feels that the transducer may be damaged or cavitation is occurring.

10.5.3. Results: Imaging and Lesion Tattooing

Figure 10.3 (a) shows the T1-weighted image of turkey breast tissue; with 10.3 (b) showing the resulting DICOM image with high intensity spots as the lesion tattoo plan to be uploaded onto the FUS system. Figure 10.4 shows the dissected turkey breast tissue.

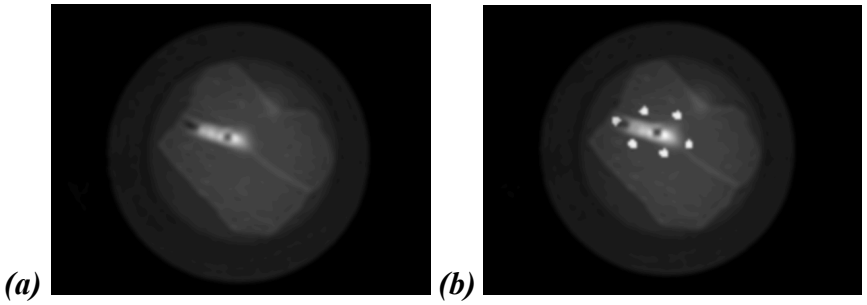

Figure 10.3: (a) T1-weighted image of turkey breast tissue and (b) the resulting DICOM image with high intensity spots as the lesion tattoo plan to be uploaded onto the FUS system.

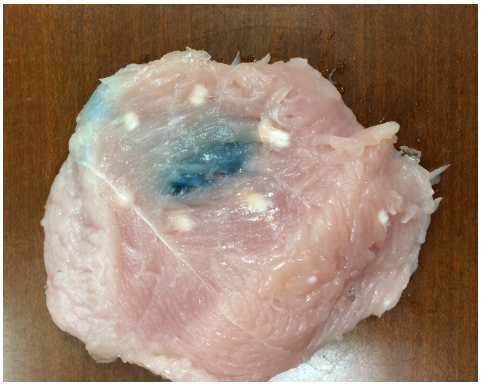

Figure 10.4: Turkey breast showing pseudo tumour and sonications around periphery.

Figure 10.5 shows a pair of sheep mammary glands imaged to assess the tissue structure and compatibility with the lesion-tattooing program. Imaging and FUS treatment was carried out 4 days post slaughter.

(a) 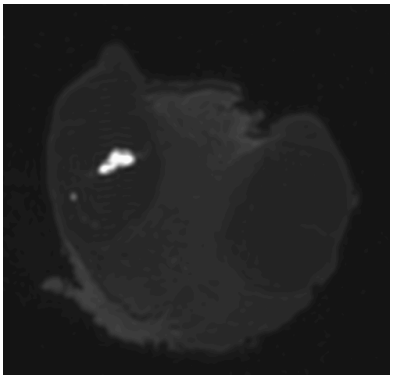 ***(b)*** 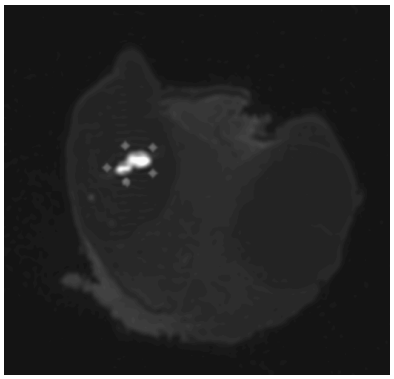

Figure 10.5: (a) T1-weighted image of sheep mammary glands and (b) the resulting DICOM image with high intensity spots as the lesion tattoo plan to be uploaded onto the FUS system.

Figure 10.6 shows the sheep mammary glands set up for FUS treatment. The image clearly shows the dispersing of gadolinium contrast agent. This is due to the sheep mammary glands containing fluid – milk from lactating. FUS treatment was unsuccessful because of the lesion dispersal and because the liquid would not heat up to high enough temperatures for tissue degradation.

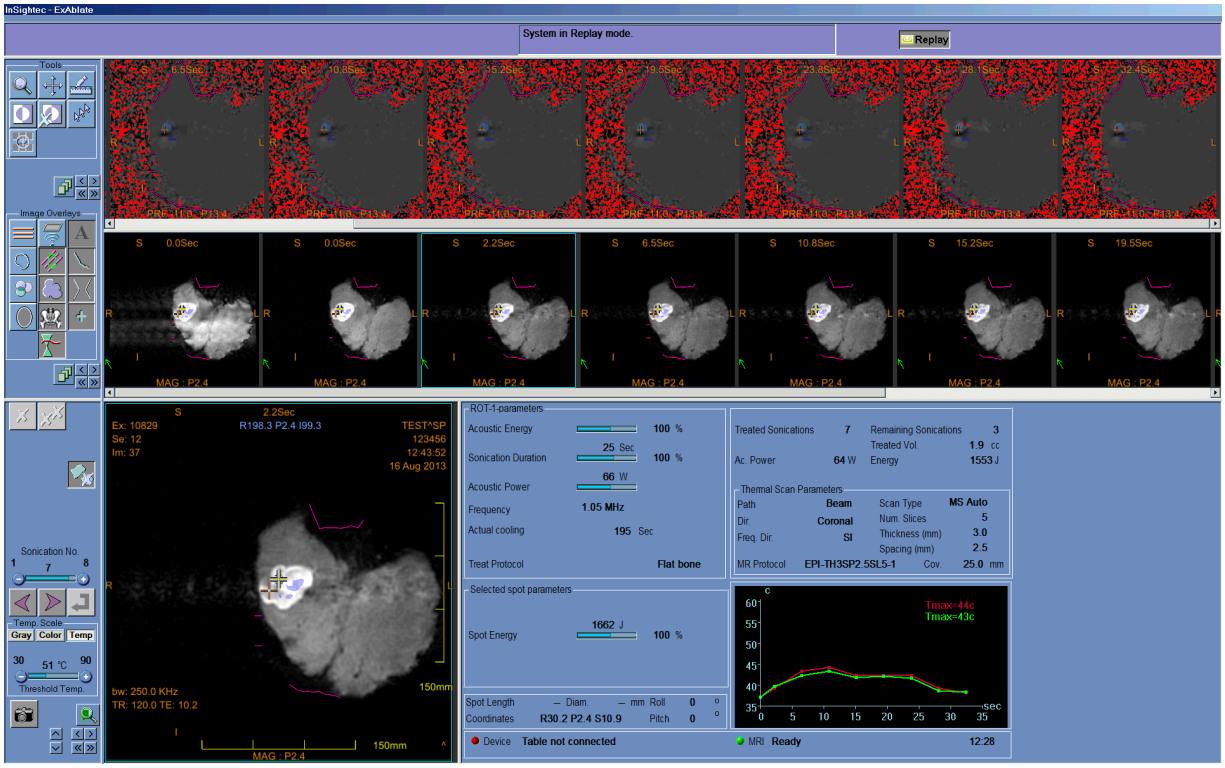

Figure 10.6: Sheep mammary glands set up for FUS treatment, showing the dispersing of contrast agent and low temperatures

Figure 10.7 shows a goat mammary gland imaged to assess the tissue structure and compatibility with the lesion-tattooing program. Imaging and FUS treatment carried out 24 hours after slaughter.

(a) 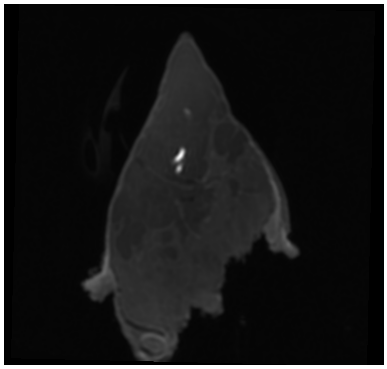 ***(b)*** 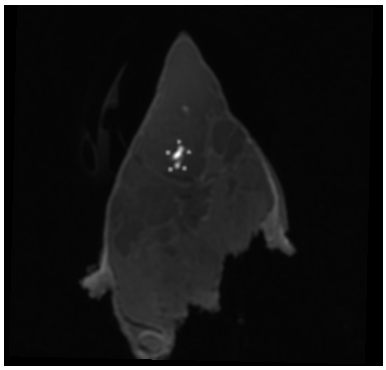

Figure 10.7: (a) T1-weighted image of a goat mammary gland and (b) the resulting DICOM image with high intensity spots as the lesion tattoo plan to be uploaded onto the FUS system.

Figure 10.8 shows the goat mammary gland set up for FUS treatment. Once again, the FUS treatment was unsuccessful due to a lack of temperature rise.

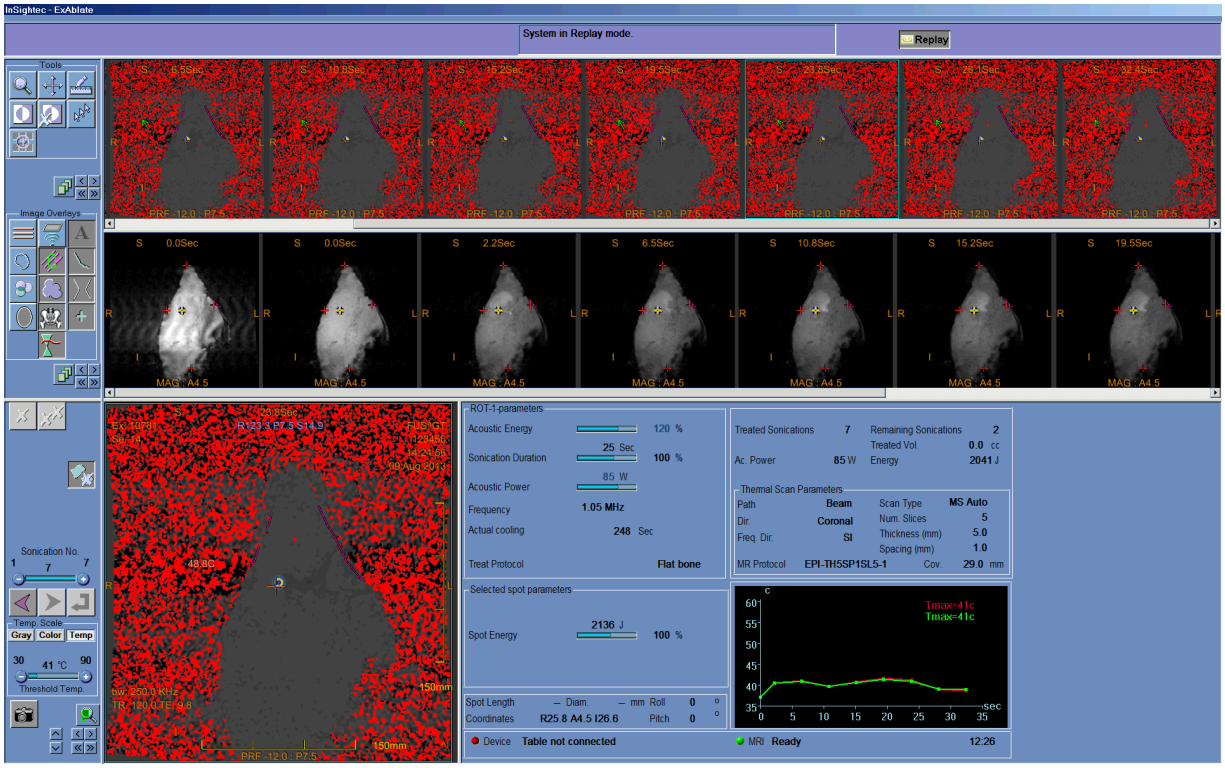

Figure 10.8: Goat mammary gland set up for FUS treatment, showing a PRF heat map and lack of increase in temperature at sonication location (41 degree Celsius is less than that needed to achieve successful thermal coagulation of cells).

10.5.4. Discussion

Sheep udders have been utilised by Bohris *et al (160)*, chosen for their fatty composition and comparison to the human breast. In this investigation, the sheep udders were full of milk and thus the pseudo lesion had dispersed and high enough temperatures could not be reached. A temperature of 55 degrees Celsius for a few seconds is needed to have a tissue degradation effect (139). Enquiries at local abattoirs led to the conclusion that all available mammary glands would be from lactating sheep.

Payne *et al* (159) described the tissue classification of goat udders and described their suitability in MRgFUS investigations. Both lactating and non-lactating goats were utilised, though the animals were alive for the experiments and the muscle tissue was targeted. In this study, temperatures were not high enough once again due to lactation, and there was a spread

of gadolinium throughout the milk. Guidance in placing the lesion could help, however it can be seen from Figure 10.8 that the majority of the udder was in fact milk. Sourcing non-lactating goat udders was also difficult.

Turkey breast tissue was the most successful of the three tissues investigated. The lesion did not disperse much in the short time frame between insertion and dissection. Dispersion of the lesion over time prompts further investigation. The FUS procedure was successful with an average maximum elevation temperature of 61 degrees Celsius for the 6 spots. The average dose diameter was 3 *mm*. Sonication duration was 20 *s*. Cooling between sonications was 52 *s*. Acoustic power was 86 *W*. Spot energy was 1730 *J*. The transducer frequency was 1.05 *MHz*. 100% of spot markers were visible upon dissection.

10.5.5. Method: Formal Palpation Tests

Here, differing spot patterns were investigated. In initial planning and in the literature it was assumed a circle template of spots would be superior. This palpation test was to see if this was true. Six different spots patterns were sonicated in turkey breasts. Two spots, 3 spots, 4 spots, a diamond of 4 spots, 4 spots clumped together and the original circle of spots were investigated.

Two independent investigators palpated the turkey breasts before and after dissection. There was no pseudo tumour to palpate and the investigators were blinded to the type of spot pattern and location. The investigators were both experienced breast imaging and HIFU researchers.

10.5.6. Results

Figure 10.9 shows the dissection of the 6 different spots patterns.

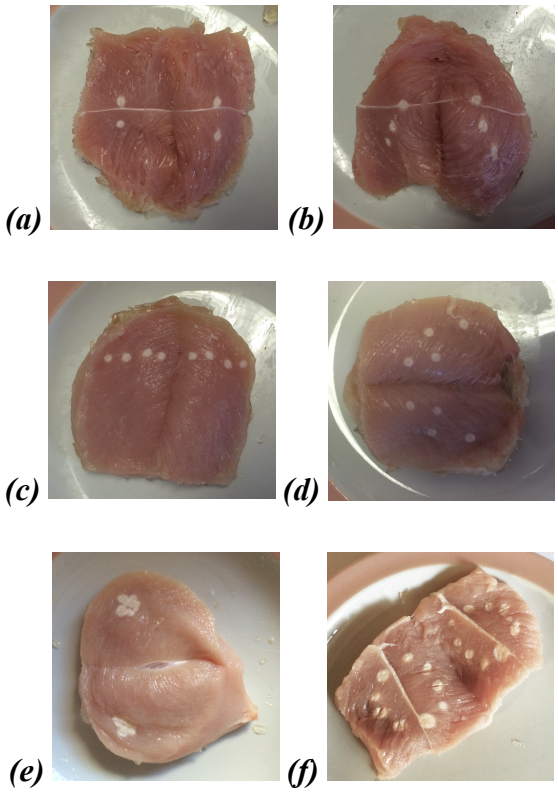

Figure 10.9: The 6 spot patterns shown after dissection.

Table 10.1 shows the results of the palpation tests.

Turkey breast	Investigator 1 before dissection	Investigator 1 after dissection	Investigator 2 before dissection	Investigator 2 after dissection
2 spots	No	Yes	No	Yes
3 spots	No	Yes	No	Yes
4 spots	No	Yes	No	Yes
Diamond	No	Yes	No	Yes
Clump	No	Yes	No	Yes
Circle	No	Yes	Yes (not certain)	Yes

Table 10.1: Results of palpation by Investigators 1 and 2 before and after dissection.

10.5.7. Discussion

Before dissection, palpation was not very successful. This may seem discouraging, however a surgeon would be more skilled in palpating and would also not be blinded as to where the occult tumour and thus template was, as they would be informed by imaging. Only when dissected and visible, were the markers palpable. This does not devalue the circle template as envisioned in Section 10.3, as the literature has shown that a circle template of sonications was 100% palpable with 0 positive tumour margins – a surgeon carried out these experiments in Schmitz *et al* (155). A skin or wire mark-up may be needed to guide palpation as presently sonications cannot be felt below the skin in this model.

10.5.8. Method: Shape and Injection Method of Pseudo Lesion

Agar, gadolinium, and food colouring were utilised in Section 10.5.1 to create a pseudo lesion that was visible on MR images and upon dissection. When producing artificial lesions to mimic the appearance of malignant lesions on MR images to be artificially resected in a study to investigate occult lesions, no food colouring should be used so that the surgeon is blinded to where the lesion is, apart from when palpating spot markers and looking at the MR images. Thus, agar mixed with gadolinium was deemed initially suitable in this section.

The method of injection was investigated here; the needle gauge size, the amount of sample to inject and the technique used to inject were varied.

The literature does not divulge methods of making lesions more than saying ‘random shaped’ and ‘approximately the same composition and volume’. Schmitz et al uses molten aqueous gel and gadopentetate dimeglumine (155).

Five phantoms using turkey breast tissue were made. The volume of agar and gadolinium were investigated, 0.5 *ml* or 1 *ml*. A simple, fan or long injection technique was accompanied to these volumes. Simple was defined as inserting the needle into the thickest part of the breast and injecting into the centre. Fan was defined as inserting the needle into a desired location within the breast, injecting some mixture, then repeating this in a different location to mimic focal disease. Long was defined similarly to simple, but as the mixture was injected, the needle was pulled out simultaneously to create a longer lesion.

These samples were imaged using T1-weighted imaging as in Section 10.5.2. This imaging was repeated 24 hours later. This was to see if the lesion ‘set’ within the tissue.

Volumes were calculated on a GE workstation using the volume calculation software. The tumour is segmented using a threshold. The slice is thickened to create a 3D rendering then this is auto contoured. This contouring is checked by eye and can be edited, then accepted and measured. An example is shown in Figure 10.10.

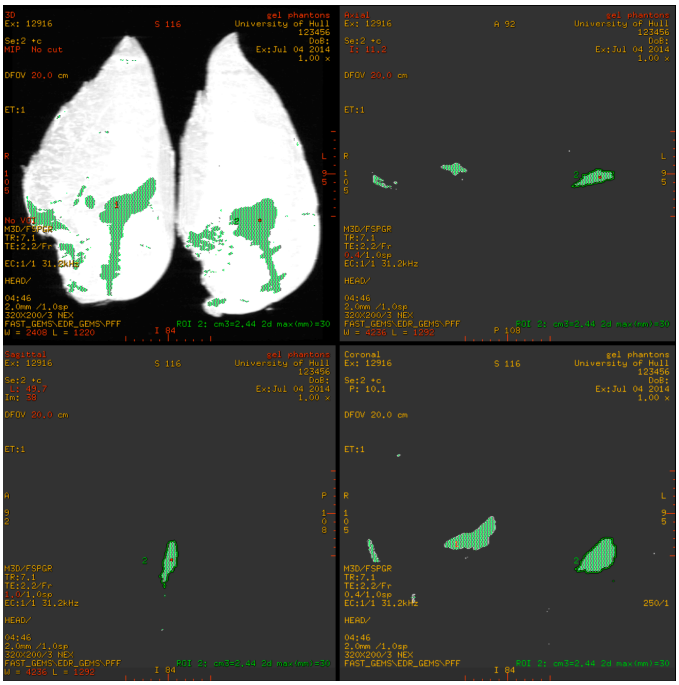

Figure 10.10: Calculating the volume of a pseudo lesion using GE software.

10.5.9. Results

Table 10.2 shows the volume of the pseudo tumour at t = 0 and t = +24 hours for the five samples and any relevant comments. Note t = 0 is approximately 10 minutes after injection.

Breast sample	Volume (cm^3)	Volume (+ 24 hours) (cm^3)	Comments
simple 0.5 *ml* tumour	2.40	11.9	Thin sample
simple 1 *m*l tumour	4.70	17.2	
fan 0.5 *ml* x 4 tumour	12.4	35.7	Not 'multi focal'
long 0.5 *ml* tumour	3.96	10.4	
long 1 *ml* tumour	3.71	12.9	Best

Table 10.2: The volume of the pseudo tumour at t = 0 and t = +24 hours for the five samples and any relevant comments.

Figures 10.11-15 show the differing pseudo tumours t = 0 and t = +24 hours for the five samples. Positioning was replicated as much as possible between the two scans.

(a) 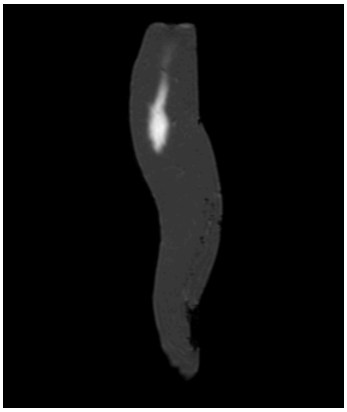 ***(b)*** 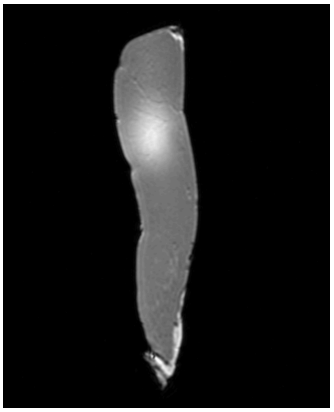

Figure 10.11: Simple 0.5 ml tumour at t = 0 and t = +24 hours.

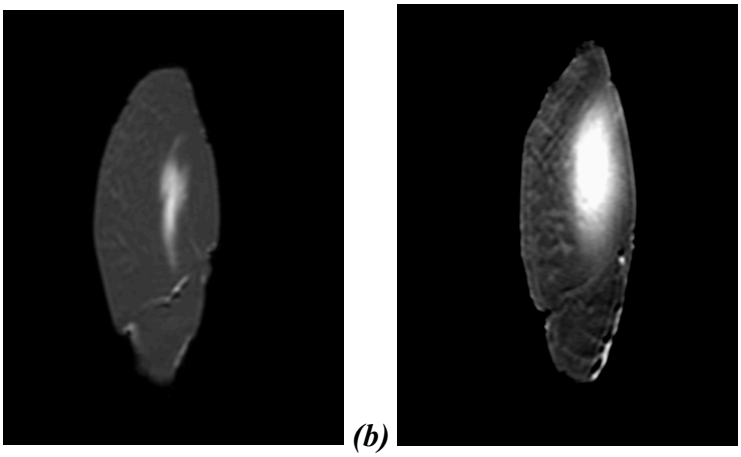

(a) *(b)*

Figure 10.12: Simple 1 ml tumour at t = 0 and t = +24 hours.

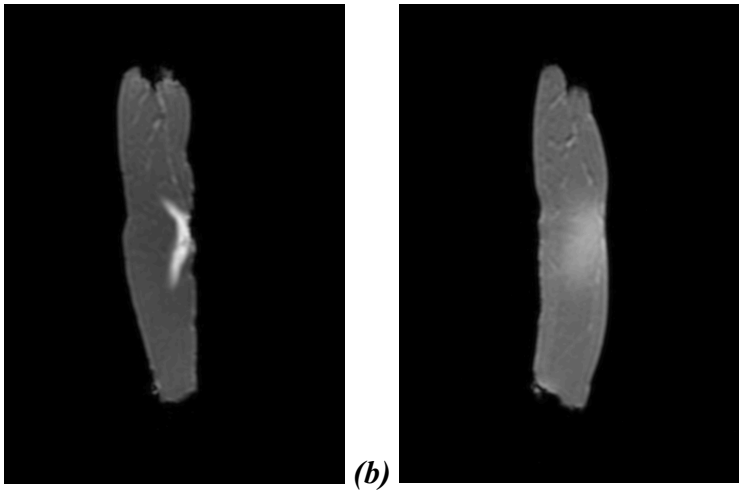

(a) *(b)*

Figure 10.13: Fan 0.5 ml x 4 tumour at t = 0 and t = +24 hours.

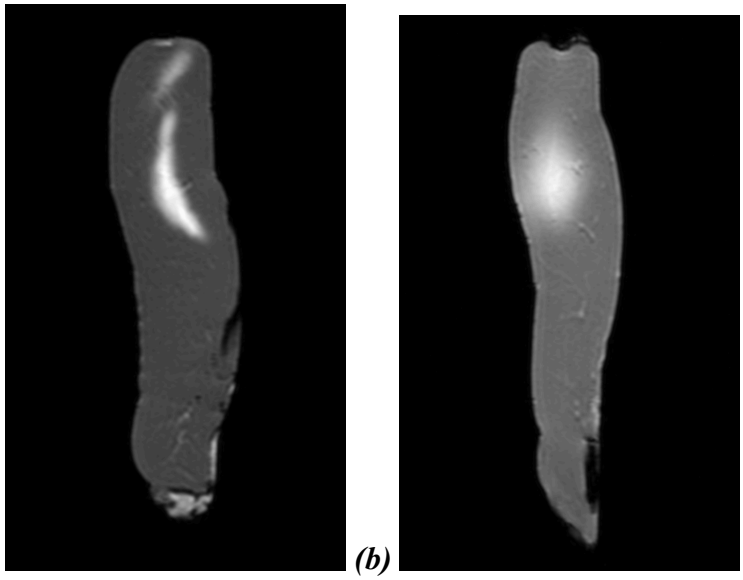

Figure 10.14: Long 0.5 ml tumour at t = 0 and t = +24 hours.

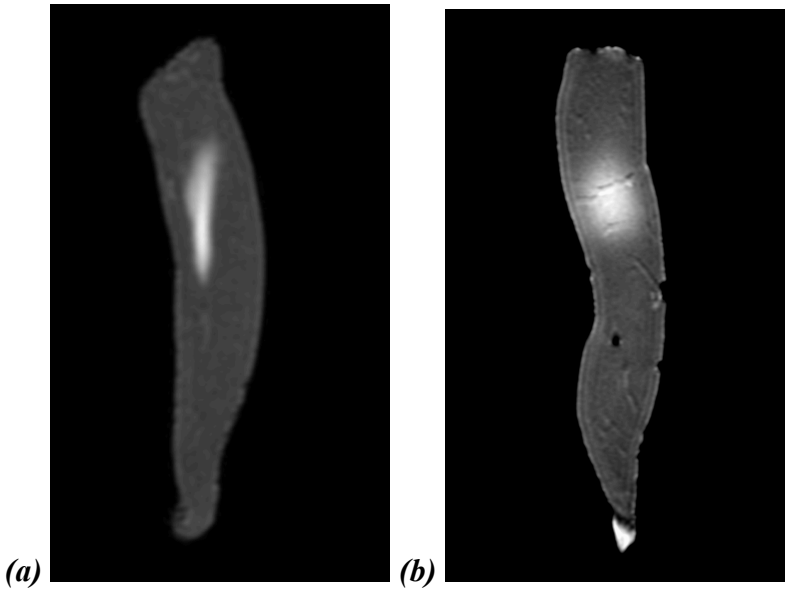

Figure 10.15: Long 1 ml tumour at t = 0 and t = +24 hours.

10.5.10. Discussion

It can be seen both qualitatively from Figures 10.11-15 and quantitatively from Table 10.2 that the lesions diffuse a lot over the 24-hour time period. The long 0.5 ml tumour diffuses the least with an increase of 163 %. The pseudo lesions may be diffusing down the muscles fibres, or through membranes depending on molecule size. The molecules need to be anchored for stability. The gadolinium molecules are the smallest, and the food colouring and agar are

relatively quite big molecules. Smaller time frames need to be investigated, with contrast agent removed.

10.5.11. Method: Diffusivity of Agar with Subtraction Images

The rate of pseudo lesion growth over a shorter and longer time scale was investigated. This was to see if the investigation should be carried out immediately, or is perhaps better once the lesion stabilised. Five turkey breasts were scanned over 2 hours and then plus 1 and 3 days. The long 0.5 *ml* injection method was used. Again, T1-weighted imaging was implemented as in Section 10.5.2, and subtraction images were processed to show growth visually.

Lesion volume calculations were carried out as in Section 10.5.8.

10.5.12. Results

Table 10.3 shows the growth in volume every 30 minutes over two hours and than at t = + 1 and 3 days. The pseudo lesions could be seen on MR images without contrast agent.

Time (mins)	Volume
0	2.24
30	2.77
60	2.75
90	2.51
120	2.69
Plus 1 day	3.96
Plus 3 days	4.12

Table 10.3: Growth of pseudo tumour volume over two hours and then at t = + 1 and 3 days.

Figure 10.16 shows the pseudo lesion at t = 0, at t = +3 days, and the subtraction of the two showing the growth of the pseudo tumour over time.

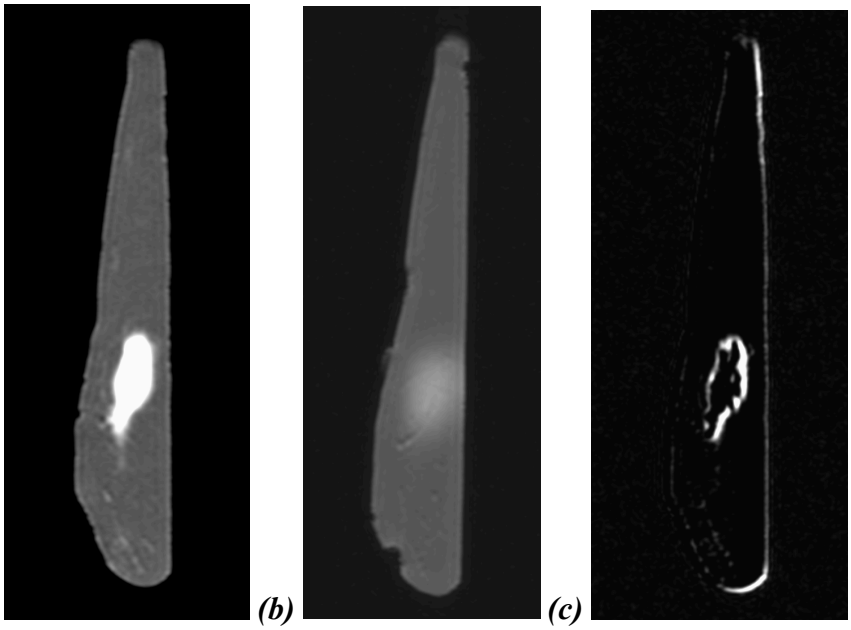

Figure 10.16: The pseudo lesion at (a) t = 0, (b) at t = +3 days, and (c) the subtraction of the two showing the growth.

10.5.13. Discussion

There was still significant diffusion of the pseudo lesion without gadolinium over time. Over three days there was an 80% increase in volume. Within a two hour period there was a 20% increase in volume. This indicates that the sooner the lesion tattooing experiment can be carried out, the better. Gadolinium was not needed to achieve contrast on MR images.

10.5.14. Method: Pseudo Lesion Chemical Composition

The reason for diffusivity of the pseudo lesion was postulated to be the chemical used - agar. The molecule needs to be anchored, whether it is large or sticky. The chemistry department at the University of Hull suggested alginic acid. Alginic Acid is a natural compound often used to mimic mucus in medical experiments. It has an almost neutral pH and is inexpensive.

20% molecular weight alginic acid was compared to agar gel. A 0.5 ml long injection technique using a 19G needle was used. For reference, 10% molecular weight is 1g per 10 ml water.

Imaging and volume calculation was carried out as in Sections 10.5.2 and 10.5.8.

10.5.15. Results

Figure 10.17 shows the increase in volume over time for the two chemicals.

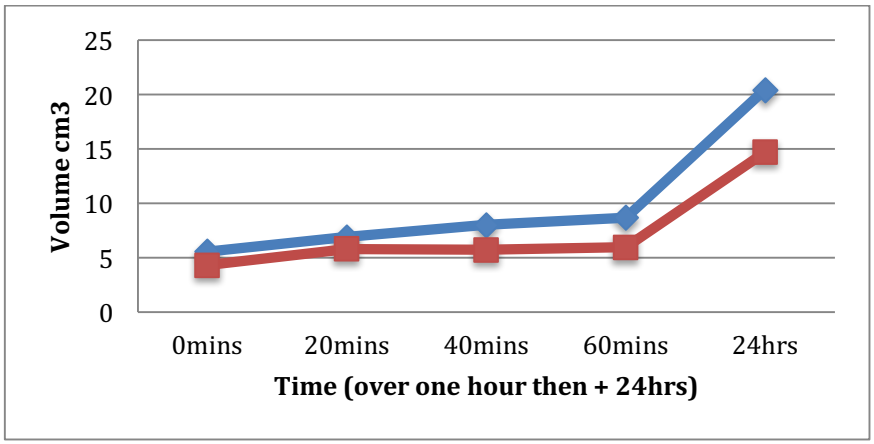

Figure 10.17: Growth of pseudo lesions made with alginic acid (Red) versus agar (Blue).

10.5.16. Discussion

Alginic acid has a marginally smaller diffusivity compared to agar. Alginic acid undergoes a percentage change of 242%, whilst agar undergoes a percentage change of 268%. The reduced increase in volume of the alginic acid lesion may be attributed to its increased stickiness.

10.5.17. Method: Turkey or Chicken

Since chicken and turkey are similar in composition, the two were investigated to compare the rate of diffusivity of the pseudo lesion. It was thought that perhaps the muscle fibres may be different between the two and those would be tracks for which the lesion chemicals could diffuse down.

Lesions were made as described in Section 10.5.14 using alginic acid in two chicken breasts and two turkey breasts. Imaging and volume calculations were carried out as in Section 10.5.14. The breasts were scanned every half hour from 9am until 3.30pm and then plus 24 hours. The experiment was repeated twice.

10.5.18. Results

Figures 10.18 and 10.19 show the graphs of pseudo lesion growth over time for chicken and turkey for both repeats of the experiment.

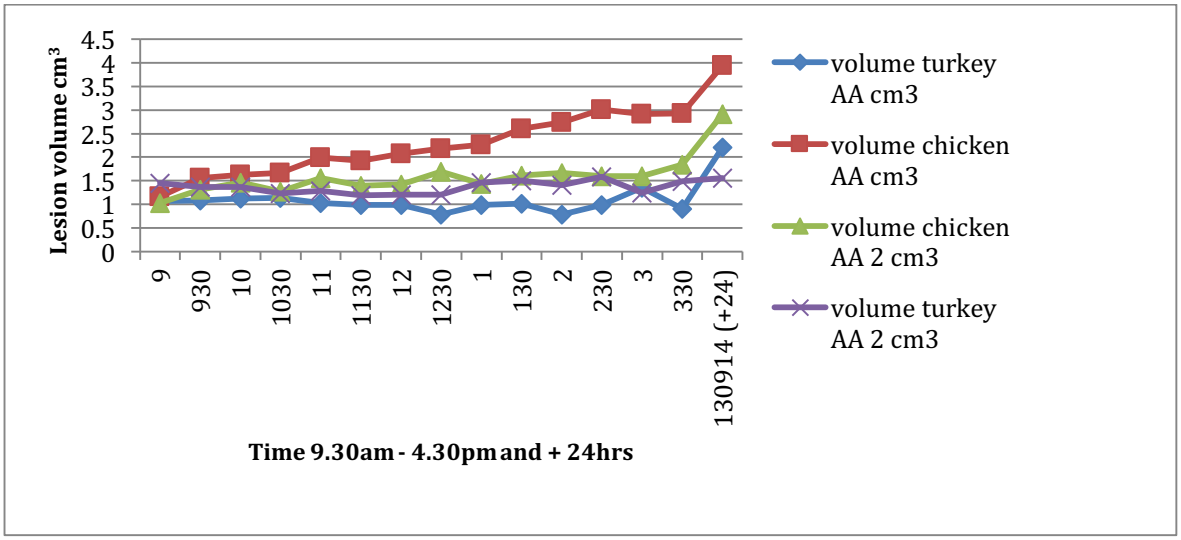

Figure 10.18: Comparing chicken and turkey – Experiment 1.

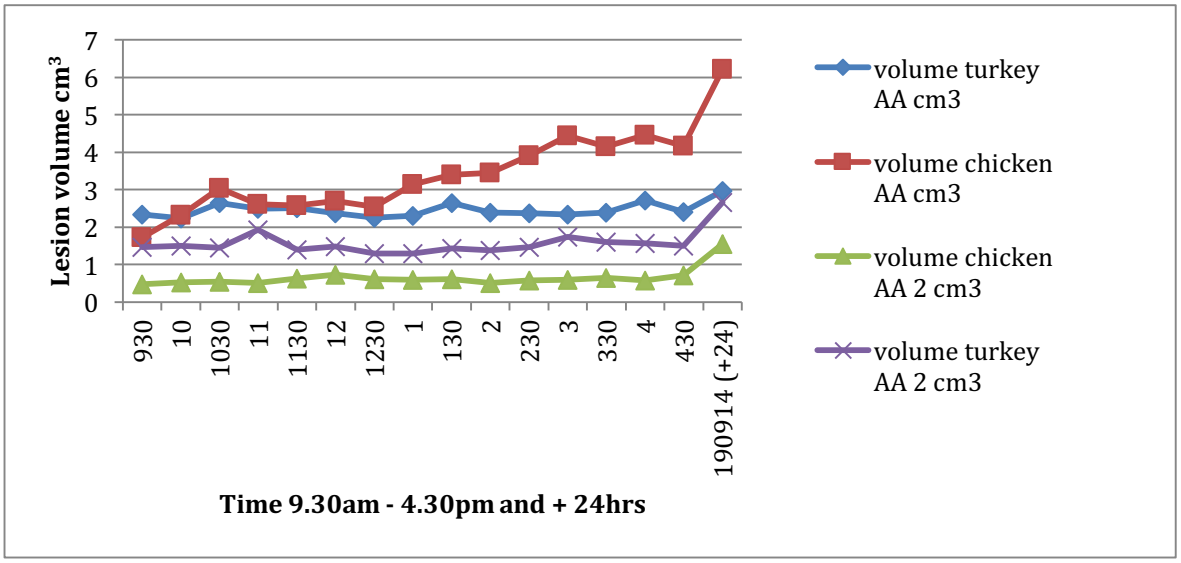

Figure 10.19: Comparing chicken and turkey – Experiment 2.

10.5.19. Discussion

Turkey shows the least growth in tumour size in both experiments and so chicken was not deemed a more suitable alternative to negate pseudo lesion diffusivity.

10.5.20. Conclusions

The aim of these preliminary experiments was to optimise an animal breast tumour model with pseudo lesion for future lesion tattooing experiments.

Firstly, turkey was deemed the most suitable animal tissue due to potentially more suitable models such as sheep and goat having complications if the animal was lactating, and unfortunately local abattoirs were only able to supply lactating animals.

Formal palpation tests were unsuccessful, but this was concluded to be due to investigators not being surgically trained as in the literature. Studies have shown that a circle of palpable markers result in no positive margins in turkey breast tissue (155).

The shape and injection method of pseudo lesions were investigated, with long 0.5 ml being best. The volumes of the different pseudo lesions were measured initially and then plus 24 hours. The lesions had diffused a lot and thus a smaller time scale to measure volume increase was needed as well as a longer time period to see if the lesion stabilized. Over a short time scale the lesion did not grow drastically and so any lesion tattooing experiments must be set up and completed as quickly as possible. The logistics of an experiment is outlined in the next section, and a full study would include numerous samples to be prepared as well as the time of a surgeon.

Next, a larger, stickier molecule was investigated to try and anchor the pseudo lesion upon injection. Agar was compared to alginic acid, of which the latter was found to have less diffusivity.

Turkey was compared to its similar counterpart of chicken, to see if the muscle fibres were of differing composition to prevent diffusivity, turkey was found to be marginally better.

In conclusion, a turkey breast animal model with a long 0.5 *ml* alginic acid pseudo tumour was found to be optimal, so long as the lesion tattooing experiment was carried out within 2 hours of injection.

10.6. Full Test of Lesion Tattooing in a Turkey Breast Tissue with Pseudo Tumour Model

The aim of this experiment was to investigate MRgFUS as a method for preoperative localisation of non-palpable breast tumours by assessing the visual presentation and palpability of MRgFUS created lesions an optimal animal model with pseudo lesion, and to thereby assess the accuracy of the in-house written MATLAB program to segment the lesion

from MR images, to plan the lesion tattoo sonication spots and its compatibility with the MRgFUS system.

The sonication spots are expected to appear discoloured (appearing as cooked areas of tissue) and should feel stiffer upon manual palpation if agreeing with previous studies (155). Food colouring was added to the artificial lesion so it was visible to the eye upon dissection.

10.6.1. Method: Breast Tissue Phantom and FUS Set-up

An artificial non-palpable lesion was created in the turkey breast by injecting a mixture of alginic acid and blue food colouring (1 *ml* in total) into the central thickest part of the breast using the long injection method. This created a lesion that was both visible to the eye upon dissection and visible on MR images. The breast was placed in a jug of gelatine, which was allowed to set, creating a breast phantom suitable for MRgFUS procedures. A body part cannot be placed directly on top of the transducer, as there is a safety margin to prevent skin burns and to prevent damage via reflection of ultrasound back to the transducer, thus the gelatine allows this elevation. Figure 10.20 shows the injecting of the artificial lesion mixture and Figure 10.21 shows the set breast phantom.

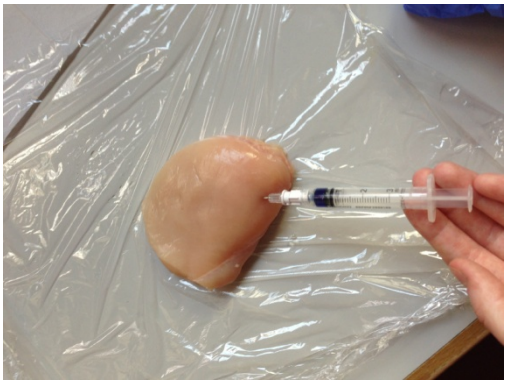

Figure 10.20: Injecting the alginic acid and food colouring mixture into the centre of the turkey breast.

Figure 10.21: The turkey breast suspended in the set gelatine.

A DQA was carried out to ensure the system was working correctly. The DQA phantom was then replaced with the breast phantom. Figure 10.22 shows the breast phantom in an MR safe container filled with degassed water with an acoustically transparent mylar window at the bottom and an acoustically absorbent plate at the top.

Figure 10.22: The turkey breast phantom in a container filled with degassed water with an acoustic window at the bottom and acoustically absorbent plate at the top.

The breast phantom was positioned above the transducer's mylar membrane, and a lubricant/water mix was used to give acoustic coupling between the bed's mylar membrane and the turkey phantom container's mylar membrane.

10.6.2. Method: Imaging and MATLAB Image Processing

T1-weighted images were acquired using an ExAblate plan bone protocol. T1-weighted FSPGR (fast spoiled gradient-echo) images were acquired. Images were acquired in all 3 planes for planning with the following parameters: repetition time/echo time (TR/TE),

4.512 *ms*/2.1 *ms*; field of view, 32x32 *cm*; matrix, 256x256; flip angle, 15°C; slice thickness 2 *mm*; slice spacing 1 *mm*; 25 (variable with sample size); NEX 8; Bandwidth, ±244 *Hz*; frequency direction, right to left. These images were then pushed from the 3.0 T workstation to another PC in the department so that the images could be saved on a USB for MATLAB processing in real time whilst the breast phantom was still on the FUS table.

The images from the MR workstation were loaded into the MATLAB lesion tattooing program. A suitable slice showing the artificial tumour was found. The artificial tumour was segmented (with a signal value = 1400) as shown in Figure 10.23. The 'fill and add margin' button created a convex hull of this outline, adding a blue margin (10 *mm*) as shown in Figure 10.24. The 'add sonication spots (auto)' button was used to create 5 spots and their radius was set to 2.5 *mm*. This radius was set as a reasonable estimation, however the FUS system will create cigar shaped sonications at a size controlled by the bone protocol chosen in later stages (either bone 15 or bone 20). Figure 10.25 shows the resulting DICOM image with high intensity spots as the lesion tattoo plan to be uploaded onto the FUS system. The series was saved to a USB to be transferred to the FUS system for ablation. This MATLAB processing step takes 5 minutes, so clinically may be acceptable whilst the patient is still on the bed in position for HIFU treatment.

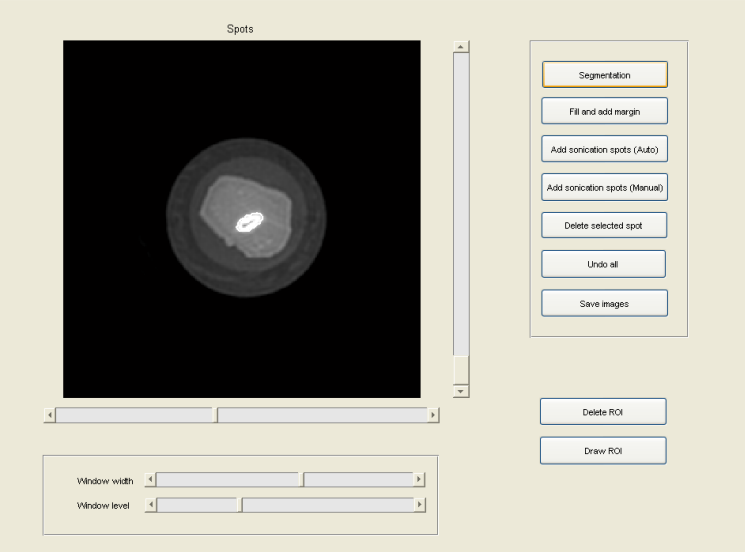

***Figure 10.23*: Outline of the artificial tumour in the lesion tattooing program.**

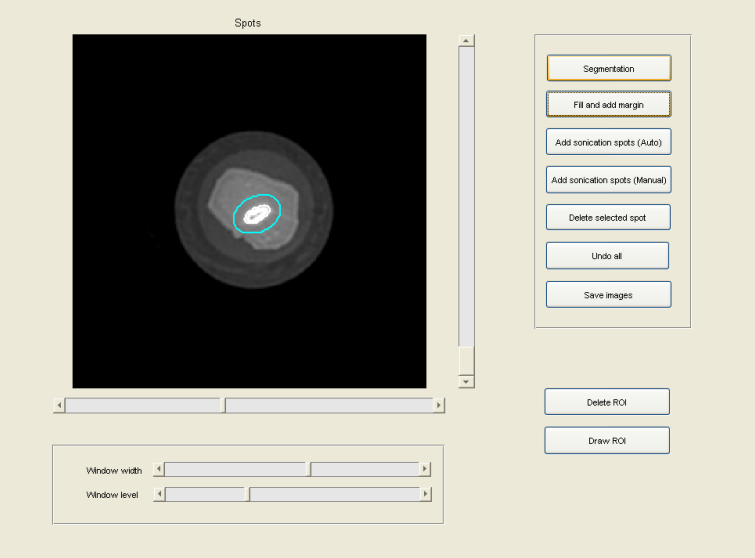

Figure 10.24*: *Outline after convex hull and adding a margin of 10mm in the lesion tattooing program.

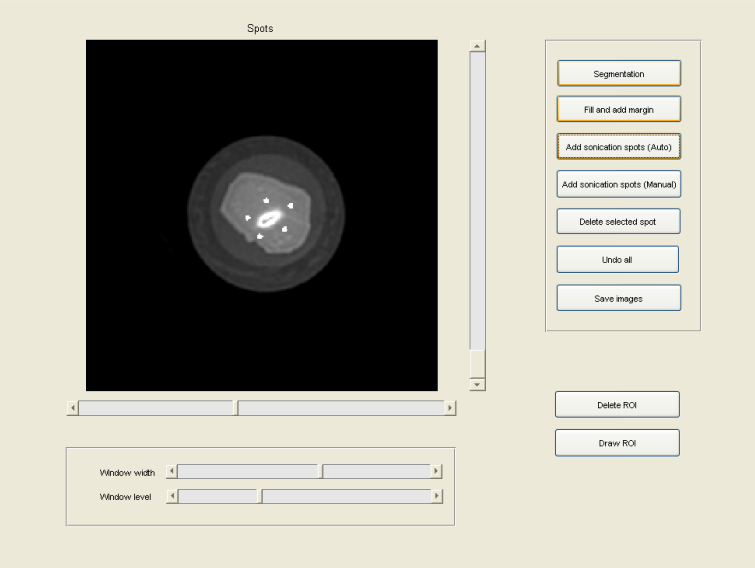

Figure 10.25: Final image of planned lesion tattoo spots as high intensity pixels in the lesion tattooing program.

10.6.3. Method: Lesion Tattooing of the Breast Phantom

The bone protocol was chosen for this procedure, which is less powerful than the breast protocol, set as such to account for bone attenuation of ultrasound. Localiser images were taken and the transducer was calibrated in the sagittal and axial planes. MR images were taken (note these images are exactly the same as the images taken previously to be processed

by MATLAB since the phantom had not moved). Fifteen sagittal, 15 coronal and 64 axial images were loaded. The MATLAB processed images were uploaded from the USB as CT images (64 axial), even though they are MR images. This was the only way that the two sets of images may be loaded and registered together. The two sets of images were registered by matching up the unprocessed and processed images visually. This was simple and no manual registration was needed since the two sets of images were exactly the same apart from the overlay of planned sonication spots on the processed set of images. Figure 10.26 shows the register stage. The turquoise appearance of the high intensity regions (artificial tumour and planned spots) is due to the CT adjustable brightness.

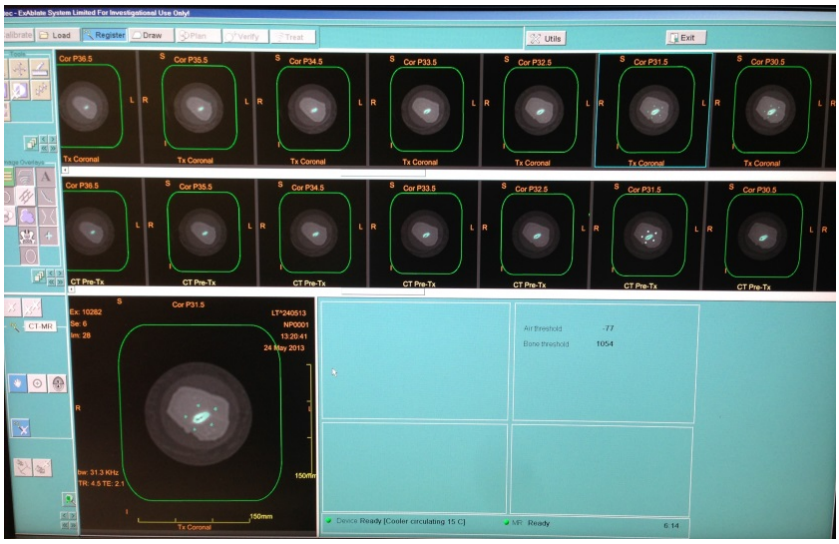

Figure 10.26: The register stage. The two sets of axial images are aligned and registered.

A skin line was drawn at the bottom of the phantom so the system knew where the safety margin for treatment would be. Limited energy density regions were drawn at the edges of the gelatine phantom to mark where the US beam could not go. A region of treatment had to be drawn but sonication spots may be placed anywhere within safety considerations, so an arbitrary polygon was drawn. The treatment protocol was changed to ‘bone 20’, instead of the commonly used ‘bone 15’, which created larger cigar shaped sonications to help ensure the spots could be seen upon dissection as it was more likely that they would be cut though. Fiducial markers also had to be added, a provision used for treatment in vivo to monitor movement. In the plan stage, sonication spots were added directly on top of the 5 spots created by MATLAB. The panic button must be tested at this point and any parameters such as acoustic energy may be adjusted. Next, in the verify stage, a sub lethal dose of focused

ultrasound is applied to an arbitrary spot away from the region to be treated (yellow cross shown in Figure 10.27). The user must then look at the temperature maps and place a marker where the FUS system has actually sonicated. This enables the system to make sure it is heating where the user is telling it to heat. This stage is done in the coronal and axial planes. Figure 10.28 shows reflection, Figure 10.29 shows cavitation and Figure 10.30 shows the final temperature achieved. These should not reach dangerous levels in the verification stage but are important to monitor in the treat stage at higher energies.

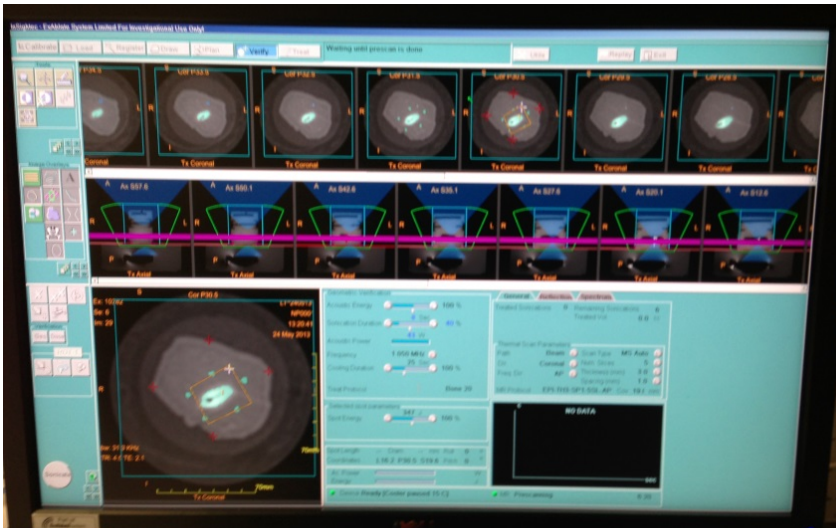

***Figure 10.27*: The yellow marker placed where the verification sonications will be carried out in the coronal plane.**

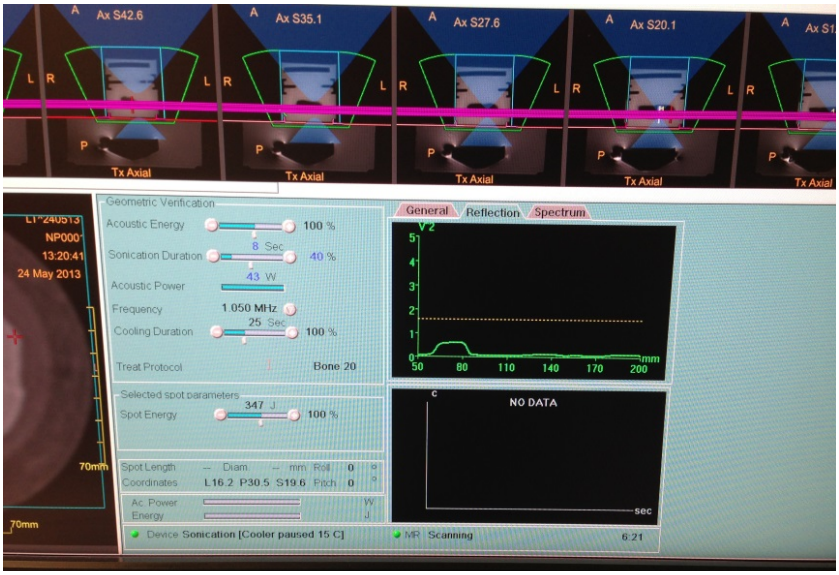

***Figure 10.28*: Graph to show the amount of reflection coming back to the transducer. If it reaches the threshold the sonication must be stopped to avoid damage to the transducer.**

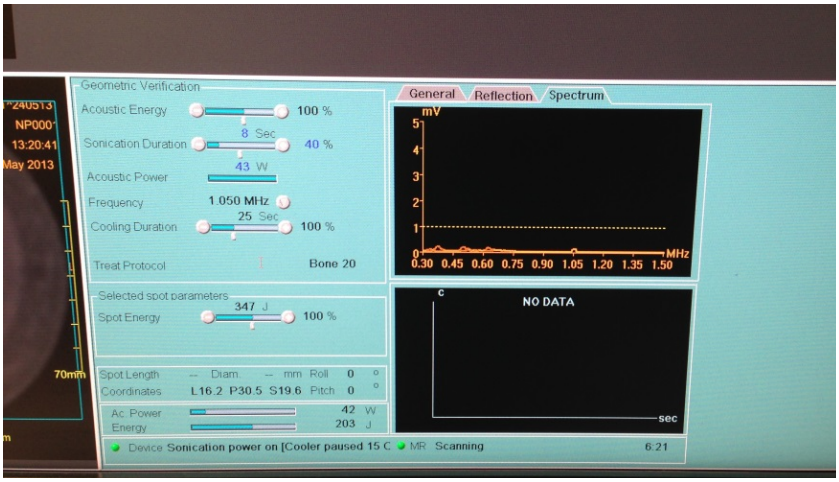

***Figure 10.29*: Cavitation spectrum. If the threshold is reached the sonication must be stopped to avoid uncontrollable and sudden temperature rises.**

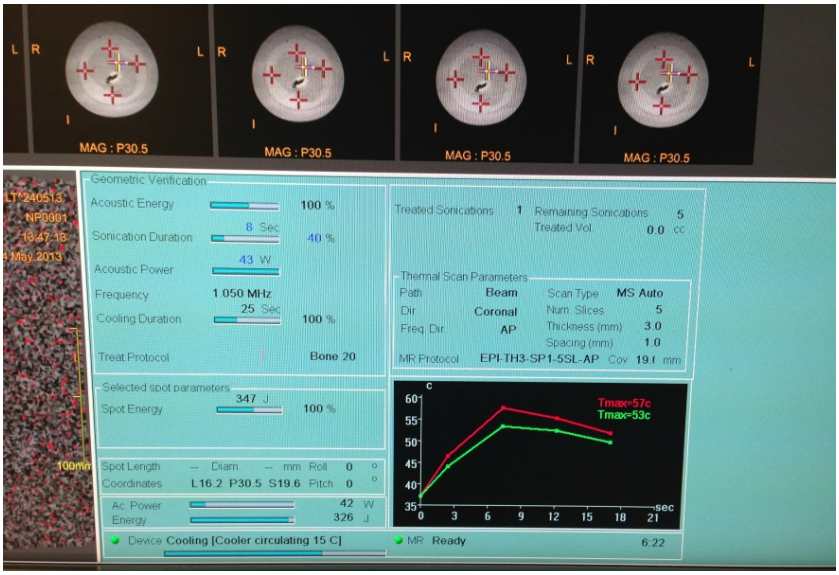

***Figure 10.30*: The final temperature graph (time versus temperature) showing a sub lethal dose.**

Once the user is content that the system is calibrated for treatment, the treat stage may be completed. The 5 spots were sonicated in turn with a cooling period of 52 seconds between each sonication. The user must be alert and monitor the reflection, temperature and cavitation graphs. There is an emergency stop button if the user feels that the transducer may be damaged or cavitation is occurring. A solution to avoiding such damage is to tilt the transducer; however this was not necessary in this experiment. Figure 10.31 shows the treat stage.

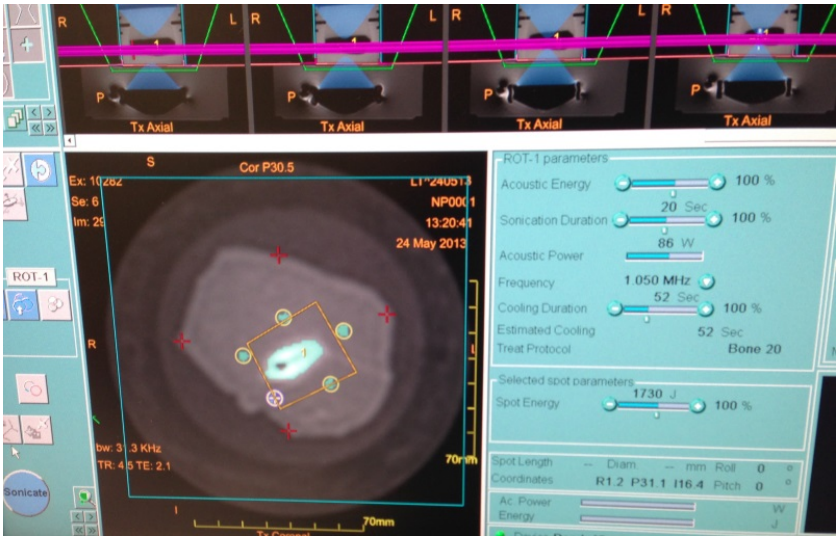

***Figure 10.31*: The treat stage. The highlighted spot is where the first sonication will be.**

After sonication, post-ablation MR images (standard T1-, T2-weighted and Proton Density) were taken on the MR workstation. The breast phantom was removed from the MRgFUS bed and the breast itself was removed from the gelatine. A knife was used to dissect the turkey breast in half to show the artificial tumour and lesion tattoos. The dissected breast was then examined and palpated.

10.6.4. Results

The average maximum elevation temperature was 63 degrees Celsius for the five spots. The average dose diameter was 3 *mm*. Sonication duration was 20 *s*. Cooling between sonications was 52 *s*. Acoustic power was 86 *W*. Spot energy was 1730 *J*. The transducer frequency was 1.05 *MHz*. 100% of spot markers were visible on post ablation MR-images and upon dissection.

The FUS system allows sonications to be reviewed in replay mode and the user can save snapshots to a CD. Sonication 5- 9 were the lesion tattoo spots. Sonications 1-4 were sub lethal dose verification sonications. All treatment sonications were monitored in the coronal plane. Figure 10.32 shows the first four sonicated spots of tissue in purple (sonications 5- 8) and the next sonication (9) to be carried out. Figure 10.33 shows the same as a PRF temperature map.

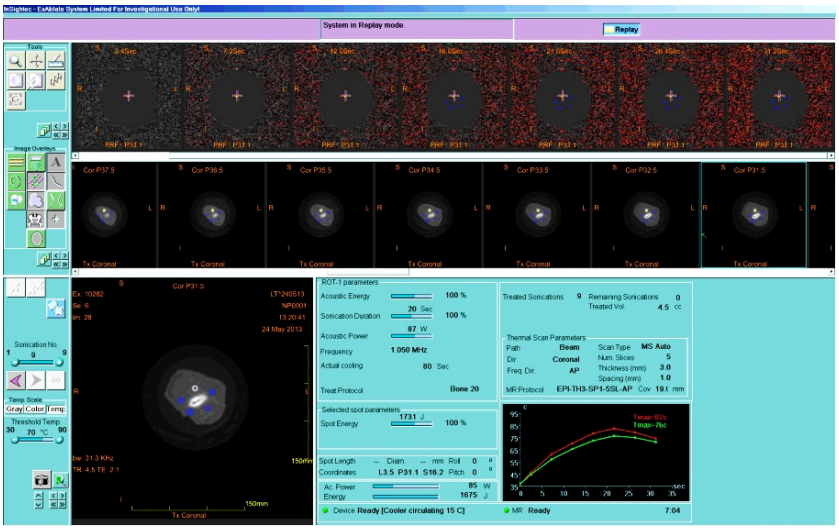

***Figure 10.32*: The first four lesion tattoo spots are shown in purple, and the final planned spot to be sonicated is highlighted in white.**

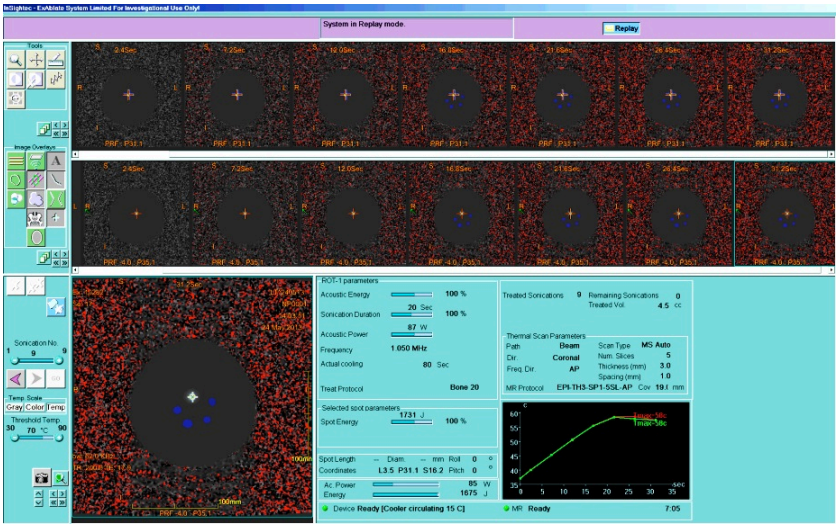

***Figure 10.33*: The PRF temperature map of the first four lesion tattoo spots (shown in purple), and the final planned spot to be sonicated is highlighted in white.**

Figure 10.34 shows the FUS systems calculated treated areas for all 5 sonications. The high intensity spots and high intensity artificial lesion from the MATLAB processed MR images are shown as turquoise, caused by the CT adjustable brightness. The size of the sonication spots is planned by the round yellow marker (Seen in Figure 10.31 showing the treat stage), and this correlates well to the purple areas showing sonicated spots of tissue. It was not possible to get a snapshot of the round yellow markers pre-ablation and the purple post-ablated tissue on the same image. The MRgFUS procedure was completed in 30 minutes.

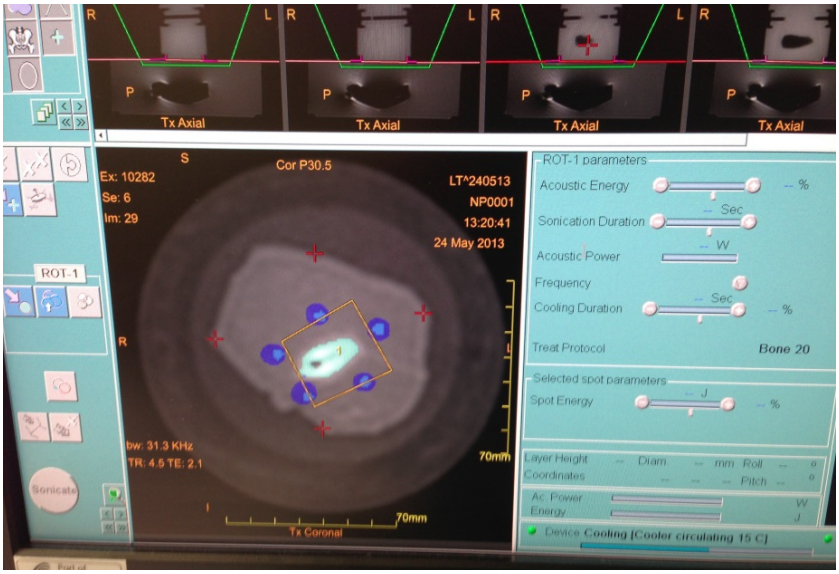

***Figure 10.34*: A photo taken after all lesion tattoo spots were sonicated. Sonicated tissue areas are in purple. The turquoise is not the area of planned spots, just the CT brightness of the MATLAB processed images.**

Figure 10.35 shows a T1-weighted MR image taken immediately after sonication. The artificial tumour can be seen clearly due to the gadolinium contrast agent. All 5 ablated lesion tattoo spots can also be seen as bright spots.

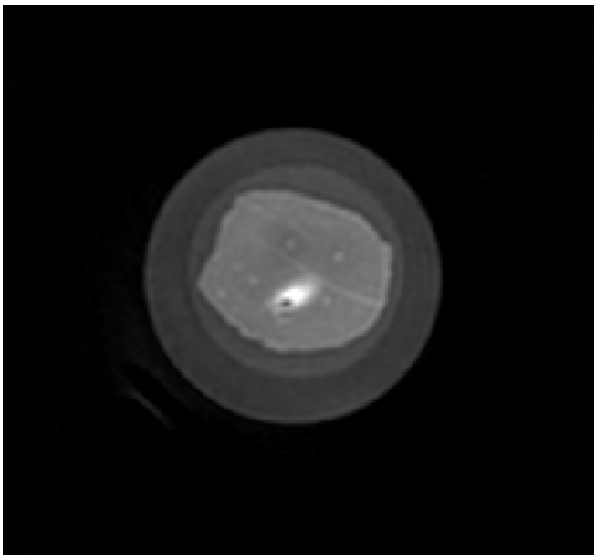

Figure 10.35: T1-weighted MR image post-ablation.

Figure 10.36 shows a T2-weighted MR image taken immediately after sonication. The artificial tumour is not as clear here. All 5 ablated lesion tattoo spots can also be seen as dark spots with white highlights. The spots are seen clearer on the T2 image than on the T1 image.

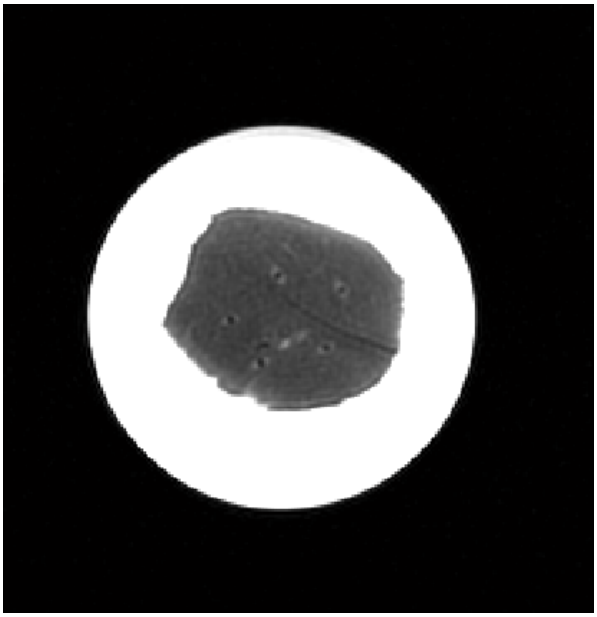

Figure 10.36: T2-weighted MR image post-ablation.

Figure 10.37 shows a PD-weighted MR image taken immediately after sonication. The artificial tumour can be seen as a bright area. All 5 ablated lesion tattoo spots can also be seen as dark spots, they are not as clear as the T2-weighted MR image but are still visible.

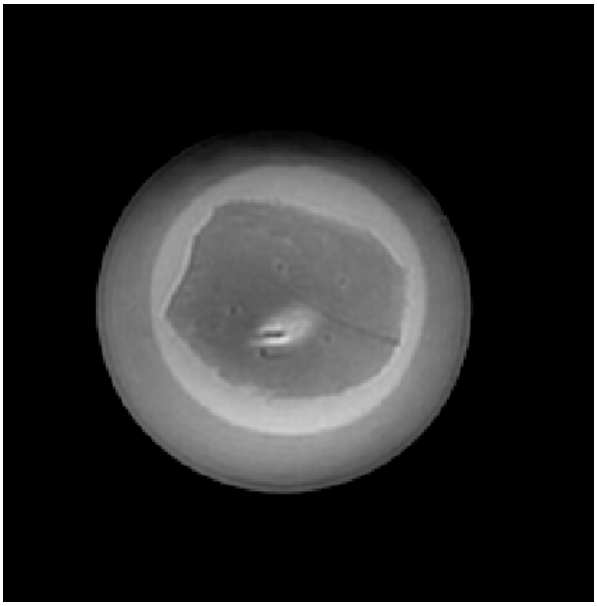

Figure 10.37: Proton density-weighted MR image post-ablation.

Figure 10.38 shows the breast removed from the gelatine phantom. The injection location can be seen with remnants of the blue food colouring; however there is no external indication of thermal damage or discolouration due to the MRgFUS procedure in the form of skin burns or other manifestations.

Figure 10.38: Breast before dissection.

Figure 10.39 shows the dissected breast tissue. The artificial tumour is visible as the blue area due to the blue food colouring. It is surrounded by the 5 sonication spots, clearly 'cooked' and presenting as white tissue. The placement of spots matches the MATLAB planned lesion tattoo (Figure 10.25), the pre-ablation plan on the FUS workstation (Figure 10.31), the post-ablation purple areas of tissue ablation on the FUS workstation (Figure 10.34) and the post-ablation T1-, T2- and PD-weighted MR images (Figures 10.35-37). See Figure 10.40 for a comparison of these images. The artificial tumour was nonpalpable upon dissection. The 5 sonications were palpated and felt to be stiffer than the surrounding, un-ablated breast tissue but could not be felt before dissection.

Figure 10.39: Breast after dissection.

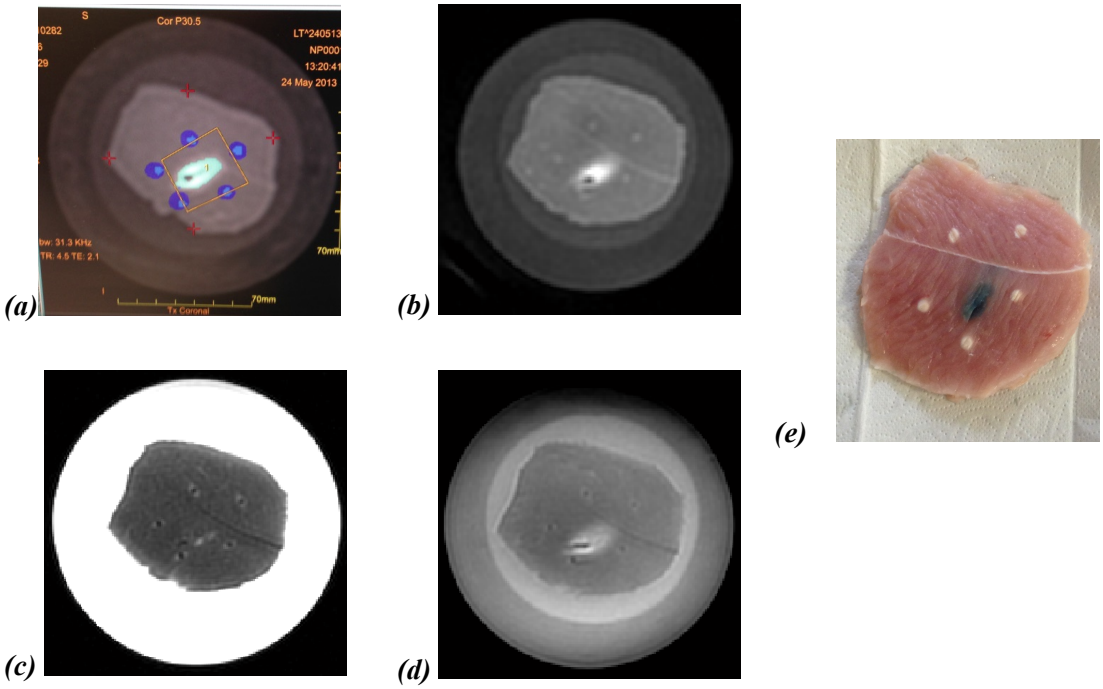

Figure 10.40: A comparison of the dissected breast tissue and MR images.

10.6.5. Discussion and Conclusions

This experiment has proved that successful MRgFUS lesion tattooing is conceivable with an optimised animal model. The post-ablation MR images and dissection of the turkey breast revealed that the sonications were made in the desired places and the hypothesis that these

sonications would be tougher than surrounding tissue and would appear the colour of cooked turkey was correct.

The MATLAB lesion tattooing program achieved the aims required. It can create a template of planned sonication spots for a lesion tattoo by automatically segmenting the tumour, creating a convex hull, adding a margin and automatically placing a desired number of spots around this margin. The processed images can be uploaded onto the FUS system with ease and the MATLAB processed images are fully compatible with the system. One improvement would be to enable the user to choose the location of the first spot plotted around the outline of the lesion tattoo margin.

The advantages of using MRgFUS for pre-surgical localisation are clear. It is non-invasive and does not require the insertion of a needle wire, which is the current technique used in UK hospitals. It allows any shape of tumour to be delineated, which needle wire localisation does not. Another advantage is that the tumour can be removed in total, leaving it intact for pathologic examination after surgery.

A question to ask is up to how long before surgery may a patient have this procedure carried out for it to still be effective? With a needle wire, the procedure for pre-surgical localisation of the tumour would be done the same day of the surgery. With MRgFUS, the tissue is necrosed and would not heal, so perhaps an advantage of MRgFUS lesion tattooing is that the time frame is more flexible.

There are, as with any treatment, some disadvantages that must be considered. Some patients have described pain, and have experienced skin burns with full ablation of breast tumours using MRgFUS. Patients would have local anaesthetic and mild sedation for the procedure to manage pain. These solutions would also help alleviate anxiety and claustrophobia if these feelings were experienced. Skin burns are avoided by adhering to strict guidelines preventing some breast configurations from undergoing MRgFUS procedures. There are FUS safety margins of the chest wall and the distance between the tumour and skin surface. MRgFUS is also an expensive procedure, accounting for the cost of the MRI scanner and FUS system. However, additional costs for reoperation could be eradicated with lesion tattooing if it was found to be an improved technique upon needle wire placement (leading to less positive margins). Patient anxiety and stress from further operation would also be

removed. There are also time constraints to consider, if an MRgFUS procedure takes longer than NW placement, then patient anxiety will be amplified.

The limitations of this particular experiment are acknowledged. Turkey breast is commonly used for breast mimicking phantoms, but it is very different from the human breast with respect to the absence of adipose and fibroglandular tissue. Also, manual palpation was not carried out by a surgeon. It should be noted that ex vivo tissue is cooler than in vivo and so the surrounding tissue of the sonications may be stiffer. Therefore it is proposed that in vivo sonications may be more palpable.

Future work should compare NWL to lesion tattooing in this animal model, with palpation and resection carried out by a trained breast surgeon. In the long term, a clinical trial should be envisioned to ultimately compare MRgFUS lesion tattooing to needle-wire localisation in breast cancer patients.

The aims of this chapter have been achieved; 1) to build a clinical tool to plan breast conserving surgery utilising MRgFUS as a means for creating non-invasive markers; 2) to optimise an animal breast tissue and pseudo tumour model; and 3) to carry out formal palpation tests as proof of feasibility.

11. Thesis Summary

Almost four years have passed since starting the work in this thesis. Breast cancer is still the most common cancer in women and the most common cause of cancer death in women. According to statistics, 48,000 women in the UK have died since this work was started (4).

The work presented here concentrates on standardising non-invasive and non-ionising advanced diffusion MRI to diagnose types and subtypes of breast cancer, and to plan breast-conserving surgery using MRI and focused ultrasound. With shifts in healthcare technology, and a push toward personalised care for individual patients with inter- and intra-heterogeneous breast cancer, these kinds of imaging and treatment planning are essential.

Firstly, the role of MRI in breast cancer was presented. MRI has the ability to probe cancer physiognomies such as heterogeneity, angiogenesis and proliferation. In Part 1, the main focus of this thesis, Intravoxel Incoherent Motion (IVIM) imaging was optimised and applied in healthy volunteers and then clinically in pre neoadjuvant breast cancer patients to understand and better characterise the tumour microenvironment of breast cancer, especially in malignancy types and molecular subtypes. Several studies have proven the potential of IVIM in breast cancer, with the original model proposed in the 1980s becoming more popular due to technological advances.

There is variability in the IVIM parameters in the literature, and no consensus on the MRI protocol or the fitting method to use to calculate the IVIM parameters from MR images. To achieve a standardisation, in Chapter 5, optimisation of IVIM protocols was carried out using a far-reaching and robust statistical method over several iterations, producing a protocol to precisely calculate the three IVIM parameters (D, diffusion, f, perfusion fraction and D^*, micro capillary 'pseudo' diffusion). An optimal set of b-values ideally creates good quality images for viewing a lesion, enables precise post processing, and will be part of a clinically feasible protocol i.e. usable on the majority of MR scanners and in a short scan time. The b-value protocol (Protocol F) produced and applied in a clinical trial was: 0, 10, 24, 46, 71, 135, 221, 355, 567, 900 s/mm^2 with a scan time of less than 5 minutes.

Various fitting methodologies and IVIM models used in the literature were compared using normal tissue data from healthy volunteers in Chapter 6, and the segmented fitting method of signal data from images was deemed most precise. Several protocols were

investigated from the iterations presented in Chapter 5. The final, clinically optimal protocol from the fourth iteration of optimisation unsurprisingly had the best repeatability and lowest mean squared error. The breast is an organ in which a measurable perfusion fraction has been disputed, but this work supports that there are measurable micro capillary networks in healthy breast tissue. Protocol F is shown in Figure 11.1 for two repeats – the images are of good quality and enabled precise fitting.

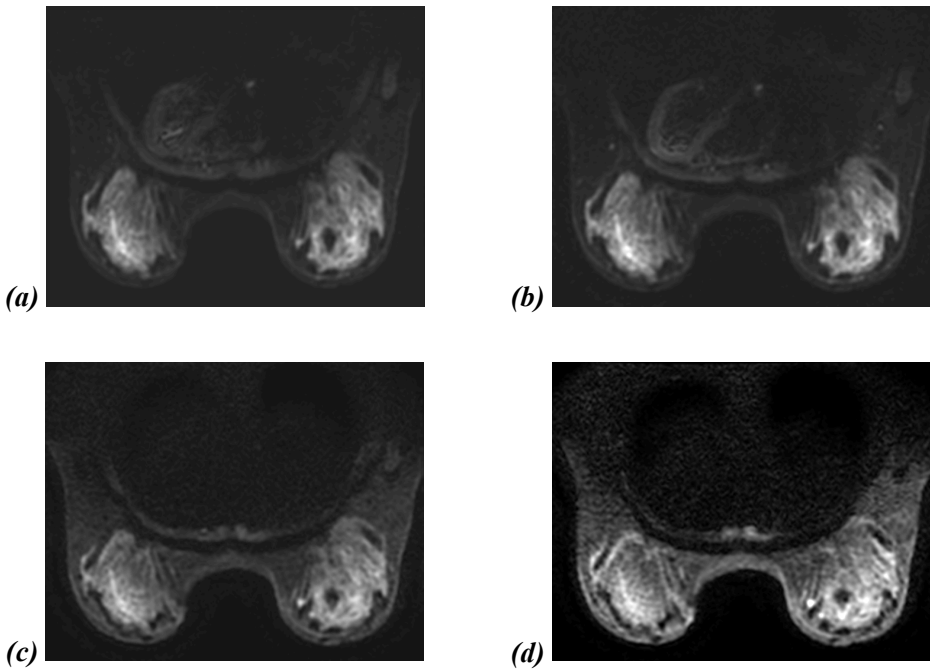

Figure 11.1: Protocol F in a healthy volunteer b = 0 s/mm^2 (top) and b = 900 s/mm^2 (bottom) for repeats 1 (a, b) and 2 (c, d). Repeatability for D_m, D, f and D* ranged from 8 – 85%.

In chapter 7, a pilot study in 19 patients proved the feasibility of optimised IVIM and the chosen fitting method in breast cancer patients at the CMRI. Then, a full clinical study using Protocol F was carried out in 58 patients to fit IVIM parameters and investigate their correlation with tumour physiognomies characterised by subtyping. Significant differences between malignancy and normal tissue in the contralateral breast were found. Several more significant differences in tumour grade and type were found. The results for *f*, *D* and *D** agree well with previously reported values in the literature. Considering Table 4.1 which summarises relevant breast IVIM literature; *D* is of the order of 0.001 to 0.0001 mm^2/s; *D** is of the order of 0.01 to 0.001 mm^2/s; and *f* ranges up to 30% (0.30). Using IVIM to

quantitatively identify tumour subtypes has the potential to add specificity to multiparameteric MRI exams, enable diagnosis through imaging, benefit therapy making it tailored and earlier, and could even minimise the need for biopsies and pathological diagnosis.

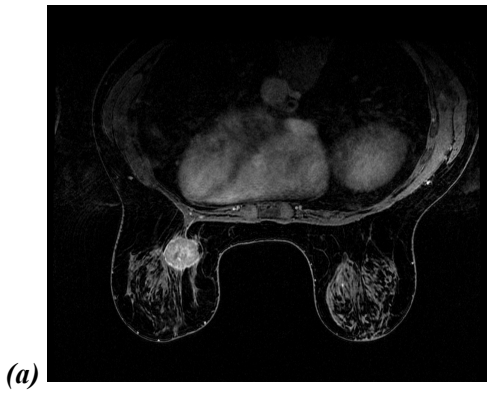

(a)

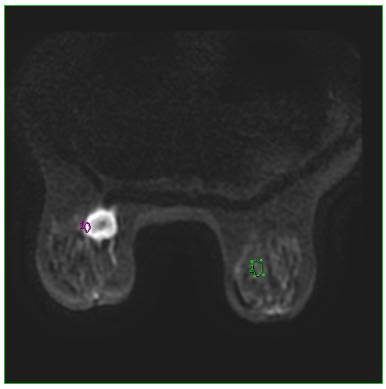

(b)

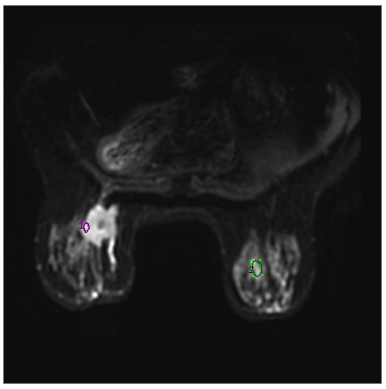

(c)

Figure 11.2: Protocol F in a breast cancer patient (a) Post contrast T1-weighted anatomical scan showing lesion in left breast (bright) and IVIM images (b) b = 0 s/mm^2 and (c) b = 900 s/mm^2 with ROIs in the malignant lesion (pink) and normal parenchyma (green). Age, 45 years; reason for scan, pre NAC staging; lesion type, IDC, grade 3, triple negative; treatment, NAC. f = 0.0661, D_m = 0.000613, D = 0.000552 , D* = 0.00549.

In Chapter 8, the optimised b-value scheme was supported by Monte Carlo simulations, calculating expected mean squared errors over 50,000 runs. Real data from clinical studies lay within these limits.

In Chapter 9, a computed DWI tool was built as an adjunct to the IVIM scan so that clinicians can generate traditionally used higher b-value images if desired. This cDWI tool generates better quality images with less noise than acquired DW-images.

Additionally, in Part 2, Chapter 10 furthers research of MRI and high intensity focused ultrasound as tools for surgical planning. A clinical surgical planning tool is presented, along with the optimisation of an animal pseudo tumour model using turkey and alginic acid, and then a full feasibility test was documented. Utilising MRgFUS to mitigate reoperation and positive tumour margin status would be beneficial for breast cancer patients undergoing breast-conserving surgery.

11.1. Future Work

Future work in IVIM in breast cancer should develop this optimised protocol in a larger cohort of pre neoadjuvant patients to confirm IVIM's suitability to diagnose types and subtypes of breast cancer. Non-optimised protocols have been utilized in subtyping cancers with significant results in 2015 (79). Full tumour analysis, instead of single slice in the most malignant part of the tumour, would be beneficial in quantifying the IVIM parameters more precisely and perhaps more accurately. Recent literature in 2016 has applied non-optimised IVIM in predicting response to chemotherapy in breast cancer patients, with significant differences found for D and f between pathologic complete response (pCR) and non-pathologic complete response (113). Confirming the correlation of IVIM parameters to the molecular structure of cancer is also of importance, through phantom work such as measuring flow through micro tubes and measuring diffusion in different breast cancer sub type cell cultures. Quantitative MRI has been shown to improve upon morphological imaging. The ultimate goal is to present a scan that can diagnose and have the potential to predict prognostic outcomes based on quantitative imaging to be part of a personalised medicine regime.

Future work in terms of lesion tattooing for pre surgical localisation should compare existing methods of standard of care pre surgical localisation (e.g. needle wire placement) against lesion tattooing in such an optimised animal model, then in human breast cancer patients. Surgical expertise should be implemented in future studies. This is a non-invasive means of delineating commonly occult tumours, which has the potential to minimize reoperation rates and local recurrence.

12. Bibliography

Stuart W. Young, Magnetic Resonance Imaging: Basic Principles, Second Edition, Raven Press, New York City, 1988.

Donald W. McRobbie, MRI From Picture to Proton, Second Edition, Cambridge University Press, New York City, 2007.

Daniel B Kopans, Breast Imaging, Second Edition, Lippincott – Raven Publishers, Philadelphia, New York, 1997.

Ferenc A. Jolesz, MRI-Guided Focused Ultrasound Surgery, Informa Healthcare USA, New York City, 2008.

Junru Wu, Emerging Therapeutic Ultrasound, World Scientific Publishing, Singapore, 2006.

13. References

1. Mansfield P, Maudsley AA. Medical imaging by NMR. The British journal of radiology. 1977;50(591):188-94.

2. Barron AR. Physical Methods in Chemistry and Nano Science: OpenStax CNX; 2015.

3. MRI Scanner Schematic: Coronary Heart Publishing Ltd 2016 [Available from: http://cardiologyhd.com.

4. Breast Cancer Now Statistics 2016 [Available from: http://breastcancernow.org/about-breast-cancer.

5. Macmillan Cancer Support Statistics 2016 [Available from: http://www.macmillan.org.uk/information-and-support/breast-cancer.

6. Breast Cancer Care Statistics Update 2015. 2015.

7. Phipps RF, Perry PM. Familial Breast-Cancer. Postgrad Med J. 1988;64(757):847-9.

8. Cancer Research UK Statistics 2016 [Available from: http://www.cancerresearchuk.org/about-cancer/type/breast-cancer/where-this-breast-cancer-information-comes-from.

9. Anders CK, Fan C, Parker JS, Carey LA, Blackwell KL, Klauber-DeMore N, et al. Breast Carcinomas Arising at a Young Age: Unique Biology or a Surrogate for Aggressive Intrinsic Subtypes? Journal of Clinical Oncology. 2011;29(1):E18-E20.

10. Anders CK, Hsu DS, Broadwater G, Acharya CR, Foekens JA, Zhang Y, et al. Young age at diagnosis correlates with worse prognosis and defines a subset of breast cancers with shared patterns of gene expression. Journal of Clinical Oncology. 2008;26(20):3324-30.

11. Russo J, Moral R, Balogh GA, Mailo D, Russo IH. The protective role of pregnancy in breast cancer. Breast Cancer Research. 2005;7(3):131-42.

12. National Cancer Institute: Genetics of Breast and Gynecologic Cancers. 2016.

13. Anders C. Understanding and Treating Triple-Negative Breast Cancer. Oncology-Ny. 2008;22(11):1233-9.

14. Bae SY, Lee SK, Koo MY, Hur SM, Choi MY, Cho DH, et al. The prognoses of metaplastic breast cancer patients compared to those of triple-negative breast cancer patients. Breast cancer research and treatment. 2011;126(2):471-8.

15. Koboldt DC, Fulton RS, McLellan MD, Schmidt H, Kalicki-Veizer J, McMichael JF, et al. Comprehensive molecular portraits of human breast tumours. Nature. 2012;490(7418):61-70.

16. Mack LA, Lindsay RL, Temple WJ. Breast Conservation Surgery: Methods. Methods Cancer Diagn. 2008;1:557-68.

17. Rouanet P, Pujol H. Conservative Surgery of Breast-Cancer - Changes in Ideas and Methods. Presse Med. 1993;22(21):1005-9.

18. NICE guidelines: Early and locally advanced breast cancer: diagnosis and treatment. NICE.org.uk2015.

19. Polyak K. Heterogeneity in breast cancer. J Clin Invest. 2011;121(10):3786-8.

20. Horak ER, Harris AL, Stuart N, Bicknell R. Angiogenesis in Breast-Cancer - Regulation, Prognostic Aspects, and Implications for Novel Treatment Strategies. Breast Cancer: From Biology to Therapy. 1993;698:71-84.

21. Jelicic I, Kapicl TI, Lakic T, Miladinovic M, Lovrenski A, Hardi LV. Evaluation of changes in the Hormone receptor, Her2 status and Ki-67 proliferation following administration of neoadjuvant chemotherapy in breast cancer. Virchows Arch. 2015;467:S59-S.

22. Choi SY, Chang YW, Park HJ, Kim HJ, Hong SS, Seo DY. Correlation of the apparent diffusion coefficiency values on diffusion-weighted imaging with prognostic factors for breast cancer. Brit J Radiol. 2012;85(1016):E474-E9.

23. Basser PJ. Inferring microstructural features and the physiological state of tissues from diffusion-weighted images. NMR in biomedicine. 1995;8(7-8):333-44.

24. Bonekamp S, Corona-Villalobos CP, Kamel IR. Oncologic applications of diffusion-weighted MRI in the body. Journal of Magnetic Resonance Imaging. 2012;35(2):257-79.

25. Cakir O, Arslan A, Inan N, Anik Y, Sarisoy T, Gumustas S, et al. Comparison of the diagnostic performances of diffusion parameters in diffusion weighted imaging and diffusion tensor imaging of breast lesions. European journal of radiology. 2013;82(12):e801-6.

26. Iima M, Le Bihan D, Okumura R, Okada T, Fujimoto K, Kanao S, et al. Apparent Diffusion Coefficient as an MR Imaging Biomarker of Low-Risk Ductal Carcinoma in Situ: A Pilot Study. Radiology. 2011;260(2):364-72.

27. Le Bihan D. Apparent Diffusion Coefficient and Beyond: What Diffusion MR Imaging Can Tell Us about Tissue Structure. Radiology. 2013;268(2):318-22.

28. Nogueira L, Brandao S, Matos E, Nunes RG, Ferreira HA, Loureiro J, et al. Diffusion-weighted breast imaging at 3 T: preliminary experience. Clinical radiology. 2014;69(4):378-84.

29. Onishi N, Kanao S, Kataoka M, Iima M, Sakaguchi R, Kawai M, et al. Apparent Diffusion Coefficient as a Potential Surrogate Marker for Ki-67 Index in Mucinous Breast Carcinoma. Journal of Magnetic Resonance Imaging. 2015;41(3):610-5.

30. Paran Y, Bendel P, Margalit R, Degani H. Water diffusion in the different microenvironments of breast cancer. NMR in biomedicine. 2004;17(4):170-80.

31. Tan SL, Rahmat K, Rozalli FI, Mohd-Shah MN, Aziz YF, Yip CH, et al. Differentiation between benign and malignant breast lesions using quantitative diffusion-weighted sequence on 3 T MRI. Clinical radiology. 2014;69(1):63-71.

32. Pickles MD, Gibbs P, Lowry M, Turnbull LW. Diffusion changes precede size reduction in neoadjuvant treatment of breast cancer. Magnetic resonance imaging. 2006;24(7):843-7.

33. Woodhams R, Matsunaga K, Kan S, Hata H, Ozaki M, Iwabuchi K, et al. ADC mapping of benign and malignant breast tumors. Magnetic resonance in medical sciences : MRMS : an official journal of Japan Society of Magnetic Resonance in Medicine. 2005;4(1):35-42.

34. Hahn EL. Spin Echoes. Phys Rev. 1950;77(5):746-.

35. Hagmann P, Jonasson L, Maeder P, Thiran JP, Wedeen VJ, Meuli R. Understanding diffusion MR imaging techniques: From scalar diffusion-weighted imaging to diffusion tensor imaging and beyond. Radiographics : a review publication of the Radiological Society of North America, Inc. 2006;26:S205-U19.

36. Le Bihan D, Breton E, Lallemand D, Grenier P, Cabanis E, Laval-Jeantet M. MR imaging of intravoxel incoherent motions: application to diffusion and perfusion in neurologic disorders. Radiology. 1986;161(2):401-7.

37. Carr HY, Purcell EM. Effects of Diffusion on Free Precession in Nuclear Magnetic Resonance Experiments. Phys Rev. 1954;94(3):630-8.

38. Stejskal EO, Tanner JE. Spin Diffusion Measurements: Spin Echoes in the Presence of a Time-Dependent Field Gradient. J Chem Phys. 1965;42(1):288-+.

39. Lebihan D, Breton E, Lallemand D, Desbleds MT, Aubin ML, Vignaud J, et al. Contribution of Intravoxel Incoherent Motion (Ivim) Imaging to Neuroradiology. J Neuroradiology. 1987;14(4):295-312.

40. Lebihan D, Breton E, Aubin ML, Lallemand D, Vignaud J. Study of Cerebrospinal-Fluid Dynamics by Mri of Intravoxel Incoherent Motions (Ivim). J Neuroradiology. 1987;14(4):388-95.

41. Lebihan D, Breton E, Lallemand D, Aubin ML, Vignaud J, Lavaljeantet M. Separation of Diffusion and Perfusion in Intravoxel Incoherent Motion Mr Imaging. Radiology. 1988;168(2):497-505.

42. Lebihan D. Intravoxel Incoherent Motion Imaging Using Steady-State Free Precession. Magnet Reson Med. 1988;7(3):346-51.

43. Lebihan D, Turner R, Macfall JR. Effects of Intravoxel Incoherent Motions (Ivim) in Steady-State Free Precession (Ssfp) Imaging - Application to Molecular-Diffusion Imaging. Magnet Reson Med. 1989;10(3):324-37.

44. Bogner W, Gruber S, Pinker K, Grabner G, Stadlbauer A, Weber M, et al. Diffusion-weighted MR for differentiation of breast lesions at 3.0 T: how does selection of diffusion protocols affect diagnosis? Radiology. 2009;253(2):341-51.

45. Dixon WT. Separation of Diffusion and Perfusion in Intravoxel Incoherent Motion Mr Imaging - a Modest Proposal with Tremendous Potential. Radiology. 1988;168(2):566-7.

46. Rydhog AS, van Osch MJP, Lindgren E, Nilsson M, Latt J, Stahlberg F, et al. Intravoxel incoherent motion (IVIM) imaging at different magnetic field strengths: What is feasible? Magnetic resonance imaging. 2014;32(10):1247-58.

47. Iima M, Le Bihan D. Clinical Intravoxel Incoherent Motion and Diffusion MR Imaging: Past, Present, and Future. Radiology. 2016;278(1):13-32.

48. Barbier EL, Lamalle L, Decorps M. Methodology of brain perfusion imaging. Journal of magnetic resonance imaging : JMRI. 2001;13(4):496-520.

49. Onega T, Beaber EF, Sprague BL, Barlow WE, Haas JS, Tosteson ANA, et al. Breast Cancer Screening in an Era of Personalized Regimens A Conceptual Model and National Cancer Institute Initiative for Risk-Based and Preference-Based Approaches at a Population Level. Cancer. 2014;120(19):2955-64.

50. Coleman WB. Breast Cancer Personalized Medicine Challenges and Opportunities. American Journal of Pathology. 2013;183(4):1036-7.

51. Bando H, Ikeda T, Tachi K, Tanaka Y, Iguchi A, Tohno E, et al. The preoperative MRI is useful for planning personalized local treatment in early breast cancer patients without increasing unnecessary extensive surgery. Breast. 2011;20:S36-S.

52. Einstein A. Investigations of The Theory of Brownian Motion 1905 [371-81].

53. Weidner N, Semple JP, Welch WR, Folkman J. Tumor Angiogenesis and Metastasis - Correlation in Invasive Breast-Carcinoma. New Engl J Med. 1991;324(1):1-8.

54. Weidner N, Semple J, Welch W, Folkman J. Tumor Angiogenesis Correlates with Metastasis in Invasive Breast-Carcinoma. Lab Invest. 1991;64(1):A15-A.

55. Folkman J, Watson K, Ingber D, Hanahan D. Induction of Angiogenesis during the Transition from Hyperplasia to Neoplasia. Nature. 1989;339(6219):58-61.

56. Image: Sofia C, Importance of Controlled Mitosis, 2016, Web Blog. Available at : http://cikguaziniwadisofia.blogspot.co.uk/2012/04/importance-of-controlled-mitosis.html. Accessed: June 2016

57. Image: Marsala Biotech Inc., Angiogenesis, Website. Available at: http://www.marsalabiotech.com/technology/#e10a. Accessed: June 2016

58. Image: Zoki K, Animation Still of: Nanoparticle Drug Delivery in Cancer Therapy, MakeAGIF website. Available at: http://makeagif.com/vY0gkm. Accessed: June 2016

59. Le Bihan D. Intravoxel Incoherent Motion Perfusion MR Imaging: A Wake-Up Call. Radiology. 2008;249(3):748-52.

60. Koh DM, Collins DJ, Orton MR. Intravoxel incoherent motion in body diffusion-weighted MRI: reality and challenges. AJR American journal of roentgenology. 2011;196(6):1351-61.

61. Cercueil JP, Petit JM, Nougaret S, Soyer P, Fohlen A, Pierredon-Foulongne MA, et al. Intravoxel incoherent motion diffusion-weighted imaging in the liver: comparison of mono-, bi- and tri-exponential modelling at 3.0-T. European radiology. 2015;25(6):1541-50.

62. Panek R, Borri M, Orton M, O'Flynn E, Morgan V, Giles SL, et al. Evaluation of diffusion models in breast cancer. Med Phys. 2015;42(8):4833-9.

63. Bennett KM, Schmainda KM, Bennett R, Rowe DB, Lu HB, Hyde JS. Characterization of continuously distributed cortical water diffusion rates with a stretched-exponential model. Magnet Reson Med. 2003;50(4):727-34.

64. Zhu LH, Cheng QH, Luo WB, Bao LJ, Guo G. A comparative study of apparent diffusion coefficient and intravoxel incoherent motion-derived parameters for the characterization of common solid hepatic tumors. Acta Radiol. 2015;56(12):1411-8.

65. Zhu L, Zhu LJ, Shi H, Wang HH, Yan J, Liu BR, et al. Evaluating early response of cervical cancer under concurrent chemo-radiotherapy by intravoxel incoherent motion MR imaging. BMC cancer. 2016;16.

66. Zhou Y, Liu J, Liu C, Jia J, Li N, Xie L, et al. Intravoxel incoherent motion diffusion weighted MRI of cervical cancer - Correlated with tumor differentiation and perfusion. Magnetic resonance imaging. 2016;34(8):1050-6.

67. Yang DM, Kim HC, Kim SW, Jahng GH, Won KY, Lim SJ, et al. Prostate cancer: correlation of intravoxel incoherent motion MR parameters with Gleason score. Clin Imag. 2016;40(3):445-50.

68. Zhang L, Murata Y, Ishida R, Ohashi I, Yoshimura R, Shibuya H. Functional evaluation with intravoxel incoherent motion echo-planar MRI in irradiated salivary glands: A correlative study with salivary gland scintigraphy. Journal of Magnetic Resonance Imaging. 2001;14(3):223-9.

69. Luciani A, Vignaud A, Cavet M, Van Nhieu JT, Mallat A, Ruel L, et al. Liver Cirrhosis: Intravoxel Incoherent Motion MR Imaging-Pilot Study. Radiology. 2008;249(3):891-9.

70. Lemke A, Laun FB, Simon D, Stieltjes B, Schad LR. An In Vivo Verification of the Intravoxel Incoherent Motion Effect in Diffusion-Weighted Imaging of the Abdomen. Magnet Reson Med. 2010;64(6):1580-5.

71. Woodhams R, Ramadan S, Stanwell P, Sakamoto S, Hata H, Ozaki M, et al. Diffusion-weighted imaging of the breast: principles and clinical applications. Radiographics : a review publication of the Radiological Society of North America, Inc. 2011;31(4):1059-84.

72. Zhang JL, Sigmund EE, Chandarana H, Rusinek H, Chen Q, Vivier PH, et al. Variability of renal apparent diffusion coefficients: limitations of the monoexponential model for diffusion quantification. Radiology. 2010;254(3):783-92.

73. Lemke A, Stieltjes B, Schad LR, Laun FB. Toward an optimal distribution of b values for intravoxel incoherent motion imaging. Magnetic resonance imaging. 2011;29(6):766-76.

74. Zhang JL, Sigmund EE, Rusinek H, Chandarana H, Storey P, Chen Q, et al. Optimization of b-value sampling for diffusion-weighted imaging of the kidney. Magnetic resonance in medicine : official journal of the Society of Magnetic Resonance in Medicine / Society of Magnetic Resonance in Medicine. 2012;67(1):89-97.

75. Pang Y, Turkbey B, Bernardo M, Kruecker J, Kadoury S, Merino MJ, et al. Intravoxel incoherent motion MR imaging for prostate cancer: an evaluation of perfusion fraction and diffusion coefficient derived from different b-value combinations. Magnetic resonance in medicine : official journal of the Society of Magnetic Resonance in Medicine / Society of Magnetic Resonance in Medicine. 2013;69(2):553-62.

76. Baron P, Dorrius MD, Kappert P, Oudkerk M, Sijens PE. Diffusion-weighted imaging of normal fibroglandular breast tissue: influence of microperfusion and fat suppression technique on the apparent diffusion coefficient. NMR in biomedicine. 2010;23(4):399-405.

77. Tamura T, Usui S, Murakami S, Arihiro K, Akiyama Y, Naito K, et al. Biexponential Signal Attenuation Analysis of Diffusion-weighted Imaging of Breast. Magnetic resonance in medical sciences : MRMS : an official journal of Japan Society of Magnetic Resonance in Medicine. 2010;9(4):195-207.

78. Sigmund EE, Cho GY, Kim S, Finn M, Moccaldi M, Jensen JH, et al. Intravoxel incoherent motion imaging of tumor microenvironment in locally advanced breast cancer.

Magnetic resonance in medicine : official journal of the Society of Magnetic Resonance in Medicine / Society of Magnetic Resonance in Medicine. 2011;65(5):1437-47.

79. Cho GY, Moy L, Kim SG, Baete SH, Moccaldi M, Babb JS, et al. Evaluation of breast cancer using intravoxel incoherent motion (IVIM) histogram analysis: comparison with malignant status, histological subtype, and molecular prognostic factors. European radiology. 2016;26(8):2547-58.

80. Cho GY, Moy L, Zhang JL, Baete S, Lattanzi R, Moccaldi M, et al. Comparison of Fitting Methods and b-Value Sampling Strategies for Intravoxel Incoherent Motion in Breast Cancer. Magnet Reson Med. 2015;74(4):1077-85.

81. Liu C, Liang C, Liu Z, Zhang S, Huang B. Intravoxel incoherent motion (IVIM) in evaluation of breast lesions: comparison with conventional DWI. European journal of radiology. 2013;82(12):e782-9.

82. Liu C, Wang K, Chan Q, Liu Z, Zhang J, He H, et al. Intravoxel incoherent motion MR imaging for breast lesions: comparison and correlation with pharmacokinetic evaluation from dynamic contrast-enhanced MR imaging. European radiology. 2016.

83. Bokacheva L, Kaplan JB, Giri DD, Patil S, Gnanasigamani M, Nyman CG, et al. Intravoxel incoherent motion diffusion-weighted MRI at 3.0 T differentiates malignant breast lesions from benign lesions and breast parenchyma. Journal of magnetic resonance imaging : JMRI. 2014;40(4):813-23.

84. Iima M, Yano K, Kataoka M, Umehana M, Murata K, Kanao S, et al. Quantitative Non-Gaussian Diffusion and Intravoxel Incoherent Motion Magnetic Resonance Imaging Differentiation of Malignant and Benign Breast Lesions. Investigative radiology. 2015;50(4):205-11.

85. Suo S, Lin N, Wang H, Zhang L, Wang R, Zhang S, et al. Intravoxel incoherent motion diffusion-weighted MR imaging of breast cancer at 3.0 tesla: Comparison of different curve-fitting methods. Journal of magnetic resonance imaging : JMRI. 2015;42(2):362-70.

86. Liu CL, Liang CH, Liu ZY, Zhang SX, Huang B. Intravoxel incoherent motion (IVIM) in evaluation of breast lesions: Comparison with conventional DWI. European journal of radiology. 2013;82(12):E782-E9.

87. Cho GY, Kim S, Jensen JH, Storey P, Sodickson DK, Sigmund EE. A versatile flow phantom for intravoxel incoherent motion MRI. Magnetic resonance in medicine : official journal of the Society of Magnetic Resonance in Medicine / Society of Magnetic Resonance in Medicine. 2012;67(6):1710-20.

88. Fakhran S, Alhilali L, Kale H, Kanal E. Assessment of Rates of Acute Adverse Reactions to Gadobenate Dimeglumine: Review of More Than 130,000 Administrations in 7.5 Years. Am J Roentgenol. 2015;204(4):703-6.

89. McDonald RJ, McDonald JS, Kallmes DF, Jentoft ME, Murray DL, Thielen KR, et al. Intracranial Gadolinium Deposition after Contrast-enhanced MR Imaging. Radiology. 2015;275(3):772-82.

90. Jambor I, Merisaari H, Aronen HJ, Jarvinen J, Saunavaara J, Kauko T, et al. Optimization of b-value distribution for biexponential diffusion-weighted MR imaging of normal prostate. Journal of magnetic resonance imaging : JMRI. 2014;39(5):1213-22.

91. Leporq B, Saint-Jalmes H, Rabrait C, Pilleul F, Guillaud O, Dumortier J, et al. Optimization of intra-voxel incoherent motion imaging at 3.0 Tesla for fast liver examination. Journal of magnetic resonance imaging : JMRI. 2015;41(5):1209-17.

92. Dyvorne H, Jajamovich G, Kakite S, Kuehn B, Taouli B. Intravoxel incoherent motion diffusion imaging of the liver: Optimal b-value subsampling and impact on parameter precision and reproducibility. European journal of radiology. 2014;83(12):2109-13.

93. Liao Y, Urayama S, Fukuyama H. Optimal Protocols and Analysis Strategies for Intravoxel Incoherent Motion Mill. Med Phys. 2015;42(6):3215-6.

94. Sigmund EE, Cho GY, Kim S, Finn M, Moccaldi M, Jensen JH, et al. Intravoxel Incoherent Motion Imaging of Tumor Microenvironment in Locally Advanced Breast Cancer. Magnet Reson Med. 2011;65(5):1437-47.

95. Cho GY, Moy L, Kim SG, Baete SH, Moccaldi M, Babb JS, et al. Evaluation of breast cancer using intravoxel incoherent motion (IVIM) histogram analysis: comparison with malignant status, histological subtype, and molecular prognostic factors. European radiology. 2016;26(8):2547-58.

96. Taouli B, Beer AJ, Chenevert T, Collins D, Lehman C, Matos C, et al. Diffusion-weighted imaging outside the brain: Consensus statement from an ISMRM-sponsored workshop. Journal of magnetic resonance imaging : JMRI. 2016.

97. Dorrius MD, Dijkstra H, Oudkerk M, Sijens PE. Effect of b value and pre-admission of contrast on diagnostic accuracy of 1.5-T breast DWI: a systematic review and meta-analysis. European radiology. 2014;24(11):2835-47.

98. Shrager RI, Weiss GH, Spencer RG. Optimal time spacings for T2 measurements: monoexponential and biexponential systems. NMR in biomedicine. 1998;11(6):297-305.

99. Cramer H. Citation Classic - Mathematical-Methods of Statistics. Cc/Phys Chem Earth. 1983(28):18-.

100. Rao CR. Information and the Accuracy Attainable in the Estimation of Statistical Parameters. Resonance. 2015;20(1):78-90.

101. Anastasiou A, Hall LD. Optimisation of T2 and M0 measurements of bi-exponential systems. Magnetic resonance imaging. 2004;22(1):67-80.

102. Dula AN, Gochberg DF, Does MD. Optimal echo spacing for multi-echo imaging measurements of Bi-exponential T2 relaxation. J Magn Reson. 2009;196(2):149-56.

103. Zhang QW, Wang YX, Ma HT, Yuan J. Cramer-Rao Bound for Intravoxel Incoherent Motion Diffusion Weighted Imaging Fitting. 2013 35th Annual International Conference of the Ieee Engineering in Medicine and Biology Society (Embc). 2013:511-4.

104. Firbank MJ, Coulthard A, Harrison RM, Williams ED. A comparison of two methods for measuring the signal to noise ratio on MR images. Phys Med Biol. 1999;44(12):N261-N4.

105. Brennan P, Silman A. Statistical methods for assessing observer variability in clinical measures. Bmj. 1992;304(6840):1491-4.

106. Freiman M, Afacan O, Mulkern RV, Warfield SK. Improved Multi B-Value Diffusion-Weighted MRI of the Body by Simultaneous Model Estimation and Image Reconstruction

(SMEIR). Medical Image Computing and Computer-Assisted Intervention (Miccai 2013), Pt Iii. 2013;8151:1-8.

107. Yamada I, Aung W, Himeno Y, Nakagawa T, Shibuya H. Diffusion coefficients in abdominal organs and hepatic lesions: Evaluation with intravoxel incoherent motion echo-planar MR imaging. Radiology. 1999;210(3):617-23.

108. Lemke A, Laun FB, Klauss M, Re TJ, Simon D, Delorme S, et al. Differentiation of Pancreas Carcinoma From Healthy Pancreatic Tissue Using Multiple b-Values Comparison of Apparent Diffusion Coefficient and Intravoxel Incoherent Motion Derived Parameters. Investigative radiology. 2009;44(12):769-75.

109. Chandarana H, Kang SK, Wong S, Rusinek H, Zhang JL, Arizono S, et al. Diffusion-Weighted Intravoxel Incoherent Motion Imaging of Renal Tumors With Histopathologic Correlation. Investigative radiology. 2012;47(12):688-96.

110. Bisdas S, Klose U. IVIM analysis of brain tumors: an investigation of the relaxation effects of CSF, blood, and tumor tissue on the estimated perfusion fraction. Magn Reson Mater Phy. 2015;28(4):377-83.

111. Fujima N, Yoshida D, Sakashita T, Homma A, Tsukahara A, Tha KK, et al. Intravoxel incoherent motion diffusion-weighted imaging in head and neck squamous cell carcinoma: Assessment of perfusion-related parameters compared to dynamic contrast-enhanced MRI. Magnetic resonance imaging. 2014;32(10):1206-13.

112. Pieper CC, Sprinkart AM, Meyer C, Konig R, Schild HH, Kukuk GM, et al. Evaluation of a Simplified Intravoxel Incoherent Motion (IVIM) Analysis of Diffusion-Weighted Imaging for Prediction of Tumor Size Changes and Imaging Response in Breast Cancer Liver Metastases Undergoing Radioembolization A Retrospective Single Center Analysis. Medicine. 2016;95(14).

113. Che S, Zhao X, Ou Y, Li J, Wang M, Wu B, et al. Role of the Intravoxel Incoherent Motion Diffusion Weighted Imaging in the Pre-treatment Prediction and Early Response Monitoring to Neoadjuvant Chemotherapy in Locally Advanced Breast Cancer. Medicine (Baltimore). 2016;95(4):e2420.

114. Lang TA, Altman DG. Basic statistical reporting for articles published in biomedical journals: the "Statistical Analyses and Methods in the Published Literature" or the SAMPL Guidelines. International journal of nursing studies. 2015;52(1):5-9.

115. Razali NW, Yap Bee Power comparisons of Shapiro–Wilk, Kolmogorov–Smirnov, Lilliefors and Anderson–Darling tests. Journal of Statistical Modeling and Analytics. 2011;2(1):21-33.

116. Pang YX, Turkbey B, Bernardo M, Kruecker J, Kadoury S, Merino MJ, et al. Intravoxel incoherent motion MR imaging for prostate cancer: An evaluation of perfusion fraction and diffusion coefficient derived from different b-value combinations. Magnet Reson Med. 2013;69(2):553-62.

117. Le Bihan D, Breton E, Lallemand D, Aubin ML, Vignaud J, Laval-Jeantet M. Separation of diffusion and perfusion in intravoxel incoherent motion MR imaging. Radiology. 1988;168(2):497-505.

118. Blackledge MD, Leach MO, Collins DJ, Koh DM. Computed diffusion-weighted MR imaging may improve tumor detection. Radiology. 2011;261(2):573-81.

119. Ortendahl DA, Hylton NM, Kaufman L, Crooks LE, Mills CM, Davis PL, et al. Calculational Tools for the Retrospective Evaluation of Nmr Imaging Procedures. Investigative radiology. 1984;19(5):S34-S.

120. Ortendahl DA, Hylton NM, Kaufman L, Crooks LE, Mills CM, Davis PL. Computational Techniques in Nmr Imaging. Ieee T Bio-Med Eng. 1984;31(8):569-.

121. Riederer SJ, Suddarth SA, Bobman SA, Lee JN, Wang HZ, Macfall JR. Automated Mr Image Synthesis - Feasibility Studies. Radiology. 1984;153(1):203-6.

122. Kuroki Y, Nasu K. Advances in breast MRI: diffusion-weighted imaging of the breast. Breast cancer. 2008;15(3):212-7.

123. Ueno Y, Takahashi S, Ohno Y, Kitajima K, Yui M, Kassai Y, et al. Computed diffusion-weighted MRI for prostate cancer detection: the influence of the combinations of b-values. The British journal of radiology. 2015;88(1048):20140738.

124. Ueno Y, Takahashi S, Kitajima K, Kimura T, Aoki I, Kawakami F, et al. Computed diffusion-weighted imaging using 3-T magnetic resonance imaging for prostate cancer diagnosis. European radiology. 2013;23(12):3509-16.

125. Shimizu H, Isoda H, Fujimoto K, Kawahara S, Furuta A, Shibata T, et al. Comparison of acquired diffusion weighted imaging and computed diffusion weighted imaging for detection of hepatic metastases. European journal of radiology. 2013;82(3):453-8.

126. McDonald RJ, McDonald JS, Bida JP, Carter RE, Fleming CJ, Misra S, et al. Intravenous Contrast Material-induced Nephropathy: Causal or Coincident Phenomenon? Radiology. 2016;278(1):306.

127. McDonald JS, McDonald RJ, Carter RE, Katzberg RW, Kallmes DF, Williamson EE. Risk of intravenous contrast material-mediated acute kidney injury: a propensity score-matched study stratified by baseline-estimated glomerular filtration rate. Radiology. 2014;271(1):65-73.

128. Bodammer N, Kaufmann J, Kanowski M, Tempelmann C. Eddy current correction in diffusion-weighted imaging using pairs of images acquired with opposite diffusion gradient polarity. Magnetic resonance in medicine : official journal of the Society of Magnetic Resonance in Medicine / Society of Magnetic Resonance in Medicine. 2004;51(1):188-93.

129. Tamura T, Murakami S, Naito K, Yamada T, Fujimoto T, Kikkawa T. Investigation of the optimal b-value to detect breast tumors with diffusion weighted imaging by 1.5-T MRI. Cancer imaging : the official publication of the International Cancer Imaging Society. 2014;14:11.

130. Thomassin-Naggara I, De Bazelaire C, Chopier J, Bazot M, Marsault C, Trop I. Diffusion-weighted MR imaging of the breast: advantages and pitfalls. European journal of radiology. 2013;82(3):435-43.

131. Takanaga M, Hayashi N, Miyati T, Kawashima H, Hamaguchi T, Ohno N, et al. [Influence of b value on the measurement of contrast and apparent diffusion coefficient in 3.0 Tesla breast magnetic resonance imaging]. Nihon Hoshasen Gijutsu Gakkai zasshi. 2012;68(3):201-8.

132. Pereira FP, Martins G, Figueiredo E, Domingues MN, Domingues RC, da Fonseca LM, et al. Assessment of breast lesions with diffusion-weighted MRI: comparing the use of different b values. AJR American journal of roentgenology. 2009;193(4):1030-5.

133. Grant KB, Agarwal HK, Shih JH, Bernardo M, Pang YX, Daar D, et al. Comparison of calculated and acquired high b value diffusion-weighted imaging in prostate cancer. Abdominal imaging. 2015;40(3):578-86.

134. Bittencourt LK, Attenberger UI, Lima D, Strecker R, de Oliveira A, Schoenberg SO, et al. Feasibility study of computed vs measured high b-value (1400 s/mm(2)) diffusion-weighted MR images of the prostate. World journal of radiology. 2014;6(6):374-80.

135. Maas MC, Futterer JJ, Scheenen TW. Quantitative evaluation of computed high B value diffusion-weighted magnetic resonance imaging of the prostate. Investigative radiology. 2013;48(11):779-86.

136. Gatidis S, Schmidt H, Martirosian P, Nikolaou K, Schwenzer NF. Apparent diffusion coefficient-dependent voxelwise computed diffusion-weighted imaging: An approach for improving SNR and reducing T2 shine-through effects. Journal of magnetic resonance imaging : JMRI. 2016;43(4):824-32.

137. National Statistics via Health and Social Care Information Centre, NHS Breast Screening Program Statistics (NHS England), 2016. Available at: https://www.gov.uk/government/statistics/breast-screening-programme-england-statistics-for-2014-to-2015. Accessed Febuary 2016.

138. Turnbull LW, Brown SR, Olivier C, Harvey I, Brown J, Drew P, et al. Multicentre randomised controlled trial examining the cost-effectiveness of contrast-enhanced high field magnetic resonance imaging in women with primary breast cancer scheduled for wide local excision (COMICE). Health Technol Asses. 2010;14(1):1-+.

139. Tempany CM, McDannold NJ, Hynynen K, Jolesz FA. Focused ultrasound surgery in oncology: overview and principles. Radiology. 2011;259(1):39-56.

140. Sapareto SA, Dewey WC. Thermal dose determination in cancer therapy. International journal of radiation oncology, biology, physics. 1984;10(6):787-800.

141. Moonen CT. Spatio-temporal control of gene expression and cancer treatment using magnetic resonance imaging-guided focused ultrasound. Clinical cancer research : an official journal of the American Association for Cancer Research. 2007;13(12):3482-9.

142. McDannold NJ, Jolesz FA. Magnetic resonance image-guided thermal ablations. Top Magn Reson Imaging. 2000;11(3):191-202.

143. Rieke V, Butts Pauly K. MR thermometry. Journal of magnetic resonance imaging : JMRI. 2008;27(2):376-90.

144. Cady B. Traditional and future management of nonpalpable breast cancer. Am Surg. 1997;63(1):55-8.

145. Coburn NG, Chung MA, Fulton J, Cady B. Decreased breast cancer tumor size, stage, and mortality in Rhode Island: an example of a well-screened population. Cancer Control. 2004;11(4):222-30.

146. Liberman L, Kaplan J, Van Zee KJ, Morris EA, LaTrenta LR, Abramson AF, et al. Bracketing wires for preoperative breast needle localization. AJR American journal of roentgenology. 2001;177(3):565-72.

147. Rissanen TJ, Makarainen HP, Mattila SI, Karttunen AI, Kiviniemi HO, Kallioinen MJ, et al. Wire localized biopsy of breast lesions: a review of 425 cases found in screening or clinical mammography. Clinical radiology. 1993;47(1):14-22.

148. Vuorela AL, Ahonen A. Preoperative stereotactic hookwire localization of nonpalpable breast lesions with and without the use of a further stereotactic check film. Anticancer Res. 2000;20(2B):1277-9.

149. Homer MJ. Nonpalpable breast lesion localization using a curved-end retractable wire. Radiology. 1985;157(1):259-60.

150. Kelly P, Winslow EH. Needle wire localization for nonpalpable breast lesions: sensations, anxiety levels, and informational needs. Oncol Nurs Forum. 1996;23(4):639-45.

151. Smith LF, Rubio IT, Henry-Tillman R, Korourian S, Klimberg VS. Intraoperative ultrasound-guided breast biopsy. American journal of surgery. 2000;180(6):419-23.

152. Cox CE, Furman B, Stowell N, Ebert M, Clark J, Dupont E, et al. Radioactive seed localization breast biopsy and lumpectomy: can specimen radiographs be eliminated? Annals of surgical oncology. 2003;10(9):1039-47.

153. Bennett IC, Greenslade J, Chiam H. Intraoperative ultrasound-guided excision of nonpalpable breast lesions. World journal of surgery. 2005;29(3):369-74.

154. Tafra L, Fine R, Whitworth P, Berry M, Woods J, Ekbom G, et al. Prospective randomized study comparing cryo-assisted and needle-wire localization of ultrasound-visible breast tumors. American journal of surgery. 2006;192(4):462-70.

155. Schmitz AC, van den Bosch MA, Rieke V, Dirbas FM, Butts Pauly K, Mali WP, et al. 3.0-T MR-guided focused ultrasound for preoperative localization of nonpalpable breast lesions: an initial experimental ex vivo study. Journal of magnetic resonance imaging : JMRI. 2009;30(4):884-9.

156. Bitton RR, Kaye E, Dirbas FM, Daniel BL, Pauly KB. Toward MR-guided high intensity focused ultrasound for presurgical localization: focused ultrasound lesions in cadaveric breast tissue. Journal of magnetic resonance imaging : JMRI. 2012;35(5):1089-97.

157. Hipp E, Fan X, Partanen A, Vosicky J, Pelizzari CA, Straus CM, et al. Quantitative evaluation of internal marks made using MRgFUS as seen on MRI, CT, US, and digital color images - a pilot study. Physica medica : PM : an international journal devoted to the applications of physics to medicine and biology : official journal of the Italian Association of Biomedical Physics. 2014;30(8):941-6.

158. Image: InSightec, MRgFUS system with GE MR scanner, 2014. Available at: http://www.insightec.com

159. Payne A, Todd N, Minalga E, Wang Y, Diakite M, Hadley R, et al. In vivo evaluation of a breast-specific magnetic resonance guided focused ultrasound system in a goat udder model. Med Phys. 2013;40(7):073302.

160. Bohris C, Jenne JW, Rastert R, Simiantonakis I, Brix G, Spoo J, et al. MR monitoring of focused ultrasound surgery in a breast tissue model in vivo. Magnetic resonance imaging. 2001;19(2):167-75.